Nanoscale Electrocatlyst for Chemicalnd Biolgical Sensor

Zhu, Nan; Chi, Qijin; Ulstrup, Jens

Publication date:
2014

Document Version
Peer reviewed version

Technical University of Denmark

Nanoscale Electrocatalysts for Chemical and Biological Sensors

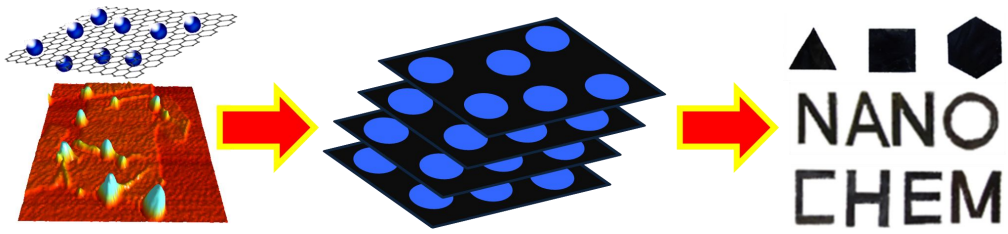

Ph. D. Thesis
Nan Zhu
Department of Chemistry
Technical University of Denmark
2013

DTU Chemistry
Department of Chemistry

Technical University of Denmark

Nanoscale Electrocatalysts for Chemical and Biological Sensors

Nan Zhu

Ph. D. Thesis

Department of Chemistry
Technical University of Denmark

November 2013

DTU Chemistry
Department of Chemistry

Preface and Acknowledgements

This thesis is submitted in candidacy for the PhD degree from Technical University of Denmark (DTU). This research project was carried out at Nanochemistry Group, Department of Chemistry, Technical University of Denmark under the supervision of Professor Jens Ulstrup and Associate Professor Qijin Chi. Financial supports from Department of Chemistry, Technical University of Denmark and NanScience Center, University of Copenhagen are acknowledged.

First of all, I would like to express my appreciation towards my two supervisors Professor Jens Ulstrup and Associate Professor Qijin Chi for their highly inspirational guidance and willingness to share their immense knowledge in all aspects in theory and practice. Their instructions, countless hours of discussion, regular meetings and guidance help me steer in the right direction during the PhD period. I also owe a great gratitude to Associate Professor Jingdong Zhang for always having an interest in my project, helping in experiments and hours of discussion. I am grateful to all group members at NanoChemistry Group for their support as well as creating a friendly and active scientific atmosphere. Additionally, I would also like to thank Professor Tõnu Pullerits, Department of Chemical Physics, Lund University with kindness and supervision for my doing a large portion of this dissertation in his laboratory during an external research stay. In this context, I especially appreciate to Kaibo Zheng, Mohamed Abdellah, Qiushi Zhu, Khadga Jung Karki and Associate Professor Sophie Canton for their effective help.

Finally, I would like to express my special appreciation to my family for their support and patience. I would also like to thank to all my friends both in Denmark and China.

Kongens Lyngby, 30 November, 2013

Nan Zhu

Abstract

This dissertation describes scientific research that covers preparation and use of two classes of designed inorganic hybrid nanostructures (nanoparticles and graphene) as electrocatalysts in interfacial molecular and biomolecular electron transfer and electrocatalysis. Emphasis is on both fundamental properties of the nanostructures and on their use in chemical and biological sensing devices at the single-molecular scale. The project is focused on electroactive (or redox) *Prussian blue* nanoparticles (PBNPs) as well as on graphene and quantum dots (QDs). The results have offered significant interests in understanding of fundamental electronic properties of hybrid nanomaterials and their potential applications in next generation ultra-sensitive chemical sensors and biosensors.

As the first man-made coordination compound, *Prussian Blue* (PB) has a long history dating back over 300 years ago (the first synthesis in 1704). This interesting material has recently been used broadly as an electron transfer (ET) catalyst for new chemical and biological sensors. We have initiated efforts in synthesis, functional characterization and applications of PB in novel nanostructured forms focused on controlled-size PB nanoparticles (PBNPs). Fast and reversible interfacial PBNP ET on an Au (111) electrode surface modified with functional alkanethiols was detected. In terms of ET characteristics, assembled on a solid surface in a two-dimensional array these nanoparticles behave like a large redox molecule such as a metalloenzyme in the electrocatalytic reduction of H_2O_2 and glucose oxidation, suggesting a tunneling mechanism. Furthermore, the interfacial electrochemical ET and electrocatalysis of PBNPs immobilized on Au(111)-electrode surfaces modified by variable-length differently functionalized thiol-based self-assembled molecular monolayers (SAMs) have been explored. The SAMs are terminated by positively (–NH_3^+) and negatively charged groups (-COO^-) as well as by neutral hydrophobic groups (-CH_3). In addition, three-dimensional networks of cross-linked [Poly(ethyleneimine) (PEI)] onto which PBNPs are attached by electrostatic forces have been fabricated and assembled on single-crystal Au(111) electrode surfaces to

enhance electrocatalysis resulting from the 3D nanostructure skeleton. *In situ* AFM of the different assembled layers in the electrolyte solution shows molecular scale structures on the surface, in keeping with electrochemical behavior.

To increase the conductivity of PBNPs as an active electrode, reduced graphene oxide (RGO) and PBNPs were exploited as building ingredients to prepare with increased electrical conductivity and functional variability nanohybrid electrocatalysts, which are further transformed into free-standing graphene papers. PBNPs doped graphene paper shows highly efficient electrocatalysis towards reduction of hydrogen peroxide and can be used as flexible chemical sensors for potential applications in detection of hydrogen peroxide or/and other organic peroxides. The as-prepared PBNPs-RGO paper is further capable of biocompatible accommodation of enzymes for development of freestanding enzyme based biosensors and as a potentially platform for electrocatalytic energy conversion.

Graphene/PBNPs paper obtained using Au filter substrate shows high electrical conductivity, outstanding mechanical strength, excellent thermal stability, and structural uniformity. This type of paper has good electrochemical performance. Strong electrocatalysis property has, furthermore, been achieved using these mixed materials. This variety of flexible active electrodes can be freely used for electrocatalytic monitoring H_2O_2, glucose or other analytes.

A new method based on one-step oil/water (O/W) two phase induced interfacial self-assembly of RGO nanosheets into graphene nanofilms has been refined. The method shows high efficiency for incorporation of CdSe quantum dots (QDs) into nanofilms to prepare QDs doped graphene nanostructures. Confined QDs interact closely with RGO to promote and to significantly enhance photoinduced electron or energy transfer between RGO and CdSe QDs, which could hold promise for their applications as photovoltaic materials in solar cells.

Dansk résumé

Denne ph.d.-afhandling beskriver videnskabeligt arbejde der omhandler præparation og brug af to klasser af designede uorganiske hybride nanostrukturer (nanopartikler og grafen) som elektrokatalysatorer i interfacial molekylær and biomolekylær elektronoverførsel (ET) og elektrokatalyse. Der er lagt vægt både på nanostrukturernes fundamentale egenskaber og på deres anvendelse i kemiske og biologiske sensorer i enkeltmolekyleskala. Projektet er fokuseret på elektroaktive (redox) nanopartikler af Prøjsiskblåt (PBNPs) og analoge heraf (PBA), så vel som på grafen og "kvanteprikker" (quantum dots, QD). Resultaterne har betydning for den fundamentale forståelse af biologisk elektrisk ladningstransport, og for elektroniske egenskaber og anvendelser i næste-generation ultra-følsomme biosensorer og andre biofysiske komponenter.

Prøjsiskblåts (PB) historie går mere end 300 år tilbage. Dette spændende materiale er for nylig taget i brug som katalysator for ET processer i nye kemiske og biologiske sensorer. Vi har indledt projekter inden for syntese, funktionel karakterisering og anvendelser af PB i ny nanostruktureret form med fokus på PBNPs af veldefineret kontrolleret størrelse (her 5-7 nm). Hurtig PBNP ET på en Au (111)-elektrodeoverflade modificeret med monolag af funktionaliserede alkanthioler kunne påvises. I immobiliseret form på en fast overflade i et todimenalt "array" udviser nanopartiklerne ET karakteristika, der ligner tilsvarende egenskaber hos store redoxmolekyler eller metalloenzymer i H_2O_2's og glukoses elektrocatalytiske processer, hvad der stærkt indikerer mekanismer baseret på den kvantemekaniske tunneleffekt. Elektrokemisk ET og elektrokatalyse med PBNPs immobiliseret på Au(111)-elektrodeoverflader modificeret med molekylære monolag (SAMs) af thioler med varierende længde og funktionaliseret med positivt ($–NH_3^+$) og negativet elektrisk ladede ($-COO^-$) eller med neutrale hydrofobe endegrupper ($-CH_3$) blev videre undersøgt systematisk. Desuden er tredimensionale netværk af krydsbundent Poly(ethyleneimine) (PEI)], hvortil PBNPs er sammenknyttet med elektrostatiske kræfter blevet fremstillet og samlet på enkeltkrystal Au(111)-elektrodeoverflader med

henblik på øget elektrokatalyse fra denne tredimensionelle nanostrukturs skelet. *In situ* AFM af de forskellige immobiliserede lag i elektrolytopløsningen viser overfladestrukturer i molekylær skala, i overesstemmelse med de elektrokemiske data.

I en fortsættelse af PBNP's elektrokatalytiske egenskaber blev ledningsevne og elektrokemiske egenskaber hos PBNPs immobiliseret på reduceret grafenoxid (RGO) and PBNPs undersøgt. Disse er mulige byggesten i forbedrede funktionelle nanohybride elektrokatalysatorer, yderligere overført til fritstående grafenpapirform. PBNP-dopet grafenpapir viste meget effektiv elektrokatalyse over for reduction af hydrogenperoxid, af potential betydning som fleksible kemiske sensorer i kommende anvendelse til påvisning af hydrogenperoxid og/eller organiske peroxider. Det fremstillede PBNP–RGO papir er biokompatibelt og kan indkorporere enzymer i udvikling af nye fritstående enzymbaserede biosensorr og som platform for elektrokatalytisk energiomsætning.

Grafen/PBNP papir på Au-filtersubstrat viste høj elektrisk ledningsevne og termisk stabilitet, stor mekanisk styrke, høj strukturel ensartethed samt glimrende elektrokemiske egenskaber, herunder elektrokatalytiske egenskaber. Denne hybridtype af fleksible aktive elektrodematerialer kan videre anvendes til bestemmelse af H_2O_2, glucose og anden enzymbaseret højfølsom elektrokatalyse.

Endelig er en ny ét-trins O/W interfaces teknik til hurtig fabrikation af grafennanolag med store overflader og overfladedopet med CdSe QDs blevet udviklet. RGO and CdSe QDs vekselvirker tæt i denne type blandede RGO-CdSe QD nanomaterialer, afspejlet i ny finstruktur og stærkt øget effektivitet i fotoinduceret ET og energioverførselsprocesser.

Abbreviations

AFM	Atomic force microscope
CV	Cyclic voltammetry or cyclic voltammogram
DTSP	Dithiobis (succinimidyl propionate)
EIS	Electrochemical impedance spectroscopy
ET	Electron transfer
EXAFS	Extended x-ray absorption fine structure
FTIR	Fourier transform infrared spectroscopy
GO	Graphene oxide
GOD	Glucose oxidase
NPs	Nanoparticles
QDs	Quantum dots
O/W	Oil/Water two phase interface method
PB	Prussian blue
PBNPs	Prussian blue nanoparticles
PEI	Poly (ethyleneimine)
RHE	Reversible hydrogen electrode
RGO	Reduced graphene oxide
SEM	Scanning electron microscope
SAM	Self-assemble monolayer
SAMs	Self-assemble monolayers
TA	Transient absorption
TEM	Transmission electron microscope
UV-Vis	Ultraviolet and visible spectrophotometer
XRD	X-ray diffraction

Table of Contents

Part I: Introduction to Research Background

1. General Introduction

This dissertation describes scientific research that covers preparation and use of some specifically designed inorganic hybrid nanostructures (nanoparticles and graphene) as electrocatalysts in interfacial molecular and biomolecular electron transfer and electrocatalysis. Emphasis is on both fundamental properties of the nanostructures and on their use in chemical and biological sensing devices, especially at the single-molecular scale. The project is particularly focused on electroactive (or redox) *Prussian blue* nanoparticles (PBNPs) as well as on graphene and quantum dots (QDs). The results have offered significant interests in understanding of fundamental electronic properties of hybrid nanomaterials and their potential applications in next generation ultra-sensitive chemical sensors and biosensors.

In the following sections, nanotechnology and nanostructures are briefly introducted first (including Inorganic hybrid nanostructured materials, such as PBNPs and graphene), followed by the description of their electrocatalytic applications in the field of biological and chemical sensors.

1.1 Nanotechnology and Nanostructures

Nanotechnology is all around us in our daily life and encountered in important applications below the sub-microscopic level. Nanotechnology is based on the manipulation at atomic and molecular scale to at dimensions between approximately 1 and 100 nm, and first proposed by the famous physicist Richard Feynman in his talk “There’s Plenty of Room at the Bottom.” in 1959.[1, 2] The nanoworld is distinct from the macroscopic world that we are normally accustomed to face in life and applications. Other aspects of particular physical or chemical performance in nanotechnology appear their scales, such as quantum mechanical features, faster

electron/ion transport, improved plasticity, noticeable thermal and optical properties, higher reactivity and activity, etc.[1, 2]

In order to measure and detect the properties of this nanoscopic size range, the old technology could not keep up the pace with unpredictable laws of quantum mechanics. Many promising new methods and tools have been developed in nanotechnology to acquire knowledge about physical or chemical phenomena at nanoscale, and to probe new nanomaterials with novel properties and functions for a wide range of applications. Nowadays, nanotechnology involves physical, chemical, biological and other knowledge of interdisciplinary extending to scales ranging right down to individual atoms and molecules.[3]

At the same time, nanotechnology also leads to new economic challenges and opportunities in the scientific realm. Nanostructure is one of the most important properties for nanotechnology, extending to dimensions of one hundred thousand times less than the diameter of a human hair.[4] Nanostructures have a broad range of inclusions and cover many distinct kinds of structures (such as nanofilms, nanotube, nanosheets, nanorods, nanoflowers, nanoparticles and quantum dots) classified by the dimensions and shapes at the nanoscale. Scientists are also trying to engineer nanostructures at an incredible pace. As noted, the research of nanostructures draws people in from interdisciplinary fields including physics, chemistry, biology and engineering. From clean energy solutions to molecular recognition and medical applications, nanostructures are taking the world of nanoscience and nanotechnology by storm.

1.2 Electrocatalysis for Biological and Chemical Sensors

Electrocatalysis is the name for catalytic processed in which catalyst participates in electrochemical reactions, brought to work as biosensor analytical devices, used for the detection of analyte.[6] The development of chemical sensors and biosensors for practical devices has driven introduced worldwide scientific research activity during

the last 20 years. With a growing inventory of nanomaterials and nanofabrication techniques, a noteworthy tendency of chemical or biological biosensor technology is likely to push towards nanotechnology, with discoveries of novel nanomaterials for the fabrication of functional nanostructure-based devices at the nanoscale.[7]

Nanomaterials are exquisitely suitable for chemical or biological sensors. Surface catalytic reactions and electrocatalysis are known to be very sensitive to the atomic-level structure of the heterogeneous interface and the nanoscale.[8] The nanoscale properties of nanostructured materials play an important role in enhancing the electrocatalysis efficiency, resulting from maximize the surface over volume ratio in practical applications.[9] Different dimensions and types of the nanostructure-based biosensor materials, such as nanoparticles, nanotubes, nanorods, nanowires, or graphene-based devices are being studied regarding their biosensing performance and future potential development.[7] Nanobiosensors demonstrate unique bioreceptor probe function that is highly selective for target analyte molecules, with rapid and low cost reaction often using specific local home-made designs.[10]

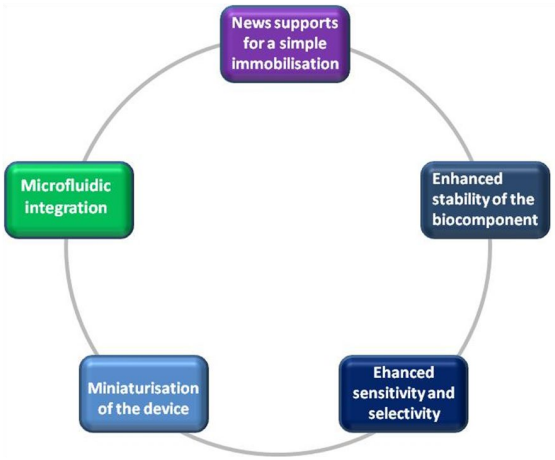

Figure 1.1. Contributions of nanotechnology to the development of biosensors with commercial promise.[2]

Nanotechnology contributions for these offer of biosensors with commercial promise is shown in Fig. 1.1. Nowadays widespread application in the fields of microfluidic integration, miniaturization of the devices, enhanced sensitivity and selectivity, enhanced stability of the biocomponent and new supports for simple immobilization.[2]

1.3 Outline of the Dissertation

This dissertation consists of four main parts. Part I gives a general introduction of the research background. Part II and III are the detailed project parts. Part II describes the Prussian blue nanoparticles self-assembled as nanostructures for electron transfer and applications in sensors and biosensors. Part III concerns the graphene-supported nanoparticles or quantum dots hybrid nanomaterials for electrocatalysis and photoinduced ET. Finally, Part IV includes a concluding summary and two appendices.

There are five chapters in Part I. Following the introduction of Nanotechnology, nanostructures, and electrocatalysis for biological and chemical sensors in Chapter 1, Chapter 2 describes inorganic hybrid nanostructured materials, including Prussian blue (PB), Prussian Blue Nanoparticles (PBNPs) and their structure and electrochemical properties, as well as the applications in sensors and biosensors. Another new recent famous nanomaterial graphene and graphene paper is also introduced. Chapter 3 provides background and knowledge about self-assembled monolayers (SAMs) based nanotechnology, especially for gold-thiol SAMs and their applications in the field of electrochemistry for biosensors. Chapter 4 gives basic principles of the enzyme catalysis kinetics. The experimental methods and technology section are described in chapter 5, mainly focusing on electrochemistry (reference electrode of reversible hydrogen electrode, cyclic voltammetry, diffusion-controlled systems, diffusion-less systems and so on) and principles and modes of electrochemical in situ AFM section.

Part II contains three chapters that describe work on Prussian blue nanoparticles self-assembled nanostructure for electron transfer and applications in sensors and biosensors. Chapter 6 describes electron transfer and electrocatalysis of Prussian blue nanoparticles Self-assembled on modified Au (111) surfaces. Chapter 7 discusses electron transfer and electrocatalysis of Prussian blue nanoparticles immobilized on surfaces with different chemical properties. Chapter 8 provides a study of three-dimensional nanostructure of Prussian blue nanoparticles as biosensors for high electrocatalysis.

Part III concerns graphene-based hybrid nanomaterials for electrocatalysis and spectroscopy. Chapter 9 describes graphene paper doped with chemically compatible Prussian blue nanoparticles as novel type nanohybrid electrocatalyst. Chapter 10 discusses gold-filter assisted graphene paper-PBNPs on a gold substrate for electrocatalysis. Chapter 11 demonstrates Oil/Water two phase synthesized graphene-QDs used for enhanced electron or energy transfer processes.

The key references cited in the thesis are listed at the end of each chapter.

1.4 References

[1] S. Vaddiraju, I. Tomazos, D.J. Burgess, F.C. Jain, and F. Papadimitrakopoulos, *Biosensors and Bioelectronics*, **2010**, *25*, 1553-1565.

[2] V. Scognamiglio, *Biosensors and Bioelectronics*, **2013**, *47*, 12-25.

[3] F.C. Adams and C. Barbante, *Spectrochimica Acta Part B*, **2013**, *86*, 3-13

[4] C. T. Sang, *"What are Nanostructures?"*, May **1998**, site from website at *http://www.phys.ufl.edu/~tschoy/nanostructure.html*

[5] Site from website at *http://en.wikipedia.org/wiki/Nanostructure,* 30/10, **2013**.

[6] T. Anthony, W. George and K. Isao, *Biosensors: Fundamentals and Applications*. Oxford, UK: Oxford University Press, **1987**, p.770.

[7] S. Roy and Z. Gao, *Nano Today*, **2009**, *4*, 318-334.

[8] G. A. Somorjai and Y. Li, *Introduction to Surface Chemistry and Catalysis*, Wiley & Sons, Hoboken, **2010**.

[9] M. T. M. Koper, *Nanoscale*, **2011**, *3*, 2054-2073.

[10] G. A. Urban, *Meas. Sci. Technol.*, **2009**, *20*, 012001 (18pp).

2. Inorganic Hybrid Nanostructured Materials

Inorganic hybrid nanostructured materials, such as nanoparticles, nanowires, nanofilms, nanotubes, graphene, etc, have developed immensely over the past decade. These types of nanomaterials for specific nanofabrication in conjunction with technology and tools as nanodevices apply in many fields. In the study, PBNPs and graphene were selected as nanostructured research materials, with good performance in biosensor areas, self-assembly and spectroscopy.

2.1 *Prussian* Blue (PB) and *Prussian* Blue Nanoparticles (PBNPs)

As a material, Prussian Blue (PB) has a long history back to over 300 years ago, famous as an attractive blue pigment. This interesting material has also been widely used as an electron transfer (ET) catalyst for the development of chemical and biological sensors.

2.1.1 Introduction to PB

Prussian blue, with the chemical formula of $Fe_4[Fe(CN)_6]_3$,[1] was first synthesized accidentally by a paint maker Diesbach around 1704. The discovery of PB was actually the outcome of an experiment going wrong. Diesbach originally planned to receive cochineal red, but he made across creating this dark blue inorganic compound, with good performance as the first cheap, stable and lightfast blue pigment, and since then widely used as dye-materials for centuries.[1] Fig. 2.1 shows the image of Prussian blue paint.

The reason why PB appears with a strong blue color is due to photo-induced electron transfer (ET) from Fe (II) in a carbon hole to Fe (III) in a nitrogen hole, with an adsorption wavelength around 680 nm of orange-red light for this mixed-valence compound. Except for use as a traditional blue-dye pigment for a long time, PB also has the property of being electroactive, which was first reported by Neff in 1978.[2]

PB formed thin layers on a platinum foil electrode surface by electrochemical deposition. This pioneering work has since then opened a new field in the fundamental research for this classical pigment.[3] Furthermore, Itaya first found another important behavior of PB in 1984, which could catalyze electrochemical reduction of hydrogen peroxide and O_2.[4,5]

Figure 2.1 Image of PB paint.[1]

After discovering the property of electrocatalysis for reduction, other studies were described to PB recently mixes with enzymes as a biosensor probe to detect analytes, such as glucose, galactose lactate, cholesterol, choline, etc. In addition, it can also be used as food biosensors for our daily life.[5]

2.1.2 Structures and Fundamental Properties of PB

PB is a complicated coordinate compound. However, chemical synthesis of PB is quite straightforward by mixing of an Fe (III) salt and hexacyanoferrate (II) or an Fe (II) salt and hexacyanoferrate (III)[3, 6] Keggin and Miles first reported the crystallographic structure of PB from powder diffraction patterns.[7] Generally, previous literature divided the crystal structure of PB into two forms, soluble and insoluble. The only distinction is in fact whether or not a potassium cation is the

present in the formula. The formula of $KFe[Fe(CN)_6]$ represents the soluble form of this material, while the formula of $Fe_4[Fe(CN)_6]_3$ stands for the insoluble form.[8]

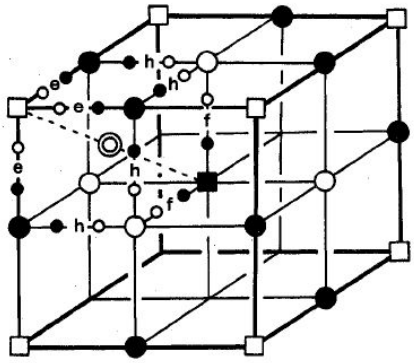

Figur 2.2. The unit cell of PB in space group Pm3m.[3] Big black solid circle: Fe(II); Small black solid circle: C; Big hollow circle: Fe(III); Small hollow circle: N.

The unit cell of PB structure is shown in Fig. 2.2. Fe (II) and Fe (III) are located on the a face-centered cubic lattice. Fe (II) ions are surrounded octahedrically by carbon atoms, while Fe (III) ions are surrounded octahedrically by nitrogen atoms.[3]

The dimensions of cubic unit cell are 10.2 Å, and the corresponding average distances are Fe(Ⅲ)-N = 2.03 Å, Fe(Ⅱ)-C = 1.92 Å and C-N = 1.13 Å after investigating several single crystals of x-ray diffraction.[4,6,8,9] This structure, with a channel diameter around 3.2 Å, supports templates for the diffusion of small molecules passing through this crystal for further application in the catalysis field.[5]

2.1.3 Electrochemical properties of PB

Since Neff first discussed electrochemical properties of the PB materials, PB modified electrodes have become widely popular materials for many potential applications.[2] The classic well-known cyclic voltammogram (CV) of reversible reduction and oxidation of PB is shown in Fig. 2.3, which demonstrates the

electrochemical behavior of a PB modified glass carbon electrode. Two pairs of sharp peaks result from the oxidation-reduction process of PB. The peaks in the lower potential range of about 0.15 V (vs Ag/AgCl) corresponds to the conversion between Prussian Blue and Prussian White (Everitt salt). The transfer of four electrons is compensated by entrapment of potassium cations in the reaction according to Eq. 2.1 (1). The sharpness of the redox peaks in the CV of Prussian blue/Prussian white indicates high quality of the PB layers and transfer of more than a single electron.[3]

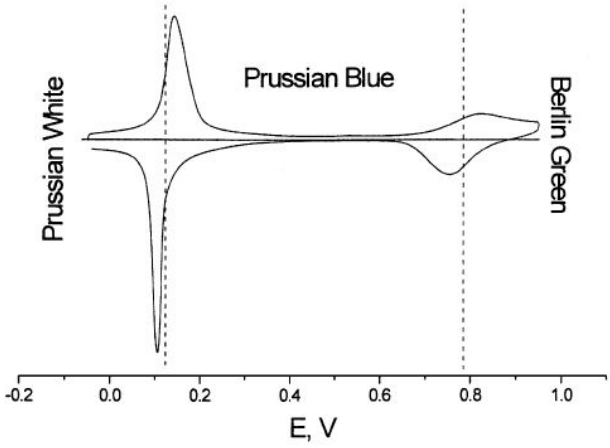

Figure 2.3. Typical cyclic voltammogram of *Prussian* Blue modified smooth (polished to mirror) glassy carbon electrodes. Electrolyte: 0.1M KCl, 40 mVs^{-1}, the reference electrode is Ag/AgCl.[3]

At the same time, the set of redox peaks in the higher potential range of about 0.8 V in correspondence with the transformation between Prussian Blue and Berlin Green (sometimes also named Prussian Yellow). The redox reactions are described by the following equations as Eq. 2.1 (2).

The finding that PB is electroactive has opened important implications for further application of the PB paints as an electroanalytical material in the area of chemical sensors and biosensors.

$$\textbf{(1) } Fe_4^{III}[Fe^{II}(CN)_6]_3 + 4K^+ + 4e^- \leftrightarrow K_4Fe_4^{II}[Fe^{II}(CN)_6]_3$$

"Insoluble PB" **Prussian White- PW (Everitt salt)**

$$\textbf{(2) } Fe_4^{III}[Fe^{II}(CN)_6]_3 + 3A^- \leftrightarrow Fe_4^{III}[Fe^{II}(CN)_6A]_3 + 3e^-$$

"Insoluble PB" **Prussian White- BG**

Eq. 2.1 Reactions of Prussian blue,[5] where A is the anion supplied by the electrolyte.

2.1.4 Applications of PB for Chemical Sensors and Biosensors

Being one of the most traditionally used electrochemical mediators for analytical applications, PB has been found a wide use in the sensor and biosensor field during the last decades, especially the functions from PBNPs.[5] Nano-sized particles have unique physical and chemical properties, often showing very interesting peculiarities unmatched by their bulk counterpart.[10] Taking PBNPs as the redox center for ET controlling and electrocatalysis in the senors and biosensing process is necessary.

2.1.4.1 PB for H_2O_2 Sensors

The first report on the PB-based electrocatalytic behavior of H_2O_2 was by Itaya and co-workers in 1984.[11] When low-molecule weight of H_2O_2 (or O_2) diffuses into the PB lattice structure, it will be located rapidly at the center of each vacancy. This molecule is entrapped by four divalent high-spin iron ions on average that could generate a catalytic reduction of H_2O_2 through a four-electron transfer.[5] H_2O_2 is completely reduced to water before diffusing out of the PB structure, with the reaction and schematic diagram shown in Fig. 2.4.[3]

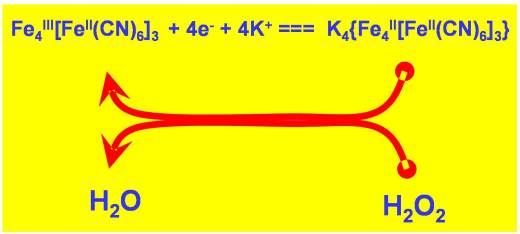

Figure 2.4. Electron transfer and electrocatalytic reactions towards reduction of H_2O_2 by PB.

Selective detection of H_2O_2 is needed and useful for several practical reasons. First, H_2O_2 is a deleterious chemical agent as a waste side product in ground water or rain from atomic power stations and industry.[12, 13] Additionally, H_2O_2 is used to disinfect beverage or food packages, water pools, and then detecting the cleanness from the residual concentration.[14, 15] Furthermore, H_2O_2 is a side product from about 90% of catalytic reactions by oxidases, which demonstrates that measuring H_2O_2 is one of the most important methods in research enzymes and other proteins.[3]

The electrocatalytic operating potential is a key parameter for analytical detections. The fact that PB modified electrodes can reduce H_2O_2 at optimal potentials allows to detect H_2O_2 in the potential range of -0.05 to 0.05 (versus Ag/AgCl) with reasonably high sensitivity. This character is able to avoid or significantly reduce the interference resulting from electrochemical oxidation of common electroactive species including ascorbic acid, uric acid and paracetamol in many practical samples.[16, 17] PB modified electrodes, such as graphite, glass carbon, carbon paste, gold or platinum electrodes, thus offer a powerful method for detecting H_2O_2 at the low potentials.

2.1.4.2 PB-mediated Enzymes Biosensors

Due to the high sensitivity and selectivity in detecting H_2O_2, PB has been called an "artificial peroxidase" in many systems.[5] Especially in the low potential detection of H_2O_2 was found to be more important in most operation of oxidase-based enzyme biosensors,[3] and the measurement of H_2O_2 to be directly proportional to the substrate

concentration of enzyme.[5] Since H_2O_2 is the side product of catalysis reaction by oxidase enzymes, the chemical formula reaction is represented as Eq.2.2,

Substrate + O_2 + Oxidase enzyme ↔ product (oxidised substrate) + H_2O_2

Eq. 2.2. Chemical formula reaction of producing H_2O_2 as side product by oxidase enzymes of catalysis reaction.[3]

Because of the mixed valence in the compound of PB, the PB coupled enzymes can detect both electrocatalytic oxidation and reduction.[18] Right now, more than 10 different enzymes can be brought to be blended with PB for the detection of substrates, with low detection limit, wide linear range, and high sensitivity.[5] The schematic diagram of a PB-based biosensor is shown in Fig. 2.5.

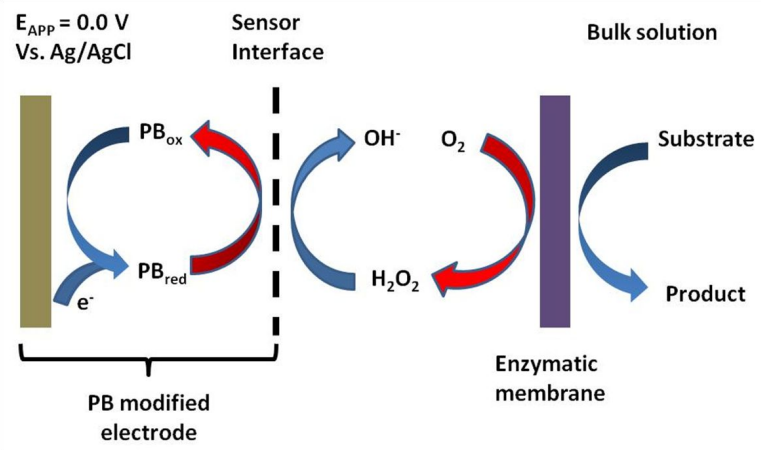

Figure 2.5. Schematic diagram of PB-based biosensor with an oxidase enzyme for electrocatalysis.[5]

Among these enzymes and substrates for biosensors, due to the importance and high stability of natural substrate, glucose oxidase (GOD) has always been a model enzyme to detect the particular of glucose. Meanwhile, GOD was also the first enzyme immobilized on the PB modified carbon electrode, which played an important role in the development of PB mediated electrochemical biosensors.[5]

The schematic diagram of GOD-PB for catalytic glucose in detail is shown in Fig. 2.6. First, glucose diffuses from the bulk solution to the surface of the glucose oxidase film, and is then oxided to gluconate and H_2O_2 in the O_2 environment through the process. At the same time, H_2O_2 is generated by controlled electrochemical PB oxidation and reduction. This type of biosensor system is reproduced and very stable for a long time.[19] Furthermore, the PB-GOD electrode also has a wide pH range of activity in natural environment, which provides a powerful stimulus to scientists and support a promising method for the practical biosensor field.[5]

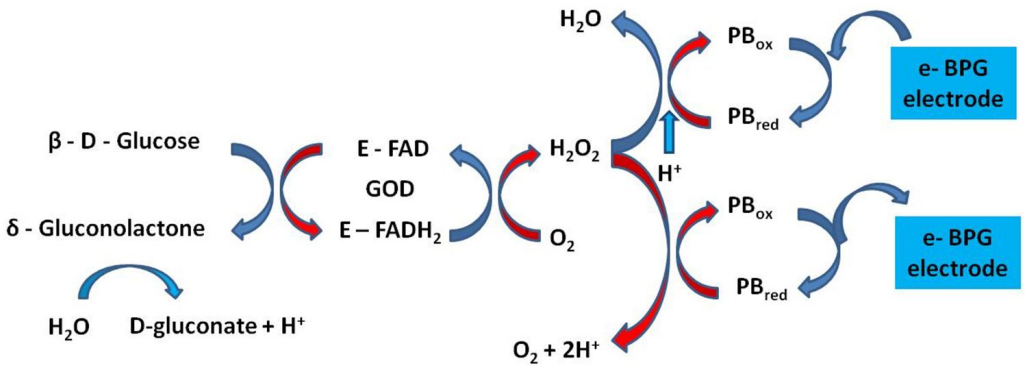

Figure 2.6. Schematic diagram of GOD-PB modified electrode to glucose.[19]

Other oxidase enzymes coupled with PB have been reported addressing detection of real matrices, for example, lactate, choline, cholesterol and galactose. In addition, some enzymes with PB biosensor have been developed for food and have shown

good performance towards lysine, glutamate, oxalate, alcohol, amine, formate, galactose, fructosyl etc.[5] The function of PB based biosensors will be very promising in the practical application in food, environment, pollution and clinical analysis, resulting from the properties such as low detection limit, wide linear range and high sensitivity. These PB-mediated biosensors have a potential commercial development in the future.[5]

2.2 Graphene and Graphene Papers

Graphene is a single atom thick plane of layered graphite, which was first fabricated using the Scotch tape method by Novoselov, Geim, et al in 2004.[20] Carbon atoms in graphene are arranged in a regular symmetrical hexagonal shape, with the one layer of two-dimensional structure different from graphite, carbon nanotubes or fullerenes.[21]

Due to its many favorable properties, such as being ultra-thin, mechanically ultra-strong, nearly transparent to light, an excellent conductor of heat and electricity, completely isolated to be regards as freestanding and stable under ambient conditions,[22] graphene has been becoming a most important and promising material (Fig. 2.7). Because of the extraordinary behavior of graphene, the Noble Prize of Physics in 2010 was motivated as “for groundbreaking experiments regarding the two-dimensional material graphene” to Konstantin Novoselov and Andre Geim from University of Manchester.[23]

Recent years, graphene has become potentially highly attractive for numerous applications resulting from its supreme properties, and many breakthroughs in the areas of graphene-based research have been reported.[24] Graphene is the thinnest known material with a theoretical thickness of 0.34 nm in the universe, and it is also the strongest material ever measured. Other good characteristics as, giant room temperature intrinsic electron mobility of 25,000 $cm^2/V{\cdot}s$ [25], zero effective mass, sustained electric current densities six orders of magnitude higher than that of

copper,[26] larger surface area of 2600 m^2/g and specific capacity of 540 mAh/g.[21] Furthermore, record thermal conductivity of 3,000 WmK^{-1},[27] optical absorption of light less than 2.3%,[28] intrinsic mechanical strength of 130 GPa, Young's modulus about 1 TPa,[29] complete impermeability to gases,[30] and finally, quantum phenomena in a bench top experiment.[22]

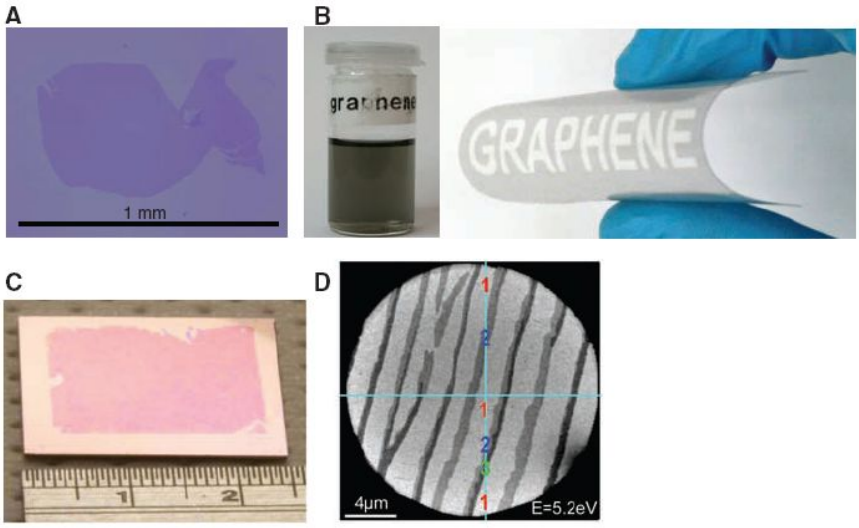

Figure 2.7. Preparation of graphene. (A) Graphene nanosheets prepared on Si wafer by the scotch tape technique. (B) Left: Solution of graphene obtained by ultrasound cleavage of graphite in chloroform. Right: Printed highly conductive and robust graphene on different substrates. (C) The first graphene grows on Ni wafers and then is transferred onto a Si wafer. (D) State-of-the-art SiC wafer with atomic terraces covered by different layers of graphene (one, two and three layers, indicated 1, 2 and 3).[22]

Graphene papers are a novel type of layered materials emerged very recently. Since the pioneering work of Ruoff and co-workers in 2007,[31,32] graphene paper has added an attractive form to the scientific catalogue of rapidly surging graphene based nanomaterials. Graphene papers can be made from either graphene oxide (GO) or reduced graphene oxide (RGO) through wet-chemical methods,[33, 34] which is relatively simple and low cost procedures that involve chemical synthesis and vacuum filtration of individual and liquid suspended graphene nanosheets.[32] As a

free-standing material (no substrate supported), graphene paper has several remarkable characters, reflected by high practical electrical conductivity, mechanical robustness, excellent thermal stability, structural uniformity, and geometric flexibility.[32] These features have altogether enabled expanding the application scope of graphene materials to a much wider range of various demands. Several possible applications have been demonstrated mainly at the laboratory level, for example, the use for flexible sensors,[35-40] energy storage,[41-49] biocompatible materials,[50-52] and even antibacterial agents.[53, 54] Morphology and structure of first reported graphene oxide paper were shown in the Fig. 2.8.[32]

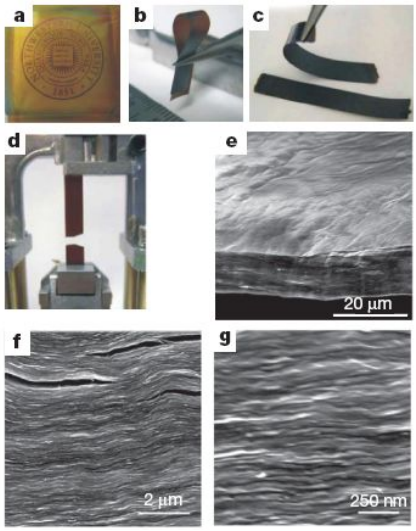

Figure 2.8. Morphology and structure of first reported graphene oxide paper.[32] a) 1mm thick of graphene oxide paper; b) folded 5 mm thick semitransparent film of graphene oxide paper; c) folded 25 mm thick strip; d) strip after fracture from mechanical strength. e-g) cross section view of 10 mm thick graphene oxide paper in Low-, middle- and high-resolution SEM.

Functionalization is an essential step for most possible applications of graphene papers, because this material itself lacks the desired specific functions such as catalysis, redox activity and molecular recognition. Decoration of graphene paper with nanoparticles (NPs) represents one of the most attractive ways for catalytic

functionalization of this material that can be consistently used, for example, for sensing devices and energy conversion.[31]

2.3 References

[1] M. B. Evans, *Artist's Pigments: The Accidental Discovery of Prussian Blue Paint* Site from the website: *http://painting.about.com/cs/colourtheory/a/prussianblue.htm*

[2] V. D. Neff, *J. Electrochem. Soc*., **1978**, *125*, 886-887.

[3] A. A. Karyakin, *Electroanalysis*, **2001**, *13*, 813-819.

[4] K. Taya and I. Hida, *Acc. Chem. Res.*, **1986**, *19*, 162-168.

[5] F. Ricci and G. Palleschi, *Biosensors and Bioelectronics*, **2005**, *21*, 389-407.

[6] J. C. Wojde, I. .P. R. Moreira, S. T. Bromley and F. Illas, *The Journal of Chemical Physics*, **2008**, *128*, 044713.

[7] J.F. Keggin and F.D. Miles, *Nature*, **1936**, *137*, 577.

[8] H. J. Buser, D. Schwarzenbach, W. Petter and A. Ludi, *Inorganic Chemistry*, **1977**, *16*, 2704-2710

[9] F. Herren, P. Fischer, A. Ludi, and W. Halg, *Inorg. Chem*. **1980**, *19*, 956-959.

[10] Q. J. Chi, O. Farver, and J. Ulstrup, *P. Nat. Acad. Sci.* USA **2005**, *102*, 16203-16208.

[11] K. Itaya, N. Shoji and I. Uchida, *J. Am. Chem. Soc.*, **1984**, *106*, 3423

[12] W.B. Nowall and W.G. Kuhr, *Electroanalysis* **1997**, *9*, 102.

[13] Y. Wang, J. Huang, C. Zhang and J. Wei, X. Zhou, *Electroanalysis*, **1998**, *10*, 776.

[14] B. Strausak and W. Schoch, *European Patent Application*, EP 0136973, **1985**.

[15] A. Schwake, B. Ross and K. Cammann, *Sens. Actuators B*, **1998**, *B46*, 242.

[16] A.A. Karyakin, O.V. Gitelmacher, and E. E. Karyakina, *Anal. Chem.*, **1995**, *67*, 2419-2423.

[17] A.A. Karyakin, E. E. Karyakina and L. Gorton, *Talanta*, **1996**, *43*, 1597-1606.

[18] R. Koncki, Critical Reviews in Analytical Chemistry, **2002**, 32, 79-96.

[19] Q. Chi and S. Dong, *Anaiytica Chimica Acta*, **1995**, *310*, 429-436

[20] K. S. Novoselov, A. K. Geim, S. V. Morozov, D. Jiang, Y. Zhang, S. V. Dubonos, I. V. Grigorieva and A. A. Firsov, *Science*, **2004**, *306*, 666-669.

[21] Site from the website at *http://en.wikipedia.org/wiki/Graphene*, 24/11/2013.

[22] A. K. Geim, *Science*, **2009**, *324*, 1530-1534.

[23] Nobel Foundation announcement, **2010**.

[24] K. S. Novoselov, V. I. Falko, L. Colombo, P. R. Gellert, M. G. Schwab and K. Kim, *Nature*, **2012**, *490*, 192-200.

[25] A. S. Mayorov et al., *Nano Lett.*, **2011**. *11*, 2396-2399.

[26] J. Moser, A. Barreiro and A. Bachtold, *Appl. Phys. Lett.*, **2007**, *91*, 163513.

[27] A. A. Balandin, *Nature Mater.*, **2011**, *10*, 569-581.

[28] R. R. Nair et al. *Science*, **2008**, *320*, 1308.

[29] C. Lee, X. D. Wei, J. W. Kysar and J. Hone, *Science*, **2008**, *321*, 385-388.

[30] J. S. Bunch et al. *Nano Lett.*, 2008, *8*, 2458-2462.

[31] N. Zhu, S. Han, S. Gan, J. Ulstrup and Q. Chi, *Adv. Funct. Mater.*, **2013**, *23*, 5297-5306

[32] D. A. Dikin, S. Stankovich, E. J. Zimney, R. D. Piner, G. H. B. Dommett, G. Evmenenko, S. T. Nguyen and R. S. Ruoff, *Nature*, **2007**, *448*, 457 .

[33] S. Stankovich, D. A. Dikin, R. D. Piner, K. A. Kohlhaas, A. Kleinhammes, Y. Jia, Y. Wu, S. T. Nguyen and R. S. Ruoff, *Carbon*, **2007**, *45*, 1558 .

[34] S. Park and R. S. Ruoff, *Nat. Nanotechnol.*, **2009**, *4*, 217.

[35] F. Yavari and N. Koratkar, *J. Phys. Chem. Lett.*, **2012**, *3*, 1746.

[36] F. Xiao, Y. Q. Li, X. L. Zan, K. Liao, R. Xu and H. W. Duan, *Adv. Funct. Mater.*, **2012**, *22*, 2487.

[37] H. C. Gao, Y. X. Wang, F. Xiao, C. B. Ching and H. W. Duan, *J. Phys. Chem. C*, **2012**, *116*, 7719.

[38] F. Xiao, J. B. Song, H. C. Gao, X. L. Zan, R. Xu, and H. W. Duan, *ACS Nano*, **2012**, *6*, 100.

[39] J. Liang, Y. Huang, J. Oh, M. Kozlov, D. Sui, S. Fang, R. H. Baughman, Y. Ma and Y. Chen, *Adv. Funct. Mater.*, **2011**, *21*, 3778.

[40] B. G. Choi, H. Park, T. J. Park, M. H. Yang, J. S. Kim, S.Y. Jang, N. S. Heo, S. Y. Lee, J. Kong and W. H. Hong, *ACS Nano*, **2010**, *4*, 2910.

[41] D. W. Wang, F. Li, W. Ren, Z. G. Chen, J. Tan, Z. S. Wu, I. Gentle, G. Q. Lu and H. M. Chen, *ACS Nano*, **2009**, *3*, 1745.

[42] Y. Zhu, M. D. Stoller, W. Cai, A. Velamakanni, R. D. Piner, D. Chen and R. S. Ruoff, *ACS Nano*, **2010**, *4*, 1227.

[43] A. Abouimrane, O. C. Compton, K. Amine and S. T. Naguyen, *J. Phys. Chem. C*, **2010**, *114*, 12800.

[44] H. Gwon, H. S. Kim, K. U. Lee, D. H. Seo, Y. C. Park, Y. S. Lee, B. T. Ahn and K. Kang, *Energy Environ. Sci.*, **2011**, *4*, 1277.

[45] G. Wang, K. Sun, F. Lu, H. Sun, M. Yu, W. Jiang, C. Liu and J. Lian, *Small* **2012**, *8*, 452.

[46] X. Wang, X. Cao, L. Bourgeois, H. Guan, S. Chen, Y. Zhong, D. M. Tang, H. Li, T. Zhai, L. Li, Y. Bando and D. Golberg, *Adv. Funct. Mater.*, **2012**, *22*, 2682.

[47] F. Liu, S. Song, D. Xue and H. Zhang, *Adv. Mater.*, **2012**, *24*, 1089.

[48] D. Wang, R. Kou, D. Choi, Z. Yang, Z. Nie, J. Li, L. V. Saraf, D. Hu, J. Zhang, G. L. Graff, J. Liu, M. A. Pope and I. A. Aksay, *ACS Nano*, **2010**, *4*, 1587.

[49] Z. Li, Y. Mi, X. Lin, S. Lin, S. Yang and J. Wang, *J. Mater. Chem.*, **2011**, *21*, 13991.

[50] S. Park, N. Mohanty, J. W. Suk, A. Nagaraja, J. An, R. D. Piner, W. Cai, D. R. Dreyer, V. Berry and R. S. Ruoff, *Adv. Mater.*, **2010**, *22*, 1736.

[51] N. D. Luong, N. Pahimanolis, U. Hippi, J. T. Korhonen, J. Ruokolainen, L. S. Johansson, J. D. Nam and J. Seppala, *J. Mater. Chem.*, **2011**, *21*, 13991.

[52] Y. J. Song, K. G. Qu, C. Zhao, J. S. Ren and X. G. Qu, *Adv. Mater.*, **2010**, *22*, 2206.

[53] W. Hu, C. Peng, W. Luo, M. Lv, X. Li, D. Li, Q. Huang and C. Fan, *ACS Nano*, **2010**, *4*, 4317.

[54] S. Some, S. M. Ho, P. Dua, E. Hwang, Y. H. Shin, H. Yoo, J. S. Kang, D. K. Lee and H. Lee, *ACS Nano*, **2012**, *6*, 7151.

3. Self-assembled Monolayers (SAMs) for Nanotechnology

3.1 Introduction to Self-assembled Monolayers

Self-assembled monolayers (SAMs) provide a simple, convenient and flexible method to spontaneous chemical functionalization of the electrode surface by organic molecules, either from gas or solution assembled onto the surface of solids.[1, 2] Self-assembly is also a basic principle in nature, for example, in living cells or membranes of lipid molecules.[3] There are numerous organic molecules containing free anchor headgroups, such as thiols, disulphides, methyl, carboxyl, hydroxyl, silanes, amines, acids, etc, that covalent or non-covalent bind to specific metals, metal oxides and semiconductors, as summarized in Table 3.1.

Table 3.1 Chemical summary of adsorbates and substrates that form SAM systems[4]

Surface	Substrate	Adsorbate(s)
Metal	Au	R–SH, R–SS–R, R–S–R, $R–NH_2$, R–NC, R–Se, R–Te
	Ag	R–COOH, R–SH
	Pt	R–NC, R–SH
	Pd	R–SH
	Cu	R–SH
	Hg	R–SH
Semiconductor	GaAs (III–V)	R–SH
	InP (III–V)	R–SH
	CdSe (II–VI)	R–SH
	ZnSe (II–VI)	R–SH
Oxide	Al_2O_3	R–COOH
	TiO_2	R–COOH, $R–PO_3H$
	$YBa_2Cu_3O_{7-\delta}$	$R–NH_2$
	Tl–Ba–Ca–Cu–O	R–SH
	ITO	R–COOH, R–SH, $R–Si(x)_3$
	SiO_2	$R–Si(x)_3$

Fig. 3.1 shows a schematic diagram of SAMs. The SAM molecule contains headgroup, backbone or chain, and endgroup. The SAM forms via headgroup binding

to the surface of the substrate, while the other side of molecule (endgroup) points away from the surface and is open barely for different chemical functionalities.[3]

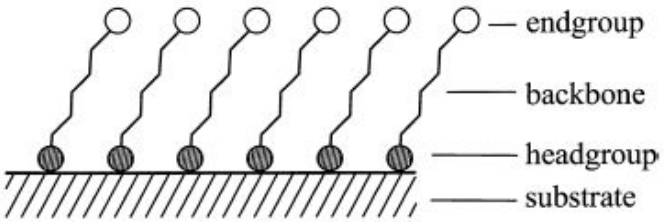

Figure 3.1. A schematic diagram of SAMs system.[3]

SAMs are particularly attractive for studies and research in nanoscience and nanotechnology for the following reasons,

(1) It is easy to fabricate SAMs without specialized equipment and environment required (e.g., Langmuir-Blodgett (LB) troughs).

(2) The nanostructures (nanoparticles, nanowires, nanotubes, collids) and surface properties (different functional endgroup) can be tuned via modification of molecular structure and functions.

(3) More complex structures can be built through the middle linker bridge.

(4) SAMs can form in different external environments and be characterized by different techniques with optical detection, electrochemistry, surface plasmon spectroscopy, etc to research molecular or metallic behavior.

(5) It is feasible to probe interfacial phenomena from SAMs, such as adhesion, friction and wetting.[1]

3.2 Au-thiol Based Surface Self-assembly

Among the substrates of metals, metal oxides and semiconductors, SAMs of alkanethiols on gold are the most extensively classic studies.[1, 5-13] The advantages of choosing Au as the substrate for SAMs are following,

(1) Gold is a relatively inert of substrate, which will be oxided by O_2 or react with most chemicals in most cases, and does not oxidize below its melting temperature. This performance makes gold very suitable for SAMs behavior under limited environmental condition without special setup for fabrication.

(2) Gold is facile to receive and prepare, and even single-crystal gold is available commercially.

(3) Gold is comparatively easy to clean, and exceptionally easy to be patterned by lithographic technique or chemical vapor deposition.

(4) Thiols(-SH) have a high affinity for gold without any side reaction, and well-defined order can be obtained. The resulting SAM structures are stable for several days.

(5) Gold is of weakly toxic and therefore biologically compatible.

(6) SAMs from gold substrate can be applied in a number of analytical techniques and spectroscopes.[1]

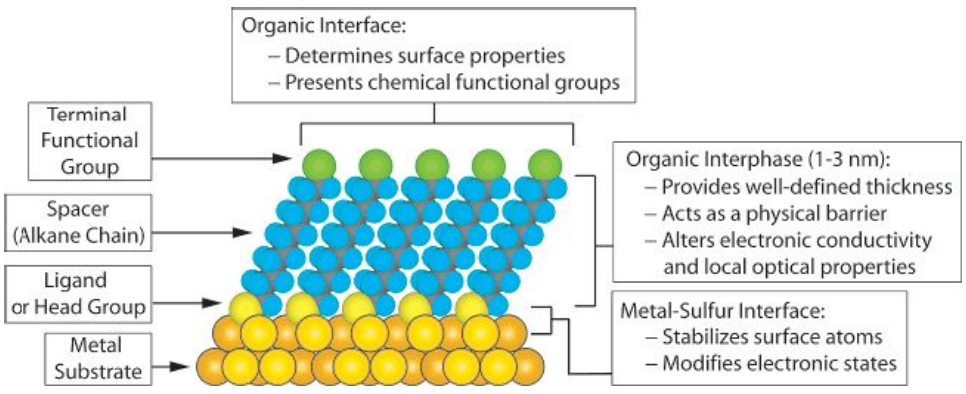

Figure 3.2. Schematic diagram of an ideal, single-crystalline alkanethiolate SAM supported on a gold (111) surface.[1]

Au (111) surface has the lowest surface free energy, and is preferred to be used as an ideal substrate for most applications.[3] Fig. 3.2 shows an ideal alkanethiolate SAM on a Au (111) surface, with the terminal group that can be further functionalized by other molecular or functional groups.

$$\mathbf{R\text{-}S\text{-}H + Au_n^0 \leftrightarrow R\text{-}S\text{-}Au + \cdot Au_n^0 + 1/2\ H_2}$$

Eq 3.1. General reaction between gold and thiol molecule.[14]

The general reaction between gold and thiol molecules can be described as the Eq 3.1. An oxidation reaction of -SH on the gold surface, at the same time with hydrogen formed by reduction. The binding energy of S-Au is in the range of approximately 167.4 kcal/mol.[14]

3.3 Electrochemistry of Self-assemblied Monolayers and Applications in Biosensors

Molecular redox center can be immobilized on the top of well-defined linker bridge self-assembled on the surface of a substrate. This redox-active SAM system provides an perfect platform to investigate the electrochemical process and electron transfer kinetics of the immobilized redox centre.[15] Due to the attractive behavior of electrochemical properties, redox-active SAM systems offer a easy way to link biomolecules for the application in biosensors. The advantage of SAMs in used in biosensor include:[2]

(1) It is easy to form well-ordered and stable monolayers

(2) Minimum resources are required for biomolecular immobilization on SAM.

(3) Various hydrophilic or hydrophobic surface functional groups can be carried out for biosensors by SAMs.

(4) Within the versatile microenvironment, molecules are biocompatible with the SAMs surface for electrochemical behavior for biosensors studies.
(5) High stability of the SAM immobilized molecules offers an important basis for a broad variety of experimental measurements.
(6) SAMs combined with surface sensitive equipment such as STM or AFM provide a research on the intrinsic quality and principle of the molecular or system towards the level of the single molecules.[2]

The layer-by-layer (LBL) assembly technique, introduced by Decher,[16-18] has been employed to improve NP immobilization as well as the electrochemical responses by alternate adsorption of NPs and oppositely charged film materials on the electrode surfaces.[19-21] Use of such methods can achieve precise control of structural film properties such as layer thickness and composition at the molecular or nanometer level.[22-25] The highly ordered LBL nanocomposite assemblies have had great appeal in electrochemistry and materials chemistry.[26]

3.4 References

[1] J. C. Love, L. A. Estroff, J. K. Kriebel, R. G. Nuzzo, and G. M. Whitesides, *Chem. Rev.* **2005**, *105*, 1103-1169.
[2] N. K. Chaki and K. Vijayamohanan, Biosensors & Bioelectronics, **2002**, 17, 1-12.
[3] F. Schreiber, *Progress in Surface Science*, **2000**, *65*, 151-256.
[4] R. K. Smith, P. A. Lewis and P. S. Weiss, *Progress in Surface Science*, **2004**, *75*, 1-68.
[5] G. E. Poirier and E. D. Pylant, *Science*, **1996**, *272*, 1145.
[6] R. G. Nuzzo and D. L. Allara, *J. Am. Chem. Soc.*, **1983**, *105*, 4481.
[7] M. D. Porter, T. B. Bright, D. L. Allara and C. E. D. Chidsey, *J. Am. Chem. Soc.*, **1987**, *109*, 3559.
[8] L. H. Dubois and R. G. Nuzzo, *Annu. Rev. Phys. Chem.*, **1992**, *43*, 437.
[9] C. D. Bain, J. Evall and G. M. Whitesides, *J. Am. Chem. Soc.*, **1989**, *111*, 7155.
[10] C. D. Bain and G. M. Whitesides, *Science*, **1988**, *240*, 62.

[11] H. A. Biebuyck, C. D. Bain and G. M. Whitesides, *Langmuir*, **1994**, *10*, 1825.

[12] P. E. Laibinis, G. M. Whitesides, D. L. Allara, Y. T. Tao, A. N. Parikh, and R. G. Nuzzo, *J. Am. Chem. Soc.*, **1991**, *113*, 7152.

[13] L. H. Dubois, B. R. Zegarski and R. G. Nuzzo, *J. Chem. Phys.*, **1993**, *98*, 678.

[14] J. Heeg, U. Schubert, F. Küchenmeister and Fresenius, *J. Anal. Chem.*, **1999**, *365*, 272-276.

[15] A. L. Eckermann, D. J. Feld, J. A. Shaw and T. J. Meade., *Coordination Chemistry Reviews*, **2010**, *254*, 1769–1802.

[16] G. Decher and J. D. Hong, *Makromol Chem-M Symp.*, **1991**, *46*, 321-327.

[17] G. Decher et al, *Science*, **1997**, *277*, 1232-1237.

[18] G. Decher, J. D. Hong and J. Schmitt, *Thin Solid Films*, **1992**, *210*, 831-835.

[19] G. X. Li, J. Zhao, X. L. Zhu and T. Lib, *Analyst*, **2008**, *133*, 1242-1245.

[20] J. W. Ostrander, A. A. Mamedov and N. A. Kotov, *J. Am. Chem. Soc.*, **2001**, *123*, 1101-1110.

[21] X. Zhang, H. Chen and H. Y. Zhang, *Chem. Commun.*, **2007**, *14*, 1395-1405.

[22] C. Y. Jiang and V. V. Tsukruk, *Adv. Mater.*, **2006**, *18*, 829-840.

[23] P. T. Hammond, *Adv. Mater.*, **2004**, *16*, 1271-1293.

[24] N. A. Kotov, Z. Y. Tang, Y. Wang and P. Podsiadlo, *Adv. Mater.*, **2006**, *18*, 3203-3224.

[25] S. J. Dong, F. Wang, J. L. Wang and H. J. Chen, *J. Electroanal. Chem.*, **2007**, *600*, 265-274.

[26] G. B. Xu, X. Q. Liu, F. Wang, S. Han and L. H. Shi, *Electroanal.*, **2010**, *22*, 963-968.

4. Enzyme Catalysis Kinetics

4.1 Enzyme Catalysis Principles

An enzyme is a unique type of protein with catalytic properties. Enzyme catalysis is the catalysis process for chemical reactions with enhanced reaction rates, in comparison to absence of enzyme.[1,2]

As shown in the schematic energetic diagram of a reaction (Fig. 4.1), the reaction rate is determined by the highest energy state, called transition state ($S^{\ddagger}$). The enzyme as a catalyst lowers the activation barrier between substrate and product, resulting in increased reaction rate without affecting the equilibrium position-forward and reverse reactions.[1, 3]

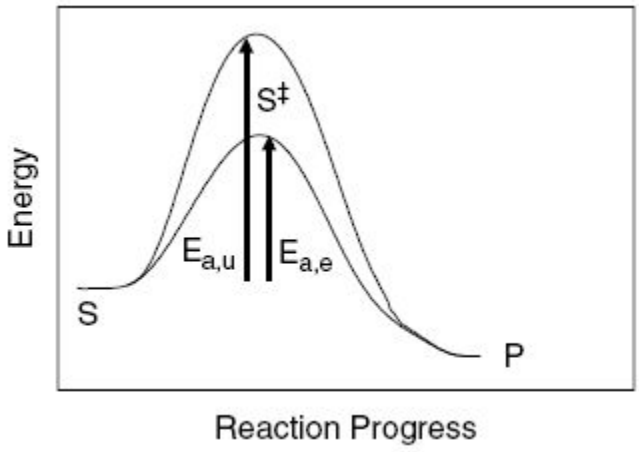

Figure 4.1. Changes in the free energy of a system undergoing a chemical reaction from substrate S to product P. Ea corresponds to the energy of activation for the forward reaction of the enzyme-catalyzed (e) and uncatalyzed (u) reaction. $S^{\ddagger}$ corresponds to the transition state.[1, 4]

4.2 Enzyme Catalysis Models: Equilibrium State and Steady State Kinetics

A simply enzymatic catalysis mechanism is normally and most simple modeled by two-step processes (as Eq. 4.1): in the first step the enzyme (E) combines with substrate (S) to come into an enzyme-substrate (ES) complex. The second step is the irreversible decoposition of the ES complex to product (P) and free Enzyme (E).[1]

$$E + S \underset{k_{-1}}{\overset{k_1}{\rightleftharpoons}} ES \xrightarrow{k_2} P + E \qquad \text{(Eq. 4.1)}$$

4.2.1 Equilibrium State Kinetics

In the Michaelis-Menten equilibrium model, the formation rate of enzyme–substrate (ES) complex is assumed to be much faster than the decomposion of the ES complex. This assumption leads to the equilibrium as Eq. 4.2. [1]

$$K_s = \frac{[E][S]}{[ES]} \qquad \text{(Eq. 4.2)}$$

The equilibrium dissociation constant of the ES complex (K_s) corresponding to the half highest concentration of substrate ($V_{max}/2$). From the equation, the lower K_s, the higher concentration of ES complex. The velocity of the catalysis reaction is Eq. 4.3:

$$v = k_{cat}[ES] \qquad \text{(Eq. 4.3)}$$

Dividing both sides of Eq (4.3) by $[E_T]$, and defining $[E_T] = [E] + [ES]$,

$$\frac{v}{[E_T]} = \frac{k_{cat}[ES]}{[E]+[ES]} \qquad \text{(Eq. 4.4)}$$

Introducing from Eq. (4.2), [E][S]/Ks instead of [ES],

$$\frac{v}{[E_T]} = \frac{k_{cat}([E][S]/K_s)}{[E]+[E][S]/K_s} \qquad \text{(Eq. 4.5)}$$

Simplification of the equation, then receives,

$$v = \frac{k_{cat}[ET][S]}{K_s + [S]} \qquad \text{(Eq. 4.6)}$$

Defining Vmax as the maximum reaction velocity, $V_{max}=k_{cat}[E_T]$,

$$v = \frac{V_{max}[S]}{K_s + [S]} \qquad \text{(Eq. 4.7)}$$

4.2.2 Steady State Kinetics

In the steady state kinetics model, it is assumed that the concentration of ES complex remains constant in time,[1] the expression is

$$\frac{d[ES]}{d[t]} = k_1[E][S] - k_{-1}[ES] - k_2[ES] = 0 \qquad \text{(Eq. 4.8)}$$

The Michaelis constant K_m is, as a transformation from (Eq. 4.8),

$$K_m = \frac{[E][S]}{[ES]} = \frac{k_{-1} + k_2}{k_{-1}} \qquad \text{(Eq. 4.9)}$$

When $k_{-1} >> k_2$, the Michaelis constant K_m is the same as equilibrium dissociation constant of the ES complex (K_s), which corresponds to the half highest concentration of substrate ($V_{max}/2$).

The velocity of enzyme catalysis reaction is:

$$v = k_{cat}[ES] \qquad \text{(Eq. 4.3)}$$

By dividing $[E_T]$, and rearranging the yield as the same process as equilibrium state, and an expression is:

$$v = \frac{V_{max}[S]}{K_m + [S]} \qquad \text{(Eq. 4.10)}$$

Thus, in the steady state case, $K_m \approx K_s$, only happens for the system when the substrate binds faster than ES complex breakdown.

4.2.3 Plot of Velocity vs [S]

In the enzyme catalysis reaction, the velocity vs substrate concentration curve takes the shape of rectangular hyperbola[1] (Fig. 4.2).

In the low substrate concentration region, where $[S] \ll K_m$, the enzyme-catalyzed process is first order with respect to [S], and v is proportional to [S]. Eq. (4.10) and Eq. (4.6) will reduce to Eq. (4.11).

$$v = \frac{k_{cat}}{K_m}[E_T][S] = \frac{V_{max}}{K_m}[S] \qquad \text{(Eq. 4.11)}$$

In this step, the limiting rate depends solely on the diffusion rate of substrate to the active site, which limit the value of k_1 between 10^8 to 10^9 M^{-1} s^{-1}.

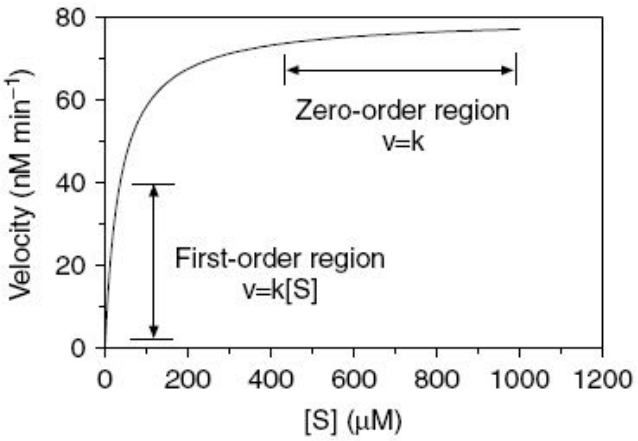

Figure 4.2. *v* vs [S] plot for an enzyme-catalyzed process following by the simplest Michaelis-Menten mechanism. In the first-order region, *v* depends linearly of [S], while v is independent of [S] in the zero-order region.[1]

In the high substrate concentration range, which is the zero order region, the reaction velocity remains constant with increasing [S]. In this region, [S] >> K_m, Eq. (4.10) and Eq. (4.6) reduces to,

$$v = k_{cat}[E_T] = V_{max} \qquad \text{(Eq. 4.12)}$$

The value of Km depends on the substrates and parameters such as temperature, pH, polarity and ionic strength, and normally turns on between 10^{-1} and 10^{-7} M. This system could directly read the value of $V_m/2$ in according to K_m.[1]

4.3 Determination of Enzyme Catalytic Parameters

The catalytic parameter k_2 (k_{cal}) and K_m can be determined directly from the Michaelis-Menten equation, Eq. 4.10. The enzyme catalytic constant is often also estimated by the linear regression to using the reciprocal of Eq. 4.10 as,

$$\frac{1}{v_0} = \frac{1}{V_{max}} + \frac{K_M}{V_{max}} \frac{1}{[S]} \qquad \text{(Eq.4.13)}$$

v_o is the initial velocity of the reaction. The linear plot of $1/v_0$ to 1/[S] is called the Lineweaver-Burk plot (Fig. 4.3). V_m and K_m can be obtained from the slope and intersection of this plot. At low concentration of substrate, small errors in v_0 results in large errors in $1/v_0$, the non-linear Michaelis-Menten method is therefore more accurate.

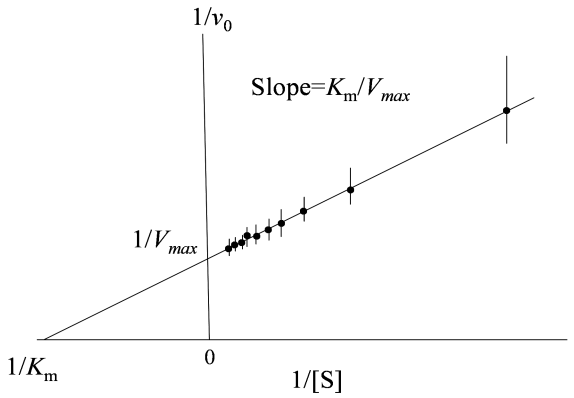

Figure 4.3. A Lineweaver-Burk or double-reciprocal plot with error bars.[2]

4.4 References

[1] G. Marangoni. *Enzyme Kinetics: A Modern Approach.* John Wiley & Sons, Inc., Hoboken, New Jersey, **2003**.

[2] D. Voet and J. G. Voet, *Biochemisty*, John Wiley & Sons, Inc., 2nd edition, **1995**, pages 351-354.

[3] H. Ikemoto, PhD thesis, Department of Chemistry, Technical University of Denmark, **2011**

[4] L. Stryer, *Biochemistry*, 3rd edition, W.H. Freeman and company, New York, **1988**.

5. Experimental Methods and Techniques

Besides the basic experimental methods used in the project, two main experimental techniques will be introduced in this chapter, electrochemistry and *in situ* atomic force microscopy (AFM).

5.1 Electrochemistry

Electrochemistry is about the interrelation of electrical and chemical effects in chemical processes, and an important branch of chemistry. It is focused on the research of chemical changes and properties produced by electric current and energy changes during the chemical reactions.[1]

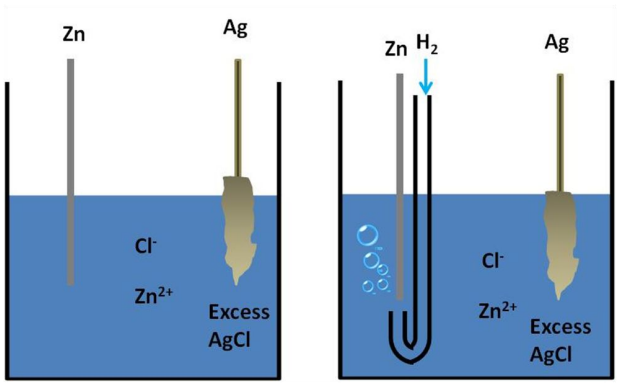

Figure 5.1 Typical electrochemical cells, (a) Zn and Ag covered with AgCl immersed in a $ZnCl_2$ electrolyte solution, (b) Pt in a stream of H_2 and Ag covered with AgCl in HCl electrolyte solution.[1]

In an electrochemical system, the chemical reaction between different chemical phases takes place , particularly, between an ionic conductor (an electrolyte) and an electronic conductor (an electrode), with electron or charge transfer in the process.[1,2] In general, electrochemical reactions are prompted by an externally electric circuit

leading to an oxidation-reduction (redox) process where electrons or charges are transferred between two phases. Electrochemistry can be separated in time or space, and is normally combined with an external applied voltage normally.[2]

Electrochemistry includes a huge array of different subjects and fields. For instance, electrochemistry applies in the nanodevices of electrocatalytic sensors, fuel cells, batteries and electrochromic displays, and further in the technologies of corrosion, electrophoresis, electroplating and electrodeposition.[1] Take a typical electrochemical cell as an example, the electrochemical reaction of Fig. 5.1b can be written schematically as (Eq. 5.1),[1]

$$\mathbf{Pt/H_2/H^+, Cl^-/AgCl/Ag} \qquad \text{(Eq. 5.1)}$$

The overall reaction is composed of two independent half reactions in their own cell part, $H^+ + e^- = H_2$. Generally, one cell is focused on the chemical reaction is working electrode, and the other one is reference electrode which is relatively stable and standardized in a constant composition.[1] When using a three-electrode cell system in the electrochemistry, a counter electrode (Pt, Au) will provide a circuit with working electrode to balance the reaction occurring in the working electrode. This is to avoid passing current over the reference electrode.[3]

5.1.2 The Reversible Hydrogen Electrode (RHE) Reference Electrode

In this work, a three-electrode system was used throughout, consisting of a reversible hydrogen electrode (RHE) as reference electrode (RE), a platinum coiled wire as counter electrode (CE), and active materials modified Au (111) or graphite as working electrode (WE) in a hanging-meniscus configuration. The RHE was freshly prepared just before measurements and checked against a saturated calomel electrode (SCE) after measurements. The benefit of the RHE as a reference electrode is that there is no contamination from reference electrode electrolyte of Cl^- or SO_4^{2-}, and the electrolyte is the same as working solution, shown in Fig. 5.2. There is therefore no

need for an electrolyte bridge for maintenance with long time measurement possible; and no diffusion potential arises.[4]

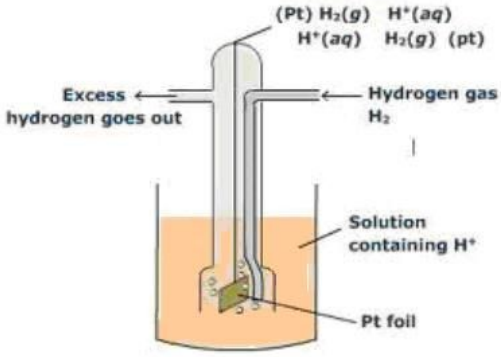

Figure 5.2. Schematic of RHE[4]

The RHE is easy to prepare in the lab freshly at the beginning of electrochemistry. A noble metal (Pt) and a super clean glass tube are starting materials in hydrogen flame and Pt is melted in the glass tube. Electrolyte of the working solution is then filled into, and then H_2 bubbled through into the tube saturated with H_2.[5, 6] The half reaction of RHE is Eq. 5.2,

$$\mathbf{2H_3O^+ + 2e^- = H_2 + 2H_2O} \qquad \text{(Eq. 5.2)}$$

The potential of the RHE depends on pH of the electrolyte, and follows the relationship as Eq. 5.3, obtained from the Nernst equation.

$$\mathbf{E^0 = -0.059 \times pH} \qquad \text{(Eq. 5.3)}$$

Due to the changing potentials by different pH values and electrolytes, the RHE is normally calibrated against the saturated calomel electrode (SCE) after measurements for standard condition.

5.1.3 Cyclic Voltammetry (CV)

Cyclic voltammetry (CV) is nearly always the first choice of technique for studying electrochemical systems.[7] Several different voltage-time functions sometimes denoted as excitation signals can drive to the working electrode, such as linear scan, differential pulse, square wave, triangular, etc.[8] Linear sweep voltammetry (LSV) is the simplest method among these potential sweep techniques. The most useful method is CV as schematically shown in the Fig. 5.3.

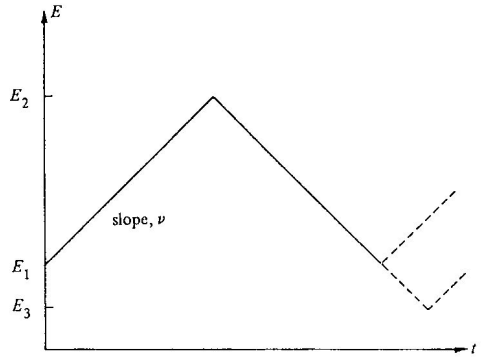

Figure 5.3. Cyclic Voltammetry curve, showing changes of potential as a function of time.[7]

In this case, the potential is initially swept from E_1, and the slope is the scan rate. On arriving at E_2, the potential sweep is reversed with the same slope until the original potential E_1 or a different potential E_3 is reached. The potential sweep can also be halted, and then reversed or continued to E_3 (Fig. 5.3). The diagram of CV is current vs. potential as a function, and the scan rates changes from a few mV/s to thousands of V/s.

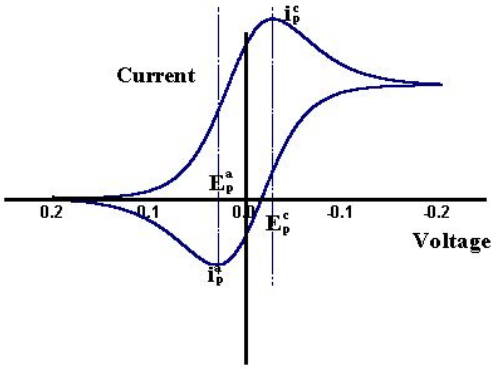

Figure 5.4. Cyclic Voltammetry for a reversible redox process (diffusion control).[7]

For the simplest electrochemical reaction process, $O + ne^- \leftrightarrow R$, the potential is swept from lower to higher potential, which is called the anodic scan, and appears an oxidation peak potential E_{pa} and peak current I_{pa}.(Fig. 5.4) While in the reverse scan, the potential is swept from higher to lower potential, which is called cathodic scan, showing up a reduction peak potential E_{pc} and peak current I_{pc}. Oxidation and reduction processes occur during the CV of electrochemistry. The formal redox potential, which represents for the equilibrium potential, is determined by the equation Eq. 5.4,

$$\mathbf{E^{0'} = (E_{pa} + E_{pc})/2} \qquad \text{(Eq. 5.4)}$$

The peak-peak separation between E_{pa} and E_{pc}, Eq. 5.5 represents the electron transfer rate.

$$\mathbf{\Delta E_p = E_{pa} - E_{pc}} \qquad \text{(Eq. 5.5)}$$

When the peak-peak separation is small, the rate constant is large and electron transfer is fast, otherwise large peak-peak separation indicates that the rate constant is small and electron transfer is slow. The CV measurements usually start from the negative potential and towards higher scan rate in order to avoid possible damaging the electrode.[7]

5.1.4 Diffusion-controlled Systems

As a simple electrochemical reaction $O + ne^- \leftrightarrow R$, it is made up of several steps of conversion from the oxidized state O to the reduced state R as shown in Fig. 5.5. The reaction rate is determined by the following four steps,[1]

(1) O mass transfer from bulk solution O_{bulk} to the electrode surface O_{surf}.

(2) Electron transfer at the electrode surface from $O_{electrode}$ to $R_{electrode}$. In this step, preceding chemical reactions or following chemical reactions might happen in the electrode surface region, with homogeneous (e.g., dimerization or protonation) or heterogeneous processes (e.g., catalytic decomposition). Other surface reactions such as adsorption, desorption or electrodeposition would sometimes take place.

(3) R mass transfer from the electrode surface R_{surf} to bulk solution R_{bulk}.

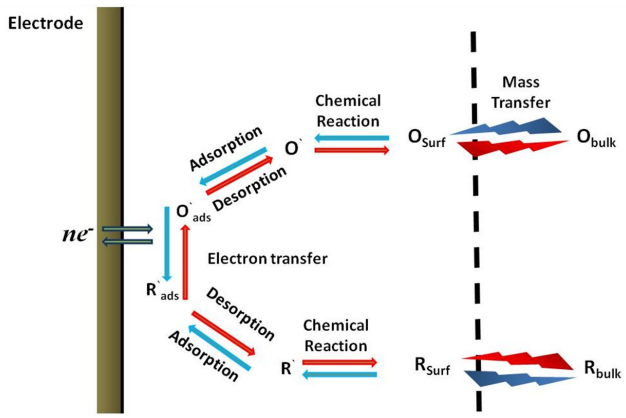

Figure 5.5. Pathway of a general electrode reaction in the electrochemical process.[1]

As the whole process described, the chemical reaction rates of the overall process are determined by both solution mass transfer of the O and R and electron transfer at the electrode surface. If the electron transfer is fast enough, it can be considered as a reversible reaction, so the rate limiting step is mass transfer in the solution by diffusion, as in Figure 5.6, where I_p^a and I_p^c are peak currents, E_p^a and E_p^c are peak potential and $E_{p/2}^a$ and $E_{p/2}^c$ stand for half-peak potential, i.e. potential at $I=I_{p/2}$.

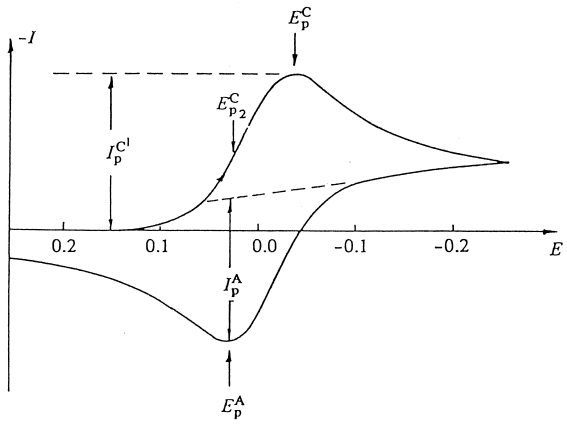

Figure 5.6. Theoretical CV for an ideal, reversible redox reaction for a diffusion-control system.[1]

The investigated molecule was first in the fully oxidized state. The potential was then swept in the direction of negative potential at a fixed scan rate, which is called a cathodic scan. The current will be increase to a maximum at the reduction potential of this molecule. The maximum cathodic peak current indicate the peak current I_{pc}, and the maximum peak potential indicated the cathodic peak potential E_{pc}. The same process also takes place when swept in the positive direction, which is termed the anodic scan. There is oxidation maximum peak during the reversible scan, with the peak potential E_{pa} and peak current I_{pa}.[9, 10]

In an ideal reversible diffusion-control system in Fig. 5.6, both reduced and oxidized states are stable. At the same time the electron transfer rate is fast enough to be independent of scan rate. The equation of an ideal diffusion-controlled system as the Nernst equation of Eq. 5.6,[1]

$$E = E^0 + \frac{RT}{nF} \ln \frac{[O]}{[R]} \qquad \text{(Eq. 5.6)}$$

Where E^0 is the formal redox potential, n is the number of electron transfer, [O] is the concentration of oxidized form, and [R] the concentration of reduced form, both at the electrode surface. For a reversible electron tranfer diffusion control system at 25 °C, the peak current I_p is given by the Randles-Sevcik equation Eq. 5.7,[1]

$$i_p = 2.69 \cdot 10^5 n^{3/2} A D_O^{1/2} v^{1/2} c_O^* \qquad \text{(Eq. 5.7)}$$

Where A is the surface area of the working electrode (cm^2), D_0 is the diffusion coefficient (cm^2/s), v is the scan rate (V/s) and c_0* is the bulk concentration (mol/cm^3). Randles-Sevcik equation indicated a linear relationship between peak current and square root of the scan rate, which provides a normal method to judge the process of diffusion control system.

5.1.5 Diffusionless-controlled Systems

When the molecules are confined on the electrode surface to form a monolayer or adlayers, there is no diffusion of the molecules in the solution. The process is then termed as diffusion less controlled system, also called surface-confined system. The ideal reversible diffusionless-controlled systems shown in the Fig. 5.7.[1]

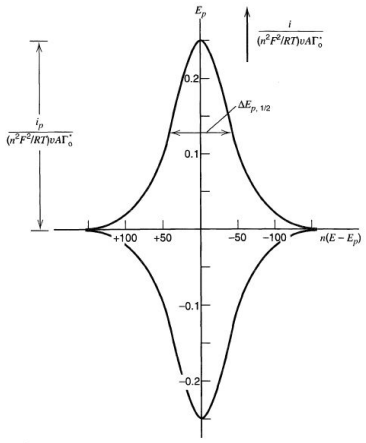

Figure 5.7. CV curve for an ideal reversible diffusionless-controlled system.[1]

In a reversible diffusionless-controlled system, the peak current I_p is given by equation as Eq. 5.8,

$$\left|I_P\right| = \frac{n^2F^2\Gamma_O\nu}{4RT} \qquad \text{(Eq. 5.8)}$$

Where Γ_0 is the surface coverage (mol/cm^2) of the adsorbed molecule during reaction. The equation predicts that the peak current is proportional to the scan rate, which is different from the square root dependence of a diffusion-controlled system.

The surface coverage is often calculated by the reductive desorption of the adlayers. For a redox process of Chapter 3, in functionalized adlayerthiol-based SAM system of R-SH bonding to the gold surface forms Au-SR, the sulfur-gold bond will be broken by reductive desorption reaching the desorption potential in a linear voltammetic scan, according to Eq. 5.9.[11]

$$\mathbf{Au\text{-}SR + e^- = Au + \text{-}SR} \qquad \text{(Eq. 5.9)}$$

The coverage of the Au-SR bond represents a one-electron cathodic process. Fig. 5.8 shows two examples of reductive desorption systems.

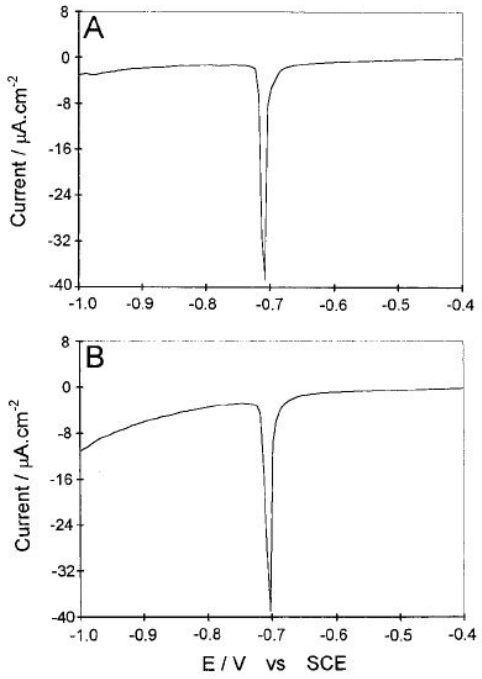

Figure 5.8. Linear scan voltammograms of reductive desorption of Au-SR in 0.1 M NaOH (pH = 13). Scan rate of 10 mV s^{-1}. (A) cysteine adsorbed on Au(111) and (B) cystine adsorbed on Au(111).[12]

The reductive desorption offers a simple and accurate method to calculate surface coverage of the adlayers, particularly suitable for thiol-based SAMs. Generally, the equation is as Eq. 5.10,

$$\Gamma_O = \left| \frac{Q}{nF} \right| \qquad \text{(Eq. 5.10)}$$

Where Q is the *charge* of the adsorbed adlayers, which can be obtained by the integration of the area of reductive desorption peak.

5.2 *In Situ* Atomic force microscopy (AFM)

Atomic force microscopy (AFM) is a technique, which offers very high image resolution and other information for a wide range of samples.[13]

AFM, first invented by Binning et al. in 1986, is currently applied to a variety of environments such as air, liquid, vacuum and for different types can be measured from different types of materials, including conductive, semiconductive, non-conductive and soft biological materials. Objects of nanoscale size or height measurements can be mapped by this fanatic technique, one example of AFM image among a variety of materials was shown in Fig. 5.9.[14]

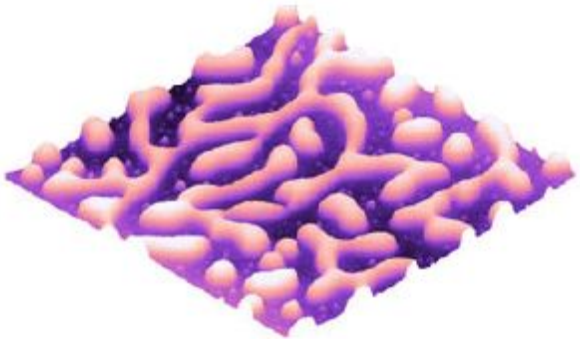

Figure 5.9. Tapping Mode AFM image of poly(methyl methacrylate) and poly(styrene) block polymer film. Scan bar 3 μm × 3 μm.[14]

5.2.1 Principles of Operation in AFM

AFM operates by scanning a sharp probe (end radius ca. 10 nm, the SEM of probe image is shown in the Fig. 5.10) scanning along a sample surface, measuring the forces acting between the tip and sample. Generally, the probe, typically a piezoelectric element, is made of silicon or silicon nitride cantilever coating with an much smaller integrated tip. The deflection from bending of cantilever depends on the

forces acting between tip and sample, and is detected by a laser focused on the cantilever.

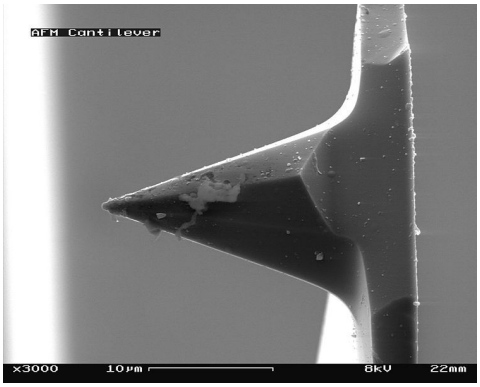

Figure 5.10. Bottom view of a kind of AFM (used) cantilever in Scanning Electron Microscope (SEM).[15]

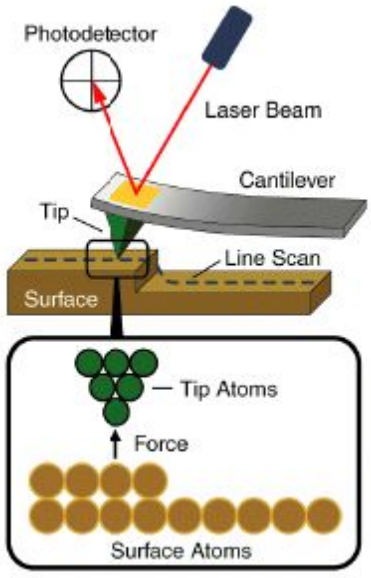

Figure 5.11. Principle of AFM.[14]

A schematic diagram is shown in the Fig. 5.11. The tip is fabricated to the end of a cantilever and approached close to the surface of the sample. The bending force of the cantilever is positive or negative resulting from the attractive or repulsive forces between tip and sample. A photodetector reflects the laser beam movement with the cantilever when scanning the sample, and records the trace of movement to obtain a high resolution image of AFM.[13] Fig. 5.11 shows the basic principle of AFM,[14] and Fig. 5.10 shows the tip and cantilever of AFM.[15]

5.2.2 Modes of Operation in AFM

The most commonly used operating modes of AFM are contact mode AFM and tapping mode AFM. A brief overview of these is given below.

5.2.2.1 Contact Mode of AFM

In the contact mode, the AFM tip is in direct soft "physical contact" with the sample surface, this is shown schematically in Fig. 5.12 for the particular case of a water drop.[16]

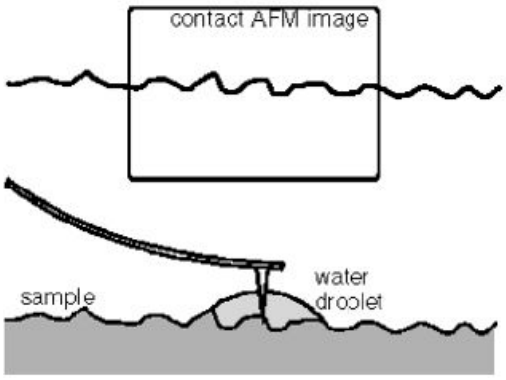

Figure 5.12. Contact mode of AFM for water drop.[16]

The deflection distance from the cantilever Δx is proportional to the force acting between tip and sample, following Hook's law F = -kΔx, where k is the spring constant of the cantilever. Using contact mode of AFM, "Atomic resolution" images with high scan speed can be achieved, and it is easier to scan rough samples with strong changes in the vertical direction of topography. However, the contact mode of AFM only measure hard samples since the tip will damage soft samples, and consequential decrease the resolution of images.[14]

5.2.2.2 Tapping Mode of AFM

In the tapping mode of AFM, there is a very short distance between tip and surface sample, and no contact directly between tip and sample surface, as shown for the water droplet.[16]

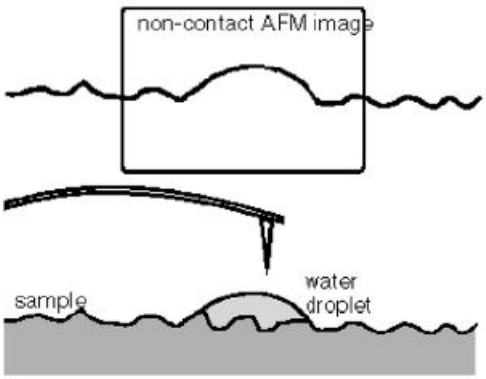

Figure 5.13. Tapping mode of AFM for water droplet.[16]

In principle, the cantilever oscillates close to its resonance frequency. The interaction between tip and sample is constant during the scanning, in the cause that the electronic feedback system confines the oscillation amplitude fixed.

When the force between tip and sample changes, it will produce a change of oscillation amplitude, as well as changes of the cantilever resonant frequency and phase. The feedback of amplitude and the vertical changes of the piezo scanner are recorded in the scanning process. The most important merit of the tapping mode is less damage to the surface of sample, which is particular suitable to soft material without destroying the samples or tips. Tapping mode eliminates a large part of the permanent shearing forces during the measurement, and almost no lateral forces. The images of tapping mode could be obtained higher lateral resolution (1-5 nm). The only drawback is that the scan speed of tapping mode is smaller than contact mode.[14]

5.3 References

[1] A. J. Bard and L. R. Faulkner, *Electrochemical Methods: Fundamentals and Applications*, New York: Wiley, **2001**, 2nd ed.

[2] Site from website at *http://en.wikipedia.org/wiki/Electrochemistry*, 20/11/2013

[3] Site from website at *http://en.wikipedia.org/wiki/Auxiliary_electrode*, 25/06/2013

[4] Site from website at *http://en.wikipedia.org/wiki/Reversible_hydrogen_electrode,* 19/04/2013

[5] C.Yu and A. Alfred, *The Journal of Physical Chemistry B*, **2004**, *108*, 9829.

[6] M. Staehler, K. Wipperman, and D. Stolten, *Joint International Meeting of the Electrochemical Society*, **2004**, abstract pp1863.

[7] D. Pletcher, R. Greff, R. Peat, L. M. Peter and J. Robinson, Southampton Electrochemistry Group, *Instrumental methods in electrochemistry*, Woodhead Publishing, **2001**.

[8] D. A. Skoog, D. M. West and F. J. Holler, *Fundamentals of analytical chemistry*, 8th edit, Thomson Brooks/Cole, **2004**.

[9] Patte Skovhus Jensen. PhD thesis, Department of Chemistry, Technical University of Denmark, **2010**.

[10] M. H. Jensen. PhD thesis, Kemisk Laboratorium A, Technical University of Denmark, Lyngby, Denmark, **1995**.

[11] M. M. Walczak, D. D. Popenoe, R. S. Deinhammer, B. D. Lamp, C. Chung, and M. D. Porter, *Langmuir*, **1991**, *7*, 2687-2693.

[12] J. Zhang, Q. Chi, J. U. Nielsen, E. P. Friis, J. E. T. Andersen, and J. Ulstrup, *Langmuir*, **2000**, *16*, 7229-7237.

[13] *http://www.afmhelp.com/index.phpoption=com_content&view=article&id=51&Itemid=57,* Siting from the website.

[14] Physics of Advanced Materials, Lecture note in Winter School, Aristotle University, Thessaloniki, Greece, **2008**.

[15] Site from website at *http://en.wikipedia.org/wiki/Atomic_force_microscopy*, 24/11/2013

[16] Site from website *http://www.eng.utah.edu/~lzang/images/Lecture_10_AFM.pdf*.

Part II: Prussian Blue Nanoparticles Self-assembled for Electrocatalysis

6. Electron Transfer and Electrocatalysis of Prussian Blue Nanoparticles Self-assembled on Modified Au (111) Surfaces

As noted in Chapter 2, Prussian Blue (PB) has a long history dating back over 300 years. This interesting material has recently been used as an electron transfer (ET) catalyst for the development of new chemical and biological sensors. This and the following two chapters mainly focus on efforts and results in synthesis, characterization and applications of PB in novel nanostructured forms focused on controlled-size PB nanoparticles (PBNPs). We have, particularly, demonstrated how to control ET and electrocatalysis of 6 nm PBNPs. Assembled on a solid surface in a two-dimensional array these nanoparticles behave like a large redox molecule such as a metalloenzyme.

6.1 Introduction of the Process

Electrocatalysis is essential in efficient electrochemical energy conversion/storage and chemical/biological sensing. Electrocatalytic processes have been widely harnessed for many applications, including organic synthesis, fuel production, sensors and biosensing.[1-6] Synthesis, characterization and application of electrocatalysis are currently approached towards the nanoscale level, and electrocatalysis at the nanoscale is emerging as core technology for meeting a variety of challenges. Nanomaterials in electron transfer (ET) controlled electrocatalysis is therefore in recent highly significant focus.

Adsorptive interaction of reactants with surface sites of the catalyst in the presence of the electric field is a key process in electrocatalytic reactions. This interaction strongly depends on the surface properties of the catalyst. Immobilized variable type

NPs have shown great potential for modified electrodes in chemical and biological applications with a view of optimizing the interaction between the NPs and target reactants. This is due to prominent NP properties such as large surface-to-volume ratio, high surface reaction activity, high catalytic efficiency, high surface concentrations of corner and edge atoms, low coordination numbers of surface atoms, and unique electronic properties. [7, 8]

As a widely used electrochemical mediator for analytical applications, PB has found broad use in fields of (bio)electrochemical sensors and biosensors during the last years. This applies especially to nano-sized PBNPs[9] which offer unique physical and chemical properties compared with their bulk counterpart. [10]

It is highly desirable that the PBNPs are water-soluble. Water solvent not only makes the synthesis process much easier than synthesis using organic solvents but also preserves the PBNP functionality for electrochemical and catalytic investigations. In addition, water is environmentally more friendly than organic solvents.

PBNPs immobilized onto an electrode surface are the redox centers in ET control and electrocatalysis in sensors and biosensing processes.[11] Ideally the NPs are uniformly immobilized on the electrode surface with identical orientation. In reality the NPs are immobilized randomly. A self-assembled monolayer (SAM) with a densely packed interface is an alternative solution because it can provide an ordered and uniform interface favorable for the NP orientation.[12] Nevertheless, the low surface NP coverage in a SAM system may restrict the sensitivity of electrochemical signals.[13] The layer-by-layer (LBL) assembly technique, introduced by Decher,[14-16] has been employed to improve NP immobilization as well as the electrochemical responses by alternate adsorption of NPs and oppositely charged film materials on the electrode surfaces.[8,17,18] Such methods can achieve precise control of structural film properties such as layer thickness and composition at the molecular or nanometer level.[19-22] The highly ordered LBL nanocomposite assemblies have had great appeal in electrochemistry and materials chemistry. [23]

PB in the form of thin polycrystalline electrodeposited films has been intensively investigated.[10] Surface preparation is assisted by favorable interactions between the electrode surface and surface groups around the ET center. Such selectivity can be improved by use of atomically planar single-crystal electrodes.[24] We have used single-crystal Au(111) as working electrodes, and different straight-chain amino-terminal thiols as linking bridges between Au(111) and PBNPs for the formation of adherent NPs.[25] NP attachment is most likely by electrostatic interactions between terminal ammonium groups in the thiol layer and the negatively charged PBNPs, shown in figure 6.1.[24, 26] Distance dependent interfacial electrochemical ET (tunneling) can be controlled by the alkanethiol chain length. The use of PBNPs as electrocatalyst in this configuration was found to improve the analytical performance for hydrogen peroxide detection based on the controlling length of the linker molecule. At the same time, the NP surface population was mapped by Atomic Force Microscopy (AFM) under the same conditions as in the electrochemical measurements (*in situ* AFM). Different functional terminal groups in Au/alkanethiol SAMs were used. In this chapter, results for amine thiol are described. These data are compared with carboxylate and methyl terminal group in Chapter 7. Three-dimensional analogues of numinous amino SAMs are discussed in Chapter 8.

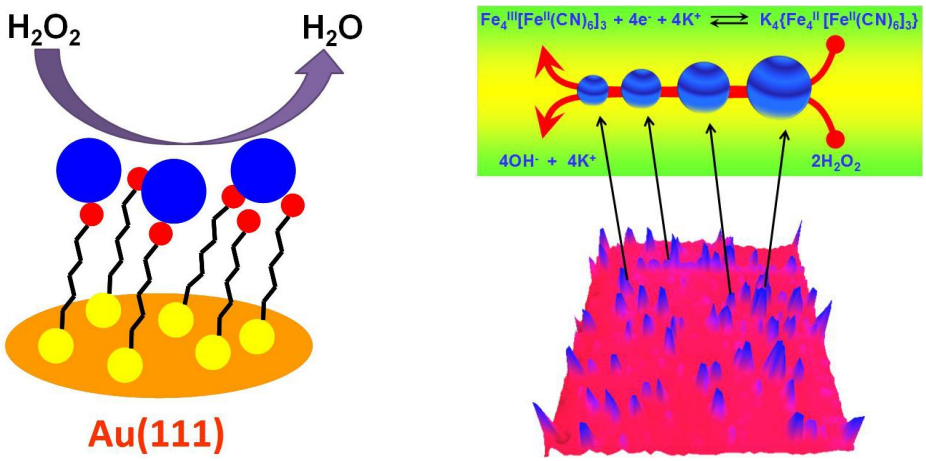

Figure 6.1 Schematic diagram of system in this chapter. (Left) Self-assembled PBNPs on the Au(111) surface; (Right) PBNPs catalysis for H_2O_2 and high-resolution AFM image.

6.2 Experimental Section

6.2.1 Materials and Reagents

$K_3[Fe(CN)_6]$ was from Riedel-de Haën (≥ 99%), $FeCl_3$ (≥ 99.5%) and $Fe(NO_3)_3$ (≥ 99.5%) from Sigma, $K_4[Fe(CN)_6]$ (≥ 99%) and H_2O_2 (≥ 99.5%) from Merck. Milli-Q (18.2 MΩ cm) water was used throughout. Different straight-chain amino-thiols, including cysteamine ($NH_2(CH_2)_2SH$, ≥ 98%, Fluka), 6-amino-1-hexanethiol, hydrochloride ($HCl{\cdot}NH_2(CH_2)_6SH$), 8-amino-1-octanethiol, hydrochloride ($HCl{\cdot}NH_2(CH_2)_8SH$), 11-amino-1-undecanethiol, hydrochloride ($HCl{\cdot}NH_2(CH_2)_{11}SH$), and 16-amino-1-hexadecanethiol, hydrochloride ($HCl{\cdot}NH_2(CH_2)_{16}SH$) from DojinDo Lab, were the highest purity commercially available and used as received. All other reagents were ultrapure grade. 0.1 M KCl (from Aldrich, ≥ 99%) solution (PH = 5) was used to prepare electrolyte solutions.

6.2.2 Synthesis of Prussian blue Nanoparticles (PBNPs)

PBNPs was prepared in three steps. In the first step, solid PB pigment was synthesized. $Fe(NO_3)_3$ (30 ml 1.3 M) solution was gradually adding into $K_4[Fe(CN)_6]$ (60 ml 0.5 M) solution with strongly stirring. The mixture immediately changed color from yellow to dark blue. When mixing was completed, the reaction mixture was vigorously stirred for another 5 min. Then the resulting mixture was washed with MillQ water by centrifuging several times at 4°C to remove the supernatant of unreacted reagents and precipate left to dry in air to obtain PB pigment.

In the second step, the PB pigment was redispersed by adding $K_4[Fe(CN)_6]{\cdot}3H_2O$ into the pigment-water suspension. To achieve the water-soluble nanoparticles, solid PB pigment (0.4 g) was suspended in 15 ml water, followed by adding $K_4[Fe(CN)_6]$ freshly prepared solution (5 ml 45 mM). The suspension was dissolved into a transparent dark blue solution with strong stirring for 4h.

In the third step, the PBNP solution was purified by using an stirred ultrafiltration cell and membrane to remove residual salts. The stirred ultrafiltration cell was assembled and the PBNP solution diluted with Milli-Q water with the membrane molecule of 3000 according to the size of PBNPs to filtration. The process was repeated 3-5 times by adding fresh Milli-Q water until the filtrate became colorless.

The PBNP concentration was controlled by UV-Vis Spectroscopy. The UV-Vis spectra of dilute PBNP solutions showed maximum absorbance around 700 nm, corresponding to the mixed-valence charge-transfer transition, Figure 6.2.

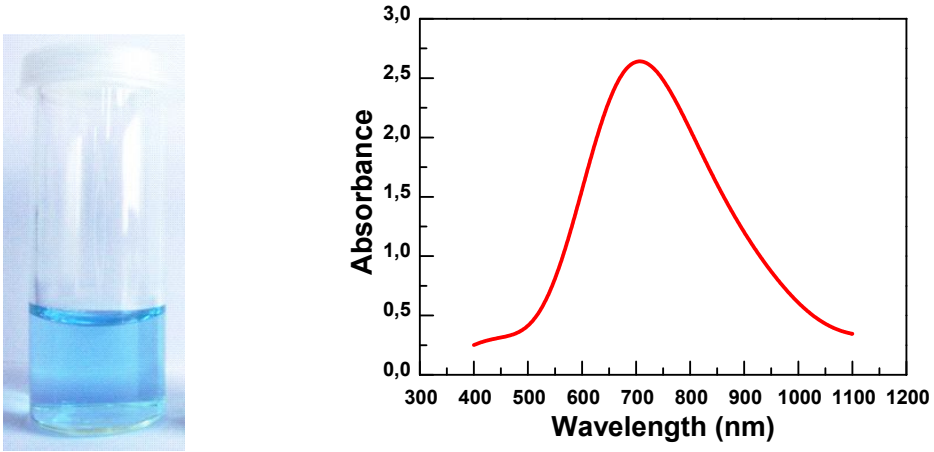

Figure 6.2. Image and UV-Vis spectrum of PBNPs in pure water with a maximum absorption around 700 nm.

6.2.3 Preparation of Self-assembed Molecular Monolayers

Au(111) electrodes were used as substrates for both electrochemistry and AFM. To prepare SAMs on Au(111) surfaces, Au(111) electrodes were freshly annealed in a H_2 flame and quenched in ultrapure water saturated with H_2 gas. They were then immersed in freshly prepared $NH_2(CH_2)_nSH$ ethanol solutions (1~10 mM) overnight

(about 20 -24 hours). After rinsing with ethanol and Milli-Q water several times, the electrodes were transferred to PBNP solutions and incubated at room temperature for several hours (2-20 hours). Prior to use, the electrodes were rinsed with Milli-Q water. The PBNP solution was checked by UV-Vis spectroscopy (Agilent Instrument Exchange Service Model G1103A) at 700 nm shown in Figure 6.2.

6.2.4 Electrochemical Measurements

All electrochemical measurements were carried out at room temperature (23 ± 2°C) using an Autolab System (Eco Chemie, Netherlands) controlled by the general-purpose electrochemical system software. A three-electrode system was used, consisting of a reversible hydrogen electrode (RHE) as reference electrode (RE), a platinum coiled wire as counter electrode (CE), and a PBNPs-$NH_2(CH_2)_nS$-Au(111) as working electrode (WE) in a hanging-meniscus configuration. The RHE was freshly prepared just before measurements and checked against a saturated calomel electrode (SCE) after measurements. All electrode potentials are referred to the SCE. Purified argon (5 N, Chrompack, Varian) was applied to purge dioxygen from electrolyte solution before the measurements, and an argon stream maintained over the solution during the measurements.

6.2.5 Electrochemical AFM Measurements

AFM Measurements were performed using a 5500 AFM System (Agilent Technologies) equipped with various working modes. For PBNPs-$NH_2(CH_2)_nS$-Au(111) systems, all images were recorded in liquid environments (0.1 M KCl), i.e., the same environments as for electrochemical measurements.

6.3 Results and Discussion

6.3.1 Microscopic Structure of Self-Assembled PBNPs on Au(111)-electrode Surfaces

The PBNP population was also obtained by counting the number of PBNPs observed by AFM. AFM images were mapped randomly at several different areas on the SAM modified Au(111) substrate surface and the average number of PBNPs per unit area calculated as the surface coverage.[31] As an example Figure 6.3 (Left) shows tapping-mode AFM image for PBNPs adsorbed on the $NH_3^+(CH_2)_6S$-Au(111) surface, controlled under the same conditions as in CV (0.1 M aqueous KCl). These results show clearly that PBNPs were present on the SAM modified gold surfaces in the electrochemical process.

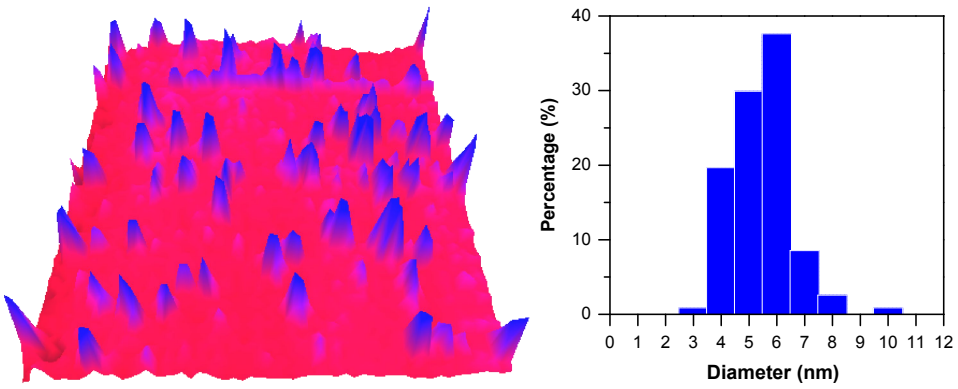

Figure 6.3. (Left) A 3D *in situ* AFM image for PBNPs assembled on a Au(111)-electrode surface modified with $NH_2(CH_2)_6SH$. The image was recorded in 0.1 M KCl solution. Scan area 500 × 500 nm^2. (Right) The size-distribution histogram for immobilized PBNPs shows a maximum of particles around 5-6 nm, which is consistent with the results obtained from TEM in Chapter 9.

As shown in Figure 6.3 Left, most of the observed PBNP structures are single NPs, with very little agglomeration. According to a representative AFM distribution histogram (Figure 6.3 Right), the mean diameter of particles was around 5-6 nm,

which is close to the value determined from TEM in Chapter 9. Although the distribution is not completely uniform, there are enough discrete PBNPs for the size analysis. The size distribution basically follows a Gaussian distribution (or normal distribution).

6.3.2 Interfacial Electron Transfer of PBNP Mono- and Sub-monolayers

A series of Au(111) electrodes with self-assembled variable-length functionalized alkanethiol linkers between the electrode and the PBNPs were investigated. The interfacial ET rate measured by cyclic voltammetry (CV) can be controlled by the variable alkyl chain length.[24]

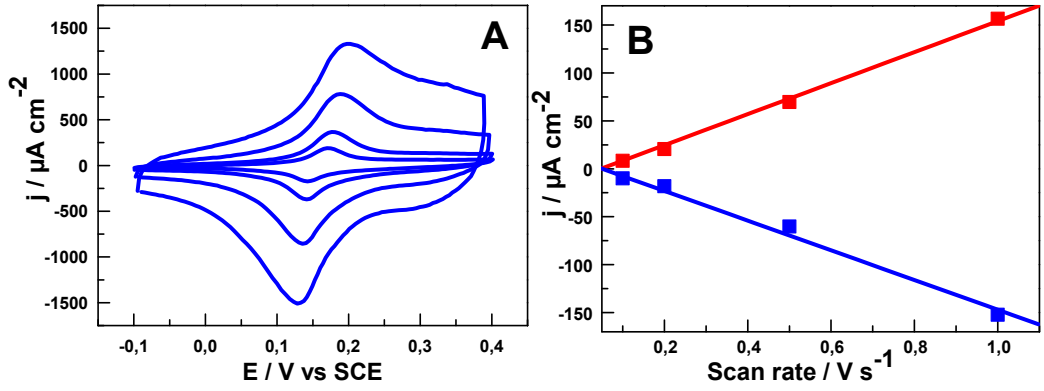

Figure 6.4. (A) Representative CVs of PBNP-$NH_2(CH_2)_6S$-Au(111) in 0.1 M KCl. Scan rates 1.0, 2.0, 5.0 and 10 V s^{-1}. (B) Linear relationship between peak currents and scan rates reflects diffusionless electrochemical behavior.

Data for the PBNPs-$NH_3^+(CH_2)_6S$-Au(111) system as a representative of the different chain length systems, are shown in Figure 6.4. Figure 6.4A shows a series of CVs for adsorbed PBNPs at different scan rates. Both anodic and cathodic peak current density increase with increasing scan rates. The sharp peak, of half-width value is

strongly indicative of an interfacial multi-ET process, specifically a 4-ET process, and uniformity of the self-assembling process. The linear relationship between peak current density and scan rate, Figure 6.4B implies that the PBNPs-$NH_3^+(CH_2)_6$S-Au(111) system complies with diffusionless behavior. Other chain lengths accord with similar behavior as C_6, which supports the generality of this pattern. Electrochemistry of 6 nm PBNPs in homogenous solution to detect only edge-plane pyrolytic graphite (EPG) electrode for a diffusion control process is shown in Figure 6.5.

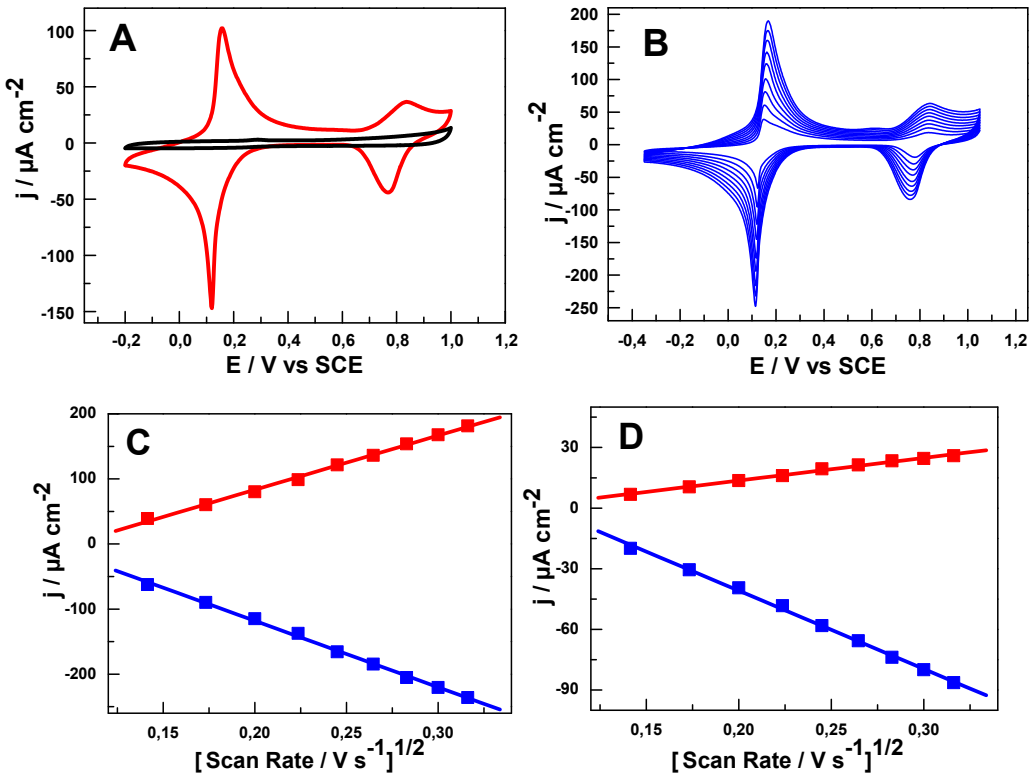

Figure 6.5. Electrochemistry of 6 nm PBNPs in homogenous solution. Bare edge-plane pyrolytic graphite (EPG) electrode. (A) Comparison of CVs in the presence (red) and absence (black) of PBNPs in 0.1 M KCl. Scan rate: 50 mV s^{-1}. (B) Representative CVs of 6 nm PBNPs in 0.1 M KCl with different scan rates 20, 30, 40, 50, 60, 70, 80 ,90, 100 mV s^{-1}. (C) Relationship between peak currents and the square root of scan rates (peak potential around 0.1 V vs. SCE, anodic current (red line) and cathodic current (blue line)) shows a diffusion controlled process. (D) Relationship between peak currents and the square root of scan rates (peak potential around 0.8 V vs. SCE, anode current (red line) and cathode current (blue line)) shows a diffusion controlled process.

CVs were obtained for all the alkanethiols, Figure 6.6. Scan rates from 0.1 to 30 V/s were acquired, except for C_{16} for which 10 V/s was the upper scan rate limit. Anodic and cathodic Faradaic signals correspond to Eq. 6.1.[24] Variation of the CVs with the alkyl chain length is reflected by the peak separation and the peak shape, both indicative of strongly distance dependent ET rates.

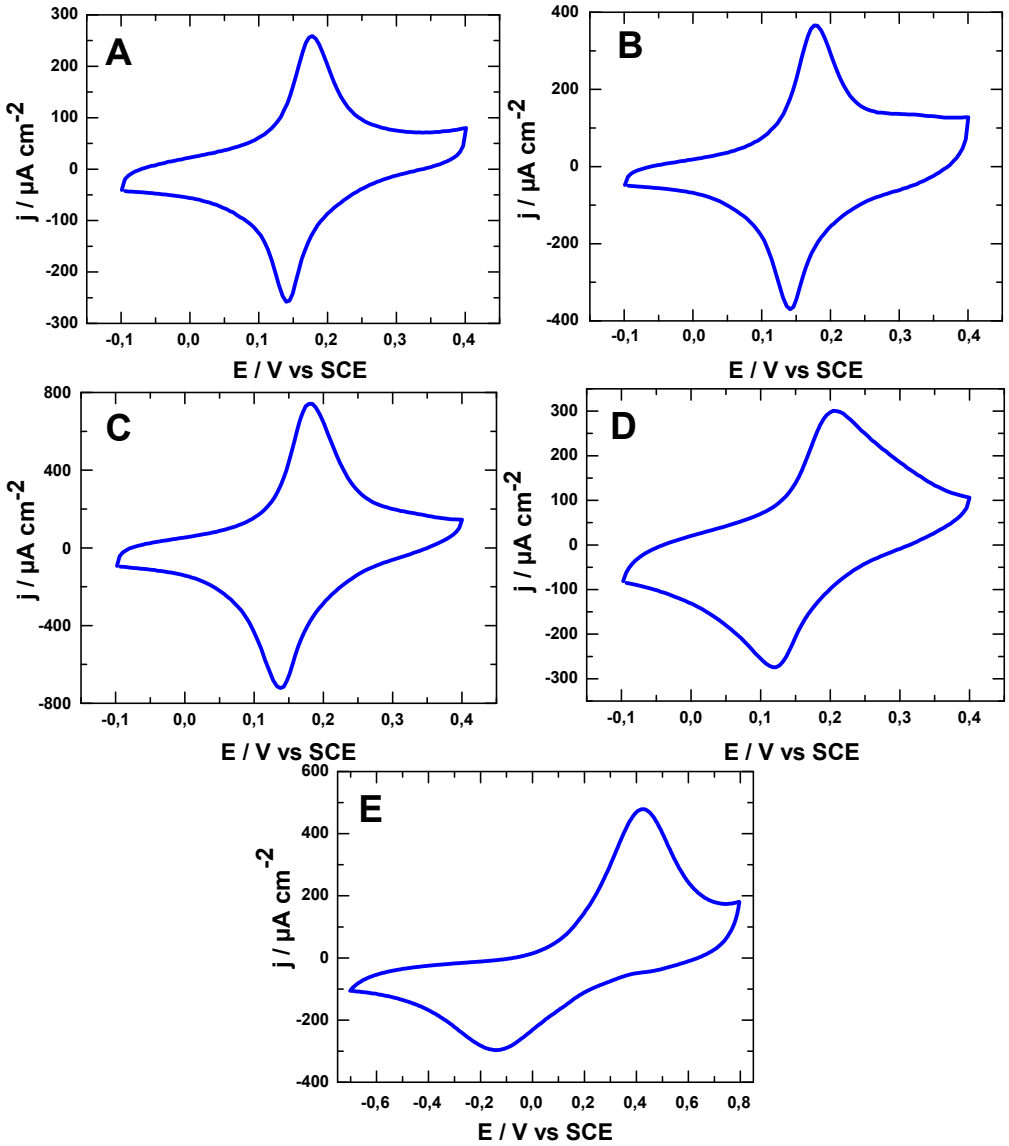

Figure 6.6. CVs for PBNP-$NH_2(CH_2)_nS$-Au (111) in 0.1 M KCl with increasing number of CH_2 units: n = 2 (A), 6 (B), 8 (C), 11 (D) and 16 (E). Scan rate 2 V s^{-1}.

Figure 6.6 shows particularly that the peak separation, $\triangle E_p$ measured at the same scan rate increases notably as the number of methylene groups in the alkyl chain spacer increases. When the alkyl chain length becomes longer, ET between the electrode and the redox center proceeds over a larger distance, slowing the overall ET rate. [28]

$$Fe_4^{III}[Fe^{II}(CN)_6]_3 + 4K^+ + 4e^- \rightleftharpoons K_4Fe_4^{II}[Fe^{II}(CN)_6]_3 \qquad \text{(Eq. 6.1)}$$

As expected, the formal PBNP redox potential (E^o) at different chain lengths is almost independent of the alkyl chain lengths for short chains, Table 6.1. The average value is around 0.150 V vs SCE. The potential was shifted to slightly more positive values for longer chain lengths. The effect is, however, small and the precise physical reason presently eludes detail.

Table 6.1. Comparison of the redox potential, SAM thickness, and PBNP population.

-(CH)$_n$-	*Formal redox potential $E^{o'}$ (mV) vs. SCE*	*Surface coverage $10^{12}\Gamma$ (mol cm^{-2})*
PBNPs-C_2-Au	149	8.6
PBNPs-C_6-Au	154	19
PBNPs-C_8-Au	152	38
PBNPs-C_{11}-Au	181	47
PBNPs-C_{16}-Au	177	163

It is also noted from Table 6.1 that the surface coverage of PBNPs first increases with increasing chain length and then passes through a maximum. This observation suggests that the stability of the PBNP adlayer is first enhanced by increasing alkyl chain length. This could imply that the packing order of the monolayer on the electrode surface increases with longer alkyl chain spacer, in accordance with other observations for long-chain alkanethiol SAMs.[28, 29] This effect, however, seems to reach saturation beyond a chain length of about ten methylene groups.

Table 6.2. Comparison of Population Estimation from AFM

-(CH)$_n$-	*Surface coverage (Electrochemical of Units) $10^{12}\Gamma$ (mol cm^{-2})*	*Population (AFM convolution corrected) $10^{12}\Gamma$ (mol cm^{-2})*	*Number of redox units per NP* in AFM image
PBNPs-C_2-Au	8.6	24	2.8
PBNPs-C_6-Au	19	48	2.5
PBNPs-C_8-Au	38	41	1.1
PBNPs-C_{11}-Au	47	159	3.4
PBNPs-C_{16}-Au	163	38	0.23

The surface coverage of the PBNPs on the Au(111) were also performed by *in site* AFM within the liquid solution, Table 6.2 and images like the ones shown in Figure 6.3 (Left). The exact gap distances are not distinguishable by AFM imaging due to the well-known convolution effect of the AFM tips.[32] Quantifying the number of self-assembled PBNPs of various small to large nanoparticle ratios based on an AFM image alone can be challenging or even misleading without careful consideration of

the fundamental physics of the metrology involved.[33] A rational model for AFM convolution correction was therefore developed. To determine the surface coverage, all the particles were assumed to be of regular spherical or square shape. Assuming the surface is fully covered with nanoparticles, the percentage of apparent nanoparticle number in the area to the ideal fully covered nanoparticle number could then be calculated and the surface coverage of nanoparticles obtained. A nanoparticle with an average size was recorded by the height of cross section profile instead of the apparent size in the images because of the AFM tip convolution effect.

From Table 6.2, the surface coverages of PBNPs between electrochemistry and AFM are seen to be little different. The reason is that one nanoparticle seen in AFM may contain several active units (Prussian blue units). The number of redox units per nanoparticle in the AFM image of different chain linker groups in the SAMs seems to be similar and around 1-3, which is reasonable for the statistical significance. This type of method provides a convenient way to research the further electrocatalytic effiency for per nanoparticle or per redox unit.

The interfacial electrochemical rate constants, k_s were estimated from the variation of the peak-peak separation on the scan rate using Laviron's formalism.[30] Details are given in Chapter 7. As a representative of the different chain length systems, the linear relation between the Laviron parameter m^{-1} and ν of PBNPs-$NH_3^+(CH_2)_6$S-Au(111) is shown in Figure 6.7A. The dependence of the ET rate constant k_s on the distance between the redox center and the electrode surface was found to accord with Eq. 6.2,[28]

$$k_s = k_0 \exp(-\beta n) \qquad \text{(Eq. 6.2)}$$

Where k_0 is a constant discussed elsewhere[24]. The ET rate constants thus decrease exponentially as the distance between the redox center and the electrode surface increases. Figure 6.7B shows the plot of the logarithm of the rate constant as a

function of the number of methylene units of PBNPs-$NH_3^+(CH_2)_nS$-Au(111). The rate constant is largely independent of the chain length up to n = 6. A clear exponential decay is, however, observed at longer chain length[24] with a meaningful decay factor of β = 0.85 per CH_2 (equivalent to ca. 0.7 $Å^{-1}$) strongly indicative of rate controlling electron tunneling through the alkanethiol SAM at longer chain lengths. This accords with interfacial ET behavior of both small molecules (ferrocene) and redox metalloproteins[24] (cytochrome *c* and azurin) and supports the view of a 6 nm PBNP as a molecular scale redox unit.

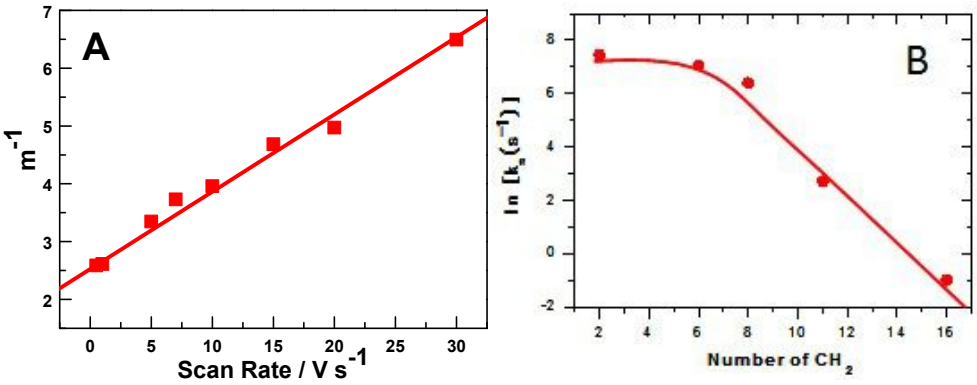

Figure 6.7. (A) *Laviron* plot for PBNP-$NH_2(CH_2)_6$S-Au (111). (B) The dependence of the rate constant on the distance denoted by the number of CH_2 units, gives a decay factor (β) of ca. 0.85 per CH_2 (i.e., equivalent to ca. 0.7 $Å^{-1}$)

6.3.3 Electrochemical Catalysis

The electrocatalysis for H_2O_2 reduction by PBNPs immobilized via different SAM linker chain lengths were evaluated by CV. CVs of H_2O_2 at SAM modified electrodes without immobilized PBNPs were recorded as controls. With PBNPs-$NH_3^+(CH_2)_2$S-Au (111) as one example, Figure 6.8 shows that a much stronger electrocatalytic effect was observed when PBNPs were present compared with electrocatalysis without PBNPs. This observation is representative for all the SAM linker molecules. Since the detailed surface coverage of different chain lengths were obtained from

voltammetric data, Table 6.1, the contribution to the H_2O_2 reduction current from each PBNP at the different variable-length SAMs can be calculated. These results are shown in Table 6.3 and demonstrate that the shorter the SAM molecular chain length, the stronger is the electrocatalytic activity for H_2O_2 reduction.

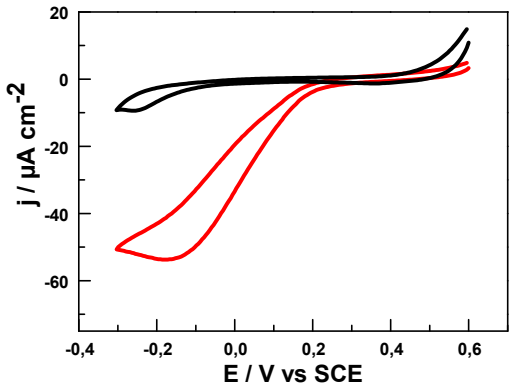

Figure 6.8. A comparison of electrocatalytic activity of H_2O_2 reduction with (red) and without PBNPs (black) for $NH_2(CH_2)_2S$-Au(111). 0.1 M KCl. 0.5 mM H_2O_2. Scan rate 20 mV s^{-1}.

Table 6.3. Comparison of PBNPs electrocatalytic activity for reduction of H_2O_2. The current density was obtained at -0.1 V for 0.1 mM H_2O_2.

-(CH)$_n$-	*Surface coverage $10^{12}\Gamma$ (mol cm^{-2}) From Units*	*Apparent current density i_{pc} (μA cm^{-2})*	*Normalized current density $10^{20} j_{cat}$ (A/per particle)*
PBNPs-C_2-Au	8.6	6.6	129
PBNPs-C_6-Au	19	7.0	61
PBNPs-C_8-Au	38	9.3	41
PBNPs-C_{11}-Au	47	6.3	22
PBNPs-C_{16}-Au	163	1.5	1.6

Electrocatalytic activity towards different concentrations of H_2O_2 from 0.05 to 1 mM for $NH_3^+(CH_2)_6S$-Au(111) are shown in Fig. 6.9. The calibration plot, Fig.6.9A shows that the current increases with increasing H_2O_2 concentration. The correlation is linear from 0.2 to 0.5 mM and remains constant after 0.5 mM, attributed to saturation of active sites on the PBNPs.

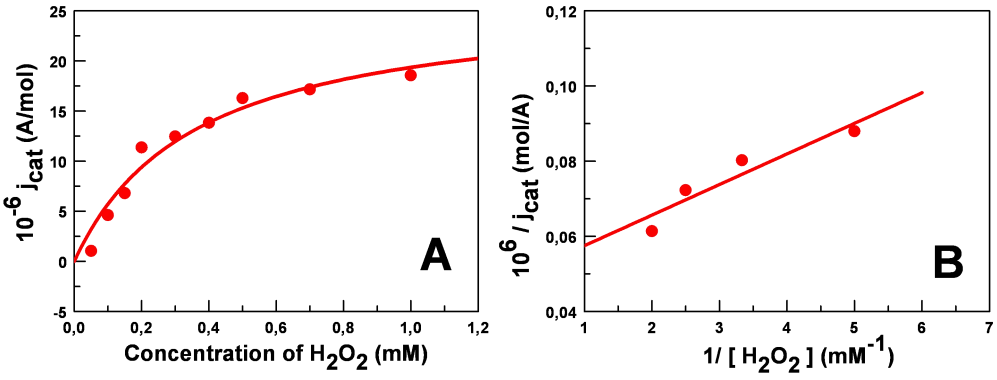

Figure 6.9. Electrocatalytic activity at different concentrations of H_2O_2 for $NH_3^+(CH_2)_6S$-Au(111). (A) Michaelis-Menten correlation for H_2O_2 concentrations from 0.05 to 1 mM. (B) Lineweaver-Burk plot of the same data.

The following approximate electrochemical version of the Michaelis–Menten equation applies for the relation between the electrocatalytic current density (j) and the substrate concentration ([S]).[34]

$$j = nF\Gamma \frac{k_{cat}[\mathrm{S}]}{K_M + [\mathrm{S}]} \qquad \text{(Eq. 6.3)}$$

where Γ is the surface coverage of the PBNPS, n the number of electrons transferred (here = 4), F the Faraday constant, K_M the apparent Michaelis constant and k_{cat} the

apparent turnover rate constant. The PBNP surface coverage was estimated voltammetrically as noted.

Eq. 6.3 gave a good fit to the experimental data with K_M = 0.36 mM and k_{cat} = 66 s^{-1}. k_{cat} is clearly much smaller than the ET rate constant for the uncatalyzed PBNP (1100 s^{-1}). This must be attributed to different rate-determining steps. While the catalytic rate is high in bulk H_2O_2 solution between PBNPs and H_2O_2, the electrocatalytic efficiency is approach dominated by concerted ET between PBNPs and H_2O_2 and interfacial ET between the PBNPs and the electtode.

The data were also analyzed by the Lineweaver-Burk equation. As for the Michaelis-Menten equation this equation correlates current density (j) to the concentration [S] in the form:

$$\frac{1}{j/\Gamma} = \frac{1}{nFk_{cat}} + \frac{K_M}{nFk_{cat}}\frac{1}{[\mathrm{S}]} \qquad \text{(Eq. 6.4)}$$

$1/(j/\Gamma)$ plotted against 1/[S] thus gives a straight line from which K_M and k_{cat} can be obtained, Figure 6.9B, using the good linear correlation in the H_2O_2 concentration range of 0.2, 0.3, 0.4, 0.5 mM. K_M and k_{cat} were found to be 0.16 ± 0.05 mM and 52 ± 4 s^{-1}, respectively, which are close to the Michaelis–Menten values.

6.4 Conclusions

We have synthesized 6 nm PBNPs and proved them to be highly efficient both in interfacial ET and as an enzyme-like nanoscale electrocatalyst. The PBNP nanomaterial is stable in water with excellent redox activity. Fast and reversible interfacial PBNP ET on a gold electrode surface modified with functional alkanethiols was detected by cyclic voltammetry with four electron transfer in the process. The ET kinetics can be controlled by adjusting the chain length of amino

terminated alkanethiols and depends exponentially on the ET distance. The decay factor (β) is 0.85 per CH_2. This feature suggests a tunneling mechanism and resembles similar observations for the redox metalloproteins[24] (cytochrome *c* and azurin) in a similar assembly. The immobilized PBNPs display, further high-efficient electrocatalysis towards the reduction of H_2O_2, and a quantitative relationship between the ET kinetics and electrocatalytic activity. Overall, we have developed a new approach to control the ET and electrocatalysis of electroactive nanoparticles such as PBNPs immobilized on solid surfaces, which offers clues to detailed understanding of ET properties and electrocatalytic characteristics.

6.4 References

[1] H. H. Thorp, *Trends Biotechnol* **1998,** *16*, 117-121.

[2] T. de Lumley-Woodyear; C. N. Campbell; E. Freeman; A. Freeman; G. Georgiou; A. Heller, *Anal Chem* **1999,** *71*, 535-538.

[3] S. O. Kelley; E. M. Boon; J. K. Barton; N. M. Jackson; M. G. Hill, *Nucleic Acids Res* **1999,** *27*, 4830-4837.

[4] E. M. Boon; D. M. Ceres; T. G. Drummond; M. G. Hill; J. K. Barton, *Nat Biotechnol* **2000,** *18*, 1096-1100.

[5] M. A. Lapierre; M. O'Keefe; B. J. Taft; S. O. Kelley, *Anal Chem* **2003,** *75*, 6327-6333.

[6] R. Gasparac; B. J. Taft; M. A. Lapierre-Devlin; A. D. Lazareck; J. M. Xu; S. O. Kelley, *J Am Chem Soc* **2004,** *126*, 12270-12271.

[7] I. Willner; B. Willner; E. Katz, *Bioelectrochemistry* **2007,** *70*, 2-11.

[8] G. X. Li; J. Zhao; X. L. Zhu; T. Lib, *Analyst* **2008,** *133*, 1242-1245.

[9] F. Ricci; G. Palleschi, *Biosens Bioelectron* **2005,** *21*, 389-407.

[10] P. A. Fiorito; V. R Goncales; E. A. Ponzio; S. I. C. de Torresi, *Chem Commun* **2005,** 366-368.

[11] Q. J. Chi; O. Farver; J. Ulstrup, *P Natl Acad Sci USA* **2005,** *102*, 16203-16208.

[12] S. Song; R. A. Clark; E. F. Bowden; M. J. Tarlov, *J Phys Chem-Us* **1993,** *97*, 6564-6572.

[13] A. M. Kuznetsov; J. Ulstrup, *Electron transfer in chemistry and biology: an introduction to the theory*. John Wiley and Sons Ltd, Chichester, UK and New York, UK: 1998.

[14] G. Decher; J. D. Hong, *Makromol Chem-M Symp* **1991,** *46*, 321-327.

[15] G. Decher, *Science* **1997,** *277*, 1232-1237.

[16] G. Decher; J. D. Hong; J. Schmitt, *Thin Solid Films* **1992,** *210*, 831-835.

[17] J. W. Ostrander; A. A. Mamedov; N. A. Kotov, *J Am Chem Soc* **2001,** *123*, 1101-1110.

[18] X. Zhang; H. Chen; H. Y. Zhang, *Chem Commun* **2007,** 1395-1405.

[19] C. Y. Jiang; V. V. Tsukruk, *Adv Mater* **2006,** *18*, 829-840.

[20] P. T. Hammond, *Adv Mater* **2004,** *16*, 1271-1293.

[21] N. A. Kotov; Z. Y. Tang; Y. Wang; P. Podsiadlo, *Adv Mater* **2006,** *18*, 3203-3224.

[22] S. J. Dong; F. Wang; J. L. Wang; H. J. Chen, *J Electroanal Chem* **2007,** *600*, 265-274.

[23] G. B. Xu; X. Q. Liu; F. Wang; S. Han; L. H. Shi, *Electroanal* **2010,** *22*, 963-968.

[24] Q. J. Chi; J. D. Zhang; J. E. T. Andersen; J. Ulstrup, *J Phys Chem B* **2001,** *105*, 4669-4679.

[25] S. Q. Liu; J. J. Xu; H. Y. Chen, *Electrochem Commun* **2002,** *4*, 421-425.

[26] A. Avila; B. W. Gregory; K. Niki; T. M. Cotton, *J Phys Chem B* **2000,** *104*, 2759-2766.

[27] A. J. Bard; L. N. Faulkner, *Electrochemical Methods*. John Wiley and Sons Ltd, Chichester, UK and New York, USA: New York, 1980.

[28] H. G. Hong; W. Park, *Langmuir* **2001,** *17*, 2485-2492.

[29] M. D. Porter; T. B Bright.; D. L. Allara; C. E. D. Chidsey, *J Am Chem Soc* **1987,** *109*, 3559-3568.

[30] E. Laviron, *J Electroanal Chem* **1979,** *101*, 19-28.

[31] M. Tominaga; M. Ohtani; I. Taniguchi, *Phys Chem Chem Phys* **2008,** *10*, 6928-6934.

[32] Z. F. Liu; L. M. Tong; T. Zhu, *Chem Soc Rev* **2011,** *40*, 1296-1304.

[33] R. I. MacCuspie; C. G. Geronimo, *Microsc Microanal* **2011,** *17*, 206-214.

[34] Q. J. Chi; J. D. Zhang; P. S. Jensen; H. E. M. Christensen; J. Ulstrup, *Faraday Discuss* **2006**, *131*, 181-195.

[35] A. Gotoh et al, *Nanotechnology* **2007**, *18*, 345609.

7. Electron Transfer and Electrocatalysis of Prussian Blue Nanoparticles Immobilized on Surfaces with Different Chemical Properties

The study described in Chapter 6 was extended to 5-6 nm hybrid Prussian Blue nanoparticles (PBNPs) immobilized on Au(111)-electrode surfaces modified by variable-length and differently functionalized thiol-based self-assembled molecular monolayers (SAMs). The SAMs were functionalized by positively ($-NH_3^+$) of Chapter 6, and negatively charged groups ($-COO^-$) as well as neutral hydrophobic groups ($-CH_3$). The surface microscopic structures of the immobilized PBNPs were again characterized by high-resolution atomic force microscopy (AFM) in aqueous electrolyte under the same conditions as in cyclic voltammetry of the PBNPs. The PBNPs disclosed fast and reversible ET on all the surfaces, controlled by adjusting the chain length of the SAM forming molecules. The rate constants were found to depend exponentially on the ET distance, with decay factors (β) of 0.9, 1.1, and 1.3 per CH_2, for SAMs terminated by $-NH_3^+$, $-COO^-$, and $-CH_3$, respectively, suggesting that the interfacial ET processes of the PBNPs follow a tunneling mechanism of Chapter 6. Highly efficient PBNP electrocatalysis of the reduction of H_2O_2 was also observed for the three different linker groups.

7.1 Introduction of the Process

As noted in Chapter 6, Prussian Blue (PB) is a prototype mixed-valence transition metal complex material. PB has been thoroughly investigated as an electron transfer (ET) mediator in amperometric sensors and biosensors,[1-3] and its electrochromic, photophysical, and magnetic properties characterized in great detail.[4,5] Due to its excellent electrocatalysis and highly sensitive detection limit, PB has been defined as "artificial peroxidase",[1] making it very attractive in oxido-reductase-based biosensing.[6,7] A number of new approaches for synthesizing PB have become available in recent years starting with the first report on the synthesis of PB films by

Neff.[8,9] Among the new approaches, nanotechnology and PB nanoparticles (PBNPs) have emerged as one of the most exciting.[10] The most commonly used method for PBNP preparation has been electrodeposition, but a shortcomining of this technique is that the resulting PBNP material is provided in the form of thick and loose films with poor adhesion.[7,11] Due to the advantage of small size, large surface-to-volume ratio, and increased surface activity, the notion of dispersed PBNPs as opposed to bulk nanomaterials has been introduced in electrocatalysis and sensing.[7,12,13]

Two iron centers in the 2+ and 3+ oxidation states constitute the core elements in the chemical and crystal structure of PB. The Fe^{3+} and Fe^{2+} ions are bridged to nitrogen and carbon atoms, respectively, through the bridging cyanide ligands.[15-18] Only small molecules such as H_2O_2, may penetrate into the PB lattice, whereas larger molecules such as uric acid, ascorbic acid, or paracetamol, can not.[14] Monitoring low levels of H_2O_2 is of great importance in enzymatic analysis, in medical and environmental control, and in various branches of industry.[8,21] In addition, the octahedral geometry[19] of the PB molecular units seems to be the cause of effective electrochemical selectivity and H_2O_2 detection free of interference.[20] The sensitivity of PB as an electron mediator in electrocatalytic H_2O_2 reduction increases as more PB is brought to participate in the electrocatalytic process.[1] However, despite extensive studies, there is still dispute over whether hexacyanoferrate species[22] may be adsorbed, as well as over the nature of the adsorbate. The latter has been considered to be one or both of the redox species of the $[Fe(CN)_6]^{3-/4-}$ couple, [23] or a more complex 'reaction product' formed from these species.[24-26]

Molecular self-assembly of PBNPs on electrode surfaces offers to pave the way for rapid, simple, and versatile PBNP surface electrocatalysis.[1,27] Low PBNP surface coverage and stability may, however, limit the activity and the electrochemical signals.[28] Self-assembled molecular monolayers (SAMs) may instead anchor PBNPs on the electrode surface and serve to develop their application as electrocatalysts and sensors. It is therefore essential to fabricate modified electrodes that assist the

immobilization as well as securing electrochemical responses of PBNP SAMs on the electrode surface.[27-31]

Self-assembly of molecular nanoscale structures, such as redox metalloproteins, has come to offer not only immobilization techniques, but also control of the interfacial ET routes.[32] Controlled ET based on surface self-assembly has been strikingly displayed for electroactive metalloproteins including representatives of the three major classes of ET proteins, i.e. the heme proteins,[33,34] the blue copper protein azurin,[35] and iron-sulfur proteins as well as several redox metalloenzymes.[36] In comparison, the uncertainty as to the exact structure of PBNPs has also been cause for uncertainty concerning the electrochemical reactions of PBNPs on the electrode surface.[3]

In this chapter, we describe extension of the study presented in Chapter 6. PBNPs were immobilized on Au (111)-electrode surfaces SAMs functionalized with two other terminal groups, so that positively or negatively charged and neutral groups can be compared. PBNPs assemble on the single-crystal Au(111)-electrode surface modified by either of the three linkers in configurations favorable for fast interfacial electrochemical ET through the linker molecules.[37] The PBNP array was further characterized by atomic force microscopy (AFM) under electrochemical potential control (*in situ* AFM). Fast and reversible electron transfer (ET) of PBNPs on all the surfaces was mapped by cyclic voltammetry (CV). ET kinetics could be controlled by the chain length of the SAM molecules, and the rate constants were found to depend exponentially on the ET distance with decay factors indicative of tunneling through the linker groups. Highly efficient electrocatalysis of the reduction of H_2O_2 was also observed in all cases, and the catalytic mechanism analyzed.

7.2 Experimental Section

7.2.1 Materials

PBNPs were prepared as described in Chapter 6, by a modification of Gotoh's method,[38] with the specified size around 5-6 nm. Highest purity straight-chain amino-thiols of 6-amino-1-hexanethiol, hydrochloride ($HCl{\cdot}NH_2(CH_2)_6SH$), 8-amino-1-octanethiol, hydrochloride ($HCl{\cdot}NH_2(CH_2)_8SH$), 11-amino-1-undecanethiol, hydrochloride ($HCl{\cdot}NH_2(CH_2)_{11}SH$), and 16-amino-1-hexadecanethiol, hydrochloride ($HCl{\cdot}NH_2(CH_2)_{16}SH$) were all from DojinDo Lab. Cysteamine ($NH_2(CH_2)_2SH$, ≥ 98%) was from Fluka. The straight-chain methyl-terminated thiols 1-Butanethiol ($CH_3(CH_2)_3SH$, ≥ 99%),1-Pentanethiol ($CH_3(CH_2)_4SH$, ≥ 98%), 1-Hexanthiol ($CH_3(CH_2)_5SH$, ≥ 95%), and 1-Octanthiol ($CH_3(CH_2)_7SH$, ≥ 98.5%) were from Aldrich. Straight-chain carboxyl-terminated thiol, 3-Mercaptopropionic acid ($HS(CH_2)_2COOH$, ≥ 99%), 6-Mercaptohexanoic acid($HS(CH_2)_5COOH$, ≥ 90%), 8-Mercaptooctanoic acid ($HS(CH_2)_7COOH$, ≥ 95%), and 11-Mercaptoundecanoic acid ($HS(CH_2)_{10}COOH$, ≥95%) were from Aldrich. All the thiol-based molecules were used as received. $FeCl_3$ (≥ 99.5%) and $Fe(NO_3)_3$ (≥ 99.5%) were from Sigma, $K_4[Fe(CN)_6]$ (≥ 99%) and H_2O_2(≥ 99.5%) from Merck, and $K_3[Fe(CN)_6]$ from Riedel-de Haën (≥ 99%). All other reagents and chemicals were ultrapure grade. 0.1M KCl (Aldrich, ≥ 99%) solution (pH 5) was used in the preparation of electrolyte solutions. Ethanol was from Merck (≥ 99.9%). Milli-Q (18.2 MΩ cm) water was used throughout.

7.2.2 Self-assembled Thiol-based Molecular Monolayer Preparation

The Au(111)-electrodes were used as working electrodes both in electrochemistry and AFM. The Au(111)-electrodes were annealed in a H_2 flame and quenched in ultrapure water saturated with H_2 gas. SAMs were prepared by immersing the quenched Au(111)-electrodes immediately into freshly prepared 5 mM $NH_2(CH_2)_nSH$, $CH_3(CH_2)_nSH$ and $HS(CH_2)_nCOOH$ ethanol solutions overnight (about 24 hours). After rinsing the samples with ethanol and Milli-Q water several times, the electrodes

were transferred into PBNP solutions and incubated at room temperature overnight to form self-assembling layers.

7.2.3 Electrochemical Measurements and AFM Imaging

Electrochemical measurement and in situ AFM imaging were carried out as described in Chapter 6.

7.3. Results and Discussion

7.3.1 Microscopic Structure of PBNPs on Self-Assembled Functionalized Alkanethiols

PBNPs are negatively charged but can still interact strongly with both positively and negatively charged as well as with electrostatically neutral terminal groups in the SAMs, as shown schematically in Figure 7.1. The linker groups assemble directly on Au(111) via covalent gold-thiol bonding, leaving the terminal -NH_2 (Figure7.1a), -COO^- (Figure 7.1b), and -CH_3 (Figure 7.1c) surface groups exposed to the ethanol solution. 5-6 nm PBNPs were next assembled from aqueous electrolyte onto the SAM-modified Au(111)-surfaces by electrostatic or hydrophobic interaction. The alkanethiol carbon chain is both a linking bridge and a medium for electron tunneling between the electrode and the PBNPs.[32] These systems are stable with high signal-to-noise ratios. The interfacial ET rate can, moreover, be controlled by varying the alkyl chain length. These systems thus exhibit a new case of long-range electrochemical ET, here between the electrode and the PBNPs.[32]

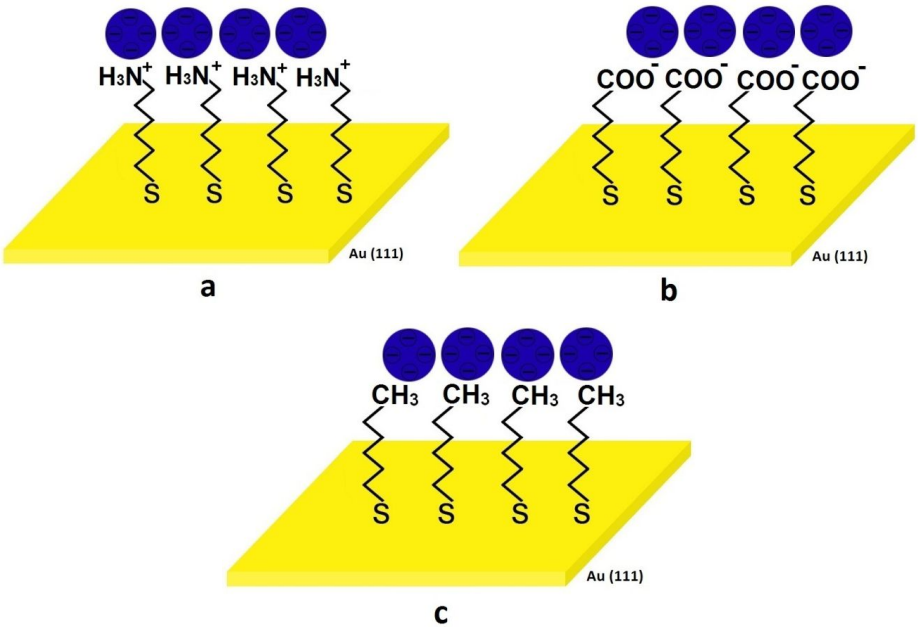

Figure 7.1. Schematic diagram showing PBNPs (blue spheres) binding as: (a) PBNP-$NH_3^+(CH_2)_nS$-Au(111); (b) PBNP-$COO^-(CH_2)_nS$-Au(111); (c) PBNPs-$CH_3(CH_2)_nS$-Au(111).

The PBNPs immobilized on the SAM-modified Au(111)-electrode surfaces were characterized by tapping mode *in situ* AFM using the same conditions as in the electrochemical investigations (0.1 M aqueous KCl). Figure 7.2 shows *in situ* AFM images of PBNPs on Au-$S(CH_2)_6NH_3^+$, Au-$S(CH_2)_5COO^-$ and Au-$S(CH_2)_5CH_3$, all of the same chain length of the linker bridge. The images were recorded for different randomly chosen substrate areas. PBNP (sub-)monolayers were observed from the images in all cases. The height distributions are shown in Figure 7.2 (Figure 7.2b, 7.2d and 7.2f). Most observed structures were single nanoparticles, with little agglomeration.

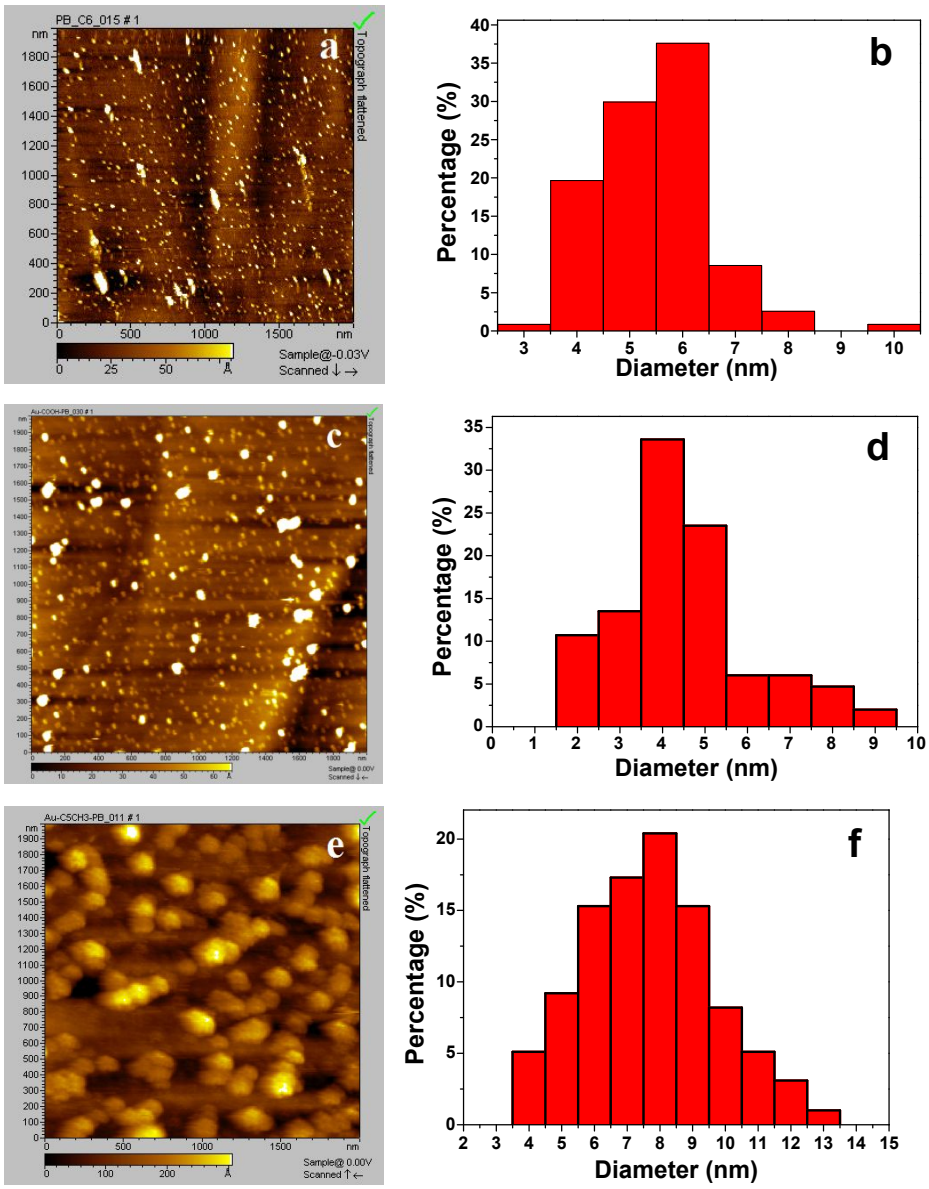

Figure 7.2. AFM images and size distribution of PBNPs on the SAM-modified Au(111)-electrode surfaces. (a) and (b) PBNP-$NH_3^+(CH_2)_6S$-Au(111); (c) and (d) PBNP-COO^- $(CH_2)_5S$-Au(111); (e) and (f) PBNP-$CH_3(CH_2)_5S$-Au(111) in the aqueous solution.

The lateral extension of the PBNPs is convoluted with the AFM tip.[37] The average nanoparticle size was therefore determined by the height of cross section profiles. The mean particle diameter was 5-6 nm for Au-$S(CH_2)_6NH_3^+$, 4-5 nm for Au-$S(CH_2)_5COO^-$, and slightly larger, i.e. 7-8 nm for Au-$S(CH_2)_5CH_3$ (Figure 7.2b, 7.2d

and 7.2f). These values were close to the values determined from TEM. The distribution is not completely uniform, but there are enough discrete PBNPs for the size analysis.

7.3.2 Electrochemistry and Interfacial Electron Transfer of PBNP Adlayers

Electrochemical techniques are uniquely sensitive to the state of the adsorbed PBNPs.[32] The PBNP assembly appeared to establish effective electronic coupling to the Au(111)-electrode surface via the different SAMs, leading to fast interfacial ET detected by CV.[35] Representative CVs for a fixed linker group chain length (six carbon atoms) with the different terminal groups Au-S$(CH_2)_6NH_3^+$, Au-S$(CH_2)_5COO^-$ and Au-S$(CH_2)_5CH_3$ are compared in Figure 7.3.

A single pair of peaks was obtained for all the three terminal groups but with different anodic and cathodic peak separation. The peak-peak separation increases in the order positive charges < negative charges < neutral, indicative of corresponding decreasing values of the interfacial electrochemical ET rate constants. The midpoint potential of the three systems are all around 150 mV vs SCE, Table 7.1, independently of the linker terminal groups and chain length (Table 7.2, 7.3 and 7.4).

Table 7.1. Comparison of ET Properties for the three different terminal groups

PBNP/SAM	*Formal midpoint potential* $E^{o'}$ *(mV) vs SCE*	*Rate constant* k_s (s^{-1})
PBNP- $NH_3^+C_6$-Au	154	1170
PBNP-COO^-C_5-Au	152	175
PBNP-CH_3C_5-Au	137	0.39

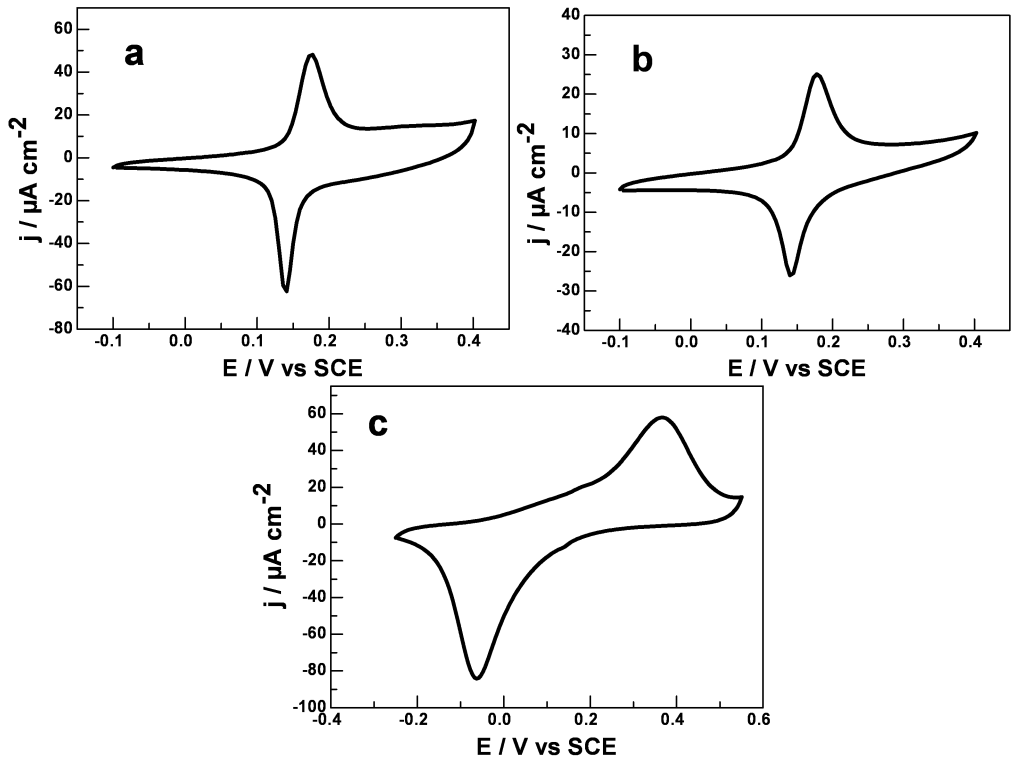

Figure 7.3. CVs for different linker terminal groups. a: PBNP-$NH_3^+(CH_2)_6$S-Au(111); b: PBNP-$COO^-CH_2)_5$S-Au(111); c: PBNPs-$CH_3(CH_2)_5$S-Au(111). Scan rate 0.5 V s^{-1}. 0.1 M KCl.

Table 7.2. Redox potential and -$NH_3^+(CH_2)_n$-terminated SAM chain lengths of Chapter 6. Scan rate 0.5 V s^{-1}.

-$NH_3^+(CH_2)_n$-	*Formal redox potential $E^{o'}$ (mV) vs SCE*	*Rate constant k_s (s^{-1})*	*Normalized current density10^{-8} j_{cat} (A/mol·M) (from 0.1 mM)*
PBNP-C_2-Au	149	1700	77
PBNP-C_6-Au	154	1170	37
PBNP-C_8-Au	152	600	24
PBNP-C_{11}-Au	181	15	13.4
PBNP-C_{16}-Au	177	0.37	0.92

Table 7.3. Redox potential and $–COO^{-}(CH_2)_n$-terminated SAM chain lengths. Scan rate 0.5 V s^{-1}.

-$COO^{-}(CH_2)_n$-	*Formal redox potential $E^{o'}$ (mV) vs SCE*	*Rate constant k_s (s^{-1})*	*Normalized current density 10^{-9} j_{cat} (A/mol·M) (from 0.2 mM)*
PBNP-COO^{-}C2-Au	147	920	142
PBNP-$COO^{-}C_5$-Au	152	175	43
PBNP-$COO^{-}C_7$-Au	142	22	29
PBNP-$COO^{-}C_{10}$-Au	188 (0.05V/s)	0.81	None

Table 7.4. Redox potential and -$CH_3(CH_2)_n$-terminated SAM chain lengths. Scan rate 0.05 V s^{-1}.

-$CH_3(CH_2)_n$-	*Formal redox potential $E^{o'}$ (mV) vs SCE*	*Rate constant k_s (s^{-1})*	*Normalized current density 10^{-8} j_{cat} (A/mol·M) (from 0.2 mM)*
PBNP-CH_3C_2-Au	140	7.7	48
PBNP-CH_3C_4-Au	144	2.5	29.0
PBNP-CH_3C_5-Au	137	0.39	24.1
PBNP-CH_3C_7-Au	125	0.05	None

The apparent rate constants, k_s were obtained from CVs at different scan rates for each system (Figure 7.4) using Laviron's method.[33,39] Both anodic and cathodic peak current densities showed a linear increase with increasing scan rates, reflecting surface electrochemical behaviour, in accordance with the nature of the assembled systems.[33] The peak separation is given by $\Delta E_p = (4RT/nF)\ ln(1/2m)$, where R is the gas constant, T the temperature, F Faraday's constant, and n (= 4) the number of electrons transferred. The parameter m is determined by k_s and the scan rate v (V s^{-1}), as $m = RTk_s/(nFv)$.[37] This relationship for the three systems is shown in Figure 7.5.

The rate constants are collected in Table 7.1. The data show that for given length of the linker, the positively charged linker group gives the largest and the neutral linker by far the smallest rate constant. Rate constants for variable lengths of the linker groups with the three different terminal groups are given in Tables 7.2-7.4. The linear relationship between peak currents and scan rates, shown in Figure 7.6, demonstrate diffusion-less electrochemical behavior.

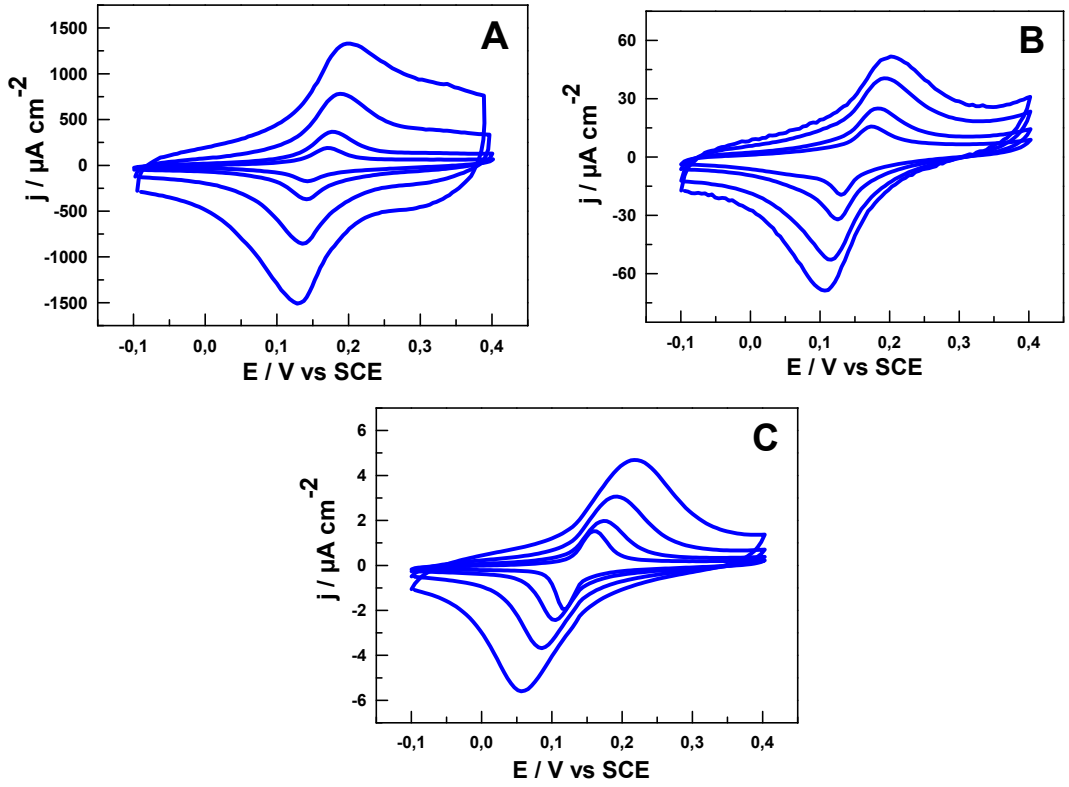

Figure 7.4. (A) CVs of PBNP-$NH_3^+(CH_2)_6$S-Au(111) in 0.1 M KCl. Scan rates 1.0, 2.0, 5.0, 10 V s^{-1}. (B) CVs of PBNP-$COO^-(CH_2)_5$S-Au(111) in 0.1 M KCl. Scan rates 0.5, 1.0, 2.0, 3.0 V s^{-1}. (C) CVs of PBNP-$CH_3(CH_2)_5$S-Au(111) in 0.1 M KCl. Scan rates 0.005, 0.01, 0.02, 0.04 V s^{-1}.

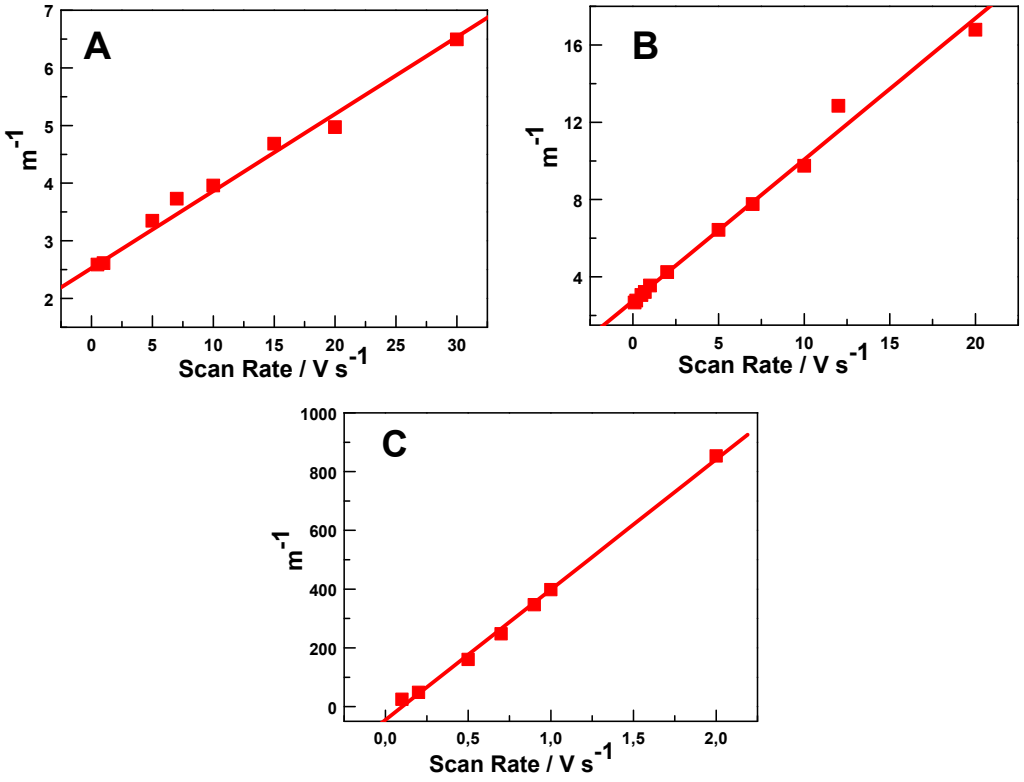

Figure 7.5. (A) *Laviron* plot showing the relation of m^{-1} vs. scan rates for PBNP-$NH_3^+(CH_2)_6$S-Au (111). (B) m^{-1} vs. scan rates for PBNP-$COO^-(CH_2)_5$S-Au (111). (C) m^{-1} vs. scan rates for PBNP-$CH_3(CH_2)_5$S-Au (111).

The correlation between ln(k_s) and the number of methylene units for different terminal linker groups are shown in Figure 7.7. The distance dependence follows Eq. 7.1[32,40]

$$k_s = k_o \exp(-\beta n) \qquad \text{(Eq. 7.1)}$$

where k_0 is a constant the meaning of which is discussed elsewhere[32]. Figure 7.7a shows that the rate constant for the $-NH_3^+$ terminal group is largely independent of distance at chain lengths up to n = 6, while a clear exponential decay is obtained at longer chain lengths. As noted, this behavior has been reported for both simple redox molecules and redox metalloproteins.[32,35] The decay factor (β) of 0.85 per CH_2 also

follows reported values and strongly suggests that electron tunneling across the SAM is a controlling factor. The SAMs with the terminal groups $–COO^-$ and $–CH_3$ follow closely a similar pattern, Figure 7.7b and 7.7c with decay factors of 1.1 and 1.3 per CH_2 unit, respectively.

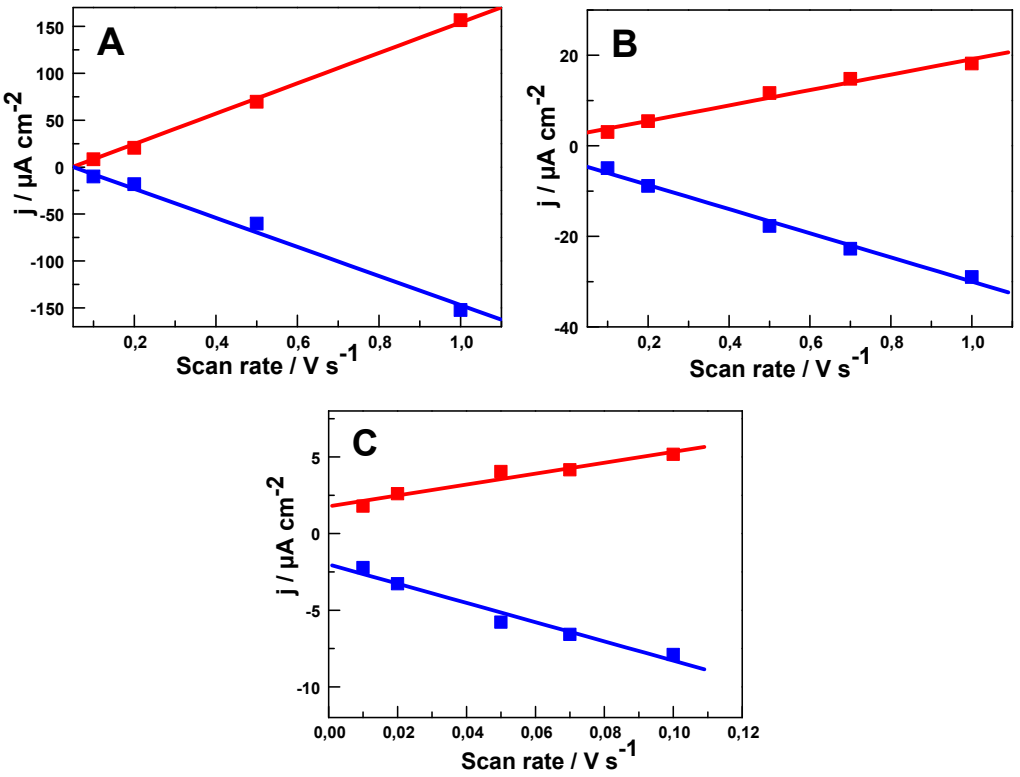

Figure 7.6. Linear relationship between peak currents and scan rates shows diffusionless electrochemical behaviour. (A) PBNP-$NH_3^+(CH_2)_n$S-Au(111); (B) PBNP-$COO^-(CH_2)_n$S-Au(111); (C) PBNP-$CH_3(CH_2)_n$S-Au(111).

The small, but significant differences in the β-values are intriguing. The PBNPs are negatively charged. This could explain both that β for the positively charged $–NH_3^+$ terminal group is the smallest and the rate constant the largest. The order of the rate constants and β-values for the other two terminal groups is less obvious. PBNPs might be expected to be exposed to electrostatic repulsion in both cases, either by

direct Coulomb repulsion or by repulsive image forces, giving smaller rate constants and larger β-values than for the $-NH_3^+$-terminated SAM. The relative strength of these two forces cannot, however, be precisely assessed. Other compensating attractive forces must also operate as the PBNPs remain firmly adsorbed on the Au(111)-electrode surface modified by these SAMs.

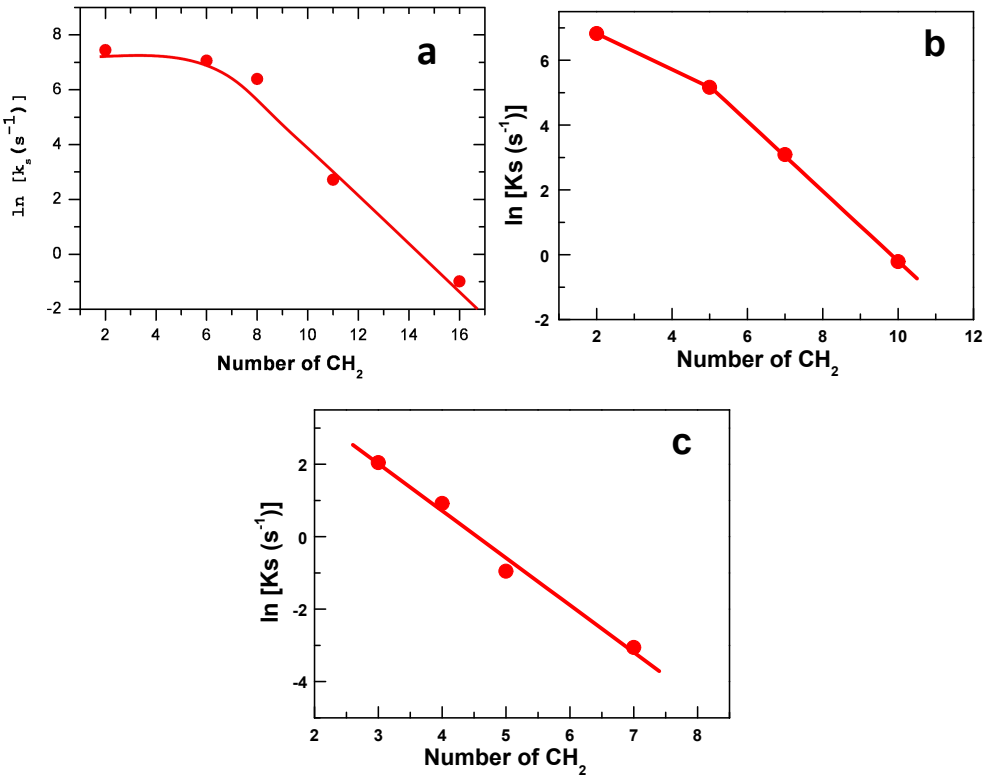

Figure 7.7. a: PBNP-$NH_3^+(CH_2)_nS$-Au(111). The dependence of the rate constants on the number of CH_2 units, gives a decay factor (β) of 0.85 per CH_2 (equivalent to 0.7 $Å^{-1}$). b: PBNP-$COO^-(CH_2)_nS$-Au(111), giving $\beta \approx 1.1$ per CH_2. c: PBNP-$CH_3(CH_2)_nS$-Au(111), giving $\beta \approx 1.3$ per CH_2.

7.3.3 Electrocatalytic Reduction of H_2O_2

The electrocatalysis of the 5-7 nm PBNPs in the electrochemical reduction of H_2O_2 to H_2O was explored. The controlled electrode/NP distance and different terminal

functional groups are additional controlling factors offered by the PBNP-based system. At the same time this process is at the core of glucose and other bioelectrochemical sensing.[10]

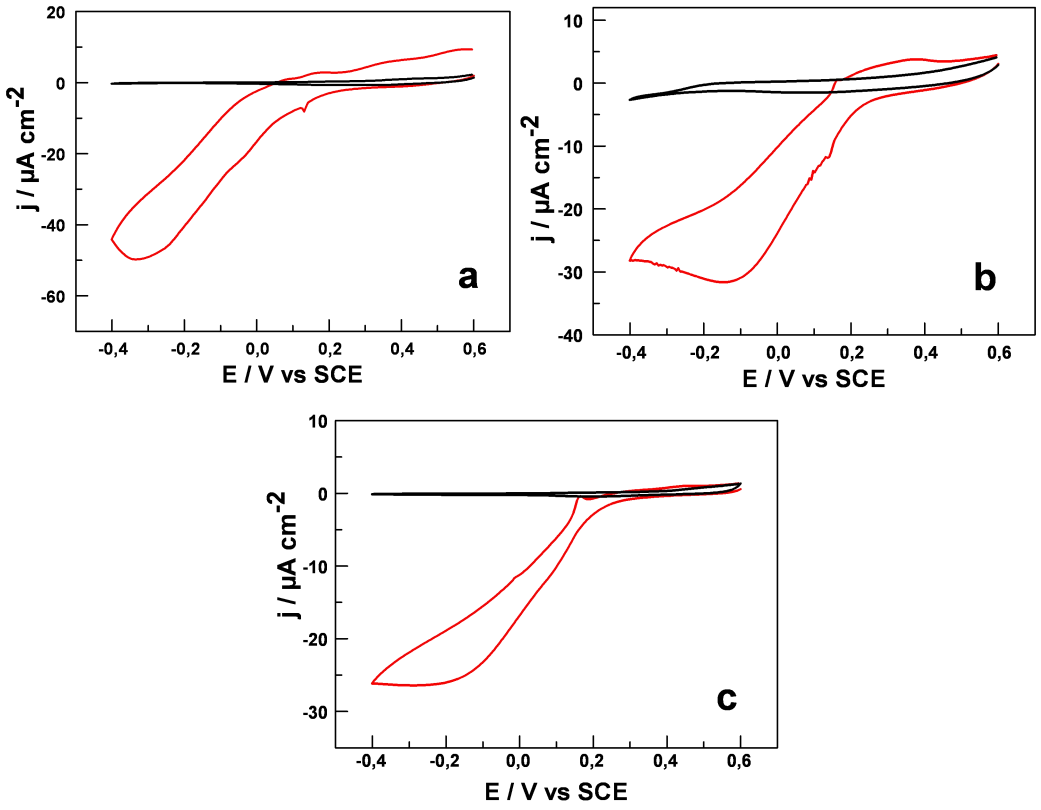

Figure 7.8. Electrocatalytic activity of differently functionalized Au(111)/SAM/PBNP interfaces in H_2O_2 reduction in the presence (red) and absence of PBNPs (black) for a: $NH_3^+(CH_2)_6S$-Au(111), b: COO^-C_5-Au(111) and c: CH_3C_5-Au(111). 0.1 M KC; 0.4 mM H_2O_2. Scan rate: 20 mV s^{-1}.

Figure 7.8 shows CVs of SAM-modified Au(111)-electrodes. (a: Au-$S(CH_2)_6NH_3^+$; b: Au-$S(CH_2)_5COO^-$; c: Au-$S(CH_2)_5CH_3$) in the presence (red) and absence (black) of PBNPs in 0.1 M KCl solution and 0.4 mM H_2O_2. A remarkable increase of the reduction current is observed in all cases when PBNPs are present compared with the absence of PBNPs. The PBNPs are obviously strongly electrocatalytically active in

electrochemical reduction of H_2O_2. Comparison of electrocatalysis of the differently terminated SAMs shows, further that the $–NH_3^+$-terminated SAMs (Figure 7.8a) is the most efficient catalyst support and the $–CH_3$ terminated SAM (Figure 7.8c) the least efficient. These observations are in striking accordance with the pattern for interfacial electrochemical ET of the PBNPs and point to interfacial electrocatalysis based on the notion of "artificial enzyme electrocatalysis".

The H_2O_2 concentration variation of PBNP electrocatalysis was further recorded, Table 7.5 and Fig.7.9. The cathodic currents increase strongly with increasing H_2O_2 concentration. Fig.7.9 shows the concentration dependence of the Au(111)/SAM/PBNP electrocatalytic currents normalized to current density per redox unit. These correlations are linear in the range 0.2-1 mM reaching saturation at higher concentrations. Electrocatalysis at variable-length alkanethiol SAMs was also tested, Tables 7.2-7.4, and found to follow a pattern resembling that for direct interfacial ET, cf. Below.

Table 7.5. Electrocatalytic H_2O_2 reduction. Catalytic current density for H_2O_2 reduction normalized to current density/redox unit. Scan rate: 20 mV s^{-1}.
(i_{cat}/surface coverage, current density in units of $10^{-6} j_{cat}$ A/mol)

SAM type	Concentration of H_2O_2 (mM)			
	0.2 mM	0.4 mM	1 mM	10 mM
PBNPs- $NH_3^+C_6$-Au	11.4	13.8	18.6	22.9
PBNPs-COO^-C_5-Au	8.6	11.0	18.2	21.1
PBNPs-CH_3C_5-Au	2.0	3.7	7.8	8.4

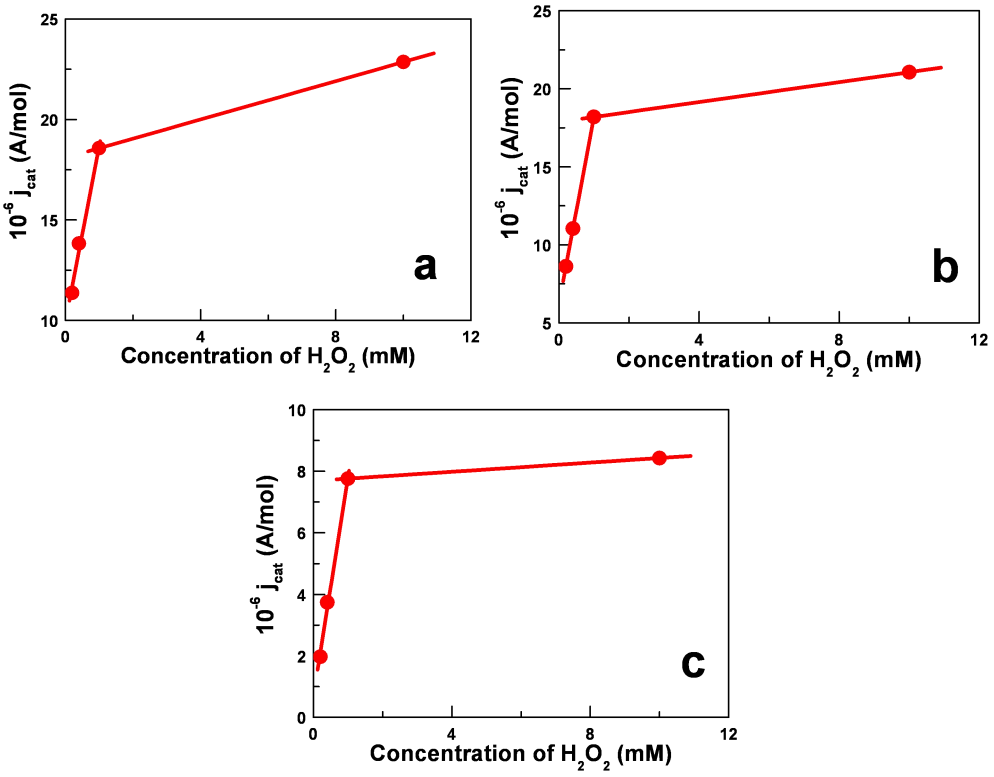

Figure 7.9. Electrocatalytic activity for H_2O_2 reduction at the three SAM/PBNP-modified Au(111)-electrode surfaces at different H_2O_2 concentrations. a : $NH_3^+(CH_2)_6S$-Au(111); b: $COO^-(CH_2)_5$-Au(111) and c: $CH_3(CH_2)_5$-Au(111). 0.1 M KCl. Scan rate: 20 mV s^{-1}.

Data for electrocatalysis of electrochemical H_2O_2 reduction at variable length of the SAM linker molecules at the three differently functionalized Au(111)/SAM/PBNP electrode surfaces are summarized Table 7.2-7.4. Chain lengths from C_2-C_{16}, C_2-C_{10} and C_2-C_7 for $NH_3^+(CH_2)_nS$-Au(111), $COO^-(CH_2)_n$-Au(111) and $CH_3(CH_2)_5$-Au(111), respectively, were addressed (0.1 M KCl + 0.2 mM H_2O_2; 20 mV s^{-1}) in Fig 7.10. In contrast to the interfacial electrochemical ET of the PBNPs, the catalytic current density decays approximately exponentially with increasing SAM chain length in the whole C_2-C_n range (n = 16, 10, 7) including the shortest linker chain lengths. The slopes are, however, much smaller than for the non-catalytic current densities, viz. 0.31, 0.33 and 0.23 µA cm^{-1} mM^{-1} for SAMs terminated by $-NH_3^+$, $-COO^-$ and $-CH_3$, respectively, but the chain length remains an important controlling factor. The

catalytic current density even drops to values lower than the values for direct ET in the non-catalytic mode when the chain is very long. This pattern is caused by the composite, two-step (really multi-step) nature of the H_2O_2 electrocatalytic process and is addressed in the following Section and see also Chapter 6.

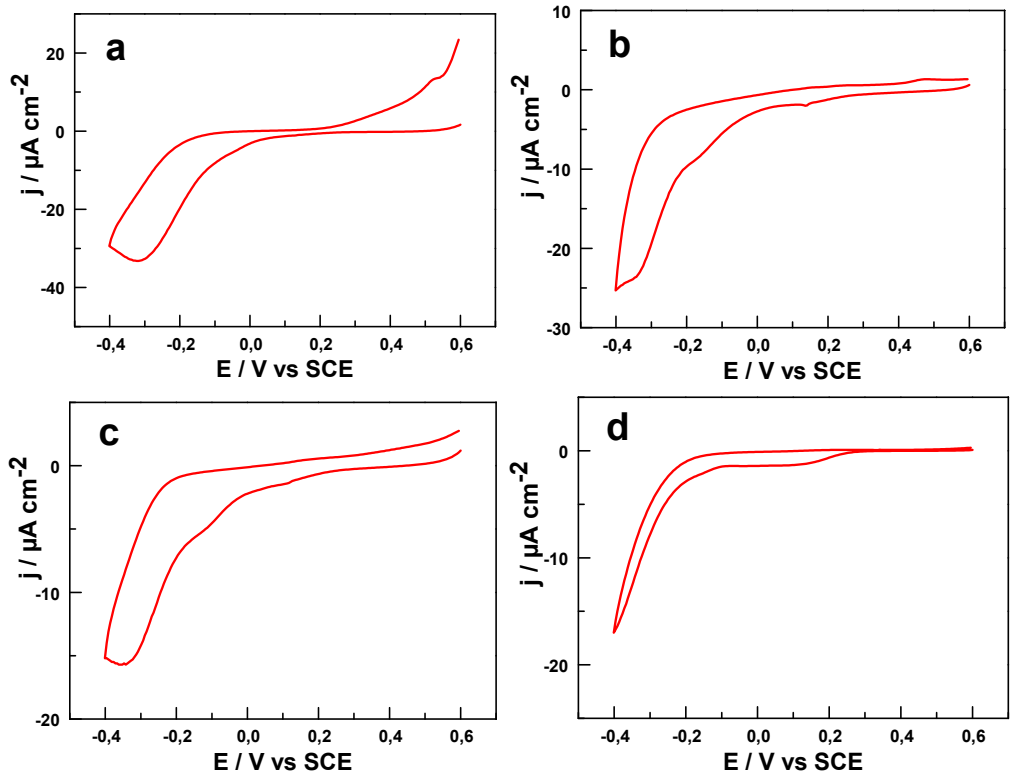

Figure 7.10. Comparison of electrocatalytic activity towards reduction of H_2O_2 for a: PBNP-COO^-C_2-Au(111); b: PBNP-COO^-C_5-Au(111); c: PBNP-COO^-C_7-Au(111); d: PBNP-COO^-C_{10}-Au(111) in 0.1 M KCl in the presence of 0.2 mM H_2O_2. Scan rate: 20 mV s^{-1}.

AFM images of the electrocatalytic Au(111)/SAM/PBNP electrode surfaces at different coverage of PBNPs-CH_3HC_5-Au(111) units and their size distribution are summarized in Fig.7.11. The corresponding solution UV-vis absorbances were (a) A = 2.70; (b) A = 0.90; (c) A = 0.28. These data were used to evaluate the concentration effect on the surface coverage of PBNPs on the Au surface. The PBNPs tend to

aggregate, when the coverage is high and appear deformed on the -CH_3 terminated SAM.

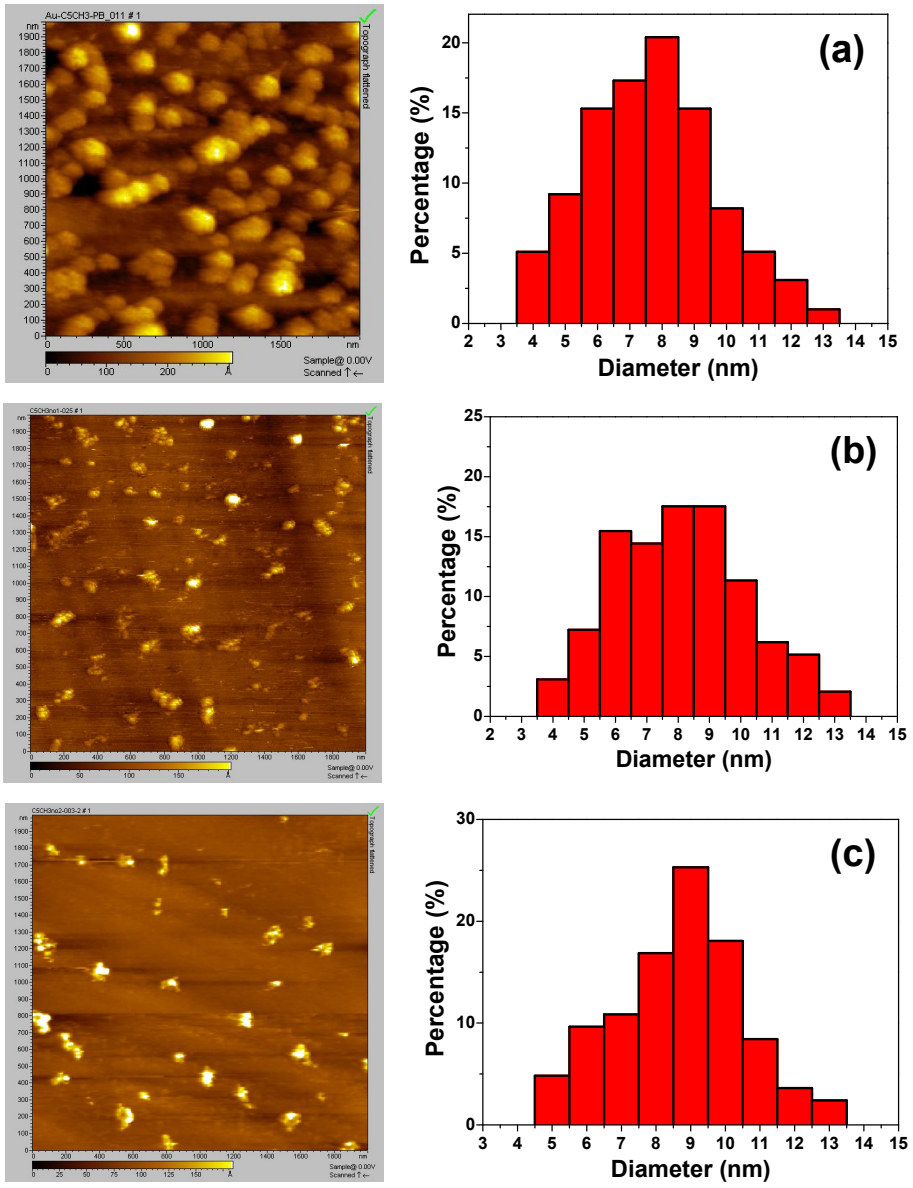

Figure 7.11. Comparison of different coverages of PBNP-CH_3HC_5-Au(111) for AFM and diameter collection. Absorption of PBNP (a) A = 2.70; (b) A = 0.90; (c) A = 0.28; at the maximum absorbance around 700 nm.

7.4 Discussions about Catalysis and Conclusions

The size of 5-6 nm PBNPs compares with the size of globular redox (metallo)enzymes. In a sense they also exhibit comparable electronic and ET properties and therefore offer the notion of "artificial redox metalloenzymes". We have exploited this analogy in two ways. Monodisperse 5-6 nm PBNPs could, first be assembled on variable-length and variably chemically terminated thiol-based SAMs on electrochemical Au(111)-electrode surfaces. *In situ* AFM could ascertain the presence of highly populated although not dense PBNP monolayers on the SAM-modified Au(111)-surfaces. CV and Laviron analysis disclosed dual distance behavior of the PBNP voltammetry. No distance dependence is observed for carbon chain lengths up to six or eight carbon atoms but is followed by a clear exponential tunneling pattern for longer carbon chains with decay factors from 0.85-1.3 per CH_2 group. This pattern is known both for ET metalloproteins such as cytochrome *c* and azurin.[32] Interfacial ET rate constants and characteristic tunneling decay factors were, further found to follow the order $-NH_3^+$ < $-COO^-$ < $-CH_3$ for the decay constants and the inverse order for the rate constants. The positively charged terminal group thus offers clearly the most facile ET route, while the order of the negatively charged and hydrophobic terminal groups is less obvious.

We have, secondly explored the PBNP-induced electrocatalysis of electrochemical reduction of H_2O_2 on the PBNP/SAM/Au(111)-surfaces. The electrocatalytic currents of the three differently terminated SAMs follows roughly the same order as for the non-catalytic PBNP CVs, i.e. $-NH_3^+$ > $-COO^-$ >> $-CH_3$, Table 7.5. The composite nature of the normalized catalytic currents is apparent from the much weaker distance dependence of the current on the number of methylene groups in the SAM linker molecules, Tables 7.2-7.4. The apparent exponential decay constants are thus only about 0.2-0.3 per CH_2 group which can easily represent weakly distance dependent but other that exponential ET rate variation. The distance dependence is strongest for the $-COO^-$ terminated SAMs and weakest for the $-CH_3$ terminated SAM. This is opposite to the behavior of direct interfacial ET and as noted, rooted in the composite

rate constant. The SAM chain length, however, remains as a controlling factor, and the catalytic rate constants even cross over and become smaller than the non-catalytic rate constants when the SAM chain is long enough and the rate constants very small.

As an illustration, following our analysis of two- or three-step electrocatalytic voltammetry for the blue copper enzymes nitrite reductase[41] and laccase,[42] and for the di-heme redox metalloprotein cytochrome c_4,[43] the steady-state rate constant for two-step electrocatalytic H_2O_2 reduction can be given the form

$$\frac{j_{cat}}{\Gamma} = \frac{k_1 k_{2-\max}\left[H_2O_2\right]}{(k_1 + k_{-1})K_M + (k_1 + k_{-1} + k_{2-\max})\left[H_2O_2\right]} \qquad \text{(Eq 7.2)}$$

This equation emerges from a view of the catalytic H_2O_2 reduction on the PBNPs as a mechanism of Michaelis-Menten form with the maximum turnover rate constant $k_{2\text{-}max}$ and Michaelis constant K_M. k_1 and k_{-1} are the rate constants for reduction and oxidation of the PBNPs, respectively across the SAM. This equation maintains Michaelis-Menten form but with a composite apparent Michaelis constant and maximum catalytic current density.[41,42] Eq.7.1 and 7.2 offer a basis for further analysis of the distance dependence of the catalytic current of the overall two-step process but additional steps are needed for complete analysis. We note that the catalytic current density takes the following two forms in the limits of long and short SAM linker molecules, respectively

$$\frac{j_{cat}}{\Gamma} = k_1 \qquad \text{and} \qquad \frac{j_{cat}}{\Gamma} \approx \frac{k_{2-\max}[H_2O_2]}{K_M + [H_2O_2]_1} \qquad \text{(Eq. 7.3)}$$

corresponding to $(k_1+k_{-1})K_M << (k_1+k_{-1}+k_{2\text{-}max})[H_2O_2]$ and the inverse of this inequality, respectively (along with $k_1 >> k_{-1}$). The former limit corresponds to the interfacial ET step being rate determining with the full distance dependence as in Fig.7.7, the latter to H_2O_2 conversion as rate determining with no distance

dependence. These limits do not represent fully the observed data which follow an intermediate relatively weak distance dependence throughout, and point to the need for including other steps, more details regarding the potential profile in the interfacial region, and other features.

Tunneling features of the interfacial electrochemical ET between the molecular scale PBNPs and the Au(111)-electrode surface through variable-length, and differently functionalized thiol-based SAMs remain, however, as a main result of the studies described in Chapter 6 and 7. The second major outcome is that the PBNPs have emerged as extremely efficient electrocatalysts and that the catalytic currents can also be controlled by the variable-length and differently functionalized SAMs. These conclusions may apply to broad ranges of interfacial electrocatalytic and bioelectrocatalytic phenomena.

7.5 References

[1] Y. N. Zhang; Z. Y. Chu; L. Shi; W. Q. Jin, *Electrochim Acta* **2011**, *56*, 8163-8167.
[2] A. A. Karyakin; O. V. Gitelmacher; E. E. Karyakina, *Anal Chem* **1995**, *67*, 2419-2423.
[3] F. Ricci; G. Palleschi, *Biosens Bioelectron* **2005**, *21*, 389-407.
[4] Y. Q. Miao; J. R. Chen; X. H. Wu; K. M. Fang; A. P. Jia; J. W. Liu, *J Nanosci Nanotechno* **2007**, *7*, 2877-2882.
[5] A. A. Karyakin; E. E. Karyakina, *Russ Chem B+* **2001**, *50*, 1811-1817.
[6] Y. Zhang; H. Q. Luo; N. B. Li, *Bioproc Biosyst Eng* **2011**, *34*, 215-221.
[7] H. Razmi; R. Mohammad-Rezaei; H. Heidari, *Electroanal* **2009**, *21*, 2355-2362.
[8] F. L. Jia; C. F. Yu; J. M. Gong; L. Z. Zhang, *J Solid State Electr* **2008**, *12*, 1567-1571.
[9] V. D. Neff, *J Electrochem Soc* **1978**, *125*, 886-887.
[10] A. A. Karyakin; E. A. Puganova, et al, *Anal Chem* **2004**, *76*, 474-478.
[11] Y. Z. Guo; A. R. Guadalupe; O. Resto; L. F. Fonseca; Weisz, S. Z. *Chem Mater* **1999**, *11*, 135-140.

[12] X. L. Luo; A. Morrin; A. J. Killard; M. R. Smyth, *Electroanal* **2006**, *18*, 319-326.
[13] N. Bowden; A. Terfort; J. Carbeck; G. M. Whitesides, *Science* **1997**, *276*, 233-235.
[14] M. P. O'Halloran; M. Pravda; G. G. Guilbault, *Talanta* **2001**, *55*, 605-611.
[15] W. C. Silva; M. Guix; G. A. Angeles; A. Merkoci, *Phys Chem Chem Phys* **2010**, *12*, 15505-15511.
[16] D. J. Schmidt; F. C. Cebeci; Z. I. Kalcioglu; S. G. Wyman; C. Ortiz; K. J. Van Vliet; P. T. Hammond, *Acs Nano* **2009**, *3*, 2207-2216.
[17] C. A. Lundgren; R. W. Murray, *Inorg Chem* **1988**, *27*, 933-939.
[18] K. B. Cederquist; R. S. Golightly; C. D. Keating, *Langmuir* **2008**, *24*, 9162-9171.
[19] K. Itaya; T. Ataka; S. Toshima, *J Am Chem Soc* **1982**, *104*, 4767-4772.
[20] F. Ricci; A. Amine; C. S. Tuta; A. A. Ciucu; F. Lucarelli; G. Palleschi; D. Moscone, *Anal Chim Acta* **2003**, *485*, 111-120.
[21] G. L. D. Gonzalez; H. Kahlert; F. Scholz, *Electrochim Acta* **2007**, *52*, 1968-1974.
[22] P. A. Christensen; A. Hamnett; P. R. Trevellick, *J Electroanal Chem* **1988**, *242*, 23-45.
[23] S. Pons; M. Datta; J. F. Mcaleer; A. S. Hinman, *J Electroanal Chem* **1984**, *160*, 369-376.
[24] J. Oslonovitch; Y. J. Li; C. Donner; K. Krischer, *J Electroanal Chem* **2003**, *541*, 163-174.
[25] C. M. Pharr; P. R. Griffiths, *Anal Chem* **1997**, *69*, 4673-4679.
[26] K. Kunimatsu; Y. Shigematsu; K. Uosaki; H. Kita, *J Electroanal Chem* **1989**, *262*, 195-209.
[27] D. Zhang; K. Zhang; Y. L. Yao; X. H. Xia; H. Y. Chen, *Langmuir* **2004**, *20*, 7303-7307.
[28] A. M. Kuznetsov; J. Ulstrup, *Electron transfer in chemistry and biology: an introduction to the theory*; Eds.; John Wiley and Sons Ltd, Chichester, UK and New York, UK, 1998.
[29] S. X. Wang; Y. Zhou; H. Niu; X. Z. Zhang, *Curr Appl Phys* **2011**, *11*, 1337-1342.
[30] Y. Lvov; K. Ariga; I. Ichinose; T. Kunitake, *J Am Chem Soc* **1995**, *117*, 6117-6123.

[31] G. Schneider; G. Decher, *Nano Lett* **2004**, *4*, 1833-1839.

[32] Q. J. Chi; J. D. Zhang; J. E. T. Andersen; J. Ulstrup, *J Phys Chem B* **2001**, *105*, 4669-4679.

[33] P. S. Jensen; Q. Chi; F. B. Grumsen; J. M. Abad; A. Horsewell; D. J. Schiffrin; J. Ulstrup, *J Phys Chem C* **2007**, *111*, 6124-6132.

[34] S. Imabayashi; T. Mita; T. Kakiuchi, *Langmuir* **2005**, *21*, 1470-1474.

[35] Q. J. Chi; O. Farver; J. Ulstrup, *P Natl Acad Sci USA* **2005**, *102*, 16203-16208.

[36] J. D. Zhang; H. E. M. Christensen; B. L. Ooi; J. Ulstrup, *Langmuir* **2004**, *20*, 10200-10207.

[37] P. S. Jensen; Q. J. Chi; J. D. Zhang; J. Ulstrup, *J Phys Chem C* **2009**, *113*, 13993-14000.

[38] A. Gotoh, et al, *Nanotechnology* **2007**, *18*, 345609.

[39] E. Laviron, *J Electroanal Chem* **1979**, *101*, 19-28.

[40] H. G. Hong; W. Park, *Langmuir* **2001**, *17*, 2485-2492.

[41] A. C. Welinder; J. Zhang; A.G. Hansen; K. Moth-Poulsen; H.E.M. Christensen; A.M. Kuznetsov; T. Bjørnholm; J. Ulstrup, *J. Phys. Chem.* **2007**, *221*, 1343-1378.

[42] V. Climent; J. Zhang; E. P. Friis; L. H. Østergaard; J. Ulstrup, *J. Phys. Chem. C* **2012**, *116*, 1232-1243.

[43] Q. Chi; J. Zhang; T. Arslan; L. Borg; G. W. Pedersen; H. E. M. Christensen; R. R. Nazmudtinov; J. Ulstrup, *J. Phys. Chem. B* **2010**, *114*, 5617-5624.

8. Three-dimensional Assembly of Prussian Blue for Efficient Electrocatalysis

In this chapter, we present data that extend the characterization of the two-dimensional PBNPs discussed in Chapter 6 and 7. Three-dimensional networks of cross-linked [Poly(ethyleneimine) (PEI)] onto which the same 5-6 nm PBNPs are attached by electrostatic forces have been fabricated and assembled on single-crystal Au(111) electrode surfaces. A self-assembled molecular monolayer (SAM) of dithiobis(succinimidyl propionate) (DTSP) on Au(111) was first prepared. The primary amine groups of the polymer were covalently immobilized onto the DTSP layer leaving free ammonium groups exposed to the solvent and providing a 3D skeleton. The immobilized DTSP layer was characterized by electrochemical reductive desorption of the AuS units and electrochemical atomic force microscopy (*in situ* AFM). PBNPs, as a redox metalloprotein mimic, were next self-assembled electrostatically in high loads on the top layer and inside this designed composite 3D nanostructure. The composite both shows strong voltammetric PBNP signals and acts as an efficient substrate for electrocatalytic reduction of H_2O_2 and glucose. *In situ* AFM of the assembled layers in the electrolyte solution shows molecular scale structures on the surface, in keeping with the electrochemical behavior.

8.1 Introduction to this Process

With their unique interconnected architecture and large surface area, which provide enhanced mass transport to active sites, three-dimensional nanostructures self-assembled on electrode surfaces is attracting increasing attention.[1-3] Due to its excellent electrocatalytic properties and high analytic sensitivity, Prussian Blue (PB), has, further, been thoroughly researched as an electron transfer (ET) mediator in amperometric sensors and biosensors of Chapter 6 and 7,[4-6] and its electrochromic, photophysical, and magnetic properties addressed.[7-10]

Self-assembled molecular monolayers (SAMs) and Langmuir–Blodgett (L.B.) films of thiol-based molecules and metalloproteins thiol derivatives have also recently attracted growing interest.[11] As noted in Chapter 6 and 7, PBNPs can be combined with SAM structures into related new composite and highly sensitive electrochemical sensor components. PBNPs can be immobilized on the electrode surface via layer-by-layer self-assembly which provides a simple and versatile method for creating a microenvironment well suited for retaining the natural nanostructure, and with high loads of electrocatalytic centers.[12-14] Single-crystal, atomically planar electrode surfaces can further improve the electrocatalytic activity, assist the formation of given molecular orientations, and decrease the background signals.[15]

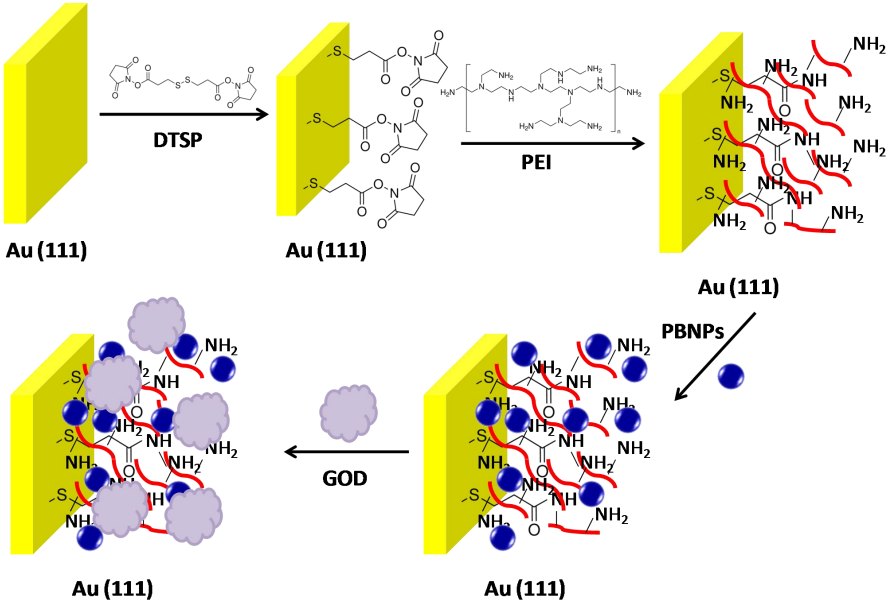

Figure 8.1 Schematic diagram of the process. PBNPs is Prussian blue nanoparticles, and GOD is glucose oxidase.

Two-dimensional PBNP SAMs were addressed in Chapter 6 and 7. PBNPs were immobilized on single-crystal Au(111)-supported variable-length thiol-based SAMs functionalized by positively charged ($-NH_3^+$), negatively charged ($-COO^-$) or neutral

hydrophobic terminal groups (-CH_3), and the ET properties of these 2D structures studied in some detail. Surface coverage and stability were, however, limitations in the operation of the 2D structures, especially in the electrocatalytic process. In this chapter, fabrication and operation of analogous three-dimensional self-assembled nanostructures on single-crystal Au(111) electrodes are described. Dithiobis(succinimidyl propionate) (DTSP) known as Lomant's reagent,[16] used as a protein or polymer cross-linking reagent by acylation of free primary or secondary aliphatic amino groups, can also assemble onto gold surfaces through the disulfide group. The terminal succinimidyl groups allow further covalent immobilization of biomolecular surface amino groups.[17] The schematic diagram in Figure 8.1 shows how a DTSP SAM was first immobilized on the Au(111) electrode surface. This was followed by covalent binding of the primary amine-containing polymer [Poly(ethyleneimine) (PEI)] immobilizing the latter on top of the DTSP SAM. The covalent interaction between DTSP and PEI leaves free ammonium groups as a basis for a 3D terminal skeleton as a strong and stable environment for the following step in which high loads of PBNPs are electrostatically self-assembled.

The composite surface nanostructures were characterized by electrochemical reductive desorption of the AuS units of the DTSP linker-based composites[18] and by *In situ* AFM directly in the electrolyte solution under electrochemical potential control to molecular scale resolution consistent with the electrochemical data. The surface coverage of electroactive PBNPs prepared by this method was found to be significantly larger than for the analogous 2D composite structures in Chapter 6 and 7. This is due to the large number of surface and internal free PEI ammonium groups that effectively assemble the negatively charged PBNPs. The resulting 3D electrochemical DTSP/PEI/PBNP composite showed strong voltammetric PBNP signals and highly efficient electrocatalytic activity both towards reduction of H_2O_2 and towards glucose oxidation in combination with immobilized glucose oxidase. This type of 3D nanostructure thus appears to provide large active surface areas resulting in strong electrochemical signals and prospects for high sensitivity of forthcoming device production.[19]

8.2 Experimental Section

8.2.1 Materials

Dithiobis(succinimidyl propionate) (DTSP), potassium monohydrogen phosphate (K_2HPO_4, ≥ 99.999%), N,N-dimethylformamide (DMF), glucose oxidase (GOD, from *Aspergillus niger*, EC 1.1.3.4. 100000-250000 units g-1), D-(+)-glucose (≥ 99.5%), Nafion® (5%), KCl (≥ 99%), $FeCl_3$ (≥ 99.5%) and $Fe(NO_3)_3$ (≥ 99.5%) were all from Sigma-Aldrich. Poly(ethyleneimine) (PEI) (Mw = 750,000, 50% w/v in H_2O) was purchased from Fluka. Potassium dihydrogen phosphate (KH_2PO_4, ≥ 99.5%), $K_4[Fe(CN)_6]$ (≥ 99%), KOH (≥ 99.995%) and H_2O_2 (30%) were from Merck. $K_3[Fe(CN)_6]$ was from Riedel-de Haën (≥ 99%). All other reagents were ultrapure grade. 0.1 M KCl PBS buffer solution, pH=7 (K_2HPO_4 and KH_2PO_4 solution) was used to prepare electrolyte solutions. 1 mM PEI was obtained by dissolving PEI in the above PBS buffer solution. Milli-Q (18.2 MΩ cm) water was used throughout.

8.2.2 Preparation of self-assembled 3D nanostructures on the electrode surface

Single-crystal Au(111) electrodes, prepared as described in Chapter 6 and 7[27] were used as working substrate in both electrochemistry and *in situ* AFM. After annealing in a H_2 flame and then quenching in Milli-Q water saturated with H_2 gas, the Au(111) electrodes were immediately immersed into freshly prepared 5 mM DTSP DMF solution and left overnight. After rinsing the samples first with DMF, and then several times with Milli-Q water, the electrodes were transferred into 1 mM PEI solution overnight. The SAM/PEI modified electrodes were transferred next into 5-6 nm PBNP solution at room temperature to form the 3D nanostructure. The PBNP synthesis is given in the same as Chapter 6 and 7.

In the glucose catalyzed process, glucose oxidase (GOD) (5 μL, 2 mg/mL) was dropped onto the surface of as prepared Au(111)-DTSP-PEI-PBNPs and left at 4°C

overnight for stabilization. 5 μL, 0.5% Nafion® coating was then dropped onto the surface to prevent GOD from leaking off.

8.2.3 Electrochemical Measurements and *in situ* AFM

A three-electrode Autolab Electrochemistry System (Eco Chemie, The Netherlands) as described in Chapter 6 and 7. Amperometric i-t response curves were recorded using a CHI 660 electrochemical workstation.

SAMs PEI modified Au(111) electrodes were the working electrode (WE). All the procedure in detail was described in Chapter 6 and 7. In-house prepared Au(111)-electrodes fabricated into a cell and tapping Mode was mostly used *in situ* AFM. Identical sample types and liquid environment conditions were used in electrochemistry and *in situ* AFM.

8.3 Results and Discussion

8.3.1 Electrochemical Properties of PBNP-based 3D SAM Nanostructures

As noted in Chapter 6 and 7, voltammetry of the electrochemical reductive desorption of n-alkanethiol self-assembled monolayers (SAMs) from a metal surface in strongly alkaline solution has been widely used to diagnose the state of thiol-based SAMs and engineering SAMs, as first reported by Porter and associates.[18, 20-22] Imabayashi et al.'s systematic studies of the relationship of the intermolecular interaction between adsorbed thiol species of different alkyl chain lengths and the peak potential (E_p) showed, for example that E_p for variable-length alkanethiols is shifted negatively by 15 mV per methylene group in the alkyl chain length.[18]

The reductive desorption of the thiol-bound Au(111)-DTSP and Au(111)-DTSP-PEI layers in 0.5 M KOH solution are compared in Figure 8.2. A reductive desorption peak was observed around -0.7 V (vs. SCE) in the first scan for Au(111)-DTSP

(Figure 8.2 black line). This accords with previous reports.[11,17,18] No reductive desorption peaks were detected in successive scans of either Au(111)-DTSP or Au(111)-DTSP-PEI (Figure 8.3A and Figure 8.3B), indicative of irreversible desorption at large negative potentials.

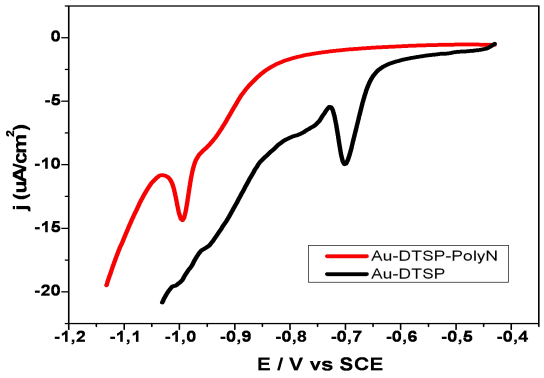

Figure 8.2. Cyclic voltammograms for reductive desorption of Au(111)-DTSP (black line) and Au(111)-DTSP-PEI (red line). 0.5 M KOH solution. Scan rate: 20 mV s^{-1}.

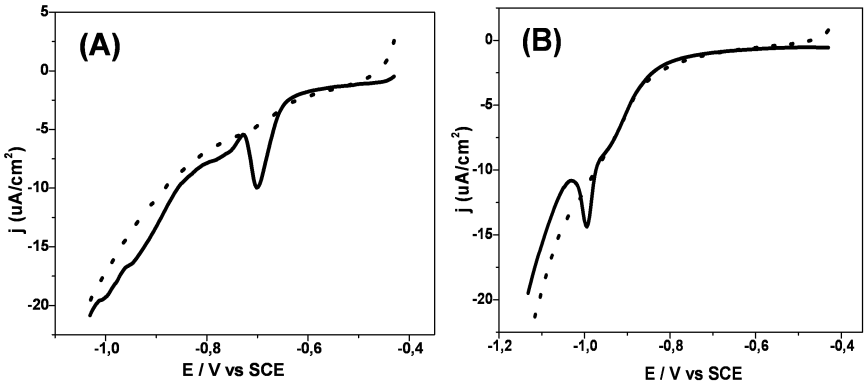

Figure 8.3. A) Cyclic voltammograms for reductive desorption of Au(111)-DTSP at first scan (solid line) and second scan (dotted line) in 0.5 M KOH solution. B) Cyclic voltammograms for reductive desorption of Au(111)-DTSP-PEI at first scan (solid line) and second scan (dotted line). 0.5 M KOH solution. Scan rate: 20 mV s^{-1}.

The Au(111)-DTSP-PEI system (Figure 8.2 red line) displayed a reduction peak around -1.0 V (vs. SCE) in the first scan. This is significantly shifted towards negative potentials compared with the peak in the absence of polymer. The covalent bond between DTSP and PEI and the large molecular mass of PEI thus invokes similar behavior as increased alkanethiol chain lengths.

The Au-S surface coverage of Au(111)-DTSP and Au(111)-DTSP-PEI was 2.05×10^{-10} mol/cm^2 and 1.26×10^{-10} mol/cm^2, respectively. This is much larger than the surface coverage of the 2D Au(111)-S(CH)$_2$-NH$_2$-PBNPs structure reported recently as only 8.6×10^{-12} mol/cm^2 in Chapter 6 and 7. The high Au-S coverage is associated with the high density of sulfur linking groups in the DTSP primary linker. The average distance between neighbouring surface Au-S units in the DTSP adlayer (assuming for simplicity a square lattice) estimated from the reductive desorption peaks is thus 0.9 and 1.15 nm for Au(111)-DTSP and Au(111)-DTSP-PEI, respectively. These values can be compared with those for a ($\sqrt{3} \times 4$)R30^o lattice of cysteamine (from *in situ* STM, two molecules per unit cell), viz. 5.7×10^{-10} mol cm^{-2} or an average intermolecular distance of 0.56 nm.[27] The ($3\sqrt{3} \times 6$)R30^o cystein lattice gives 4.0×10^{-10} mol cm^{-2} or an average distance of 1.2 nm.[27] The Au-S surface densities of the Au(111)-DTSP adlayers are thus in keeping with close to full monolayer packing of the Au-S linking units of the primary DTSP linker.

Figure 8.4 shows CVs of Au(111)-DTSP-PEI-PBNPs and Au(111)-DTSP-PEI in the potential range from -0.1 to 0.4 V. No redox peaks were detected without PBNPs (black line) but a strong pair of peaks around 0.2 V appeared for the Au(111)-DTSP-PEI-PBNP, caused by oxidation and reduction of the PBs. The oxidation peak is clearly shifted positively and the reduction peak negatively with increasing scan rates (0.02, 0.05, 0.1, 0.2, 0.5, 0.7, 1.0, 2.0, 3.0 V/s), in Figure 8.5. The observed linear relationship between peak current density and scan rate, Figure 8.6 is indicative of thin-layer voltammetric behaviour. The ET rate constant k_s was calculated as 200 ± 10 s^{-1} (based on a four-ET process). This value appears large. In view of the three-

dimensional high-density distribution of PBNPs in the DTSP/PEI matrix the rate constant must, however, necessarily accord with the notion of "apparent" and may involve both interfacial electrochemical ET and diffusion-like ET "hopping" between PBNPs in the DTSP/PEI matrix.

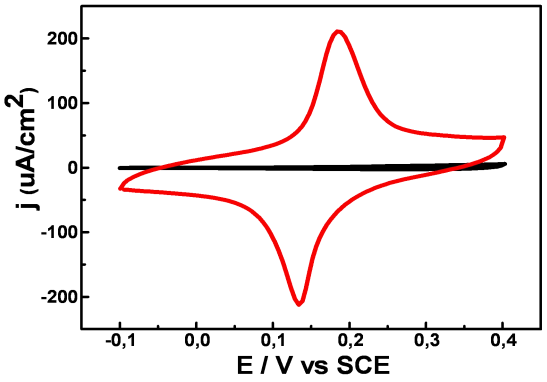

Figure 8.4. A comparison CVs of Au(111)-DTSP-PEI-PBNPs (red line) and Au(111)-DTSP-PEI (black line). 0.1 M KCl. Scan rate 50 mV s^{-1}.

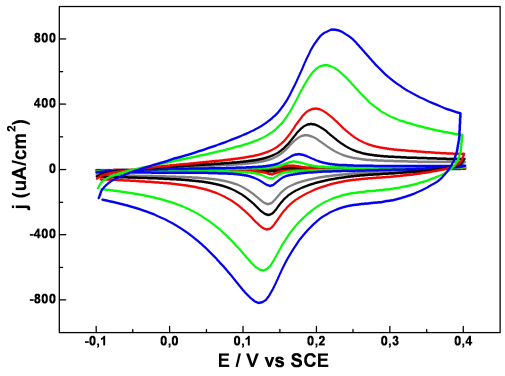

Figure 8.5. Representative CVs of Au(111)-DTSP-PEI-PBNPs. 0.1 M KCl. Scan rates 0.02, 0.05, 0.1, 0.2, 0.5, 0.7, 1.0, 2.0, 3.0 V/s.

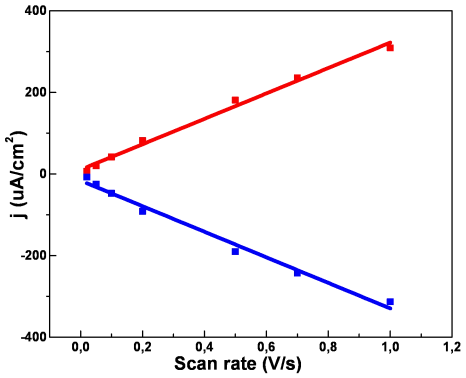

Figture 8.6. Linear relationship between peak currents and scan rates for Au(111)-DTSP-PEI-PBNP shows diffusion-less electrochemical behaviour.

8.3.2 Microscopic Structure of 3D SAM Nanostructure

The microscopic structure of the 3D SAM electrodes was characterized by *in situ* AFM, in the same 0.1 M KCl PBS buffer electrolyte solution environment as for the electrochemical process. Figure 8.7A shows *in situ* AFM of immobilized PEI on Au(111)-DTSP in a randomly chosen area of 2 × 2 μm^2. The surface appears rough with three-dimensional nanostructures, indicative that PEI covalently linked with DTSP on Au(111) offers a 3D skeleton for PBNP immobilization. The majority of the nanostructures observed when PBNPs were assembled on the Au(111)-DTSP-PEI surface (Fig 8.7B), were single nanoparticles with little agglomeration. Importantly, the PBNP nanostructure seems to be a three-dimensional property, with some 5-6 nm nanoparticles outside and some inside the adlayer. This high surface coverage of nanostructures offers highly efficient electrocatalysis.

Figure 8.7C shows *in situ* AFM images of glucose oxidase (GOD) immobilized on the Au(111)-DTSP-PEI-PBNP surface. The small granular features are attributed to adsorbed GOD molecules. Some overlayers of enzyme are seen, although not covering uniformly the whole gold surface.[24] The crystallographic dimensions of a deglycosylated GOD molecule is reported to be 6.0 nm × 5.2 nm × 7.7 nm.[28] The apparent AFM size of native GOD is larger, especially in liquid environment.[25] This

enzyme-electrode topography did not exhibit activity towards glucose, but *in situ* AFM imaging did reveal the presence of GOD self-assembled on the gold surface.[24]

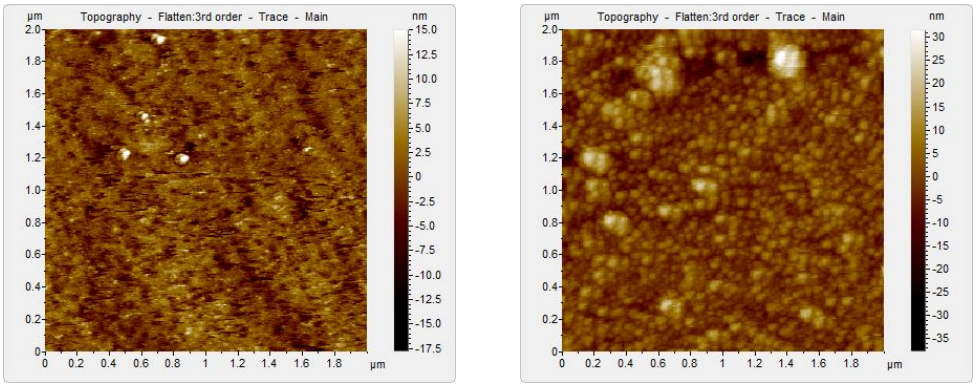

(A) **(B)**

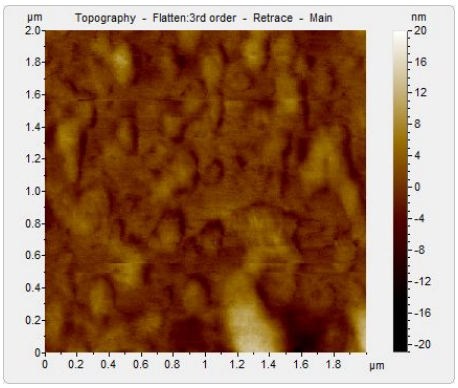

(C)

Figure 8.7. *In situ* AFM images of the microstructure of (A) Au(111)-DTSP-PEI. (B) Au(111)-DTSP-PEI-PBNPs. (C) Au(111)-DTSP-PEI-PBNPs-GOD. All images for liquid 0.1 M KCl electrolyte, pH=7.

8.3.3 Electrocatalysis of the 3D SAM Nanostructures

PB as electrochemical mediator for analytical applications has found a wide use in the biosensor field during the last years.[6] We also addressed the three-dimensional SAM PBNP nanostructures as catalytically efficient architectures towards electrocatalytic reduction of H_2O_2 and glucose oxidation as two broadly important biological metabolites.

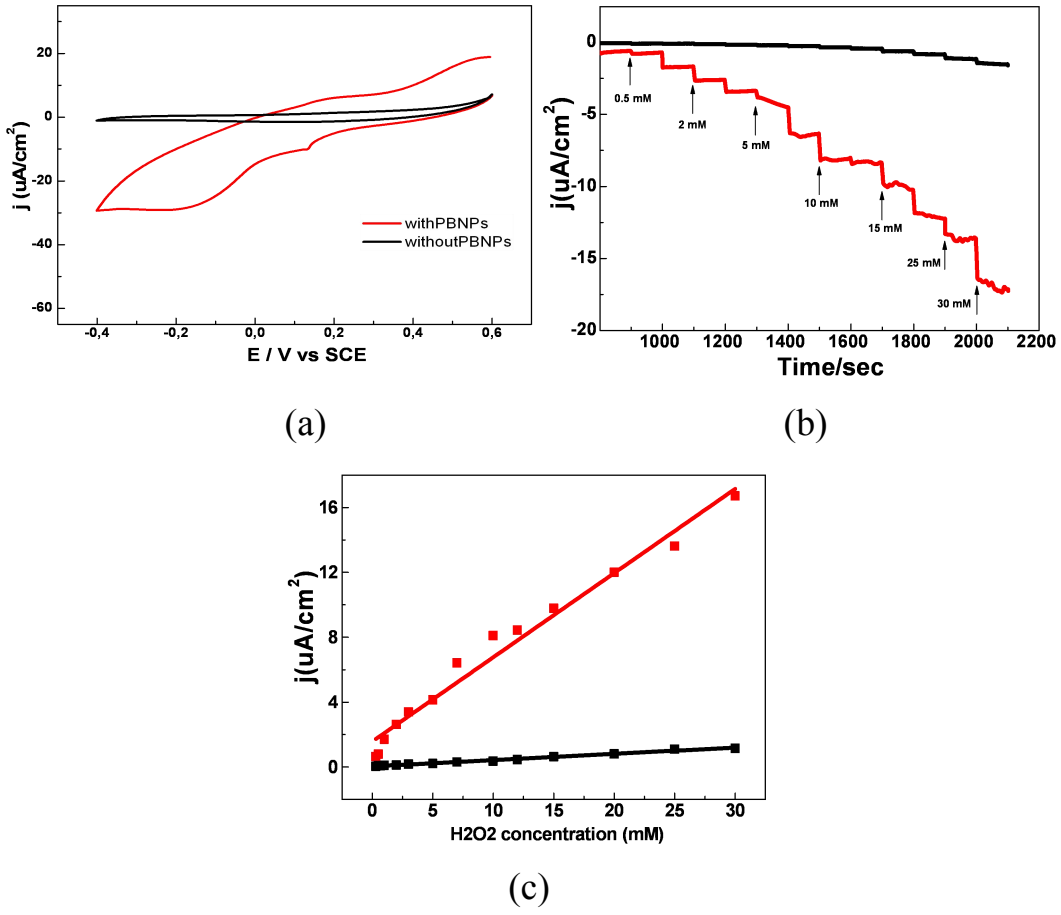

Figure 8.8. (a) Comparison of electrocatalytic activity of Au(111)-DTSP-PEI-PBNPs with 0.25 mM H_2O_2 reduction (red) and without PBNPs (black). (b) Amperometric response curve of Au(111)-DTSP-PEI-PBNPs (red) and without PBNPs (black) at a detection potential of -0.05 V vs SCE upon successive injection of different concentrations of H_2O_2 for each step under constant stirring and saturated Ar. Concentration from 0.3 to 30 mM H_2O_2. (c) Electrocatalytic activity relationship between catalytic current density and concentration of H_2O_2 for Au(111)-DTSP-PEI-PBNPs (red) and without PBNPs (black).

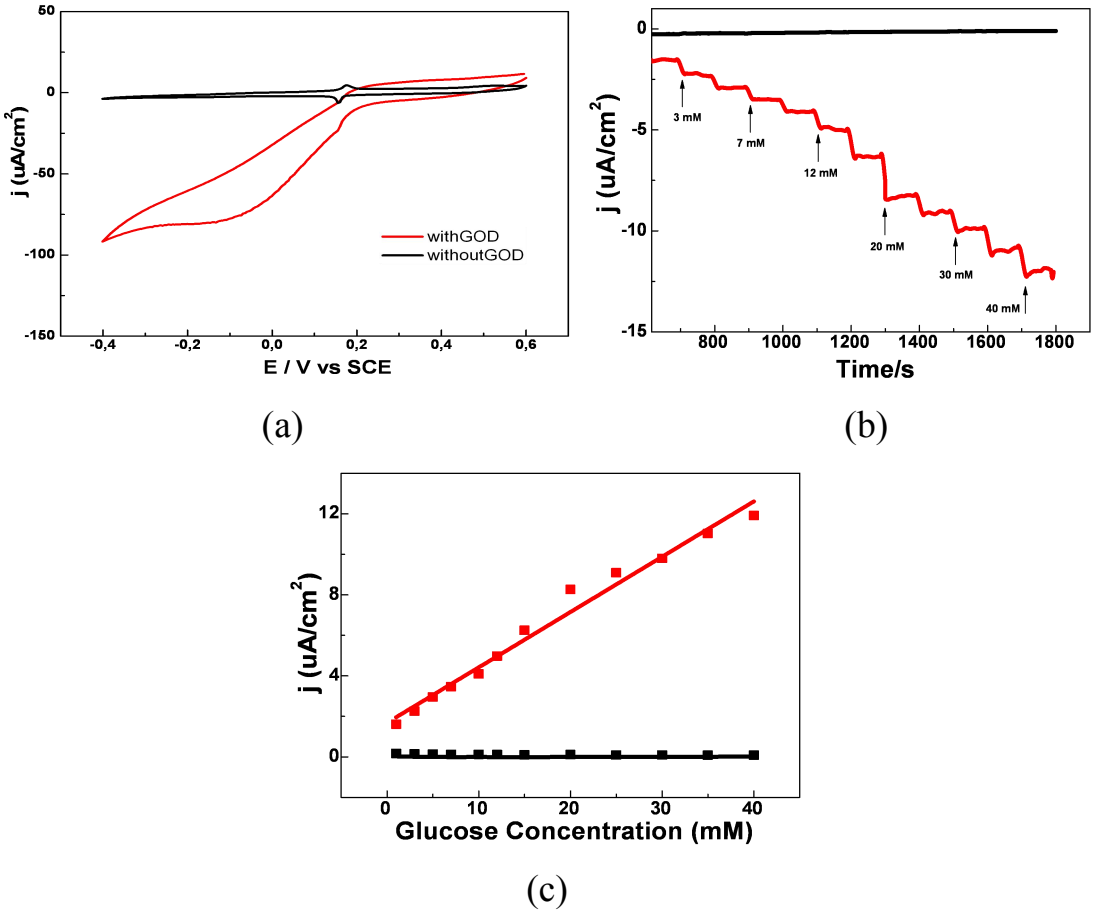

Figure 8.9. (a) Comparison of electrocatalytic activity of Au(111)-DTSP-PEI-PBNPs-GOD-Nafion in 10 mM glucose solution with GOD (red) and without GOD (black), the pairs of peaks at the potential around 0.2 V standing for the redox potential from PBNPs. (b) Amperometric response curve of Au(111)-DTSP-PEI-PBNPs-GOD-Nafion (red) and without GOD (black) at a detection potential of -0.05 V vs. SCE upon successive injection of different concentrations of glucose for each step under constant stirring. Glucose concentrations from 1 to 40 mM glucose. (c) Electrocatalytic activity relationship between catalytic current density and concentration of glucose for Au(111)-DTSP-PEI-PBNPs-GOD-Nafion (red) and without GOD (black) .

Figure 8.8a shows that a significant electrocatalytic effect in 0.25 mM H_2O_2 reduction in the Au(111)-DTSP-PEI-PBNPs system compared with the adlayer without PBNPs assembled on the surface (scan rate 0.02 V/s) was obtained. Amperometric i-t responses of Au(111)-DTSP-PEI-PBNPs to successive additions of H_2O_2 at -0.05V was also detected, Figure 8.8b (red line). The response was rapid and 95% of the steady-state current was reached within 2 s. The current density for H_2O_2 reduction

increases with increasing concentration. The calibration curve for the 3D SAM nanostructure showed a good linear response to the H_2O_2 concentration in the range 0.3-30 mM with the detection limit of 5 μM (Figure 8.8c). The wide linear range extends significantly beyond the limit for 2D nanostructures which was linear only from 0.15 mM to 0.5 mM in Chapter 6 and 7, indicating that high loading of active PBNPs has been achieved. The H_2O_2 response on Au(111)-DTSP-PEI without PBNPs under the same conditions is displayed in Figure 8.8b (black line) and Figure 8.8c (black line) for comparison and shows only a very weak response compared with the Au(111)-DTSP-PEI-PBNP surfaces.

Electrocatalysis of glucose using this sensing element can be achieved by measuring the current for the reduction of hydrogen peroxide.[26] Au(111)-DTSP-PEI-PBNPs-GOD-Nafion was selected as working electrode for catalytic oxidation of glucose. Electrocatalysis is clearly observed after adding 10 mM glucose in the electrolyte (Figure 8.9a). Amperometric i-t responses of Au(111)-DTSP-PEI-PBNPs-GOD-Nafion to successive additions of glucose at the fixed potential of -0.05V (Figure 8.9b red line) also show that the catalytic current density increases with increasing glucose concentration. The calibration curve for the 3D SAM nanostructure showed a good linear response to the glucose concentration in the range 1-40 mM with the detection limit of 10 μM (Figure 8.9c red line). This wide linear range can potentially be used in many contexts. The response without GOD was insignificant in Figure 8.9b (black line) and Figure 8.9c (black line). The amperometric responses to H_2O_2 and glucose addition are both very fast due to the interconnected 3D nanostructure. The high surface area of the 3D nanostructure that is also permeable to electrolyte thus appears to enhance significantly the sensing capacity towards H_2O_2 and glucose compared to the corresponding 2D nanostructures discussed in Chapter 6 and 7.

8.4 Conclusions

Three-dimensional self-assembled PBNP-based nanostructures on single-crystal Au(111) electrode SAMs have been fabricated. The atomically planar single-crystal

electrode surface ascertains a well-defined electrochemical microenvironment for all the further steps. A layer of dithiobis(succinimidyl propionate) (DTSP) on Au(111) was first prepared. This layer was utilized for covalent immobilization of the primary amine-containing polymer [Poly(ethyleneimine) (PEI)] onto the surface leaving free amine groups inside and outside the SAMs, exposed to the electrolyte solution and providing a 3D terminal skeleton. The three-dimensional composite Au(111)/DTSP, Au(111)/DTSP/PEI and Au(111)/DTSP/PEI/PBNP layers were characterized by voltammetry and *in situ* AFM in the same electrolyte medium as for the voltammetric data. Reductive desorption voltammetry of the Au(111)/DTSP and Au(111)/DTSP/PEI layers disclosed near closely packed layers of Au-S units with a coverage comparable to those of small functionalized alkanethiols. PBNP immobilized on the Au(111)/DTSP/PEI layers displayed strong voltammetric signals of their own, notably at least more than an order of magnitude stronger than PBNPs immobilized on two-dimensional alkanethiol based SAMs in Chapter 6 and 7, indicative of PBNP immobilization in high loads not only on the Au(111)/DTSP/PEI surface but also inside the adlayer. *In situ* AFM of the assembled different layers in the liquid electrolyte displays molecular scale resolution and a high PBNP surface coverage consistent with the electrochemical data. In addition the Au(111)/DTSP/PEI/PBNP layers exhibited highly efficient electrocatalysis of H_2O_2 reduction as well as glucose oxidation via glucose oxidase immobilized on the Au(111)/DTSP/PEI/PBNP.

Together with our study of two-dimensional alkanethiol immobilized PBNPs in Chapter 6 and 7, the three-dimensional Au(111)/DTSP/PEI/PBNP surface system has offered a new class of well characterized highly efficient substrates for electrocatalytic reduction of H_2O_2 alone and in combination with glucose oxidation, with excellent performance. Other redox enzymes may be immobilized in similar ways. The interfacial ET and electrocatalytic patterns of the self-assembled PBNPs furthermore resemble those of self-assembled redox metalloprotein mono- and multilayers. By their facile preparation, high stability, and low cost the self-assembled

PBNPs stand forward as attractive alternative materials in new approaches towards real bioelectrochemical sensing devices of broad use.

8.5 References

[1] K. Gerasopoulos; E. Pomerantseva; M. McCarthy; A. Brown; C. S. Wang; J. Culver; R. Ghodssi, *Acs Nano* **2012**, *6*, 6422-6432.

[2] Y. Chen; X. J. Yang; L. R. Guo; J. Li; X. H. Xia; L. M. Zheng, *Anal Chim Acta* **2009**, *644*, 83-89.

[3] R. P. Liang; H. Z. Peng; J. D. Qiu, *Journal of Colloid and Interface Science* **2008**, *320*, 125-131.

[4] Y. N. Zhang; Z. Y. Chu; L. Shi; W. Q. Jin, *Electrochim Acta* **2011**, *56*, 8163-8167.

[5] A. A. Karyakin; O. V. Gitelmacher; E. E. Karyakina, *Anal Chem* **1995**, *67*, 2419-2423.

[6] F. Ricci; G. Palleschi, *Biosens Bioelectron* **2005**, *21*, 389-407.

[7] Y. Q. Miao; J. R. Chen; X. H. Wu; K. M. Fang; A. P. Jia; J. W. Liu, *J Nanosci Nanotechno* **2007**, *7*, 2877-2882.

[8] A. A. Karyakin; E. E. Karyakina, *Russ Chem B+* **2001**, *50*, 1811-1817.

[9] H. Razmi; R. Mohammad-Rezaei; H. Heidari, *Electroanal* **2009**, *21*, 2355-2362.

[10] N. Bowden; A. Terfort; J. Carbeck; G. M. Whitesides, *Science* **1997**, *276*, 233-235.

[11] F. Matemadombo; P. Westbroek; T. Nyokong; K. Ozoemena; K. De Clerck; P. Kiekens, *Electrochim Acta* **2007**, *52*, 2024-2031.

[12] D. Zhang; K. Zhang; Y. L. Yao; X. H. Xia; H. Y. Chen, *Langmuir* **2004**, *20*, 7303-7307.

[13] S. X. Wang; Y. Zhou; H. Niu; X. Z. Zhang, *Curr Appl Phys* **2011**, *11*, 1337-1342.

[14] Y. Lvov; K. Ariga; I. Ichinose; T. Kunitake, *J Am Chem Soc* **1995**, *117*, 6117-6123.

[15] J. Oslonovitch; Y. J. Li; C. Donner; K. Krischer, *J Electroanal Chem* **2003**, *541*, 163-174.

[16] A. J. Lomant; G. Fairbanks, *Journal of Molecular Biology* **1976**, *104*, 243-261.

[17] M. Darder; K. Takada; F. Pariente; E. Lorenzo; H. D. Abruna, *Anal Chem* **1999**, *71*, 5530-5537.

[18] S. Imabayashi; M. Iida; D. Hobara; Z. Q. Feng; K. Niki; T. Kakiuchi, *J Electroanal Chem* **1997**, *428*, 33-38.

[19] X. J. Chen; Z. X. Chen; R. Tian; W. Yan; C. Yao, *Anal Chim Acta* **2012**, *723*, 94-100.

[20] T. Kakiuchi; H. Usui; D. Hobara; M. Yamamoto, *Langmuir* **2002**, *18*, 5231-5238.

[21] C. A. Widrig; C. Chung; M. D. Porter, *J Electroanal Chem* **1991**, *310*, 335-359.

[22] M. M. Walczak; D. D. Popenoe; R. S. Deinhammer; B. D. Lamp; C. K. Chung; M. D. Porter, *Langmuir* **1991**, *7*, 2687-2693.

[23] A. J. Bard; L. N. Faulkner, Eds.; *Electrochemical Methods*; John Wiley and Sons Ltd, Chichester, UK and New York, USA: New York, 1980.

[24] I. Almeida; A. C. Cascalheira; A. S. Viana, *Electrochim Acta* **2010**, *55*, 8686-8695.

[25] H. Muguruma; Y. Kase; N. Murata; K. Matsumura, *J Phys Chem B* **2006**, *110*, 26033-26039.

[26] J. D. Qiu; H. Z. Peng; R. P. Liang; M. Xiong, *Electroanal* **2007**, *19*, 1201-1206.

[27] Q. J. Chi; J. D. Zhang; J. E. T. Andersen; J. Ulstrup, *J Phys Chem B* **2001**, *105*, 4669-4679.

[28] H. J. Hecht; H. M. Kalisz; J. Hendle; R. D. Schmid; D. Schomburg , *J. Mol. Biol*. **1993**, 229, 153-172.

Part III: Graphene-Nanoparticle Hybrid Nanomaterials for Electrocatalysis and Photoinduced Electron Transfer

9. Graphene Paper Doped with Chemically Compatible Prussian Blue Nanoparticles as Nanohybrid Electrocatalyst

Water soluble 6 nm PBNPs was combined with reduced graphene oxide (RGO) into a new type of nanohybrid electrocatalysts. These two types of highly stable, low-cost and chemically compatible nanomaterials are exploited as building ingredients to prepare with increased electrical conductivity and functional variability nanohybrid electrocatalysts, which are further transformed into free-standing graphene papers. PBNPs doped graphene papers show highly efficient electrocatalysis towards reduction of hydrogen peroxide and can be used alone as flexible chemical sensors for potential applications in detection of hydrogen peroxide or/and other organic peroxides. The as-prepared PBNPs–RGO papers are further capable of biocompatible accommodation of enzymes for development of freestanding enzyme based biosensors. In this regard, glucose oxidase is used as an example for electrocatalytic oxidation and detection of glucose. The present work demonstrates a facile and highly reproducible way to construct free-standing and flexible graphene paper doped with electroactive catalyst. Thanks to high stability, low-cost and efficient electrocatalytic characteristics, this kind of nanohybrid material has potential to be produced on a large scale, and offers a broad range of possible applications, particularly in the fabrication of flexible sensing devices and as a platform for electrocatalytic energy conversion.

9.1 Introduction to this Process

Graphene papers are a novel type of layered materials emerged very recently. Since the pioneering work reported by Ruoff and co-workers in 2007,[1] graphene paper has added an attractive form to the scientific catalogue of rapidly surging graphene based

nanomaterials. Through wet-chemical methods,[2,3] graphene papers can be made of either graphene oxide (GO) or reduced graphene oxide (RGO) by relatively simple and low cost procedures that involve synthesis and vacuum filtration of individual and liquid suspended graphene nanosheets.[1] As a free-standing material, graphene paper has several remarkable characters, reflected by practical high electrical conductivity, mechanical robustness, excellent thermal stability, structural uniformity, and geometric flexibility.[1] These features have altogether enabled expanding the application scope of graphene materials to a much wider range of various demands. Several possible applications have been demonstrated mainly at the laboratory level, for example, the use for flexible sensors,[4–9] energy storage,[10-18] biocompatible materials,[19-21] and even antibacterial agents.[22,23] With still limited exploration to date, however, the development of graphene papers and their applications in various areas remain at the infant stage.

In other words, there is plenty of room at the bottom to explore unfulfilled potentials of graphene papers as an advanced materials source. Three major research lines towards this end are anticipated and currently being carried out in parallel: 1) refinement and optimization of preparation procedures to further enhance electrical and mechanical properties,[24-28] 2) high-resolution structural characterization towards the atomic scale understanding of structural features and their relations to physicochemical properties,[29,30] and 3) versatile modifications of graphene papers to endorse specific and new functions.[31]

Functionalization is an essential step for most possible applications of graphene papers, because this material itself lacks desired specific functions such as catalysis, redox activity and molecular recognition. Decoration of graphene paper with nanoparticles(NPs) represents one of the most attractive ways for catalytic functionalization of this material that can be consistently used, for example, for sensing devices and energy conversion. This has been achieved by several different methods such as electrodeposition,[5,6] two-phase interfacial transfer,[7] and polymer-assisted encapsulation,[20] with most studies focused on metallic and metal oxide NPs.

Also, in these studies decoration (or modifications) is limited largely to the surface of graphene papers rather than inter-layered integration of functional materials into graphene papers. Recent efforts have offered an alternative approach.[8,31-33] For example, NPs were first mixed with graphene nanosheets to prepare hybrid NPs, and this was then followed by flow-directed assembly of these individual hybrid nanosheets into graphene papers. A shortcoming of this approach is the lack of specific and robust interaction between the NPs and graphene nanosheets. This could result in poor stability (e.g., leakage) and non-uniform distribution (e.g., aggregation) of NPs in the graphene papers, as in most cases NPs are only physically confined in the papers.

Materials that possess high stability, excellent electrocatalytic activity, low-cost and scalability of mass production are ideal electrocatalysts. Prussian blue (PB) and its analogues offer these merits and are arguably representatives of such idealized electrocatalysts.[34] PB thin films, often prepared by electrochemical methods, have been extensively used as electocatalyst in electrochemical sensors and biosensors.[35-39] A latest effort by Yao and co-workers, in which PB was synthesized directly into carbon nanotubes, shows new perspectives of this material as an attractive component in preparation of carbon-PB nanocomposites and their applications in biosensing devices.[40] However, there are three drawbacks generally associated with PB materials as electrocatalysts: 1) both PB powder and thin films prepared by either electrochemical or chemical methods are highly insoluble in water, 2) the conductivity is low, and 3) PB in neutral and alkaline solutions is unstable, although the material is extremely stable in its solid form. These shortcomings have limited one exploiting the full potential of this material. For example, due to insolubility, it is hardly possible to study the PB's electroactivity and/or to prepare biologically conjugated PB hybrid materials in homogeneous aqueous solutions.

The low conductivity limits its application in electronic devices, and the lack of stability in neutral or alkaline media has excluded the coupling of PB with many oxidases that otherwise display their best catalytic activity at relatively high pH (> 8).

In this work, we have demonstrated that: 1) water soluble and highly stable PB in the form of nanoparticles (PBNPs) can be synthesized; 2) PBNPs are chemically compatible with RGO nanosheets to form stable PBNPs–RGO nanohybrid sheets; 3) the resulting nanohybrid sheets can be stored either in solid form or solution dispersions with high stability; and 4) individual nanohybrid sheets can be transformed into free-standing graphene papers for electrocatalysis and construction of flexible sensors.

9.2 Experimental Section

9.2.1 Chemicals and Materials

Graphite power (< 20 μm, synthetic), potassium persulfate ($K_2S_2O_8$, ≥ 99%), phosphorus pentoxide (P_2O_5, ≥ 98%), potassium permanganate ($KMnO_4$, ≥ 99%), potassium phosphate dibasic (K_2HPO_4, ≥ 99.999%), hydrazine hydrate solution (50-60%), sulfuric acid (H_2SO_4 , 95–97%), ammonia solution (25%), iron (III) nitrate nonahydrate $Fe(NO_3)_3$ (≥ 99.5%), and potassium chloride (KCl, ≥ 99%) were all from Sigma-Aldrich and used as received. Potassium hexacyanoferrate (III) ($K_3[Fe(CN)_6]$, 99%), potassium hexacyanoferrate(II) trihydrate ($K_4[Fe(CN)_6]\cdot 3H_2O$, ≥ 99%), potassium phosphate monobasic (KH_2PO_4, ≥ 99.5%), and hydrogen peroxide (H_2O_2, 30%) were obtained from Merck. Iron(III) chloride ($FeCl_3$, 98%) from Riedel-de Haën was used. Glucose oxidase (GOD, E. C.1.1.3.4) from Aspergillus niger (Type X-S, 100 000–250 000 U g^{-1}) and D-(+)-glucose (≥ 99.5%) were from Sigma-Aldrich. Milli-Q water (18.2 MΩ cm) was used throughout.

9.2.2 Preparation of PBNPs

PBNPs was prepared in three steps. In the first step, solid PB pigment was synthesized. $Fe(NO_3)_3$ (30 ml 1.3 M) solution was gradually adding into $K_4[Fe(CN)_6]$ (60 ml 0.5 M) solution with strongly stirring. The mixture immediately changed color from yellow to dark blue. When mixing was completed, the reaction mixture was vigorously stirred for another 5 min. Then the resulting mixture was washed with

Milli-Q water by centrifuging at 4°C for several times to remove the supernatant of unreacted reagents and left the precipitation to dry in air to obtain PB pigment.

In the second step, the PB pigment was redispersed by adding $K_4[Fe(CN)_6]\cdot 3H_2O$ into the pigment-water suspension. To achieve the water-soluble NPs, solid PB pigment (0.4 g) was suspended in 15 ml water, followed by adding $K_4[Fe(CN)_6]$ freshly prepared solution (5 ml 45 mM). The suspension was dissolved into a transparent dark blue solution with strong stirring for 4h.

The third step was purification of the PBNPs solution. Purification was performed by using a Stirred Ultrafiltration Cell and membrane to remove residual salts. Then the Stirred Ultrafiltration Cell was assembled and the PBNPs solution was put into and diluted with Milli-Q water with the membrane molecule of 3000 according to the size of PBNPs to filtration. The process was repeated 3-5 times by adding fresh MillQ water until the filtrate became colorless.

9.2.3 Preparation of Graphene Oxide(GO) and RGO

Preparing graphene oxide (GO) was divided into two steps. Firstly, prepare pre-oxidized graphite. Graphite powder (5.0 g) was slowly added into concentrated H_2SO_4 solution (7.5 ml) containing P_2O_5 (2.5 g) and $K_2S_2O_8$ (2.5 g) keeping in a hot oil bath (80°C) with strong stirring for 3 h. Aftering cooling down to the room temperature, the dark green mixture was filtered after diluting with MillQ water, and washed several times until pH of waste solution was neutral. Pre-oxidized graphite powder was collected and dried in air at room temperature overnight.

In the second step, pre-oxidized graphite powder (1.0 g) was slowly added into concentrated H_2SO_4 solution (23 ml) incubated in an ice-water bath (0 °C) and then $KMnO_4$ (3.0 g) was added into the mixture under slow stirring, the whole process was kept below 20 °C. After removing the ice-water bath, the mixture was reacted at 35 °C for 2 h with stirring, and then Milli-Q water (46 ml) was added for dilution.

Furthermore, adding Milli-Q water (140 ml) containing 2.5 ml 30% H_2O_2 solution in the mixture with the color rapidly changed to bright yellow. Moreover, the mixture was washed with 1:10 HCl solution (v/v, 250 ml) using filtration to remove residual metal ions. The crude GO suspended in Milli-Q water was centrifuged at high speed (12000 rpm min^{-1}) to collect the supernatant, which was shown to be high disperse and stable GO nanosheets. In order to remove residual salts and acids, the solution was dialyzed (MWCO of 12000-14000) for one week changing water frequently.

RGO was obtained by chemical reduction of GO with hydrazine (5%), after addition of ammonia solution and refluxing the mixture under stirring for 2 h on a water bath at 95°C. Preparation of Freestanding GO, RGO and RGO-PBNP Papers: Graphene papers were fabricated by vacuum filtration of dispersions through a nuclepore polycarbonate membrane (diameter of 47 mm, 0.2 μm pores, Whatman) using a stirred ultrafiltration cell (Millipore Corporation, USA). The thickness of GO and RGO papers was controlled by the amount of RGO dispersions. For example, most GO and RGO papers were made using the 1-5 mL stock solutions (0.2 mg mL^{-1}). PBNPs–RGO papers were fabricated by the same method but using PBNPs–RGO hybrid dispersions with a typical ratio of 1:8 (w/w, PBNPs:RGO). Prior to use, all graphene papers were subjected to annealing at 220°C for 2 h. For electrochemical measurements, GO, RGO and RGO-PBNPs papers were cut into rectangular pieces (e.g., 0.5 cm × 3 cm) with an effective area of 0.5 cm × 0.5 cm.

9.2.4 Preparation of Enzyme Containing Graphene Papers

To incorporate enzyme into the papers, GO, RGO or PBNPs-RGO papers were soaked in glucose oxidase (GOD) solutions (2-5 mg mL^{-1} GOD) at 4 °C overnight. Before used in measurements, the graphene papers were rinsed with Milli-Q water and buffer solutions at least three times, to remove loosely attached enzyme. Alternatively, GOD solution (e.g., 20 μL 5 mg mL^{-1}) was cast on the graphene papers and then dried at 4 °C overnight. These two immobilization methods yielded similar results.

9.2.5 Instrumental Methods

UV-vis measurements were carried out using an Agilent Instrument Exchange Service Model G1103A. A 5500 AFM System (Agilent Technologies) was used for AFM imaging. All images were acquired in the tapping mode. FTIR spectra were recorded with a PerkinElmer instrument (USA). The conductivity of RGO papers, PBNP films and PBNPs–RGO papers were measured by a four-point probe setup (SZT-2A, Tongchuang Electronic Co., Ltd, China). TEM imaging was performed using a Tecnai G2 T20 from FEI Company (Oregon, USA) and SEM imaging by a Carl Zeiss EVO MA10 microscope. Thermogravimetric analysis (TGA, Netzsch STA 409PC) was carried out under an N_2 atmosphere, at a relatively slow heating rate of 5 °C min^{-1}.

Electrochemical measurements were carried out at room temperature (23 ± 2°C) using an Autolab System (Eco Chemie, Netherlands) controlled by the general purpose electrochemical system software or/ and using a CHI 760C electrochemical workstation of Chapter 6-8. A three-electrode system was used throughout, consisting of a saturated calomel electrode (SCE) as reference electrode, a platinum coiled wire as counter electrode, and a piece of graphene paper as working electrode. The electrolyte used throughout was 0.1 M phosphate buffer (pH 6.0) containing 0.1 M KCl. Electrochemical impedance spectra (EIS) were recorded with an amplitude of 10 mV for various solutions without and with the $[Fe(CN)_6]^{3-/4-}$ redox probe.

9.3 Results and Discussion

The overall procedure for preparation of PBNPs-RGO nanosheets and graphene papers, with emphasis on the crucial steps, is illustrated in Scheme 9.1. In the following sections, we present first the synthesis and characterization of PBNPs and nanohybrid PBNPs-RGO sheets. This is followed by description of preparation and critical properties of PBNPs doped graphene papers. The functional tests of the

hybrid graphene papers as electrocatalysts in prototypes of electrochemical sensors and biosensors are presented in the final section.

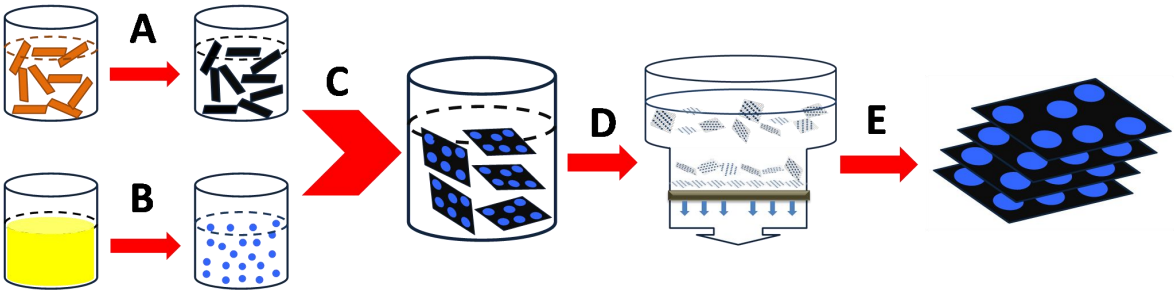

Scheme 9.1 . Schematic illustration of the experimental preparation procedures. A) Wet-chemical conversion of GO to RGO via hydrazine reduction, B) synthesis of PNBPs starting from the mixture of $FeCl_3$ and $K_4[Fe(CN)_6]$, C) preparation of PBNPs–RGO hybrid nanosheets, and D,E) processes of preparing PBNPs–RGO hybrid paper including filtration, drying and annealing. Not drawn to scale.

9.3.1. Synthesis and Characterization of PBNPs

The synthesis of PBNPs was based on a recently reported method.[41] In order to obtain pure, water soluble and highly stable NP dispersions, the procedure was refined to include three essential steps.[42] Experimental details are given in the experimental part.

The synthesized NPs were well dispersed in pure water (or/and buffer solutions) and displayed high stability. For example, the first batch sample dispersed in pure water was prepared in 2008 and stored at room temperature. The PBNP dispersions were examined by UV-vis spectroscopy, transmission electron microscopy (TEM), atomic force microscopy (AFM) and electrochemistry. After more than three years, there was no detectable aggregation or changes in physicochemical properties (the final experimental examination was carried out in 2011, after three and half years). The stability of PBNPs prepared with the present method is, thus, among the best for all so far known or ever synthesized NPs.

We have gathered the information regarding basic optical properties, morphology, size distribution and electroactivity (Figures 9.1-9.5), by systematic physical characterization using UV-vis spectroscopy, TEM, AFM and electrochemistry.

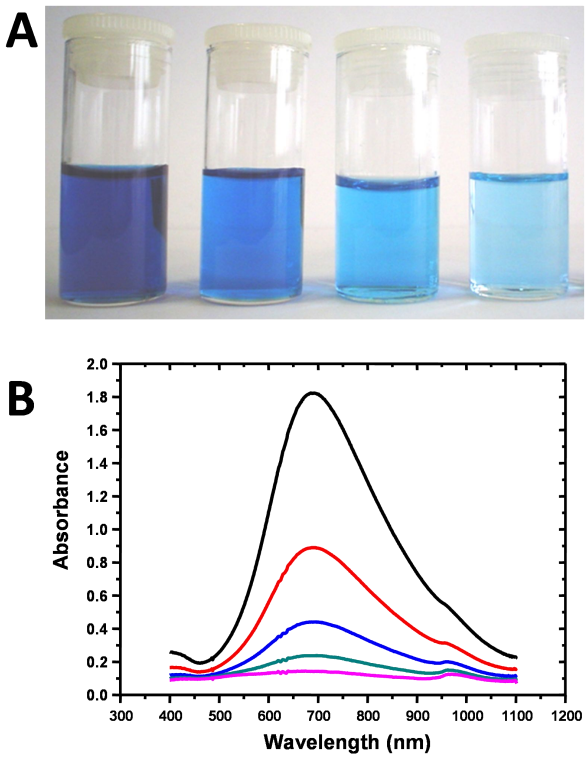

Figure 9.1. Photographs (A) and corresponding UV-Vis spectra (B) of 6 nm PBNPs dispersed in water. Different color are different concentration of the PBNPs solution.

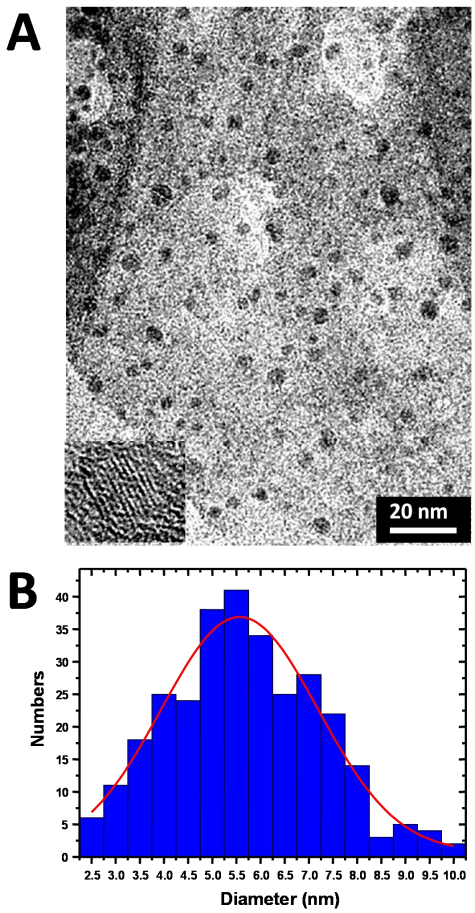

Figure 9.2. (A) TEM image and (B) size distribution of PBNPs. The inset in high-resolution TEM image shows an example of single crystalline NPs.

Low concentration PBNPs solutions are transparent and exhibit blue color (Figure 9.1A and Figure 9.6A). The absorption spectra are characterized mainly by a strong maximum absorbance around 700 nm (Figure 9.1B). As a mixed-valence compound, PB absorbs orange-red light at 680 nm, so that the transmitted light appears blue, and this characteristic is retained for colloid PBNPs dispersions. In addition, the blue color is also associated with photo-induced electron transfer from Fe(II) to Fe(III). TEM and AFM images have shown that PBNPs are spherically shaped with an average size of 5.6 nm (Figures 9.2 and 9.3). The size distribution is relatively narrow, even though the preparation of monodisperse PBNPs remains a challenge and is one of the major focuses in ongoing efforts.

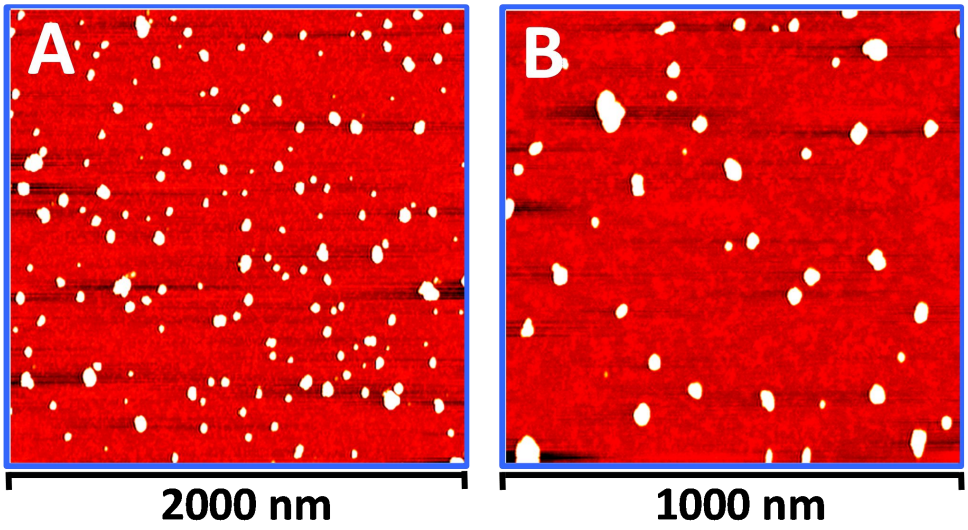

Figure 9.3. AFM images of PBNPs physically deposited on mica surfaces in air.

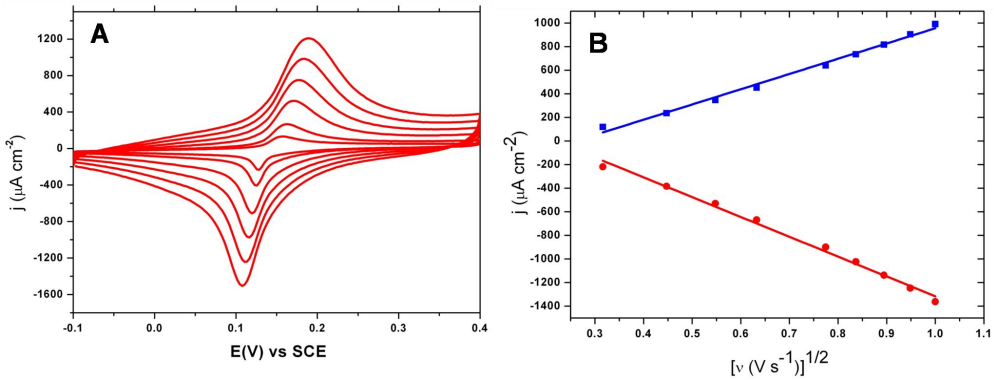

Figure 9.4. Electrochemical characterization of 5.6 nm PBNPs in homogenous solution. (A) Cyclic voltammograms obtained at Au(111) electrode with scan rates of 0.1, 0.2, 0.4, 0.6, 0.8, 1.0 V s^{-1} and (B) The correlations between the peak currents and the square root of scan rates.

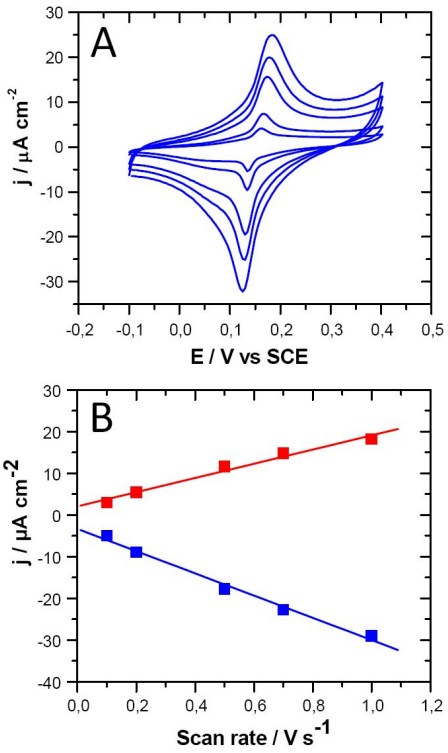

Figure 9.5. Electrochemical characterization of 5.6 nm PBNPs immobilized on SAM modified Au(111) surfaces. (A) Cyclic voltammograms of PBNPs-OOC$(CH_2)_5$S-Au(111) electrodes with scan rates of 0.1, 0.2, 0.5, 0.7, 1.0 V s^{-1} and (B) The correlations between the peak currents and the scan rates.

Furthermore, PBNPs are highly electroactive, as evidenced by electrochemical data. Well-defined cyclic voltammograms (CVs) with low background currents were obtained for PBNPs using single-crystal Au(111) as working electrodes. An example is given in Figure 9.4A, in which CVs with different scan rates are shown. The formal redox potential estimated from the midpoint of the anodic and cathodic peak potentials is around 0.15 V (vs. SCE), similar to that of PB films Chapter 6-8.[35, 36] The linear dependence of both anodic and cathodic peak currents on the square root of scan rates indicate that the electrochemical reactions are diffusion-controlled (Figure 9.4B). There is no detectable adsorption of the PBNPs on bare Au(111) surfaces. However, PBNPs can be well confined on Au(111) surfaces modified with thiol self-assembled monolayers (SAMs) via non-covalent interactions (Figure 9.5).

This observation is similar to previous reports where polymer-capping PBNPs and polycrystal gold electrodes were used,[43, 44] and also described in Chapter 6-8.

Overall, these PBNPs are seen to retain the intrinsic electroactivity of PB materials and to behave like large redox molecules such as metalloproteins.

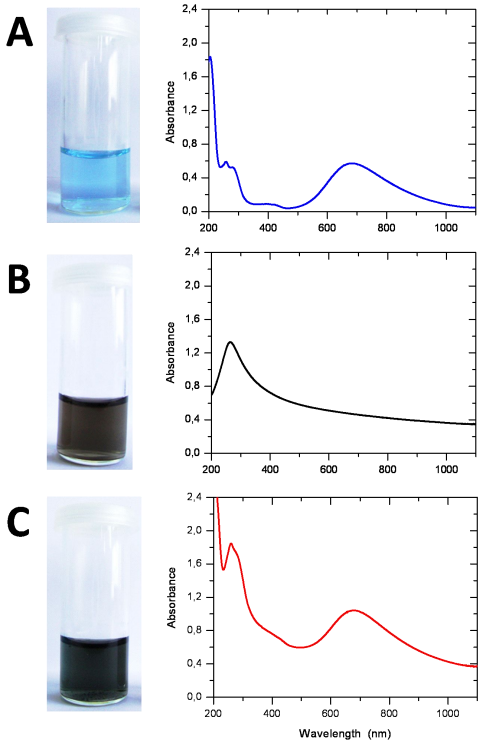

Figure 9.6 . Sample photographs (left) and UV-vis spectra (right) of various colloid dispersions. A) PBNPs (blue curve), B) RGO (black curve), and C) PBNPs–RGO hybrid (red curve) solutions.

9.3.2 Formation of PBNPs-RGO Hybrid Nanostructures

High-quality and stable GO was synthesized and characterized according to our recent report.[45] RGO was obtained by wet-chemical reduction of GO using hydrazine. As expected, chemical reduction of GO resulted in a solution color change from

yellow to dark brown and the absorption red-shifted from 231 nm to 270 nm (Figure 9.6B). These observations support that the sp^2 electronic configuration in the graphene planes was largely restored upon chemical reduction. The lateral dimensions of synthesized RGO nanosheets vary from a few hundred nanometers to one micrometer, but their thickness (≈ 0.6 nm) is within expectations for single RGO layers as proven by AFM (Figure 9.7).

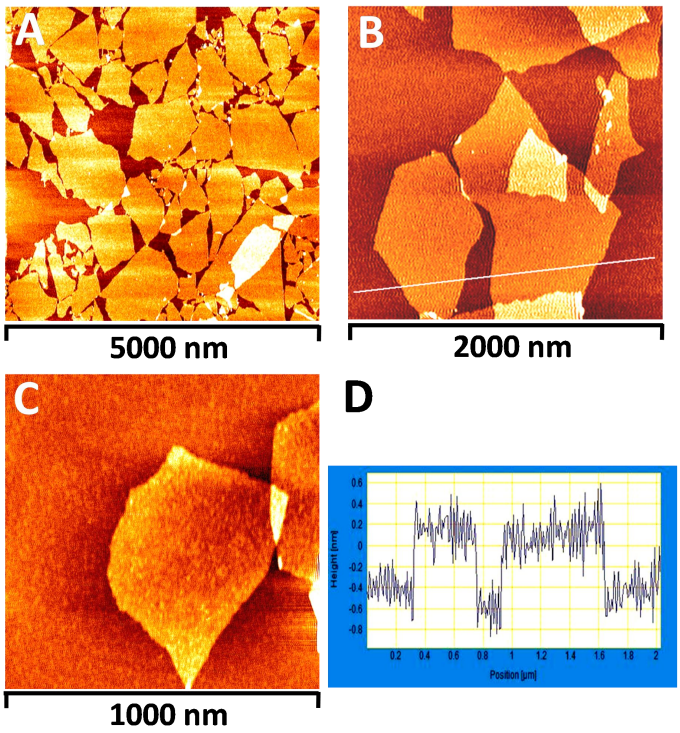

Figure 9.7. AFM images and cross-sectional analysis of RGO nanosheets. (A), (B) and (C) AFM images with different scanned areas; (D) the cross-sectional profile corresponding to the line marked in the image in (B). Scanned areas: 5 µm × 5 µm (A), 2 µm × 2 µm (B), 1 µm × 1 µm (C).

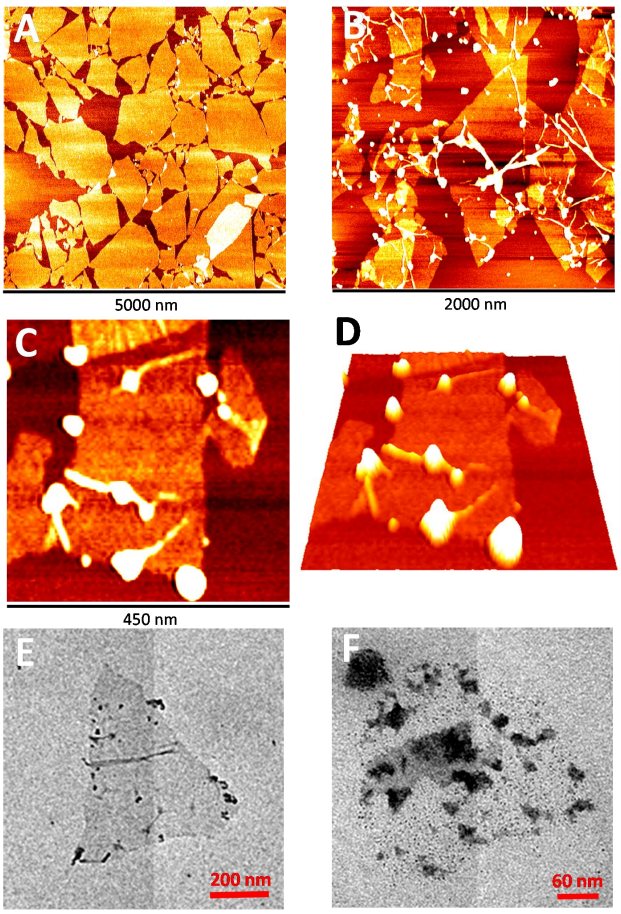

Figure 9.8 . AFM and TEM images of various nanosheets. A) An AFM image of RGO nanosheets, B) an AFM image of PBNPs-RGO hybrid nanosheets with a larger scanned area, C,D) high-resolution topography (C) and three-dimensional (D) AFM images of PBNPs–RGO hybrid nanosheets, and E,F) TEM images of PBNPs–RGO hybrid nanosheets. The AFM substrate used is mica. The scanned areas: A) 5 μm × 5 μm, B) 2 μm × 2 μm, C) and D) 0.45 μm × 0.45 μm.

To prepare PBNPs–RGO hybrids, PBNPs and RGO solutions were mixed under gentle stirring for at least two hours. This was followed by centrifugation for about 10 min. The sediment was then collected, while the supernatant was disregarded. The sediment was then re-dispersed uniformly in pure water. The PBNPs–RGO dispersion exhibits a dark green color and is characterized by two UV-vis absorption bands at 270 and 700 nm, respectively, which arise from each of the two building components (see, for example, Figure 9.6 C). Compared to RGO solutions, PBNPs-RGO

dispersions are significantly more stable. While the former lasts typically a few days before visible precipitation occurs by aggregation, the latter remains well dispersed for several months. This observation suggests that PBNPs stabilized the RGO nanosheets by preventing their hydrophobic and/or π-π stack interactions, attributed to the strongly hydrophilic and water stable features of PBNPs as described in previous section. The chemical nature of the interaction between PBNPs and RGO nanosheets is not fully understood, but a major driving force is likely to be electrostatic attraction as suggested strongly by AFM and TEM imaging observations.

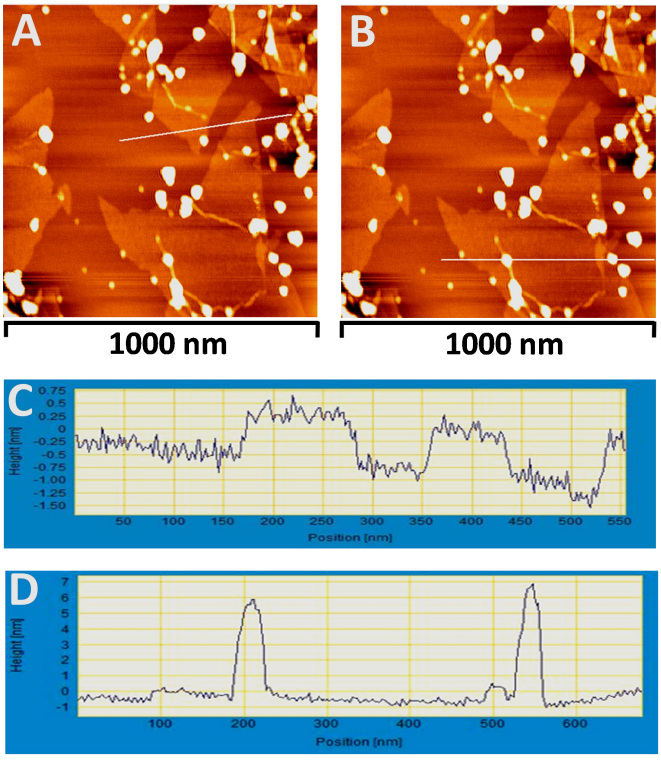

Figure 9.9. AFM images and cross-sectional analysis of PBNPs-RGO hybrid sheets. (A) and (B) the same image, (C) and (D) the cross-sectional profiles corresponding to the lines marked in (A) without and (B) with PBNPs, respectively.

AFM and TEM images show that PBNPs are adsorbed on the surfaces of RGO nanosheets with an overall uniform distribution (Figure 9.8 and 9.9). High-resolution AFM images further reveal that PBNPs are predominantly located at the edges and

wrinkles of RGO nanosheets (Figure 9.8B and 9.8C), where oxygen-containing functional groups are relatively abundant, and serve as linking groups for electrostatic attraction. This is consistent with the fact that PBNPs are stably immobilized on Au(111) surfaces modified with carboxylic groups terminated SAMs in Chapter 6 (Figure 9.5).

In short, highly stable PBNPs–RGO hybrid nanosheets can be prepared by mixing the two components. Intrinsic chemical interactions allow PBNPs to be confined on the surfaces of RGO nanosheets, predominantly adsorbed at edges and wrinkles. Electrostatic attraction appears to play a key role in the formation of PBNPs–RGO hybrids through oxygen-containing functional groups serving as linking groups.

9.3.3. Physical Properties of PBNPs Doped Graphene Papers

PBNPs doped graphene papers were prepared by flow-directed assembly of PBNPs–RGO hybrid nanosheets via vacuum filtration (Scheme 1).[1] GO and RGO papers (i.e., without PBNPs) were prepared in the same way and used as reference systems. Prior to use, the papers were annealed at 220°C for 2h to enhance electrical conductivity. The resulting PBNPs-RGO papers are mechanically robust and can be cut into patterns of any shape. Figure 9.10 A and B show examples of various patterns. These include an irregular large piece (Figure 9.10 A), triangular, rectangular and hexagonal small pieces (the top panel in Figure 9.10 B) and various letters forming "NANOCHEM" (the middle and bottom panels in Figure 9.10 B). By controlling the amount of PBNPs–RGO hybrids, the papers with 1-20 μm thickness can be steadily prepared. Without peeling off the support porous membrane (as described in the Experimental Section, polycarbonate was used in the present work), the paper-like ultrathin graphene films with the thickness down to 100-200 nm can also be constructed with reasonable reproducibility.

The prepared papers were systematically characterized to disclose their chemical components, morphology, conductivity and other physical features. Fourier transform

infrared (FTIR) spectra offer qualitative evidence for the presence of PBNPs in the graphene papers (Figure 9.11). In contrast to RGO papers, the C-N stretching vibration at 2090 cm^{-1} and Fe-C-N-Fe stretching at 500 cm^{-1} from PB[46] are clearly observed in PBNPs-RGO papers. In addition, the O-H-O bending mode around 1600 cm^{-1} is also observed,[47] an indication that water molecules are also trapped together with PBNPs in the graphene papers which could provide a microenvironment for accommodation of bio-macromolecules.

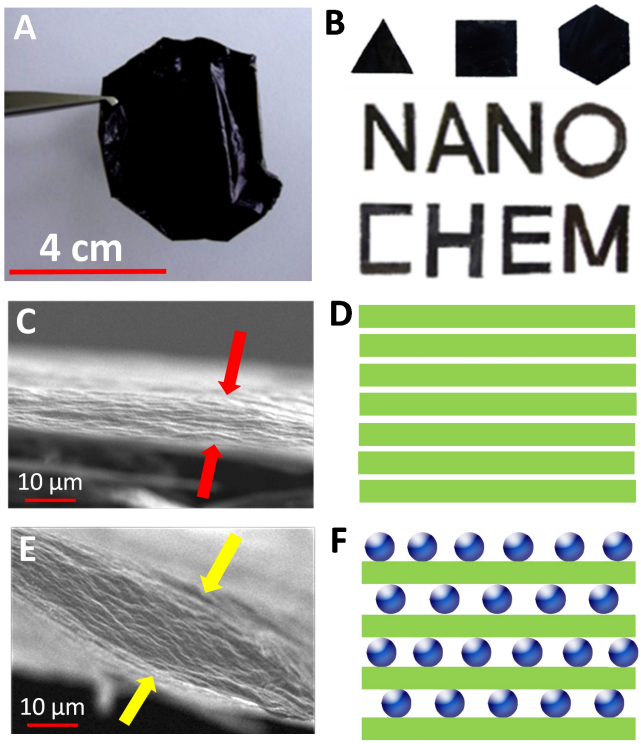

Figure 9.10 . Photographs and SEM images of graphene papers. A,B) Photographs of different-shaped patterns and letters of PBNPs–RGO papers. Cross-sectional SEM images of C) RGO and D) PBNPs–RGO papers. Schematic illustrations of proposed side-view structures of E) RGO and F) PBNPs–RGO papers.

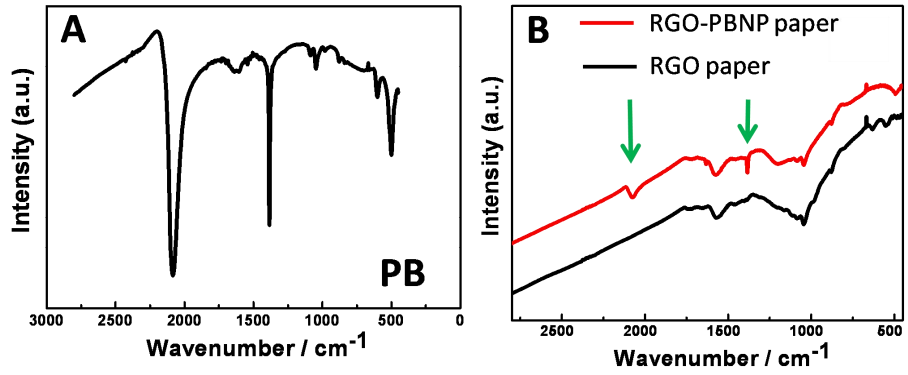

Figure 9.11. FTIR spectra of various samples. (A) PBNPs powder as a reference and (B) RGO paper (black curve) and PBNPs-RGO paper (red curve).

The surfaces of the papers are smooth, as shown by SEM (Figure 9.12). The presence of PBNPs does not roughen the paper surfaces most likely due to the small size of PBNPs (around 6 nm), but does increase the spacing between the RGO layers as revealed by the cross sectional SEM images (Figure 9.10 C, D and Figure 9.13). Compared to RGO papers, the PBNPs–RGO papers appear to be "thicker" (compare the SEM images in Figure 9.10 C and D), when the same RGO amount was used in the preparation of RGO and PBNPs-RGO papers. This is expected, because PBNPs were pre-adsorbed on the RGO nanosheets. As a result, PBNPs are intercalated between the RGO layers and uniformly distributed within the paper, as schematically illustrated by the structures proposed in Figure 9.10 E and F.

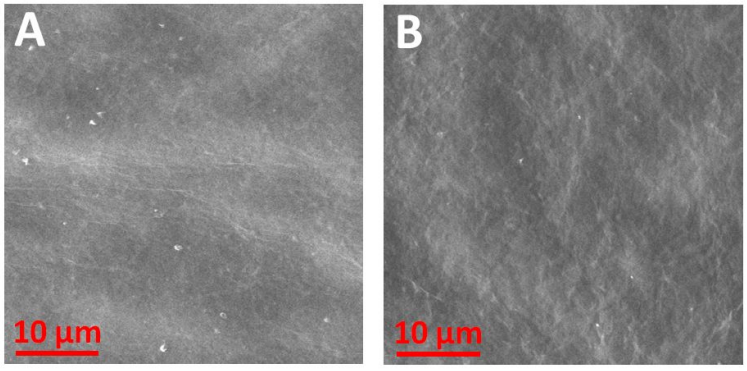

Figure 9.12. Topographic SEM images of (A) RGO and (B) PBNPs-RGO papers.

Quantification of the layer spacing in graphene papers could be interesting and desired, but needs high-resolution microscopic images which is hardly fulfilled by SEM. The SEM images shown in Figure 9.10 C and D are cross-sectional images with the aim to visualize the layered structures and to qualitatively compare the apparent structural difference of two types of graphene papers (i.e., RGO and PBNPs-RGO papers) when the same RGO amount was used in the preparation of papers. The size of synthesized single layer RGO nanosheets and PBNPs is 0.8 nm in thickness and 6 nm in diameter, respectively. For example, the PBNPs-RGO paper with an overall thickness of 1 μm is thus estimated to contain approximately 140 hybrid layers, assuming that the hybrid nanolayers are closely packed.

Thermal gravity analysis (TGA) of GO, RGO and PBNPs–RGO papers was also performed. As shown in the Supporting Information (Figure 9.14), the observations for GO and RGO papers are similar to those in previous reports.[5-7] Briefly, a slight mass loss occurred below 200° C similarly for all three types of sample, mainly due to evaporation of loosely adsorbed water. With increasing temperature, a dramatic mass drop was detected around 200°C for GO papers only, arising from decomposition of oxygen-containing functional groups. The mass loss at this temperature was also observed for RGO and PBNPs–RGO samples, but to a much lesser extent. These observations are, thus, consistent with the fact that most oxygen-containing functional groups were removed from GO by chemical reduction. Compared to RGO papers, there is an additional but slight mass loss around 500° C for PBNPs-RGO samples. This is attributed to the thermal removal of coordinated water in the PBNPs.

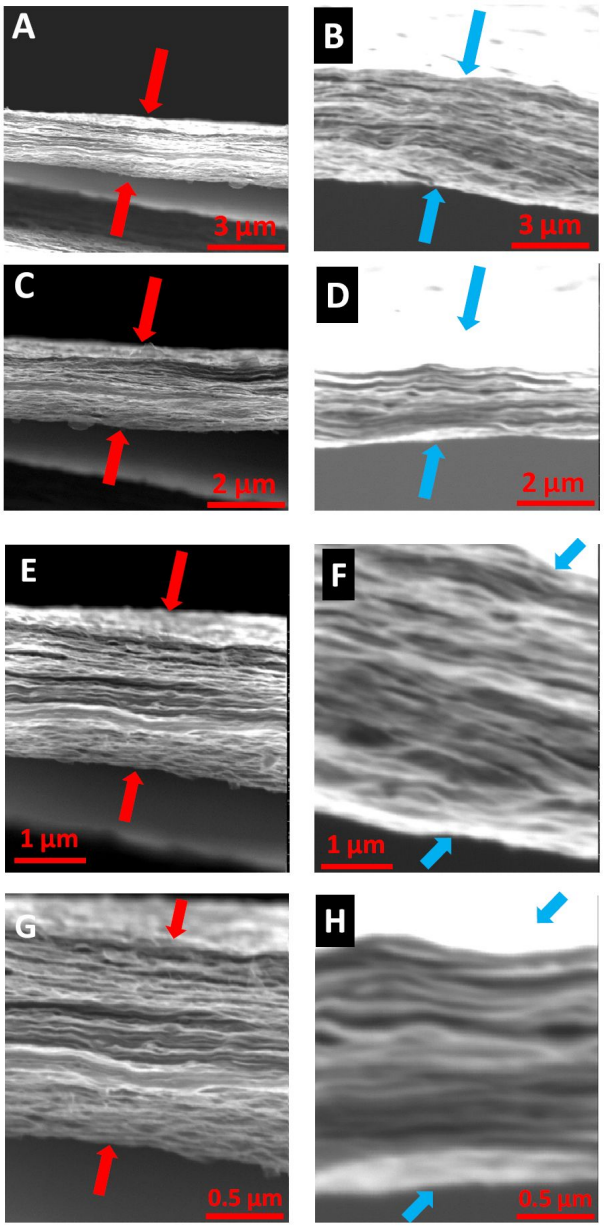

Figure 9.13. Comparison of cross-sectional SEM images of (A, C, E, G) RGO and (B, D, F, G) PBNPs-RGO papers.

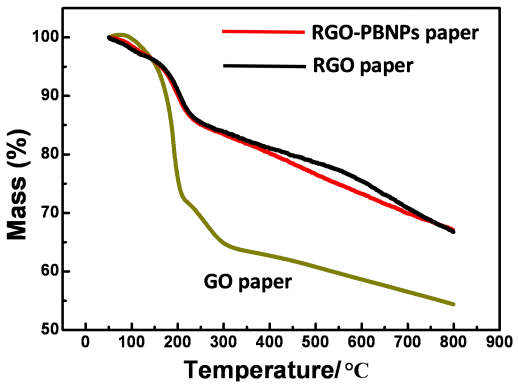

Figure 9.14. TGA analyses of GO (dark green), RGO (black) and PBNPs-RGO (red) papers.

Table 9.1. Comparison of resistance /conductivity of PBNPs films, RGO papers and PBNPs-RGO papers measured by various methods.

Resistance or Conductivity	PBNPs films	RGO papers	RGO-PBNPs papers
Four-point surface resistance (KΩ/sq)	**> 200**	**0.11**	**6.91**
Volume resistance (KΩ/sq)	**NA**	**2.47**	**5.66**
Vertical conductivity [a] (mS m^{-1})	**3.1**	**1995**	**970**

[a] The materials measured were in the form of pellets

Electrical conductivity is of crucial importance for applications of graphene papers in electronic devices and electrochemistry. To gain an overview picture, we measured three types of resistance (or conductivity) with the results provided in the Table 9.1. Pure PBNPs are poorly conductive as expected. For example, the surface resistance of

PBNPs films was too large (> 200 kΩ sq^{-1}) to be measured by the four-point probe mode. The incorporation of PBNPs into an RGO matrix results in a dramatic decrease in surface resistance down to 6.9 kΩ sq^{-1}, even if the nanocomposite still has a higher resistance than that for pure RGO papers. However, volume resistance and vertical conductivity of RGO and PBNPs-RGO papers are comparable (Table 9.1). In terms of electrochemical applications, RGO in hybrid papers can, thus, serve not only as a current collector, but also a conductivity-enhancing matrix for PBNPs. Note that all these conductivity measurements were performed in air. However, electrochemical impedance spectroscopy (EIS) offers the feasibility to evaluate apparent ionic conduction of RGO and PBNPs-RGO papers in liquid environments under potential control, as described in the next section.

9.3.4. Electroactivity of PBNPs Confined in Graphene Papers

To facilitate electrochemical measurements, graphene papers were cut into rectangular pieces (e.g., 0. 5 cm × 3 cm) as freestanding working electrodes with an active area of 0.25 cm^2 (i.e., 0.5 cm × 0.5 cm). All electrochemical measurements were conducted with a three-electrode system and the potentials are referred to a saturated calomel electrode (SCE).

PBNPs confined in graphene papers remains highly electroactive. Cyclic voltammograms (CVs) shown in Figure 9.15 A and B reveal that heterogeneous electron transfer (ET) reactions arising from confined PBNPs are reversible, with a pair of redox peaks at a formal redox potential of 0.18 V very close to that obtained for PBNPs in homogeneous solution (Figure 9.4A) or in the immobilized state (Figure 9.5) and chapter 6 and 7. The relationship between the peak currents (I_p) and scan rate (υ) was evaluated by a series plots of I_p versus υ^x with x = 0.5-1.0 (Figure 9.16). The best linear fit with a zero intercept is obtained for x = 0.7. This is an indication that the ET kinetics is controlled by mixed diffusion and surface confinement. Physical diffusion (or moving) of PBNPs within graphene papers is unlikely, but strong electronic interactions between PBNPs could be expected due to

the narrow spacing (i.e., RGO nanosheets with atomic-layer thickness) that separates PBNPs (Figure 9.10F). Such electronic interactions could lead to diffusion-like controlled behavior in electrochemical ET. The rate constant estimated by the Laviron method[48,49] is about 5.2 s^{-1}. However, this value is at best a rough approximation and to be likely underestimated due to complex rate-limiting steps (i.e., a mixture of diffusion and surface processes). An alternative explanation is that the redox transition of PB needs counter ions (cations) for charge compensation[50] and that diffusion of cations (K^+ in the present case) from the electrolyte solution into graphene papers plays a significant role in determining the ET kinetics. This notion is particularly crucial when PB materials are confined in a nanoscale space, as pointed out by a recent report where PB was located inside carbon nanotubes.[40]

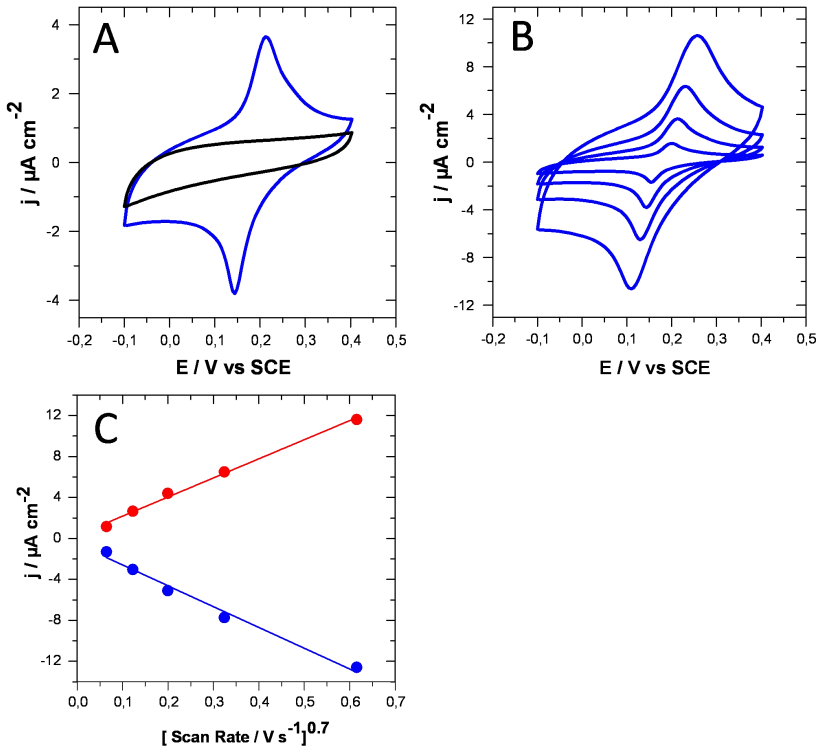

Figure 9.15. Voltammetric evaluations of electroactivity of PBNPs in graphene-PB hybrid papers. A) Comparison of cyclic voltammograms (CVs) of RGO alone (black curve) and PBNPs-RGO (blue curve) papers, scan rate 50 mV s^{-1}; B) CVs obtained at PBNPs-RGO papers with different scan rates of 20, 50, 100 and 200 mV s^{-1}; and C) the relation between the peak currents and scan rate. Electrolyte: 0.1 M phosphate buffer (pH 6.0) containing 0.1 M KCl used in all the measurements.

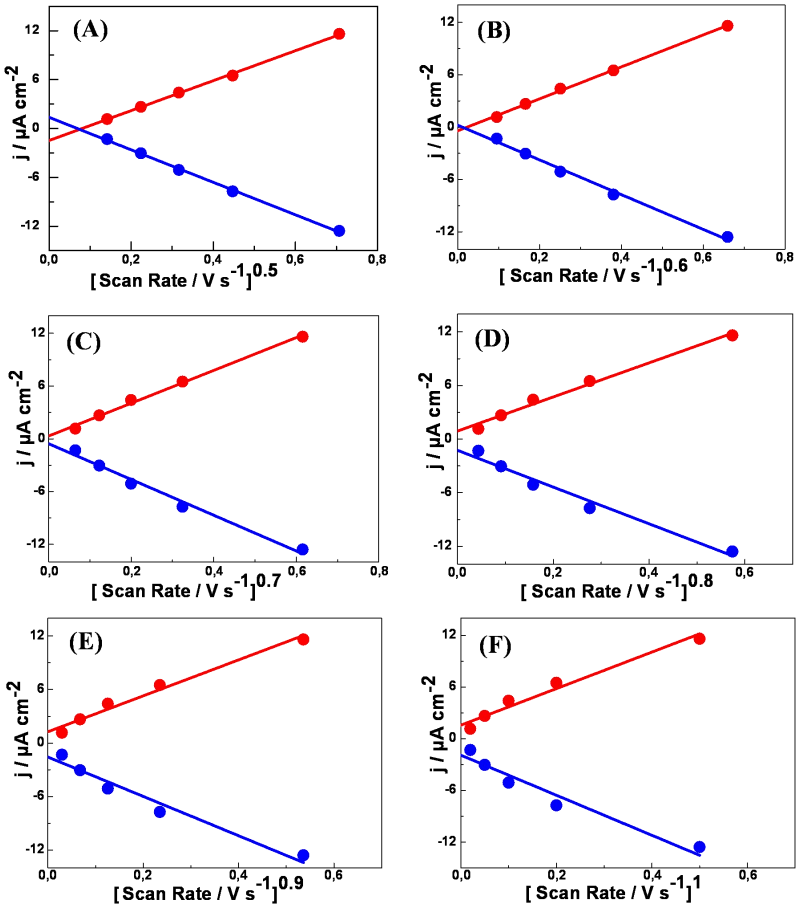

Figure 9.16. Electroactivity of PBNPs confined in graphene papers. The correlation between the peak currents and scan rate (υ^x) with x = 0.5, 0.6, 0.7, 0.8, 0.9, 1.0.

Electrochemical impedance spectra (EIS) were recorded under various experimental conditions. First, at fixed frequency, the apparent impedance of both RGO and PBNPs–RGO papers is potential-dependent and increases with potentials shifted positively (Figure 9.17A and B). Interestingly, in contrast to the conductivity measured in air (Table 9.1), PBNPs-RGO papers appear to be more conductive than RGO papers in electrochemical environments. Besides, a sharp impedance decrease is observed around 0.18 V (i.e., the PBNP formal redox potential) for PBNPs–RGO papers (Figure 9.17B).

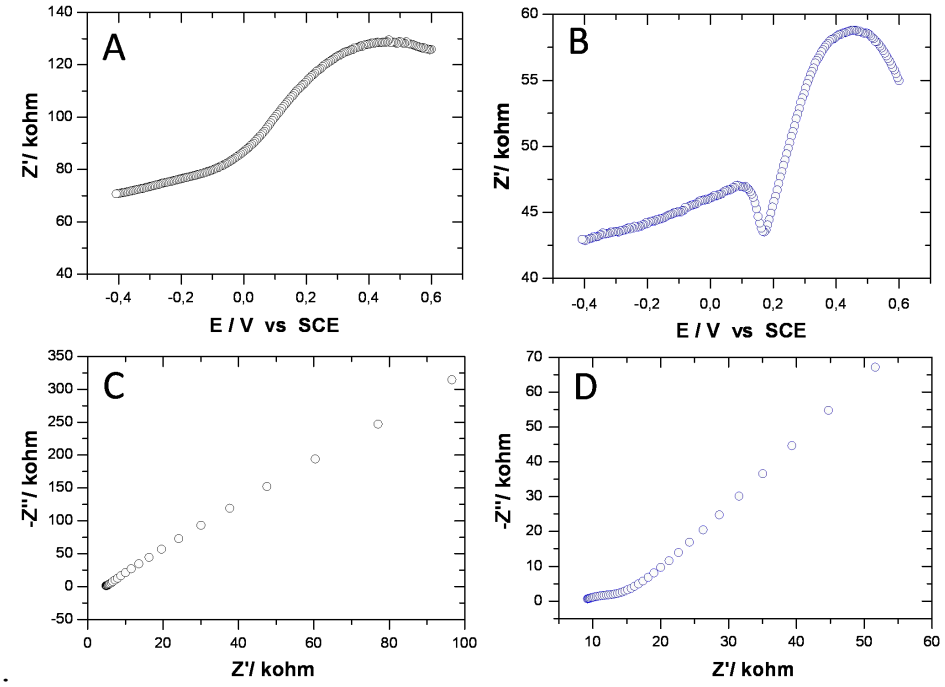

Figure 9.17. Electrochemical impedance spectra (EIS) of graphene papers. Comparison of the potential-dependent impedance spectra of A) RGO and B) PBNPs-RGO papers at a fixed frequency of 1 Hz; Nyquist plots of C) RGO and D) PBNPs-RGO papers at a fixed potential of 0.18 V (vs SCE, i.e., at the formal redox potential of PBNPs) with the frequency range of 10 000 to 0.5 Hz. Electrolyte was 0.1 M phosphate buffer (pH 6.0) containing 0.1 M KCl and an amplitude of 10 mV was used in all the measurements.

Thus, the apparent conductance of PBNPs-RGO in liquid environments is also dependent on the redox states of the PBNPs, suggesting that PBNPs-RGO papers at the equilibrium PBNP redox state have a maximum ionic conductance. This characteristics could be a notable advantage for the use of PBNPs-RGO papers in electrocatalysis and electrochemical sensors, compared to their possible applications in solid-state devices. However, the intrinsic electrical conductivity of graphene papers was in fact not modulated by liquid environments, as indicated by the intercepts at X-axis in Figure 9.17C and D as approximately 4 and 8 KΩ for RGO and PBNPs–RGO papers, respectively. The observed conductance enhancement should, thus, be attributed to electrochemical reactions of confined PBNPs.

The EIS spectra were then obtained at a fixed potential of 0.18 V for two types of papers, as compared in Figure 9.17C and D. While the EIS spectra for RGO papers are featureless (Figure 9.17C), the EIS spectra for PBNPs–RGO papers are characterized by a pseudo semicircle in the Nyquist plot (Figure 9.17D) with the ET resistance (R_{ct}) estimated as 4 kΩ. The experimental data were further fitted using an equivalent circuit, and the results are given in Figure 9.18. These observations are consistent with the voltammetric results (Figure 9.15A and B).

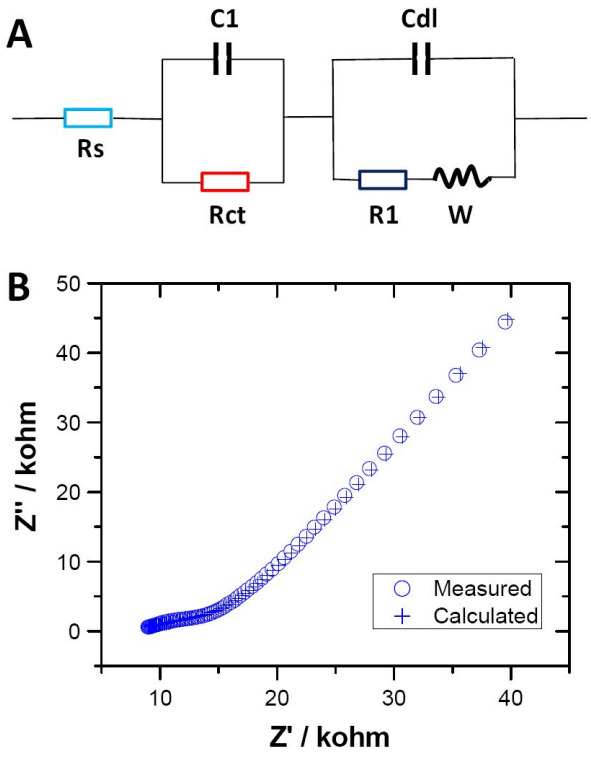

Figure 9.18. (A) A possible equivalent circuit and (B) the Nyquist plots of EIS of measured and calculated data. responses of PBNPs-RGO papers. Electrolyte: 0.1 M KCl, the frequency applied from 10000 to 0.3 Hz with an amplitude of 10 mV, the working electrochemical potential fixed at the redox formal potential of the PBNPs (i.e., 0.18 V vs. SCE).

Finally, the EIS spectra were recorded in the presence of a redox probe consisting of $[Fe(CN)_6]^{3-}$ and $[Fe(CN)_6]^{4-}$ in electrolyte solution. As expected, RGO papers favor

the diffusion controlled $[Fe(CN)_6]^{3-/4-}$ ET reaction (i.e., fast ET kinetics) (Figure 9.19), likely due to relatively high electrical conductivity of RGO. However, PBNPs-RGO papers can still be used as electrochemical working electrodes supporting external redox reaction.

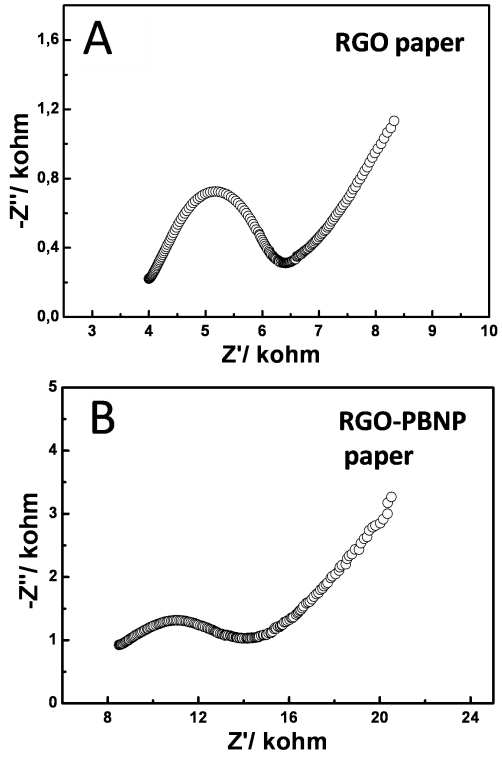

Figure 9.19. Nyquist plots of EIS responses of RGO (A) and PBNPs-RGO (B) papers to redox probe $K_3[Fe(CN)_6]/K_4[Fe(CN)_6$ in solution. Electrolyte: 0.1 M KCl containing 5 mM $K_3[Fe(CN)_6]$ and 5 mM $K_4[Fe(CN)_6]$, the frequency applied from 10000 to 0.1 Hz with an amplitude of 10 mV, the working electrochemical potential fixed at the redox formal potential of the redox probe.

9.3.5. Electrocatalysis and Enzyme Bioelectrocatalysis at Graphene Papers

As the electroactivity of PBNPs confined in RGO papers was well preserved (Section 9.3.4), we next examined their electrocatalytic activity towards reduction of hydrogen peroxide (H_2O_2). Electrocatalytic reduction of H_2O_2 started at 0.4 V (vs SCE) and

tended to reach a maximum effect at potentials more negative than -0.1 V (Figure 9.20A and Figure 9.21A). The electrocatalytic current increases with increasing H_2O_2 concentration (Figure 9.21B). In contrast, the reference RGO paper system has little activity for electrochemical reduction of H_2O_2. Direct electroreduction could not be detected until -0.2 V and with much smaller current (Figure 9.21A). The presence of PBNPs thus reduces the overpotential at least 600 mV, and enables sensitively detecting H_2O_2 at favorable potentials, for example, between 0.0 and -0.1 V. A linear relation between electrocatalytic current density (j_{cat}) and H_2O_2 concentration is observed in the range 1-7 mM, with a detection limit down to about 5 μM (Figure 9.20B). These electrocatalytic properties have laid a solid basis for further incorporation of redox enzymes as biosensing devices, which is addressed below with glucose oxidase (GOD) used as an example.

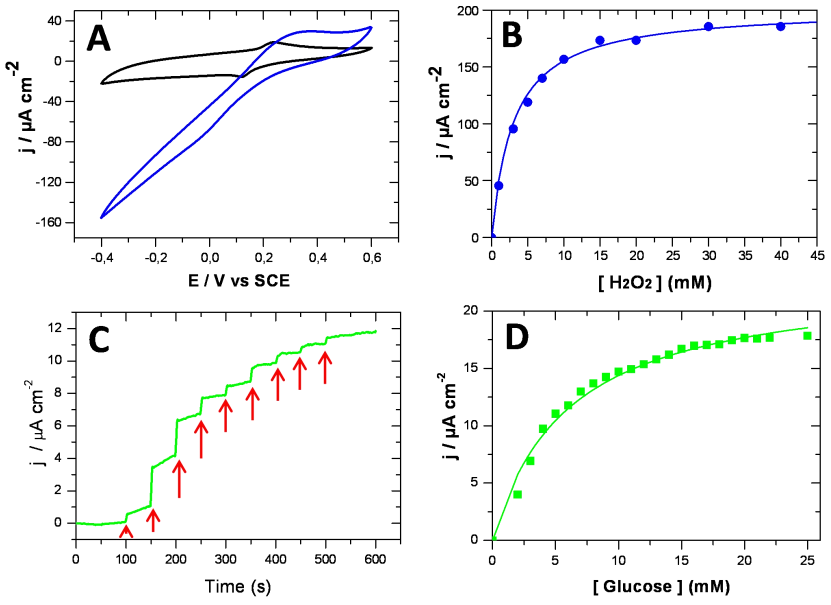

Figure 9.20. Electrocatalysis and biocatalysis. A) CVs of PBNPs-RGO paper electrodes in the absence (black curve) and presence (blue curve) of 10 m M H_2O_2; B) the dependence of electrocatalytic currents on concentrations of H_2O_2 in the range 0-40 m M at -0.1 V; C) the time course of responses of GOD-PBNPs-RGO papers to glucose at a fixed potential of -0.05 V (vs SCE) with 1 m M increment in injections; D) the dependence of electrocatalytic currents on concentrations of glucose in the range 0-25 mM . Electrolyte: 0.1 M phosphate buffer containing 0.1 M KCl (pH 6.0). Scan rate in (A): 20 mV s^{-1}.

Pure RGO paper is structurally compact (Figure 9.10C) and largely hydrophobic, which makes it chemically incompatible for direct incorporation of bio-macromolecules such as proteins and enzymes. However, the layered integration of water-soluble PBNPs results in a much open structure (Figure 9.10D) with significantly enhanced hydrophilicity. This add-in structural and chemical feature is crucial for incorporation of enzyme into graphene papers. For example, incorporation of GOD in the present work was achieved either by soaking a piece of PBNPs-RGO paper in a GOD-containing buffer solution or by casting a few drops of GOD solution onto the PBNPs-RGO paper (details in the Experimental Section).

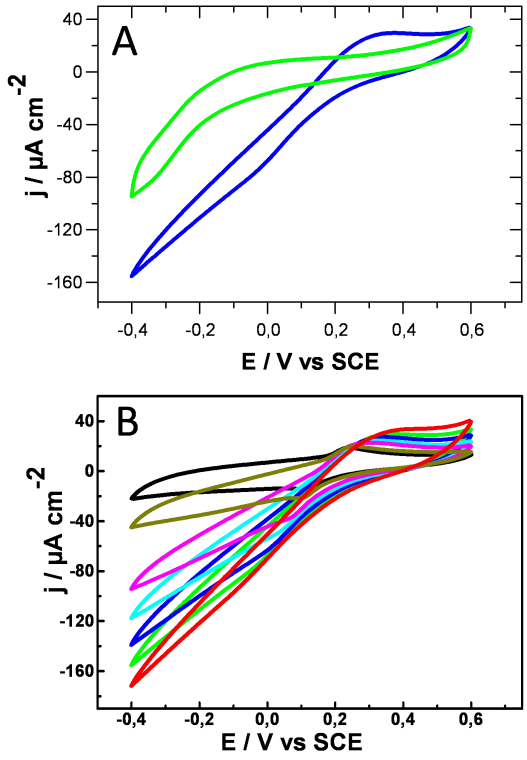

Figure 9.21. Cyclic voltammograms of (A) comparison of electroreduction of 10 mM H_2O_2 at pure RGO paper (green curve) and PBNPs-RGO paper (blue) and (B) electrocatalytic reduction of H_2O_2 at RGO-PBNPs papers with various H_2O_2 concentrations of 0, 1, 3, 5, 7, 10, 15mM. Electrolyte: 0.1 M phosphate buffer (pH 6.0) containing 0.1 M KCl. Scan rate: 20 mV s^{-1}.

The addition of GOD in the papers increases the capacitive current response due to the more hydrophilic interfaces, but does not detectably affect the ET kinetics of PBNPs, as evaluated by cyclic voltammetry (Figure 9.22A). The immobilized GOD retained its biocatalytic activity towards oxidation of glucose in the presence of dioxygen. The reduced GOD was re-oxidized by dioxygen, accompanied by generation of H_2O_2. The H_2O_2 generated was in turn electrocatalytically reduced by PBNPs in the paper and detected by the CVs (Figure 9.22B). Such a redox catalytic cycle allows quantitatively analyzing glucose at favorable potentials (e.g., 0 or -0.05 V vs. SCE) where signal interference from oxidation of ascorbic acid and/or uric acid can be avoided. Quantitative analysis was further carried out by recording the current versus time response curves upon successive injection of glucose, as shown in Figure 9.20C. The correlation between the electrocatalytic current and glucose concentration shows a linear relation up to about 6-8 mM (Figure 9.20D) with a sensitivity of 25 μA mM^{-1} cm^{-2} and the detection limit down to about 10 μM. It was found that the electrochemical analogue of the Michaelis-Menten equation for the relation between the electrocatalytic current density and the substrate concentration[51] applies and can be used to fit the experimental data. The apparent Michaelis-Menten constant (K_M) is estimated as 3.8 mM. This value is lower than those reported in most previous studies[52,53] but very close to a recently reported value (2.7 mM) where GOD was co-immobilized together with nickel oxide nanoparticles[54] on glassy carbon electrodes. A wide range of apparent K_M values (e.g., 5 to 60 mM) for this enzyme have been reported to date, mainly depending on the types of support matrix (e.g., metals, carbon electrodes and various polymers) and immobilization methods (e.g., covalent linking and non-convalent encapsulation).[52,53] Our results suggest that GOD confined in PBNPs-RGO papers shows a high binding affinity to substrate and, as such, its three-dimensional structures are well preserved.

It is noted that the detection limits of both H_2O_2 and glucose at PBNPs-RGO papers are relatively high, compared to those obtained at polymer-PB-GOD[55] or polymer-GOD-metllic NPs[56] systems. However, the present detection limit is still at the μM level. Since the blood sugar level is in the mM ranges (e.g., about 5.5 mM for the

mean normal blood glucose level in humans), the GOD-PBNPs-RGO papers should hold potential as free-standing and disposable glucose sensors for applications in fast tests of blood sugar levels. Furthermore, the present work is largely focused on the preparation and characterization of PBNPs-RGO nanohybrids. To improve the sensitivity and detection limit, it is highly desirable to further optimize fabrication of PBNPs-RGO nanohybrids based chemical sensors and biosensors in ongoing research.

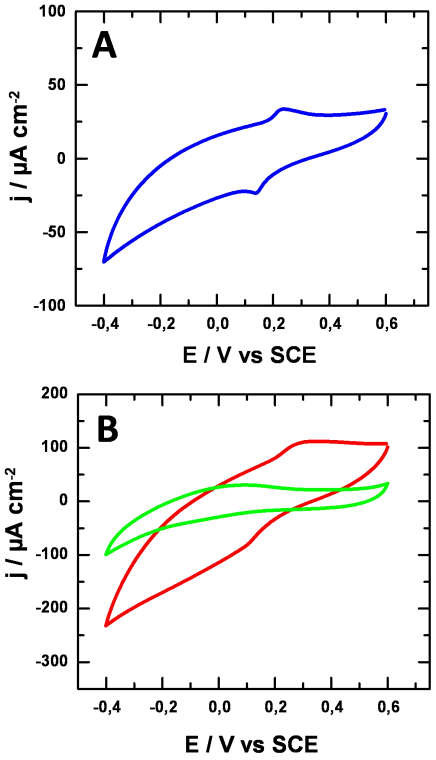

Figure 9.22. Cyclic voltammograms of (A) GOD-PBNPs-RGO papers in the absence of glucose and (B) comparison of electrocatalytic response to glucose at RGO paper (green) and GOD-PBNPs-RGO paper (red) in the presence of 10 mM glucose. Electrolyte: 0.1 M phosphate buffer (pH 6.0) containing 0.1 M KCl. Scan rate: 20 mV s^{-1}.

9.4 Conclusions

Two types of highly stable, low-cost and chemically compatible nanoscale materials, RGO and Prussian blue nanoparticles, were synthesized and used as building blocks

to prepare with increased electrical conductivity and functional variability nanohybrid electrocatalyst. Stable PBNPs-RGO hybrid sheets were formed via chemical interactions between the two components. The present approach facilitates preparation of layered doping with electroactive PBNPs and free-standing graphene papers. PBNPs doped graphene papers show high-performance electrocatalysis towards reduction of hydrogen peroxide and can be used alone as flexible chemical sensors for potential applications in detection of hydrogen peroxide or/and other organic peroxides. PBNPs-RGO papers are further capable of biocompatible accommodation of enzymes for development of free-standing enzyme based biosensors, which is exemplified by glucose oxidase in the present work. On the basis of notable advantages of high stability, low cost, and efficient electrocatalysis, this kind of nanohybrid materials has potential to be produced in a large scale and offers a broad range of possible applications as electron transfer mediators and nanoscale electrocatalysts, particularly in the fabrication of flexible sensing devices as well as in electrocatalytic energy conversion.

9.5 References

[1] D. A. Dikin, S. Stankovich, E. J. Zimney, R. D. Piner, G. H. B. Dommett, G. Evmenenko, S. T. Nguyen, R. S. Ruoff, *Nature* **2007**, *448*, 457.

[2] S. Stankovich, D. A. Dikin, R. D. Piner, K. A. Kohlhaas, A. Kleinhammes, Y. Jia, Y. Wu, S. T. Nguyen, R. S. Ruoff, *Carbon* **2007**, *45*, 1558.

[3] S. Park, R. S. Ruoff, *Nat. Nanotechnol.* **2009**, *4*, 217.

[4] F. Yavari, N. Koratkar, *J. Phys. Chem. Lett.* **2012**, *3*, 1746.

[5] F. Xiao, Y. Q. Li, X. L. Zan, K. Liao, R. Xu, H. W. Duan, *Adv. Funct. Mater*. **2012**, *22*, 2487.

[6] H. C. Gao, Y. X. Wang, F. Xiao, C. B. Ching, H. W. Duan, *J. Phys. Chem. C* **2012**, *116*, 7719.

[7] F. Xiao, J. B. Song, H. C. Gao, X. L. Zan, R. Xu, H. W. Duan, *ACS Nano* **2012**, *6*, 100.

[8] J. Liang, Y. Huang, J. Oh, M. Kozlov, D. Sui, S. Fang, R. H. Baughman, Y. Ma, Y. Chen, *Adv. Funct. Mater*. **2011**, *21*, 3778.

[9] B. G. Choi, H. Park, T. J. Park, M. H. Yang, J. S. Kim, S.-Y. Jang, N. S. Heo, S. Y. Lee, J. Kong, W. H. Hong, *ACS Nano* **2010**, *4*, 2910.

[10] D. W. Wang, F. Li , W. Ren, Z. G. Chen, J. Tan, Z. S. Wu, I. Gentle, G. Q. Lu, H. M. Chen, *ACS Nano* **2009**, *3*, 1745.

[11] Y. Zhu, M. D. Stoller, W. Cai, A. Velamakanni, R. D. Piner, D. Chen, R. S. Ruoff, *ACS Nano* **2010**, *4*, 1227.

[12] A. Abouimrane, O. C. Compto , K. Amine, S. T. Naguyen, *J. Phys. Chem. C* **2010**, *114*, 12800.

[13] H. Gwon, H. S. Kim, K. U. Lee, D. H. Seo, Y. C. Park, Y. S. Lee, B. T. Ahn, K. Kang, *Energy Environ. Sci*. **2011**, *4*, 1277.

[14] G. Wang, K. Sun , F. Lu, H. Sun, M. Yu, W. Jiang, C. Liu, J. Lian, *Small* **2012**, *8*, 452.

[15] X. Wang, X. Cao, L. Bourgeois, H. Guan, S. Chen, Y. Zhong, D. M. Tang, H. Li, T. Zhai, L. Li, Y. Bando, D. Golberg, *Adv. Funct. Mater.* **2012**, *22*, 2682.

[16] F. Liu, S. Song, D. Xue, H. Zhang, *Adv. Mater.* **2012**, *24*, 1089.

[17] D. Wang, R. Kou, D. Choi, Z. Yang, Z. Nie, J. Li, L. V. Saraf, D. Hu, J. Zhang, G. L. Graff, J. Liu, M. A. Pope, I. A. Aksay, *ACS Nano* **2010**, *4*, 1587.

[18] Z. Li, Y. Mi, X. Lin, S. Lin, S. Yang, J. Wang, *J. Mater. Chem*. **2011**, *21*, 13991.

[19] S. Park, N. Mohanty, J. W. Suk, A. Nagaraja, J. An, R. D. Piner, W. Cai, D. R. Dreyer, V. Berry, R. S. Ruoff, *Adv. Mater.* **2010**, *22*, 1736.

[20] N. D. Luong, N. Pahimanolis, U. Hippi, J. T. Korhonen, J. Ruokolainen, L.-S. Johansson, J.-D. Nam, J. Seppala, *J. Mater. Chem*. **2011**, *21*, 13991.

[21] Y. J. Song, K. G. Qu, C. Zhao, J. S. Ren, X. G. Qu, *Adv. Mater*. **2010**, *22*, 2206.

[22] W. Hu, C. Peng, W. Luo, M. Lv, X. Li, D. Li, Q. Huang, C. Fan, *ACS Nano* **2010**, *4*, 4317.

[23] S. Some, S.-M. Ho, P. Dua, E. Hwang, Y. H. Shin, H. Yoo, J.-S. Kang, D.-K. Lee, H. Lee, *ACS Nano* **2012**, *6*, 7151.

[24] S. Park, K.-S. Lee, G. Bozoklu, W. Cai, S. T. Nguyen, R. S. Ruoff, *ACS Nano* **2008**, *2*, 572.

[25] H. Chen , M. B. Muller , K. J. Gilmore , G. G. Wallace , D. Li, *Adv. Mater*. **2008**, *20* , 3557 .

[26] H. Bi, K. Yin, X. Xie, Y. Zhou, N. Wan, F. Xu, F. Banhart, L. Sun, R. S. Ruoff, *Adv. Mater*. **2012**, *24*, 5124.

[27] C. Valles, J. D. Nunez, A. M. Benito, W. K. Maser, *Carbon* **2012**, *50*, 835.

[28] S. Park, J. W. Suuk, J. An, J. Oh, S. Lee, W. Lee, J. R. Potts, J.-H. Byun, R. S. Ruoff, *Carbon* **2012**, *50*, 4573.

[29] A. R. Ranjbartoreh, B. Wang, X. Shen, G. Wang, *J. Appl. Phys*. **2011**, *109*, 014306.

[30] Y. Liu, B Xie, Z. Zhang, Q. Zheng, Z. Xu, *J. Mech. Phys. Solids* **2012**, *60*, 591.

[31] J. Xiang, L. T. Drzal, *ACS Appl. Mater. Interfaces* **2011**, *3*, 1325.

[32] Y. Tang, J. H. Gou, *Mater. Lett.* **2010**, *64*, 2513.

[33] Y. F. Li, Y. Z. Liu, W. Z. Shen, Y. G. Yang, M. Z. Wang, Y. F. Wen, *Appl. Phys. A Mater.* **2012**, *106*, 779.

[34] K. Itaya, I. Uchida, V. D. Neff, *Acc. Chem. Res.* **1986**, *19*, 162.

[35] Q. Chi, S. Dong, *Anal. Chim. Acta* **1995**, *310,* 429.

[36] A. A. Karyakin, O. V. Gitelmacher, E. E. Karyakina, *Anal. Chem*. **1995**, *67*, 2419.

[37] A. A. Karyakin, E. E. Karyakin, L. Gorton, *Anal. Chem*. **2000**, *72*, 1720.

[38] A. A. Karyakin, *Electroanalysis* **2001**, *13*, 813.

[39] F. Ricci, G. Palleschi, *Biosens. Bioelectron*. **2005**, *21*, 389.

[40] T. Wang, Y. Fu, L. Bu, C. Qin, Y. Meng, C. Chen, M. Ma, Q. Xie, S. Yao, *J. Phys. Chem. C.* **2012**, *116*, 20908.

[41] A. Gotoh, H. Uchida, M. Ishizaki, T. Satoh, S. Kaga, S. Okamoto, M. Ohta, M. Sakamoto, T. Kawamoto, H. Tanaka, M. Tokumoto, S. Hara, H. Shiozaki, M. Yamada, M. Miyake, M. Kurihara, *Nanotechnology* **2007**, *18*, 345609.

[42] H. Yan, M. Sc. thesis, Technical University of Denmark, DK-2800 Kongens Lyngby, Denmark, **2009**.

[43] J. Chen, Y. Miao, X. Wu, *Colloid J.* **2007** , *69* , 660 .

[44] Y. Miao, J. Chen , X. Wu, K. Fang , A. Jia, J. Liu, *J. Nanosci. Nanotechnol*. **2007**, *7*, 2877.

[45] S. Y. Gan, L. J. Zhong, T. S. Wu, D. X. Han, J. D. Zhang, J. Ulstrup, Q. Chi, L. Niu, *Adv. Mater.* **2012**, *24*, 3958.

[46] E. Jin, X. F. Lu, L. L. Cui, D. M. Chao, C. Wang, *Electrochim. Acta* **2010**, *55*, 7230.

[47] C. Wang, L. Zhang, Z. H. Guo, J. G. Xu, H. Y. Wang, H. W. Shi, K. F. Zhai, X. Zhuo, *Electroanalysis* **2010**, *22*, 1867.

[48] E. Laviron, *J. Electroanal. Chem*. **1979**, *101*, 19.

[49] P. S. Jensen, Q. Chi, F. B. Grumsen, J. M. Abad, A. Horsewell, D. J. Schiffrin, J. Ulstrup, *J. Phys. Chem. C* **2007**, *111*, 6124.

[50] K. Itaya, H. Akahoshi, S. Toshima, *J. Am. Chem. Soc.* **1982**, *104*, 4767.

[51] Q. Chi, J. Zhang, P. S. Jensen, H. E. M. Christensen, J. Ulstrup, *Faraday Discuss*. **2006**, *131*, 181.

[52] C. G. J. Koopal, R. J. M. Notle, *Bioelectrochem. Bioenerg*. **1994**, *33*, 45.

[53] D. W. Kimmel, G. LeBlanc, M. E. Meschievltz, D. E. Cliffel , *Anal. Chem.* **2012**, *84*, 685.

[54] A. Salimi, E. Sharifi, A. Noorbakhsh, S. Soltanian, *Biosens. Bioelectron*. **2007**, *22*, 3146.

[55] C. Chen, Y. Fu, C. Xiang, Q. Xie, Q. Zhang, Y. Su, L. Wang, S. Yao, *Biosens. Bioelectron*. **2009**, *24*, 2726.

[56] Y. Fu, P. Li, Q. Xie, X. Xu, L. Lei, C. Chen, C. Zou, W. Deng, S. Yao, *Adv. Funct. Mater*. **2009**, *19*, 1784.

[57] W. S. Hummers, R. E. Offeman, *J. Am. Chem. Soc.* **1958**, *80*, 1339.

[58] N. I. Kovtyukhova, P. J. Ollivier, B. R. Martin, T. E. Mallouk, S. A. Chizhik, E. V. Buzaneva, A. D. Gorchinskiy, *Chem. Mater.* **1999**, *11*, 771.

10. Gold-substrate Graphene Paper Entrapped Prussian Blue Nanoparticles of Electrocatalysis for Biosensors

The focus of this chapter is on electron transfer (ET) and electrocatalysis of inorganic hybrid Prussian blue nanoparticles (PBNPs) on the flexible graphene electrode. Flexible biosensors that can accommodate dramatic shape changes are instrumental for the development of portable point of care medical products, minimally invasive implantable devices, and compact diagnostic platforms. Samples based on graphene mixed with PBNPs in aqueous solution, and free-standing flexible graphene-PBNPs paper with a gold filter as an assisting substrate, has been prepared by vacuum assisted flow-filtration. The graphene/PBNPs paper obtained using Au filter substrate showed high electrical conductivity, outstanding mechanical strength, excellent thermal stability, structural uniformity, and furthermore, good electrochemical performance. Strong electrocatalytic properties have, furthermore, been achieved using these mixed materials.

Section 1. PEI Reduced RGO for Au-RGO/PEI/PBNPs/GOD

10.1 Fabrication and Characterization of Au-RGO/PEI/PBNPs/GOD

As described in the Chapter 9, graphene paper with active PBNPs was prepared, and high performance for biosensor catalysis towards H_2O_2 reduction and glucose oxidation was obtained. This chapter describes continuation of the graphene paper work, where we used Au film filter membrane (with the diameter of 25 mm) instead of traditional filter membranes, such as poly(vinylidene fluoride) (PVDF) or polycarbonate membrane, due to the high conductivity of gold directly as a substrate without heating the graphene paper in the oven for increasing its conductivity.

Generally, in order to adsorb enzymes on the graphene paper materials, polymers with positive or negative charges, or specially functional groups on the surface, are

used in the self-assembled mixture to make its structure stable by forming electrostatic or covalent interaction between polymers and enzymes. In this graphene paper, the redox active nanomaterials PBNPs were combined with a classical and representative enzyme glucose oxidase (GOD) as a best system, Poly(ethyleneimine) (PEI) with numerous -NH_2 groups on the surface combined with graphene paper were chosen, as a polymer media in the process.

There are two ways of mixing PEI into this nanostructure. One method is to first reduce GO with hydrazine solution to RGO, as descripted in Chapter 9, and then mix RGO, PBNPs and PEI directly. GOD could be then attached on mixture. The other method is to use PEI as a reducing agent for GO to RGO and also provide remaining amine groups for connection with PBNPs and GOD. This project discusses both ways for electrochemistry and electrocatalysis, respectively, and mainly focuses on the second method (PEI as a reducing agent and linker group).

In the first method, RGO and PBNPs mostly negatively charged, and PEI with lots of amine groups (positively charged) were mixed closely, so that the negatively charged GOD could interact with the rest of the amine groups. This structure could obtain a simple and convenient method for electrochemical catalysis. Pictures of the mixture directly are shown in the Figure 10.1 (Left). The left yellow porous gold membrane is the original filter substrate for graphene paper, and the right one is the Au-RGO/PEI/PB/GOD mixture(mix directly). The thickness of the graphene paper depends on the concentration for the filter process.

In the second method, PEI is covalently linked to RGO nanosheets when reducing GO to RGO. PEI matrices offer biocompatible microenviroments for accommodation of enzymes such as GOD. Figure 10.1 (Right) shows the images of Au-RGO/PEI/PB/GOD (PEI reduced GO).

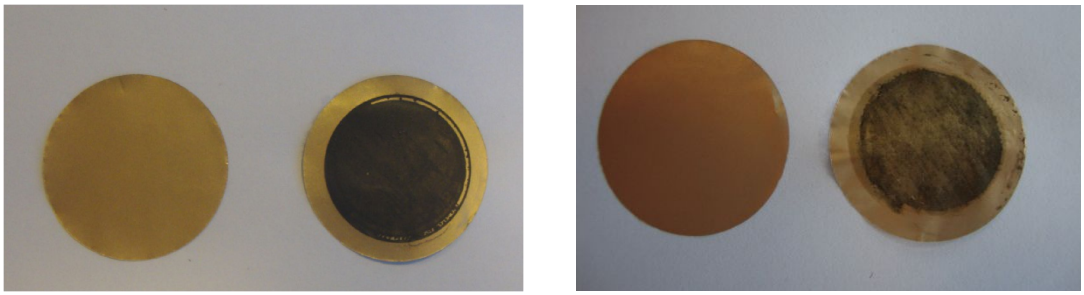

Figure 10.1 (Left) Au-RGO/PEI/PB/GOD (RGO and PEI mixed together directly); (Right) Au-RGO/PEI/PB/GOD (PEI reduced GO). Both yellow backgrounds are bare gold membranes with a diameter of 25 mm.

SEM of porous gold membrane for the filter substrate is shown in the Figure 10.2. The nanostructure of the porous gold membrane is random, and the pore diameter is around 500 nm, with nanometer scale cross section. This type of porous gold film provides a suitable substrate for graphene paper with high conductivity.

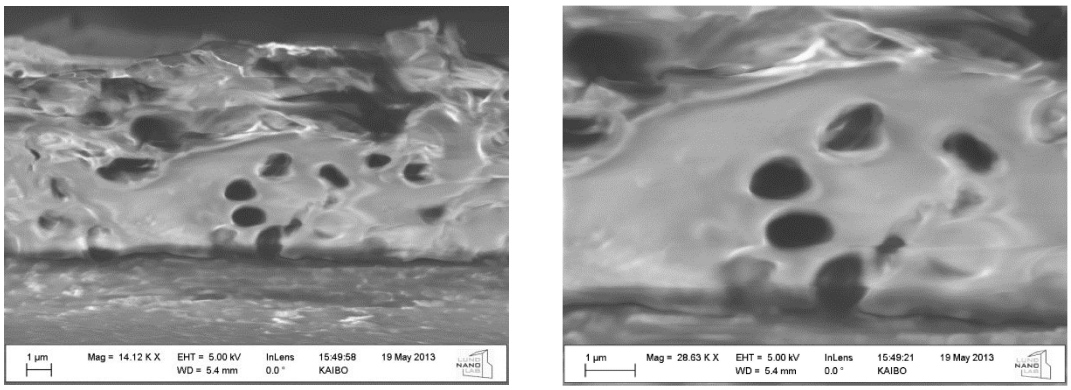

Figure 10.2. (Left) SEM of Au film membrane surface; (Right) SEM Cross section of Au film membrane.

The GO was prepared in the same way as described in Chapter 9, and the SEM or AFM images of GO and hydrazine reduced RGO recorded as described. AFM observation of RGO obviously shows the thickness of graphene nanosheet is around 1

nm, suggesting complete exfoliation of oxidized graphite close to single-layer graphene nanosheet. The high-resolution AFM images of PEI reduced GO to RGO are shown in Figure 10.3. There appears some rough structure on the graphene surface, compared to only RGO, with the hight of 2 nm, which is a bit thicker than only RGO due to the covalent interaction between PEI and GO.

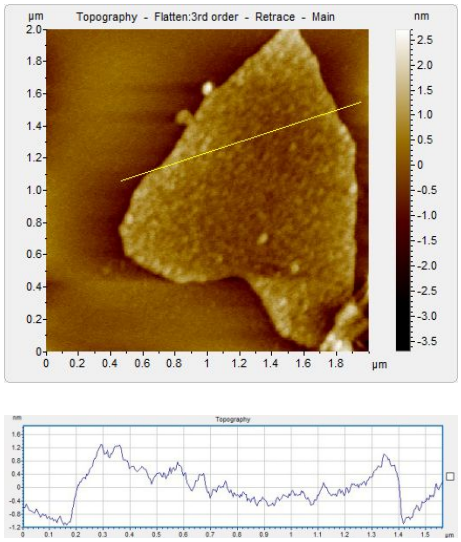

Figure 10.3. High-resolution AFM images of PEI reduced GO to RGO on mica and the height of PEI-RGO, 2 µm × 2 µm.

After fabricating graphene paper using gold film substrate and PEI reduced GO to RGO as reductive materials, SEM images from surface (Figure 10.4 (Left)) and cross section (Figure 10.4B (Right)) of Au-RGO/PEI were obtained. There appears fine structure of RGO/PEI on the surface, with some cracks. There are also several layers of graphene paper from the cross section, which obeys to the previous graphene paper explanation as described in the Chapter 9.

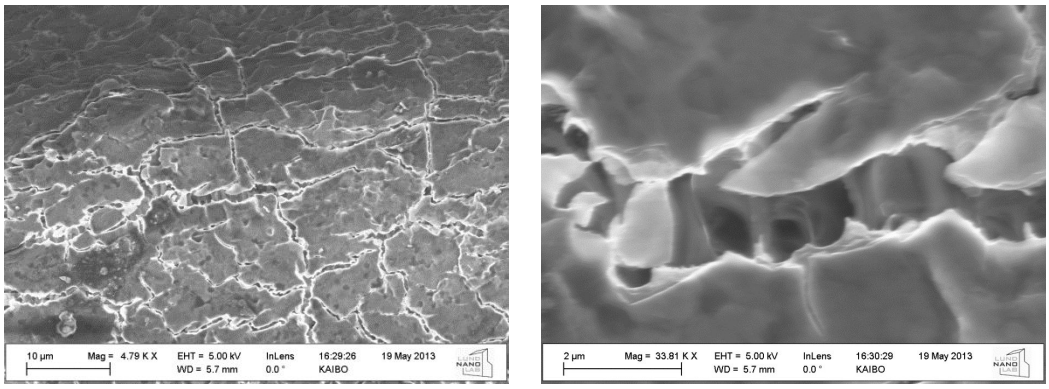

Figure 10.4 (Left) SEM of Au-RGO-PEI of surface surface (PEI reduced GO); (Right) SEM Cross section of Au-RGO-PEI (PEI reduced GO).

PBNPs as a redox active nanomaterial was also used in this work, and good performance in Chapters 6-9 for electrochemistry and electrocatalysis have been introduced. In the present chapter, PBNPs were mixed with PEI/RGO into stable composites resulting from the surface charges behavor of PBNPs either positive charge or negative charge as discussed in Chapter 7.

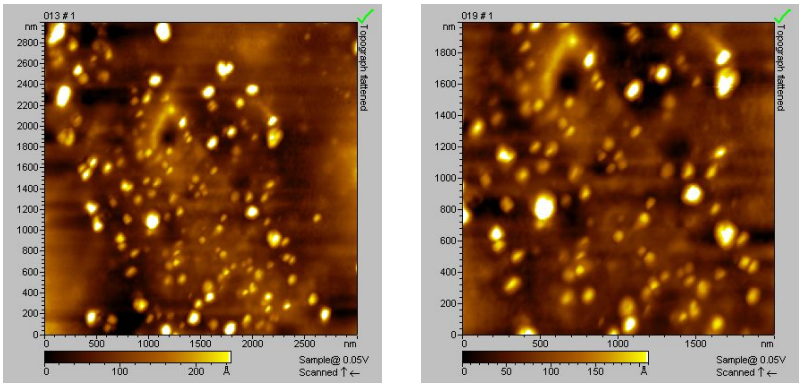

Figure 10.5. High-resolution AFM images of RGO-PEI-PB (PEI reduced GO) on mica. (Left) 3 µm × 3 µm; (Right) 2 µm × 2 µm.

The resulting stable materials were characterized broadly, and its electrocatalytic properties towards GOD catalyzed glucose oxidation have been studied. AFM and SEM images of the mixed RGO/PEI and PBNPs after centrifugation several times to remove dissociated PBNPs in solution are seen in Figure 10.5 and Figure 10.6. Most of PBNPs are anchored on the surface of the graphene nanosheets, with a few PBNPs present in the free area. Interestingly, as shown in the AFM images, PBNPs are predominantly in the overlayered and wrinkled graphene nanosheets. Notably, the smooth and uniform surface of flexible graphene nanosheet substrates appear not essential for the successful structure integration of 2D-assembly of PBNPs, where oxygen-containing functional groups are relatively abundant, and serve as linking groups for electrostatic attraction. This is consistent with the fact that PBNPs are stably immobilized on Au(111) surfaces modified with carboxylic groups terminated SAMs (Chapter 7).

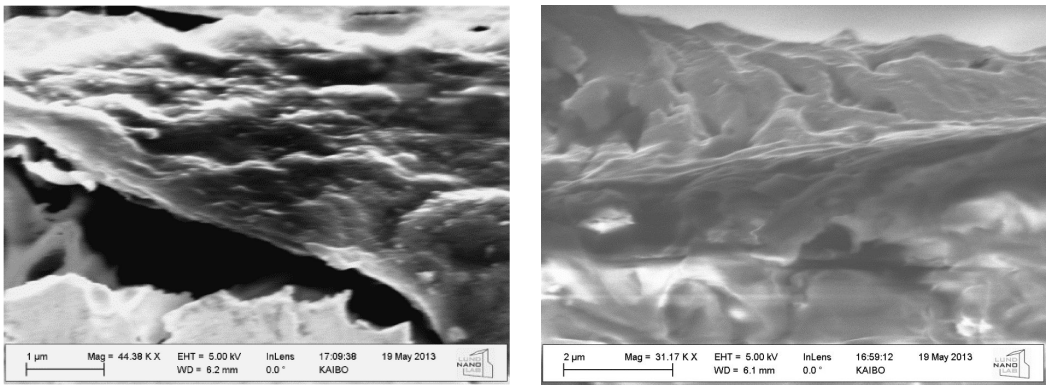

Figure 10.6 (Left) SEM of Au-RGO-PEI-PBNPs surface; (Right) SEM of Au-RGO-PEI-PBNPs cross section.

Figure 10.6 (Left) shows the Au-RGO/PEI/PBNPs surface, from which it is clearly seen that the PBNPs have a typical diameter of ≈ 6-7 nm on the surface of graphene and PEI. Some of the PBNPs were inside the graphene layers, so only part of them could be observed. Compared to the cross section of pristine Au-RGO/PEI paper

(Figure10.4B), mixing PBNPs in graphene stacking gives a thicker layer of hybrid Au-RGO/PEI/PBNPs paper (Figure10.6 (Right)), with a more porous structure than that of the pristine Au-RGO/PEI paper (Figure10.4B). This is attributed to the creation of more gaps between individual nanosheets when PBNPs acts as spacers assembled into the paper.

10.2 UV-Vis and FTIR Spectral Properties of RGO-PEI-PBNPs

UV-Vis spectra gave other evidence for the PBNPs adsorption on the surface of RGO/PEI (Figure 10.7). PBNPs are of blue color, with a maximum absorption around 700 nm (Figure 10.7), corresponding to mixed-valence charge-transfer absorbance of PBNPs. Mixing RGO/PEI solution and PBNPs solution in the volume ratio 8:1 for 1h. After high-speed centrifugation of the mixture (13000 r/min, 15 min), there is no peak at 700 nm of PBNPs from the supernatant solution (PBNPs solution alone still gives a peak after the same centrifugation speed rate and time), which demonstrated that PBNPs tend to locate on the RGO/PEI surface and are kept stable for a long period by strong electrostatic forces interaction between them.

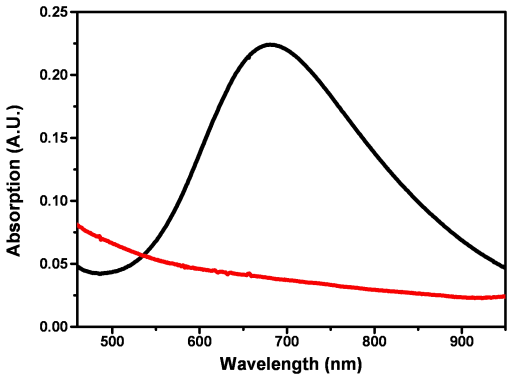

Figure 10.7. UV-Vis spectra of pure PBNPs after centrifugation (Black); and supernatant of RGO/PEI-PBNPs after centrifugation (Red), 13000 r/min, 15 min.

Further support for the formation of RGO/PEI and RGO/PEI-PB mixture was obtained by FTIR spectra as shown in Figure 10.8. Figure 10.8(A) shows the FTIR spectra of PEI-RGO and GO, where significant distinction can be seen. The following absorption bands were identified: around 3412 cm^{-1} in the GO spectra is attributed to the highly hydrophilic of GO, 1053 cm^{-1} can be seen due to C-O vibration in the epoxy group, 1380 cm^{-1} stands for the O-H vibration in the carboxyl acid, 1730 cm^{-1} represents the C=O stretching vibration in carboxylic acid (or carbonyl group).[1,3-5] After reduced by PEI, the adsorption bands at 1730 cm^{-1}, 1380 cm^{-1}, 1053 cm^{-1} almost disappear or become very weak. A new strong band appearing at around 1450 cm^{-1} demonstrates the C-N stretching vibration, which confirms the coverage of PEI on GO. Additionally, the band at 1649 cm^{-1}, which is from amide bonds vibration (-OCN-), displaced the skeletal vibration of un-oxidized graphitic domains bond at 1624 cm^{-1}.[2-4] These FTIR data of PEI-RGO confirms some of the amine groups from PEI are covalently linked to GO surface.

The spectra from the traditional method of RGO from hydrazine reduction of GO in FTIR data are shown in Figure 10.8B. There is no so big difference from the spectra of GO, which gives evidence of PEI covalently linked to GO nanosheet surface. Compared to spectra of pure RGO/PEI, RGO/PEI/PBNPs appeared an adsorption band around 2090 cm^{-1} (Figure 10.8C), corresponding to stretching vibration of CN group.[6] The adsorption band of the mixture was the same as PB pigment (Chapter 9), and the band was so weak in the mixture materials resulting from only a small amount of PBNPs in the mixture. And the adsorption band at around 500 cm^{-1} is due to the formation of the M-CN-M' structure (M=metal), which indicated the present of PB. Furthermore, the band near1600 cm^{-1} refers to O-H-O bending, attributed to present of interstitial water in the sample.[7]

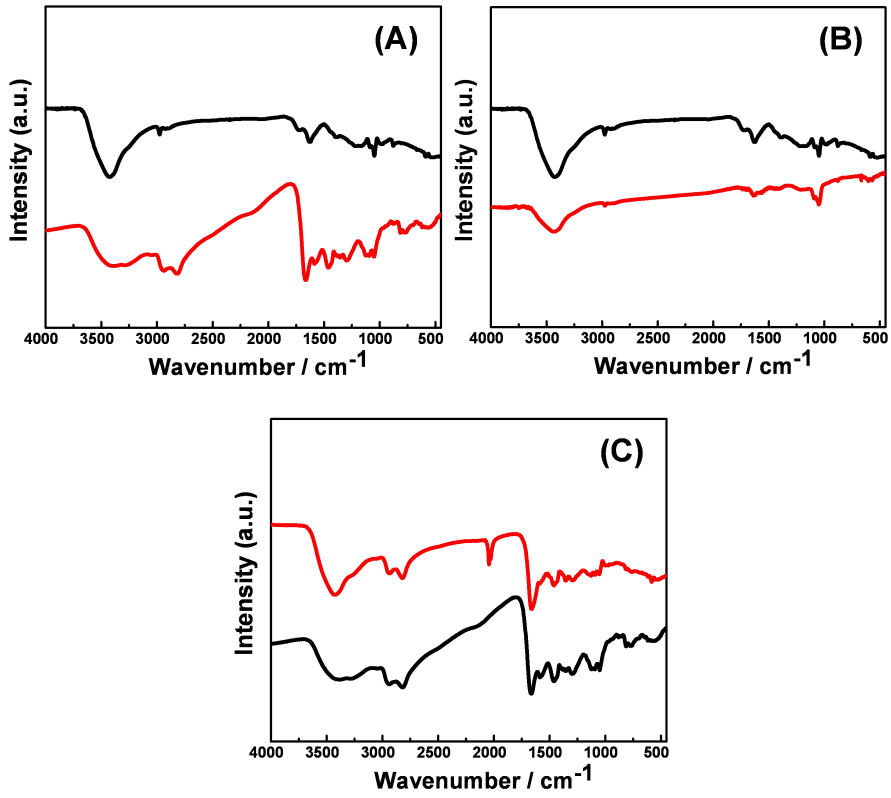

Figure 10.8. FTIR of (A) GO (Black) and PEI reduced RGO (Red); (B) GO (Black) and RGO reduced by hydrazine (Red); (C) PEI reduced GO (Black) and RGO-PEI-PBNPs (Red, PEI reduced RGO).

10.3 Au-RGO/PEI/PBNPs Graphene Paper from PEI Reduced RGO with Adsorbed GOD

The Au-RGO/PEI/PBNPs graphene paper from PEI reduced GO provides a biocompatible microenvironment for accommodation of enzymes through electrostatic encapsulation. The classical redox enzyme in the daily life is GOD, so this present work is mainly focused on the research of immobilization of GOD to detect glucose. The high-resolution AFM of GOD nanostructures are shown in Figure 10.9.

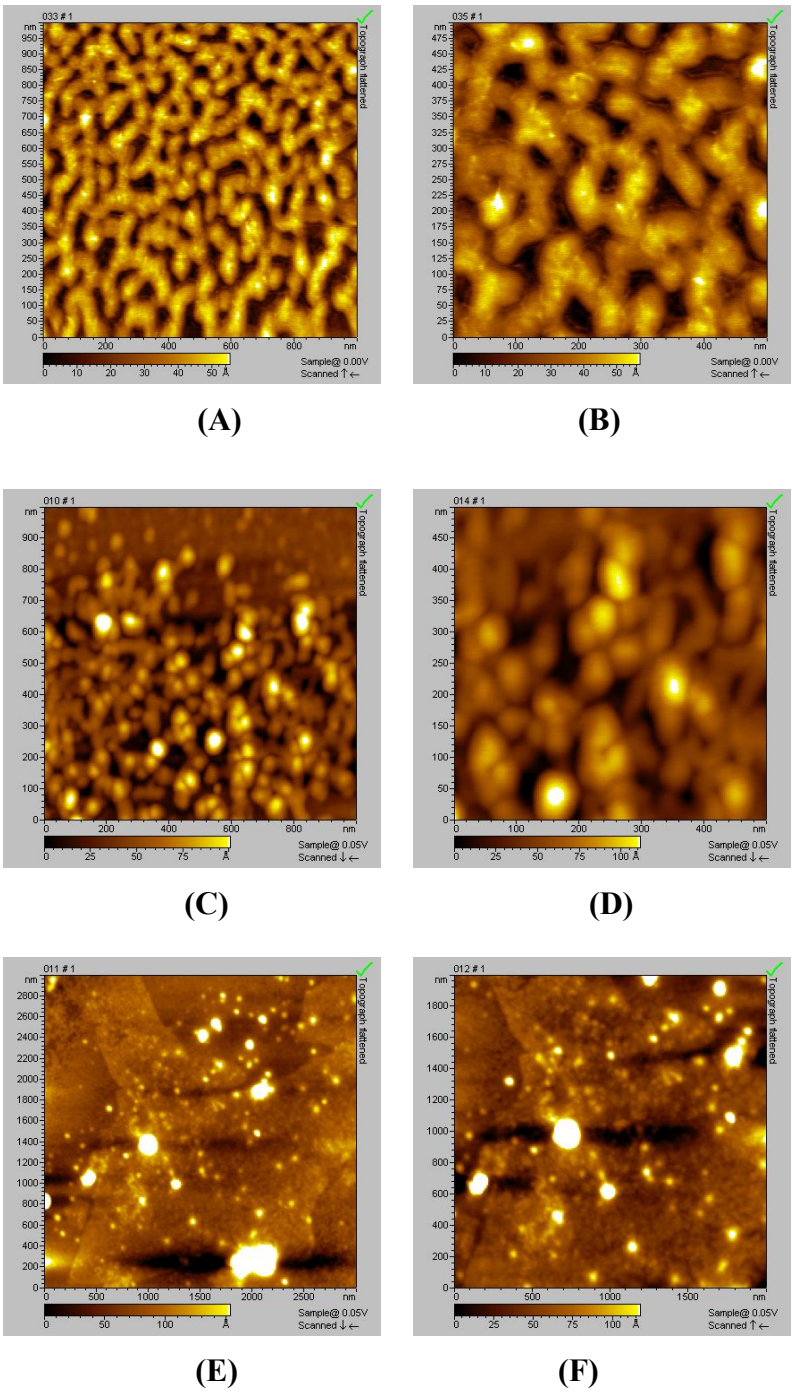

Figure 10.9. High-resolution AFM images. (A) 1 μm × 1 μm and (B) 0.5 μm × 0.5 μm of pure GOD; (C) 1 μm × 1 μm and (D) 0.5 μm × 0.5 μm of GOD-PBNPs; (E) 3 μm × 3 μm and (F) 2 μm × 2 μm of RGO-PEI-PB-GOD (PEI reduced GO).

Adhesive GOD formation looks like channels, and with close packing after mixing with PBNPs (Figure 10.9 B and C). GOD is negatively charged, while PBNPs are partly positively charged. When GO is reduced by PEI and mixed with PBNPs and GOD, most of the PBNPs and GOD were standing on the surface of PEI modified graphene nanosheets, with some big aggregation partly. Catalysis on this surface is discussed below.

UV-Vis spectra of GOD adhesion on the surface of SAM Au-RGO/PEI/PBNPs is shown in Figure 10.10. The original adsorption peak of GOD is 276 nm at the concentration of 0.2 mg/ml. When GOD is mixed together with RGO/PEI/PBNPs, electrostatic interaction results in GOD adhesion on the SAM layers. Even after centrifugation at 13000 r/min for 15 min, the adsorption of GOD from the supernatant of RGO/PEI-PBNPs-GOD was only 40% of the separate pure GOD at the same concentration, which means that the loading amount of GOD on the RGO/PEI-PBNPs was around 60%. This amount of GOD is enough to catalyze glucose oxidation in the presence of redox active materials.

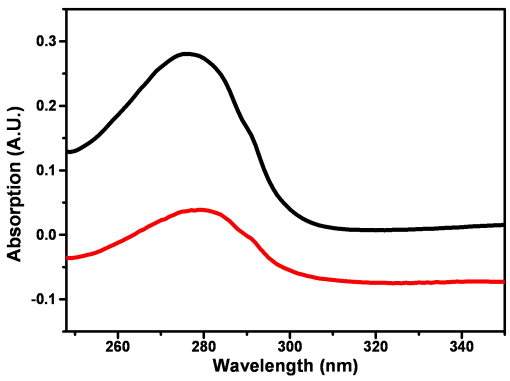

Figure 10.10. UV-Vis of pure pure GOD (0.2 mg/ml) after centrifugation (Black); and supernatant of RGO/PEI-PBNPs-GOD after centrifugation (Red), 13000 r/min, 15 min, which demonstrates a GOD loading amount around 60%.

10.4 Electrochemistry of Au-RGO/PEI/PBNPs/GOD

In the process of electrochemistry and electrocatalysis, free-standing flexible electrodes of Au-RGO/PEI/PBNPs/GOD hybrid papers could be easily directly used as working electrodes, while freely cutting the sizes and shapes is needed for practical use. Considering graphene papers of different thickness affect the electrochemical signals or electrocatalytic performance, three thickness graphene papers were prepared and measured in the electrochemistry, and the optical images shown in Figure 10.11, the thickness of the samples were 1 ml, 2 ml and 3 ml, respectively.

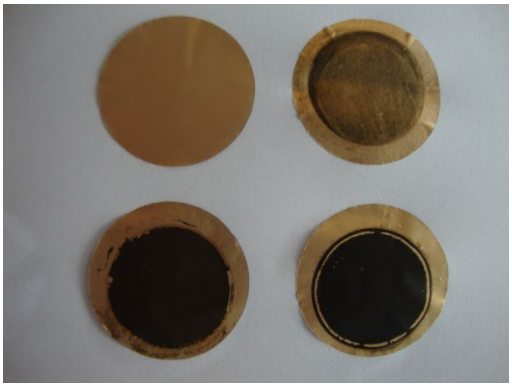

Figure 10.11. Photographs of different thickness of Au-RGO/PEI/PB/GOD (PEI reduced GO). Bare gold (top left); 1 ml concentration thickness (top right); 2 ml concentration thickness (bottom left); 3 ml concentration thickness (bottom right).

After fabricated of three electrode systems for measurement, the thickness of 1 ml graphene paper showed the best electrochemical signal compared to the other two. Figure 10.12 shows CVs of Au-RGO/PEI/PBNPs/GOD paper, in the potential range from -0.1 to 0.4 V. A pair of peaks appeared around 0.2 V, which was correlated to the position of oxidation/reduction potential of the PBNPs. Furthermore, different scan rates (0.02, 0.05, 0.1, 0.2, 0.3 V/s) of CVs show that the potential of the oxidation peak shifted positively with increasing scan rate, while the reduction peak

shifted negatively. At the same time, the peak-peak separation (which could calculate the rate constant K_s) increases with increasing scan rates. However, the formal redox potentials were almost the same at different scan rates. The rate constant was calculated as K_s=8.6 s^{-1} from the CVs.

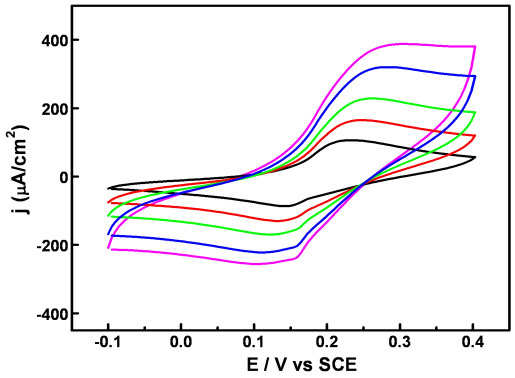

Figure 10.12. CVs at different scan rates of Au-RGO/PEI/PB/GOD (PEI reduced RGO) at 0.02, 0.05, 0.1, 0.2, 0.3 V/s.

The PBNPs in the Au-RGO/PEI/PBNPs/GOD hybrid paper interfered with restacking of the layers, and could graduatel act as pillars that separate individual graphene nanosheets and enable the electrolyte ions to penetrate more easily into the resulting hybrid graphene paper, thereby facilitating electrochemical accessibility between the nanosheets.

10.5 Electrocatalysis of Au-RGO/PEI/PBNPs/GOD

PB-based glucose biosensors have been shown to be suitable for assembly of finger stick sensors in glucose measurement in the context of diabetes.[8] Three different thickness samples of Au-RGO/PEI/PBNPs/GOD paper were tested as glucose biosensors in Figure 10.13.

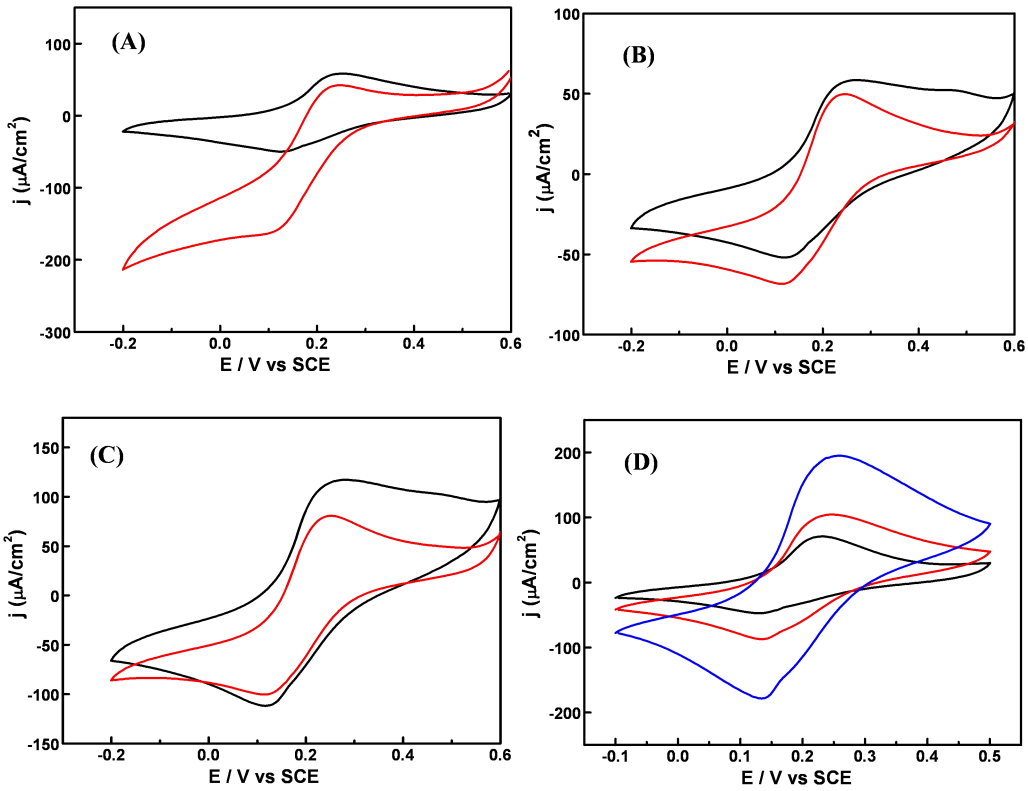

Figure 10.13. CVs of electrocatalysis glucose oxidation (10 mM) for different thickness of Au-RGO/PEI/PB/GOD (PEI reduced GO). (A) 1 ml thickness of Au-RGO/PEI/PB/GOD (PEI reduced GO) (Red) and without glucose (Black). (B) 2 ml thickness of Au-RGO/PEI/PB/GOD (PEI reduced GO) (Red) and without glucose (Black). (C) 3 ml thickness of Au-RGO/PEI/PB/GOD (PEI reduced GO) (Red) and without glucose (Black). (D) CVs of electrocatalysis glucose (10 mM) for different concentration Au-RGO/PEI/PB/GOD (PEI reduced GO), 1ml (black), 2ml (red), and 3ml (blue).

There is clearly electrocatalysis after adding 10 mM glucose in the electrolyte compared with the absence of glucose for the 1 ml thickness sample of Au-RGO/PEI/PBNPs/GOD (Figure 10.13A), but less in the 2 ml and 3 ml thickness samples (Figure 10.13B and C). When these three samples are compared (Figure 10.13D), the 1 ml thickness sample has the lowest surface coverage (4.158×10^{-4}), while 2 ml thickness sample has twice the surface coverage (7.704×10^{-4}), and the 3 ml thickness sample a three times bigger surface coverage (14.88×10^{-4}) than the 1 ml thickness sample, so the PBNPs redox active amount depends on the concentration of

samples. However, the rate constants of the three samples are almost the same (8.6 s^{-1}, 6.5 s^{-1}, and 7.5 s^{-1}, respectively), which demonstrates that the concentration of Au-RGO/PEI/PBNPs/GOD paper doesn't change the electron transfer pattern.

From the electrocatalysis comparison, the 1 ml thickness sample offers the best condition for biosensors. This sample was therefore used as electrode to monitor different concentrations of glucose.

CVs of different additions of glucose for Au-RGO/PEI/PBNPs/GOD paper (Figure 10.14A), and the amperometric response of Au-RGO/PEI/PBNPs/GOD paper to successive additions of glucose at -0.05V were recorded (Figure 10.14B). A good linear correlation was found over the range from 1 mM to 20 mM, and saturated after 20 mM, with a low detection limit 5μM.

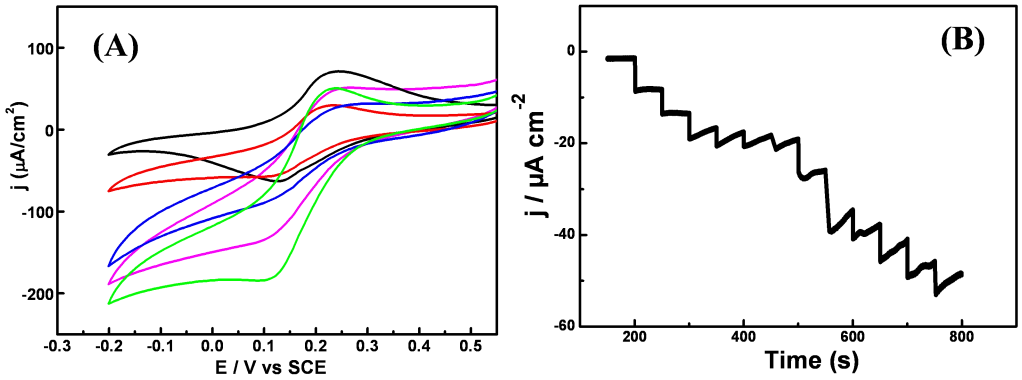

Figure 10.14. (A) CVs of different additions of glucose for Au-RGO/PEI/PBNPs/GOD paper, without glucose (Black); 3 mM (Red); 6 mM (Blue); 7 mM (Pink); 9 mM (Green). (B) Amperometric response of Au-RGO/PEI/PBNPs/GOD paper to successive additions of glucose at -0.05 V from 1 mM to 20 mM.

Section 2. RGO and PEI Mixed Directly for Au-RGO/PEI/PBNPs/GOD

The other method for Au-RGO/PEI/PBNPs/GOD is that GO is first reduced with hydrazine solution to RGO as described in Chapter 9. RGO, PBNPs and PEI are then mixed directly, followed by attaching GOD to the mixture at the last step. This method is less stable than PEI reduced RGO, but it can also very useful in the areas of biosensors, due to the fast electron transfer and direct electrocatalysis for H_2O_2 reduction.

10.6 Electrochemistry of Au-RGO/PEI/PBNPs/GOD Electrodes (PEI and RGO Mixed Directly)

Free-standing flexible electrodes of Au-RGO/PEI/PBNPs/GOD hybrid papers could be easily used as working electrodes directly in the process of electrochemistry and electrocatalysis, while freely cut the sizes and shapes are needed in the practical systems.

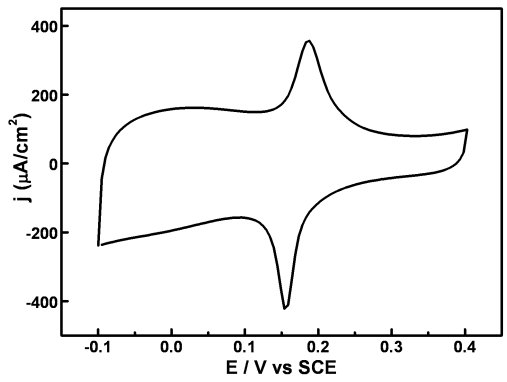

Figure 10.15. CVs of 1 ml thickness Au-RGO-PB (RGO and PB mixed directly). Scan rate: 0.1 V/s.

Au-RGO/PEI/PBNPs (RGO and PEI mixed directly) was fabricated, and then dipped into GOD solution to form Au-RGO/PEI/PBNPs/GOD by electrostatic interaction. Figure 10.15 shows a CV of Au-RGO/PBNPs paper (RGO and PEI mixed directly in the following part), controlled at the same conditions as PEI reduction of RGO. Compared with Figure 10.12, Au-RGO/PBNPs paper electrodes show clearer and larger peaks than PEI reduced RGO, and the rate constant is much bigger (32 s^{-1}) compared with 8.6 s^{-1}, which demonstrates that the electron transfer is faster for directly electrocatalysis.

Electrochemical impedance spectroscopy (EIS) was carried out to probe the impedance changes of Au-RGO/PBNPs paper. Especially the real part (Z') changed with different potentials under the fixed frequency. As a familiar active material in EIS, PBNPs in Au-RGO/PEI/PBNPs hybrid paper could be directly used as a probe for impedance instead of adding $K_3[Fe(CN)_6]$ and $K_4[Fe(CN)_6]$ in the electrolyte. In addition, Z' vs potential in the EIS was recorded by changing the potential from 0.6V to -0.4V and -0.4V to 0.6V at a fixed frequency of 1 Hz without probe solution shown in Figure 10.16A and B, which indirectly monitored the conductivity changes at different potentials.

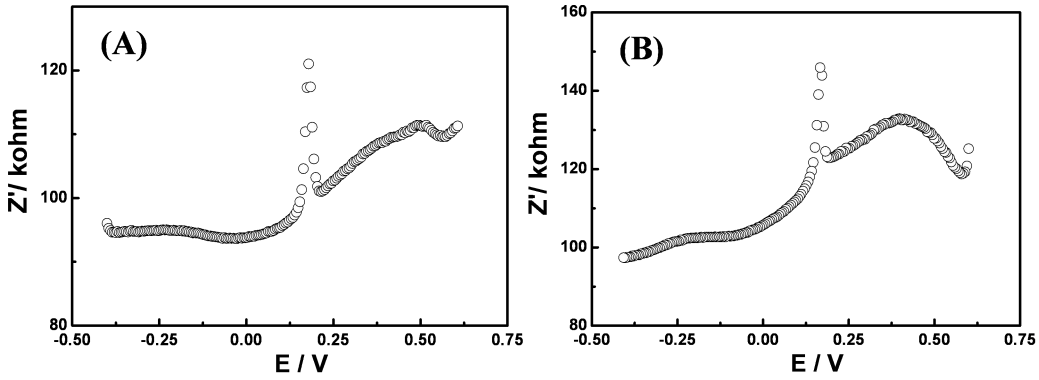

Figure 10.16. Electrochemical impedance spectra (EIS) of Au-RGO-PB (RGO and PB mixed directly) graphene papers. Comparison of the potential-dependent impedance spectra at a fixed frequency 1 Hz of (A) from -0.4 to 0.6V and (B) from 0.6 to -0.4V.

As a result, both the real part resistance of the Au-RGO/PBNPs paper decreased with lowering the electrode potential. Surprisingly, a sharp peak of high resistance appeared at around 0.2 V, close to PBNPs formal redox potential. This indicates that the active PBNPs material at the formal redox potential decreases the conductivity of Au-RGO/PBNPs paper. This phenomenon is opposite to the EIS of RGO/PBNPs paper (Chapter 9), because the Au film in Au-RGO/PBNPs paper provides an exactly high conductivity substrate for the mixture paper out of the areas of active formal potential of PBNPs. When the potential arrives at the active formal redox potential of the PBNPs, the conductivity of PBNPs becomes bigger than before, but lower than the conductivity of gold, so the overall conductivity of the Au-RGO/PBNPs paper decreases. This phenomenon might provide a new relationship to explore the active materials between conductivity and formal redox potential using Au-RGO/PBNPs paper and RGO/PBNPs paper.

10.7 Electrocatalysis of Au-RGO/PEI/PBNPs/GOD (PEI and RGO Mixed Directly)

To evaluate the electrocatalytic activity and electrochemical sensor or biosensor properties of Au-RGO/PEI/PBNPs/GOD hybrid paper (properties of PB with fast electron transport, large active surface areas, and excellent electrocatalytic activity), H_2O_2 and glucose were of considerable interest chosen as analyses, which are common used in the daily life.

Figure 10.17A shows a significant electrocatalytic effect in 10 mM H_2O_2 reduction in the Au-RGO/PBNPs paper compared with the absence of H_2O_2 added to the solution (CVs, scan rate 0.02V/s). There appears clearly a catalytic effect in the reduction of H_2O_2. After mixing PEI in the Au-RGO/PBNPs paper to form Au-RGO/PEI/PBNPs paper, there is no difference from electrocatalysis of H_2O_2 reduction (Figure 10.17B), so PEI does not influence the electrochemical and electrocatalysis process, but PEI plays an important role in the fabrication of the GOD described based on electrostatic interaction for electrocatalytic glucose oxidation. As a result, the Au-

RGO/PEI/PBNPs/GOD paper has good performance for glucose oxidation catalysis (Figure 10.17C).

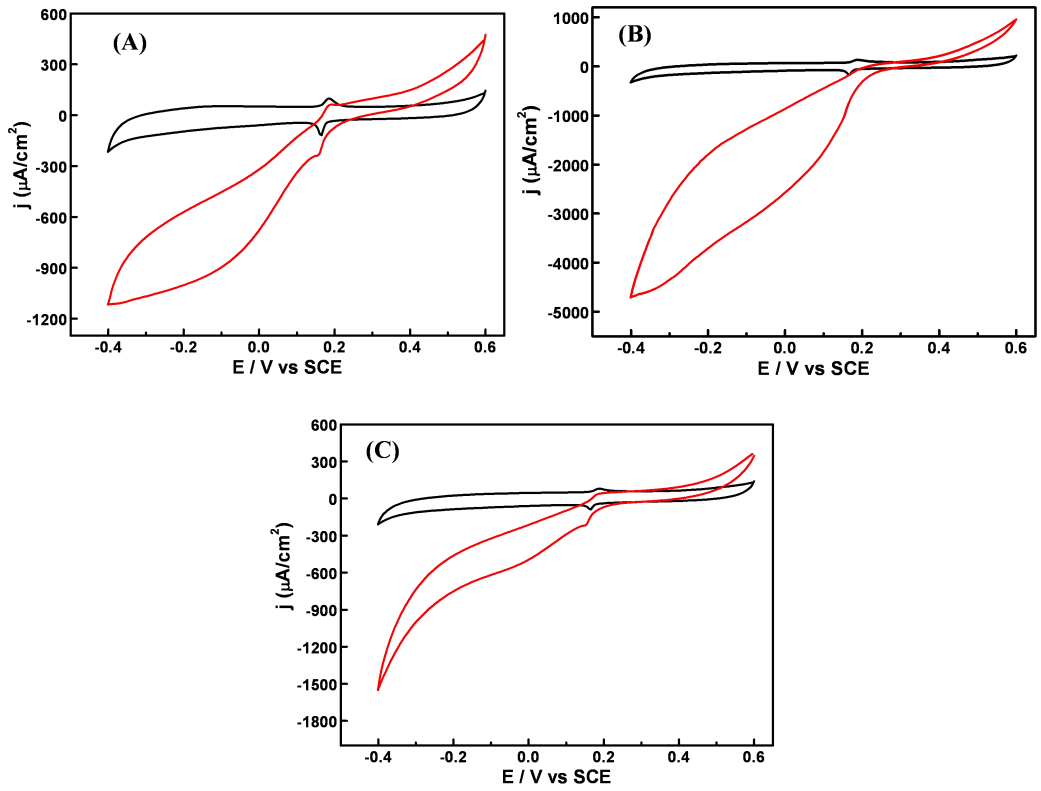

Figure 10.17. Electrocatalysis and biocatalysis of H_2O_2 reduction and glucose oxidation. (A) CVs of Au-RGO-PBNPs paper electrodes in the absence (black curve) and presence (red curve) of 10 m M H_2O_2; (B) CVs of Au-RGO-PEI-PBNPs (RGO and PEI mix directly) paper electrodes in the absence (black curve) and presence (red curve) of 10 m M H_2O_2; (C) Comparison of electrocatalytic response for Au-RGO/PB/PEI/GOD (RGO and PEI mix together) to in the absence (black curve) and presence (red curve) 10 mM glucose. Electrolyte: 0.1 M phosphate buffer (pH 6.0) containing 0.1 M KCl. Scan rate: 20 mV s^{-1} used for all CVs.

10.8 In Conclusions

We have demonstrated a new way of fabricating flexible Au-RGO/PEI/PBNPs/GOD hybrid paper by flow-directed vacuum assembly for application to sensors and biosensors. This type of flexible RGO-PBNPs paper is not only used as an electrode

directly in the electrochemical system, but also enhances significantly the poor conductivity of PB to explore the electrocatalysis properties. Meanwhile, different sizes and shapes of RGO/PBNPs paper could be acquired by choosing different casting molds as expected. This variety of flexible active electrode could be freely used for H_2O_2, glucose or other enzyme detection in the electrocatalysis. Such a large enhancement of electrical and mechanical properties by structurally integrating inorganic nanoparticles into graphene paper of the flexible electrodes will supply a novel way for broad application in biosensors and sensors.

10.9 References

[1] X. Zhou, Z. Chen, D. Yan and H. Lu, *J. Mater. Chem.*, **2012**, *22*, 13506-13516.

[2] Y. Zhang, B. A. Chen, L. M. Zhang, J. Huang, F. H. Chen, Z. P. Yang, J. L. Yao and Z. J. Zhang, *Nanoscale*, **2011**, *3*, 1446.

[3] J. H. Dai and M. L. Bruening, *Nano Lett.*, **2002**, *2*, 497.

[4] H. Kim, R. Namgung, K. Singha, I. K. Oh and W. J. Kim, *Bioconjugate Chem.*, **2011**, *22*, 2558.

[5] H. L. Guo, X. F. Wang, Q. Y. Qian, F. B. Wang and X. H. Xia, *ACS Nano*, **2009**, *3*, 2653.

[6] E. Jin, X. F. Lu, L. L. Cui, D. M. Chao and C. Wang, *Electrochim. Acta*, **2010**, *55*, 7230.

[7] C. Wang, L. Zhang, Z. H. Guo, J. G. Xu, H. Y. Wang, H. W. Shi, K. F. Zhai and X. Zhuo, *Electroanal.*, **2010**, *22*, 1867.

[8] F. Ricci and G. Palleschi, *Biosens. Bioelectron.*, **2005**, *21*, 389.

11. Graphene Nanofilms Doped with Quantum Dots for Efficient Promotion of Photoinduced Charge Separation and Electron Transfer

Due to unique opto-electronic properties determined by quantum confinement effects, semiconductor nanocrystal quantum dots (QDs) make them a promising alternative for investigations in wide research fields of nanoscience and nanotechnology, diagnostics and energy conversion, spanning analytical sciences and materials science in the past years.[1-6]

Short-band-gap semiconductor CdSe quantum dots with tunable band edge provide new opportunities to harvest energy from light in the visible region of solar light.[7-11] Electron transfer of CdSe QDs sensitized ZnO system has been discussed in the my host group at University of Lund,[12] who also introduced ultrafast time-resolved absorption and Terahertz spectroscopy.[13] For the CdSe QDs-ZnO system, electron Injection versus Auger Recombination has been studied by ultrafast dynamics.[14] Different sizes of QDs with varying the band energies modulate the vectorial charge transfer owing to size quantization effect.[11]

Advances in photovoltaics of graphene and semiconductor nanocomposites, has recently become promising candidates for energy conversion application and drawn significant attention in the area of photocatalysis.[12-14] The mixture of graphene and QDs have paved a new way for photo-driven of energy conversion.[14-17] Searching for a large area graphene nanosheets together with QDs to apply in the field of photovoltaics, therefore, holds a new promise for use widely in photocatalysts and electron transfer.

11.1 Fast Growth of Large-area Graphene Nanofilms Facilitated by the Oil/Water Interface Method

The possibility to obtain graphene nanosheets with large areas, has drawn more and more attention in the transportation and collection of photo-driven charge carriers in photovoltaic devices, along with lateral electrical conductivity.[14,15] This type of large area graphene nanosheets could also offer a big substrate for QDs loading on the surface important for the electron transfer or photoinduced charge separation process.

There are several methods for preparing large-scale graphene nanomaterials, and the wet chemical methods such as the layer-by-layer technique,[20] interfacial self-assembly,[22] vacuum filtration,[19] spin-coating,[18] and Langmuir-Blodgett (LB) technique,[21] have shown much more advantage than others for large area graphene nanosheets. The interfacial self-assembly strategies, including liquid/liquid and liquid/air, provide a special way to obtain large-area nanosheets. Among the interfacial self-assembly approaches, the oil/water (O/W) self-assembled interfaces could support a simple and convenient condition to adjust the thickness and properties of graphene nanosheets by controlling the concentration and reaction conditions.[23]

In this study, graphene nanosheets were prepared by reducing GO at O/W interfaces, with resulting RGO self-assembled as large-area nanosheets for further application. Additionally, the graphene nanosheets tend to form at the O/W interfaces, which are easily transferred to other setups of combining nanomaterials through the properties of optical transmittance, electrical conductivity, and highly reversible light-induced electrical switching.

The O/W interface fabrication for graphene nanosheets has already been reported by former colleagues in our group,[23] which is now a established technique in the group. We therefore choose the O/W interface wet chemical method to obtain large-area graphene nanosheets-based QDs for efficient promotion of photoinduced charge

separation and electron transfer.

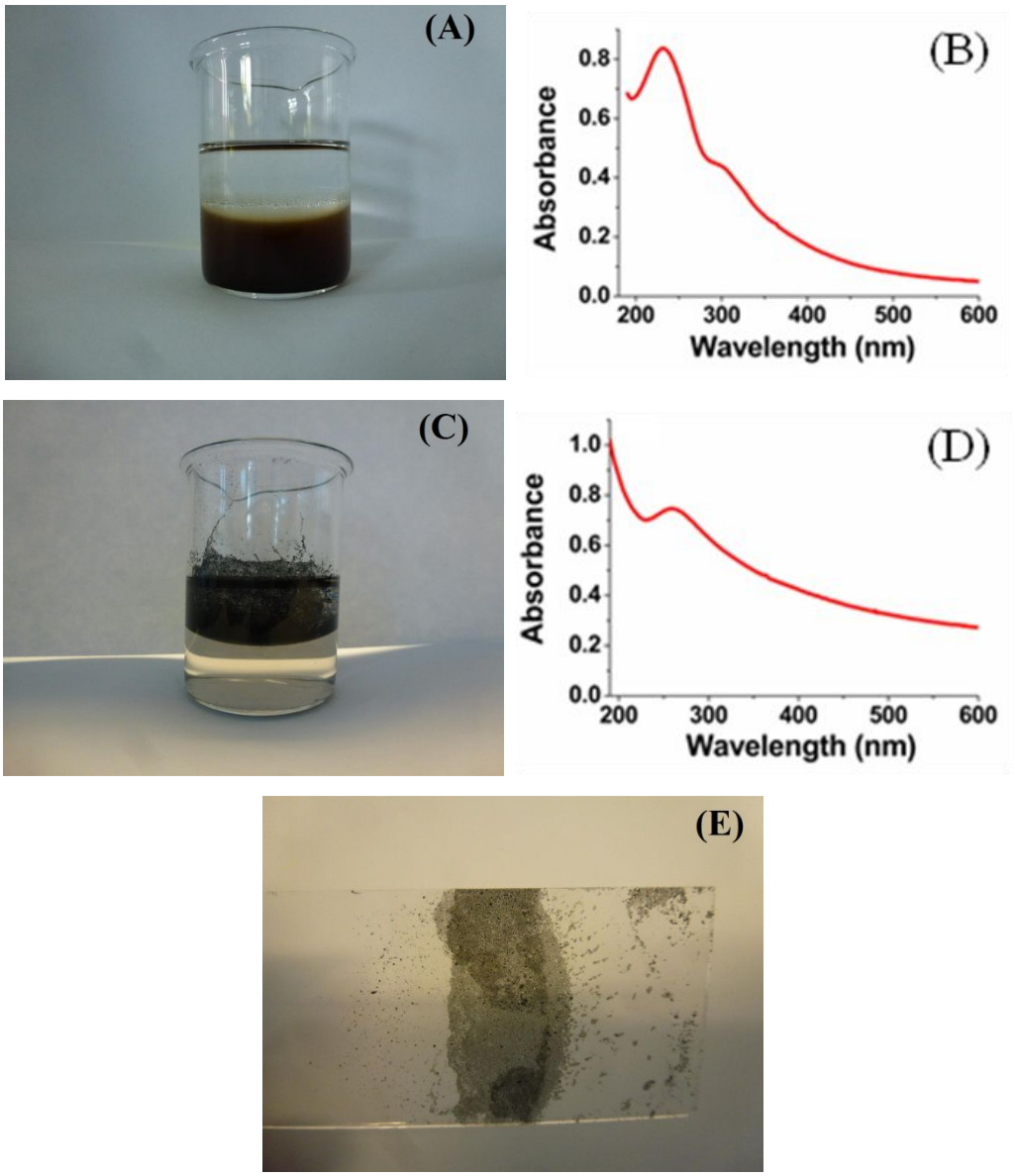

Figure 11.1. The O/W interfaces fabrication process from GO to RGO. (A) Before reaction, the bottom layer is GO in water and top layer is toluene. (B) UV-Vis spectra of GO before reaction shows two clear peaks of 231 and 310 nm. (C) After reaction, the bottom layer is water without GO, the top layer is toluene, and RGO is at the interfaces of O/W or toluene/glass. (D) UV-Vis spectra of RGO after reaction, with a clear peak of 268 nm. (E) The as-prepared graphene nanosheets were transferred onto a special substrate of quartz.

In the synthesis of graphene by the O/W interfaces method, GO water solution is automatically being the water phase, and most organic solvents such as N-methyl-2-pyrrolidone (NMP), cyclohexane, n-hexane and toluene could act as oil phase.[23] Due to our QDs in the toluene organic solvent, we choose toluene as our oil phase for the O/W interfaces fabrication.

The reaction process of O/W interfaces fabrication is shown in Figure 11.1. The high-quality GO samples were first prepared as the same way as in Chapter 9, with an average size of 1 ca. μm, and two typical absorption bands at 233 and 310 nm (Figure 11.1B). Mixing GO and toluene solution together in volume ratio of 1:1, and then separating two parts in the beaker (Figure 11.1A), left toluene in the top layer owing to the light molecule weight. After one step chemical reaction by hydrazine at 95 °C, the graphene nanosheets were spontaneously self-assembled in the interfaces between water and toluene or between toluene and glass wall. No RGO was left in the water phase as this phase is obviously transparent (Figure 11.1C). The free-standing graphene nanosheets were growth reversibly, even stable after shaking.[23] The absorption band at 268 nm (Figure 11.1D) suggests that all the GO has converted into RGO.

The as-prepared graphene nanosheets could be transferred onto a special substrate such as glass or quartz (Figure 11.1E) for the device or further application. Pre-inserting a quartz substrate into the beaker and decasting the reaction solution immediately, then leading to the spontaneous and fast growth of RGO nanosheets.

11.2 Preparation of CdSe QDs and Stability of QDs by the Oil/Water Interface Method

The oleic acid (OA) protected CdSe QDs were synthesized followed the host group's literature,[13,24] where different sizes of CdSe QDs (2.4 nm, 2.7 nm, 2.9 nm, 3.1 nm) were available, corresponding to the absorption bands at 505, 526, 542, 551 nm. All the measurements of CdSe QDs in the following were taken with 2.9 nm as examples.

The OA-capped CdSe QDs were dissolved in toluene solution, which could be used directly as oil phase together with GO in the water phase. These two phases were prepared for synthesizing large-area graphene-QDs nanosheets by the O/W interface method.

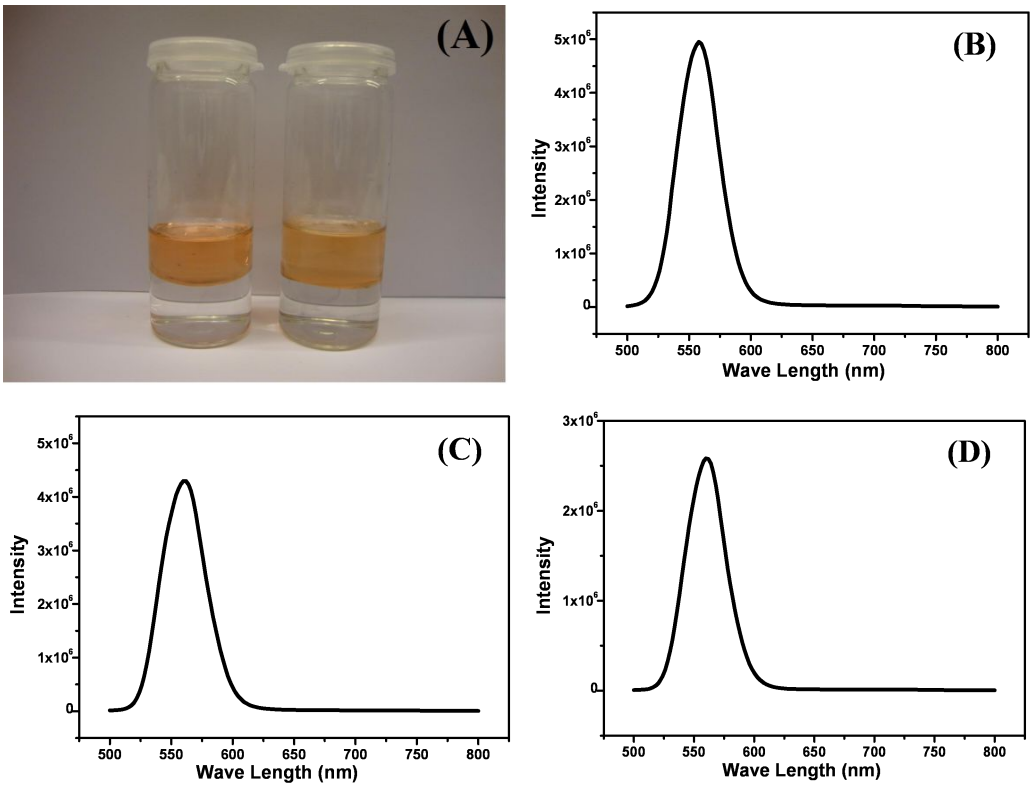

Figure 11.2. Images and fluorescence spectra of only 2.9 nm QDs in organic solution mixed with water before and after reaction. (A) Before and after O/W reaction only QDs. Top layer is QDs in toluene and bottom layer is water. (B) Fluorescence spectra of only QDs before reaction. (C) Fluorescence spectra of only QDs after reaction without hydrazine. (D) Fluorescence spectra of only QDs after reaction with hydrazine.

In order to make sure that CdSe QDs were still stable and active as QDs when reacted with hydrazine at 95°C controlling the same reduction environment for GO to RGO, photographs and fluorescence spectra of only QDs in organic solution mixed with water before and after reaction are shown in Figure 11.2. Taking 2.9 nm CdSe QDs as

an example, which appears light yellow (the color depends on the concentration) (Figure 11.2A, left), and the same color remains after reaction with hydrazine at 95°C for half a hour (Figure 11.2A, right). Furthermore, the fluorescence spectra before and after reaction gave evidence that CdSe QDs kept the peak at 557 nm without any change (Figure 11.2B and C). When treated with hydrazine in the process, there appears no big different from fluorescence spectra (Figure 11.2D).

11.3 Graphene Nanosheets Doped with CdSe QDs by the Oil/Water Interface Method

After preparing both CdSe QDs in toluene and GO in water, we mixed them together (Figure 11.3 A (left)). Before reaction, the orange color is CdSe QDs in the top layer, and dark yellow color is GO located in the bottom layer. The typical adsorption band of CdSe QDs at 542 nm from UV-Vis and the intensity of 1.1 a.u. is shown in Figure 11.3B. After reaction with hydrazine at 95°C for half a hour, the water phase became clear and colorless, while QD phase changed to dark color forming RGO doped with CdSe QDs (Figure 11.3 A (Right)). When carefully examined the QDs phase showed that most of the RGO-QDs layer standed at the interface between toluene and water, and some of them located on the glass wall as planned. The adsorption peak intensity at 542 nm of QDs from the toluene phase with only 0.2 a.u. (Figure 11.3C) was showing that only 18% CdSe QDs is left in the toluene phase. Both photographs and spectroscopy demonstrated that CdSe QDs were doped on the surface of the graphene nanosheets, due to hydrophobic interactions between graphene and CdSe QDs. After transferring RGO-QDs onto the quartz surface (Figure 11.3 D), it is dark brown as graphene color (the color of QDs is very weak compared with graphene), and there was no adsorption peak of UV-Vis at 542 nm (Figure 11.3E) and no fluorescence at 560 nm due to the quench effect of graphene for CdSe QDs.

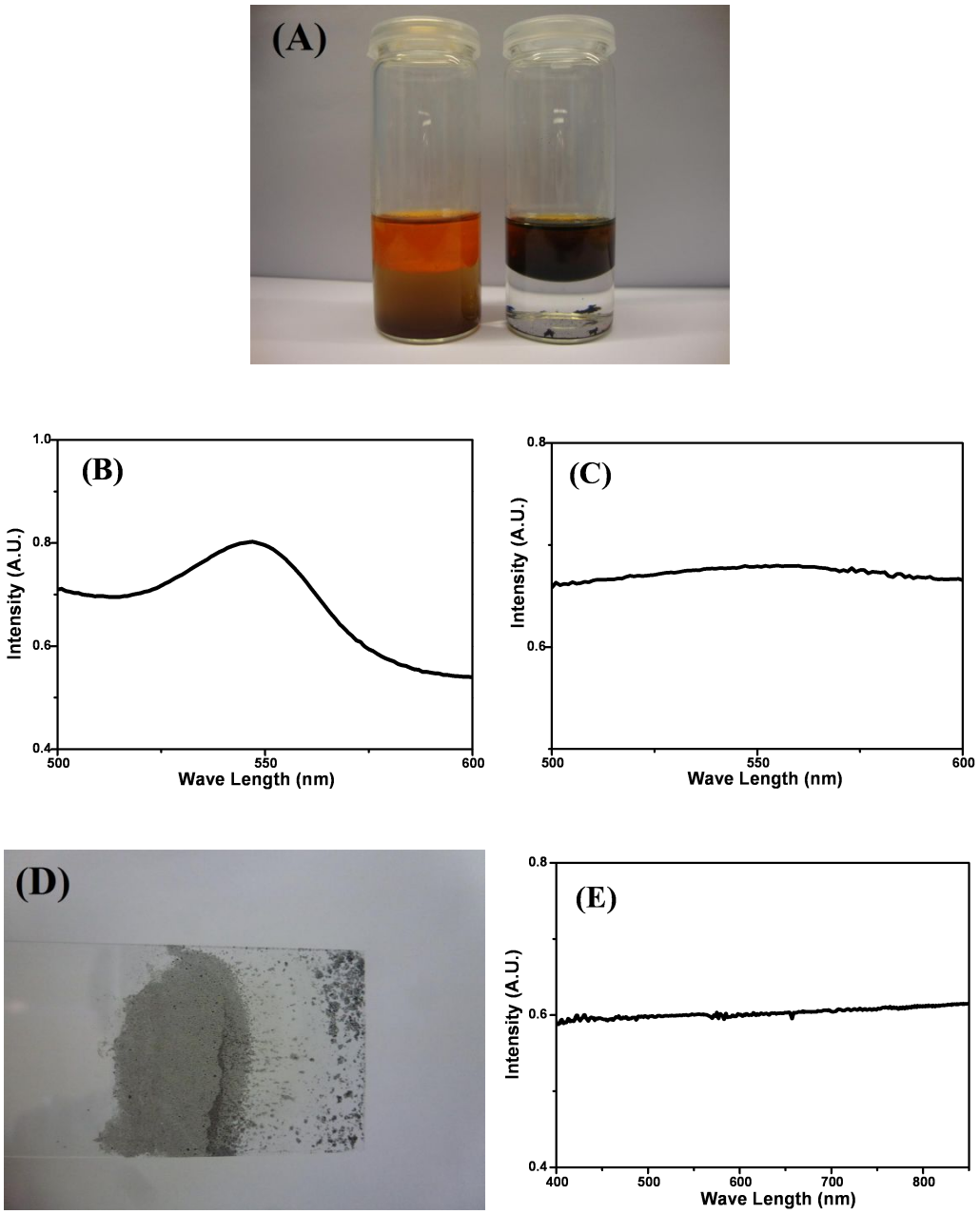

Figure 11.3. Preparation and UV-Vis spectra of both 2.9 nm CdSe QDs in toluene and GO in water using the O/W interface method. (A) Photographs of QDs and GO before and after O/W reaction. (Left) Top layer is QDs in toluene and bottom layer is GO in water. (Right) After reaction with most RGO-QDs in the interface between toluene and water. (B) UV-Vis spectra of original QDs. (C) UV-Vis spectra of QDs in toluene after reaction. (D) The as-prepared RGO-QDs were transferred onto a quartz substrate. (E) UV-Vis spectra of RGO-QDs on the quartz from the interface of O/W after reaction.

11.4 Characterization of RGO-QDs

Microscopic images of high-resolution AFM and TEM of RGO-QDs are shown in Figure 11.4 to Figure 11.8. From the AFM image of RGO obtained by O/W interface technique in Figure 11.4, large-area graphene nanosheets in the 1.5 μm × 1.5 μm, with the height around 1 nm are seen. At the same time, AFM of only CdSe QDs are measured in Figure 11.5, along with the height of 3 nm. When graphene nanosheets doped with CdSe QDs, most of the QDs tend to adsorb on the surface of graphene, seldom in the free solution (Figure 11.6).

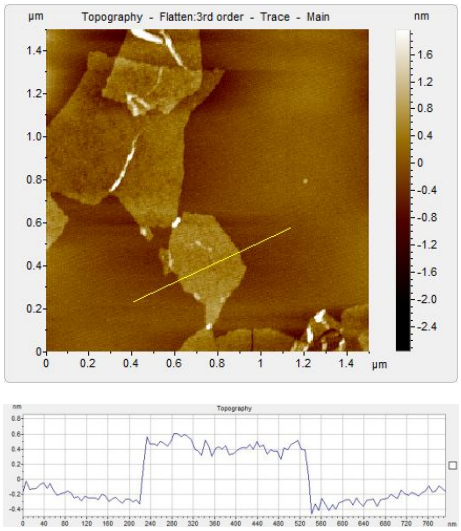

Figure 11.4. High-resolution AFM of only RGO from O/W reaction on mica and the height of RGO.

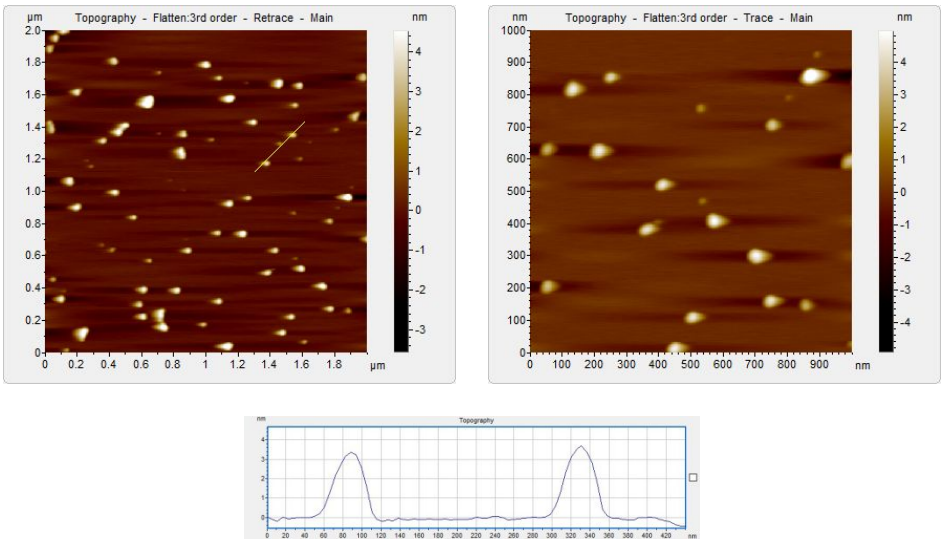

Figure 11.5. High-resolution AFM of only QDs from O/W reaction on mica and the height of QDs.

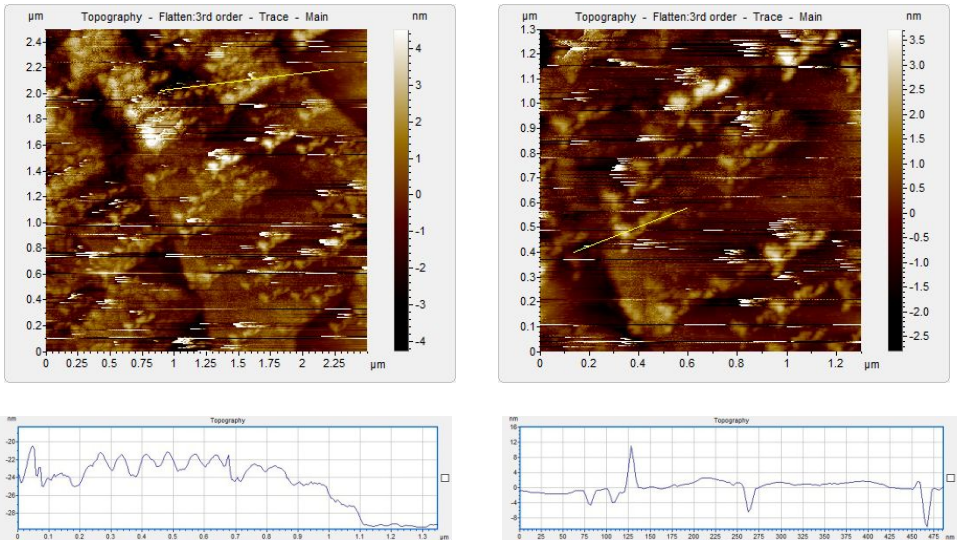

Figure 11.6. High-resolution AFM of RGO-QDs from O/W reaction on mica and height of RGO-QDs after O/W reaction from AFM images.

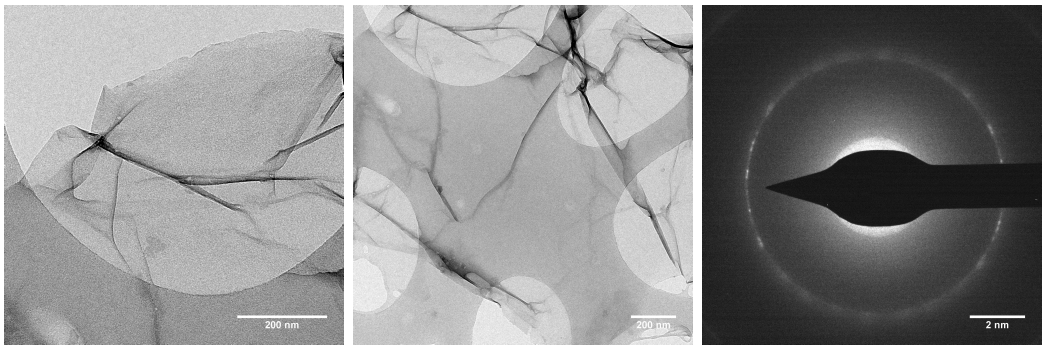

(A) **(B)** **(C)**

Figure 11.7. High-resolution TEM images of only RGO from O/W reaction. (A) and (B) TEM of only RGO. (C) Crystal structure of RGO.

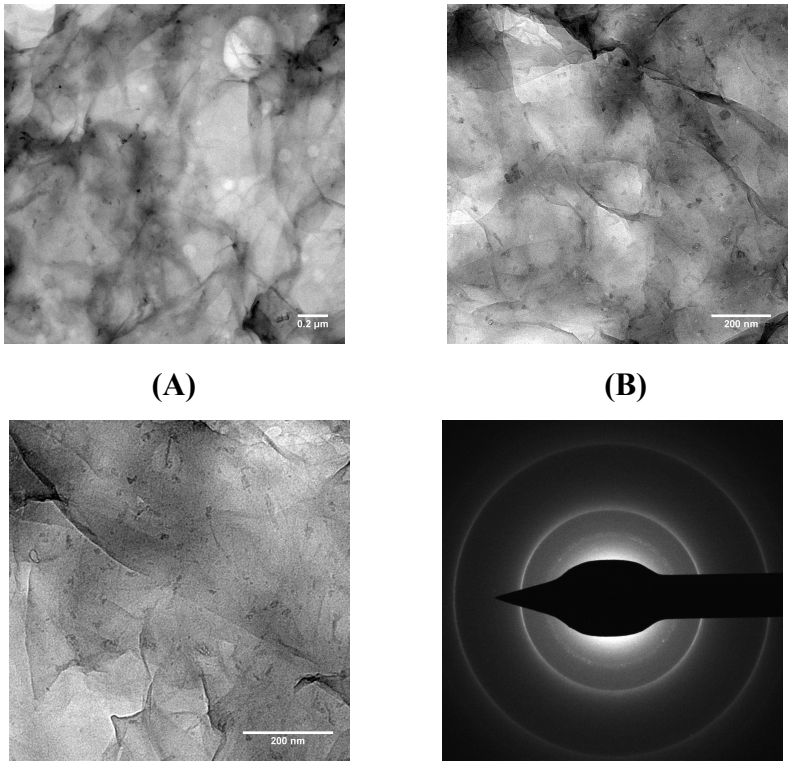

(A) **(B)**

(C) **(D)**

Figure 11.8. High-resolution TEM images of RGO-QDs from O/W reaction. (A), (B) and (C) TEM of RGO-QDs from O/W reaction. (D) Crystal structure of RGO-QDs.

There is either one or several layers in the only RGO nanosheet sample in TEM (Figure 11.7), and with high-resolution TEM for the crystal structure of RGO was (002).[25] The graphene nanosheets were random, and some parts with wrinkles or overlaps, which provide a good platform for loading nanoparticles or nanomaterials.

After mixing RGO and CdSe QDs together in O/W, there appear distinctly numerous QDs on the graphene nanosheet surface, especially in the wrinkle or overlapping areas (Figure 11.8). And the crystal structure of (111), (220), and (311) respectively, were expected in the high-resolution TEM.[26] (Figure 11.8D)

11.5 Structure and Transient Absorption Analysis of RGO-QDs

The crystal structure of CdSe QDs, RGO and RGO-QDs was studied by XRD, Figure 11.9. The wide peak of black line indicates to (002) of O/W treated RGO in XRD.[25] The red and blue lines stand for pure CdSe QDs and O/W treated CdSe QDs. The peaks at 2θ around 26.0, 42.0, and 49.0, correspond to the crystal of (111), (220) and (311) respectively.[26] After reaction by the O/W interface method obtained RGO-QDs (green line), the peaks of CdSe and RGO remain the same, which demonstrates that there is no mutual influence between RGO and CdSe QDs, in addition, no new crystal structure was either formed from this process.

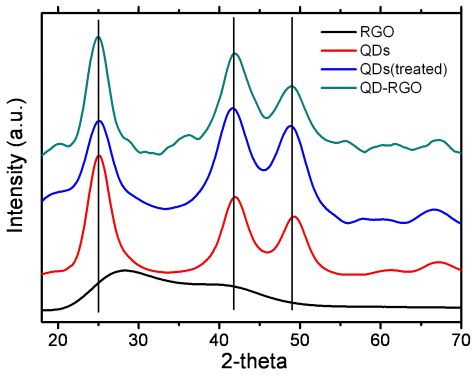

Figure 11.9. XRD crystal structure of CdSe QDs, RGO and RGO-QDs. (Black) XRD of only RGO; (Red) XRD of only QDs; (Blue) XRD of only QDs treated by O/W system; (Green) XRD of RGO-QDs after O/W two phase system.

Another region spectra method used for structure analysizing was EXAFS (Extended X-ray Absorption Fine Structure) of the RGO-CdSe QDs samples. EXAFS is the oscillating part of the spectrum for the absorption edge from 50 eV, and extending to about 1000 eV above the edge.[27-31] The local structural information for the atoms could be achieved by mathematical analysis for this region. Compared to other structural approaches, EXAFS provides the atom's local environment for widespread application, especially for quantitative analysis of noncrystalline materials. The single-atom properties such as coordination number, distance of neighboring atoms and disorder of neighboring atoms, are analyzed within one material. Experimentally EXAFS supports more accurate structure for systems of amorphous crystalline solids, also including low thermal or static disorder.[27-31]

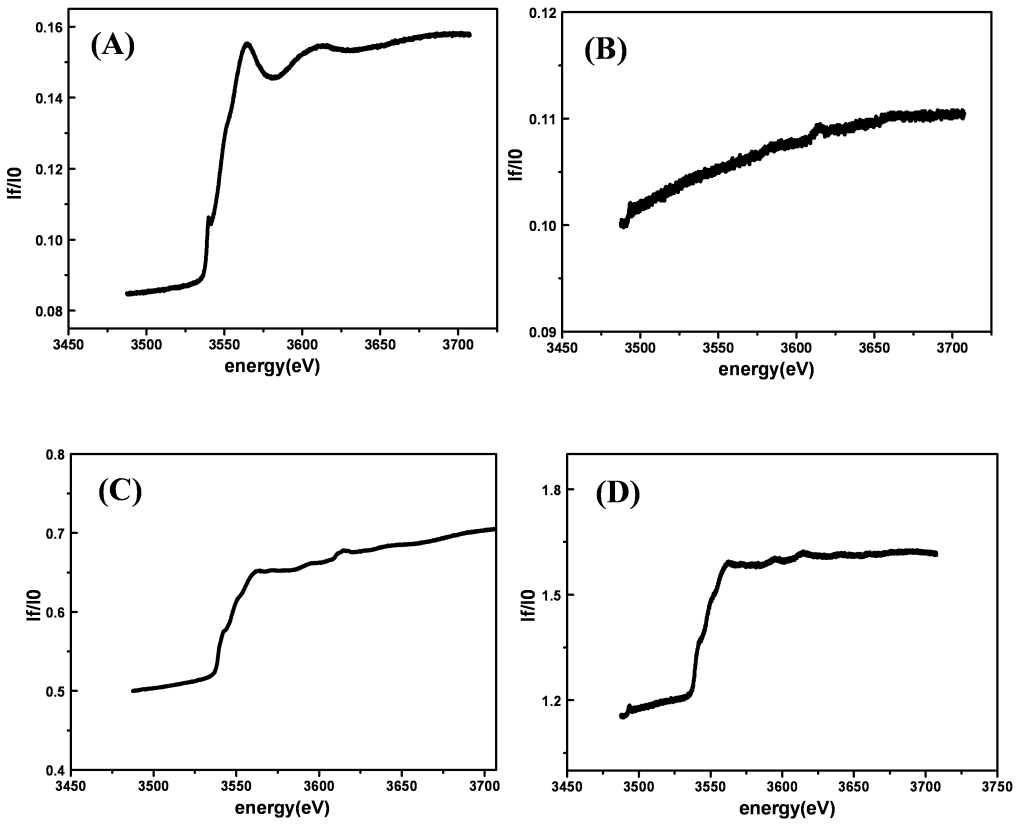

Figure 11.10. The element Cd of EXAFS for CdSe QDs, RGO and RGO-QDs measured by synchrotron beam radiation. (A) Cd of EXAFS for the RGO-QDs from the O/W method. (B) Cd of EXAFS of only RGO. (C) Cd of EXAFS for only CdSe QDs. (D) Cd of EXAFS for toluene layer of RGO-QDs O/W two phase method.

The element Cd of EXAFS for all the O/W prepared samples were measured by synchrotron beam (Figure 11.10). There is no EXAFS signal for only RGO nanosheets due to the structure of graphene (Figure 11.10B). Some fine-structure appears for detecting pure CdSe QDs (Figure 11.10C), which kept the same after reacting in the O/W interface method (Figure 11.10D). However, big changes of the fine structure of RGO-CdSe QDs sample were found around 3555 eV and 3615 eV, which gives a confirmation for the fine-structure difference after CdSe QDs doping onto the surface of the graphene nanosheets. The detailed explanation are unknown till recently, but the mechanism will be supported by future techniques.

Time-resolved transient absorption spectroscopy (pump-probe) of three systems were measured to compare the electron or energy transfer process during the fabrication of RGO-CdSe QDs. In the only RGO sample, there is nearly no drop during the delay time (Figure 11.11 (Left)). The reason is that photoexcited graphene undergoes ultrafast relaxation to lower excited states, with optical phonon lifetime barely exceeding 1 ps.[13, 32]

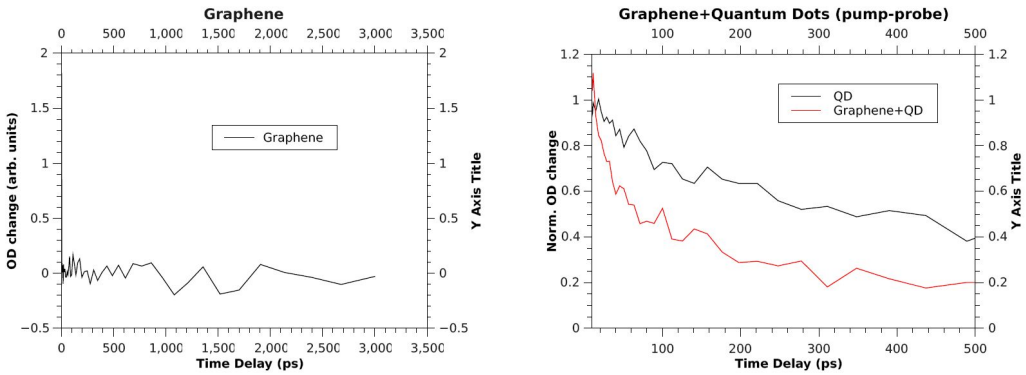

Figure 11.11.Time-resolved transient absorption spectroscopy (pump-probe) of RGO, CdSe QDs and RGO-QDs. (Left image) Time-resolved transient absorption spectroscopy (pump-probe) for only RGO sample; (Right image) Time-resolved transient absorption spectroscopy (pump-probe) for QDs (black) and RGO-QDs (Red).

A wide drop in signal can be resolved from the pure CdSe QDs, which gives the same delay time as reported (Figure 11.11 (Right) Black line).[12] Interestingly, in the RGO-CdSe QDs system, there is an initial minor drop in signal during the first ca. 20 ps (Figure 11.11 (Right) Red line). The different transient absorption among these systems can be the result of electron or energy transfer between RGO and CdSe QDs. The real principle of this process, whether it is electron transfer for QDs, or energy transfer between the two nanomaterials, is still being explored.

To support the explanation regarding interaction between RGO and CdSe QDs, other techniques are needed to judge electron or energy transfer during this process. Spectral techniques such as, THZ spectroscopy, Coherent anti-Stokes Raman spectroscopy (CARS) and ultraviolet electron spectroscopy (UPS), will be analyzed to explore RGO-CdSe QDs system in the next step.

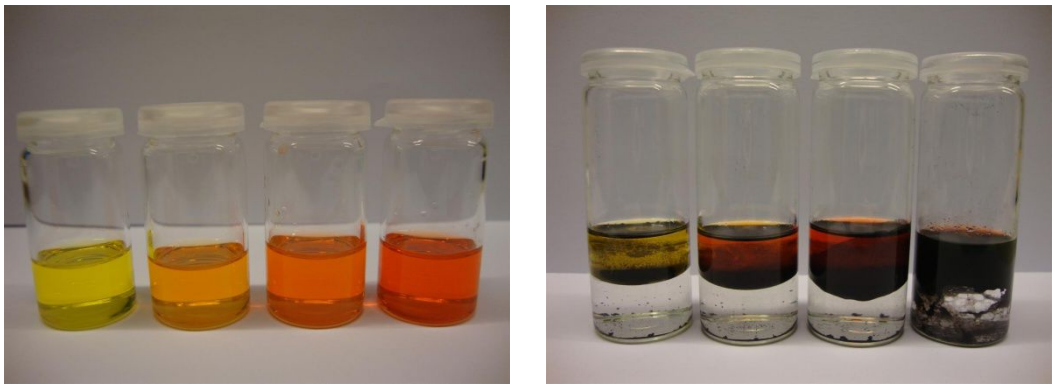

(A) **(B)**

Figure 11.12. Different sizes of RGO-QDs prepared by the O/W two phase interface method. (A) Different sizes of CdSe QDs in toluene and after reaction (B) Different sizes of CdSe QDs after reaction by the O/W two phase interface method. The sizes of CdSe QDs in the photographs from left to right were 2.4nm, 2.7nm, 2.9nm, 3.1nm with the absorption peaks of 505 nm, 526 nm, 541 nm, 551 nm, separately.

In addition, other sizes of CdSe QDs were synthesized for RGO-CdSe QDs system to

discuss size-dependent effects of efficient promotion of photoinduced charge separation and electron transfer (Figure 11.12A). Four sizes of 2.4 nm, 2.7 nm, 2.9 nm and 3.1 nm were obtained, corresponding to the absorption bands at 505, 526, 542 and 551 nm with different colors. Figure 11.12B shows RGO-CdSe QDs samples after O/W interface method. Different linker protected CdSe QDs instead of oleic acid (OA) is also a perspective for RGO-CdSe QDs system.

11.6 Conclusion and Perspectives

We have developed a new method of O/W interfaces technique for fabricating fast one-step large-area graphene nanosheets doped with CdSe QDs on the surface. The mixture of graphene and QDs pave a new way for photo-driven energy conversion.

This kind of mixed nanomaterials of RGO-CdSe QDs shows close interaction between RGO and CdSe QDs, and obtaining a new fine-structure from EXAFS. Furthermore, incorporation of QDs into graphene nanosheets for significant enhancement of photoinduced charge transportation from electron or energy transfer is discussed based on time-resolved transient absorption spectroscopy and other techniques. Although the principle of delay time changes is not clear now, it will hopefully be supported by other data from THZ spectroscopy, CARS or Ups methods. Therefore, fast one-step large-area graphene nanosheets doped with CdSe QDs will be widely used in the field of photovoltaics for photocatalysts and electron or energy transfer.

11.7 References

[1] (a) M. G. Bawendi, M. L. Steigerwald and L. E. Brus, *Annu. Rev. Phys. Chem.*, **1990**, *41*, 477; (b) A. P. Alivisatos, *Science*, **1996**, *271*, 933; (c) A. L. Efros and M. Rosen, *Annu. Rev. Mater. Sci.*, **2000**, *30*, 475; (d) A. D. Yoffe, *Adv. Phys.*, **2001**, *50*, 1.
[2] (a) C. Burda, X. Chen, R. Narayanan and M. A. El-Sayed, *Chem. Rev.*, **2005**, *105*, 1025; (b) A. M. Smith and S. Nie, *Acc. Chem. Res.*, **2010**, *43*, 190.

[3] A. L. Rogach, *Semiconductor Nanocrystal Quantum Dots*, ed., Springer, Wien, Austria, **2008**.

[4] X. Michalet, F. F. Pinaud, L. A. Bentolila, J. M. Tsay, S. Doose, J. J. Li, G. Sundaresan, A. M. Wu, S. S. Gambhir and S. Weiss, *Science*, **2005**, *307*, 538.

[5] U. Resch-Genger, M. Grabolle, S. Cavaliere-Jaricot, R. Nitschke and T. Nann, *Nat. Methods*, **2008**, *5*, 763.

[6] M. Amelia, C. Lincheneau, S. Silvi and A. Credi, *Chem. Soc. Rev.*, **2012**, *41*, 5728–5743

[7] G. I. Hodes, *J. Chem.*, **1993**, *33*, 95.

[8] G. Sasha and H. Gary, *J. Phys. Chem.*, **1994**, *98*, 5338.

[9] A. J. Nozik, *Physica E-Low-Dimensional Systems & Nanostructures*, **2002**, *14*, 115.

[10] Z. L. Wang, *J. Phys. Chem*. **2000**, *104*, 1153.

[11] A. Kongkanand, K. Tvrdy, K. Takechi, M. Kuno, and P. V. Kamat, *J. Am. Chem. Soc*. **2008**, *130*, 4007-4015

[12] K. Žídek, K. Zheng, C. S. Ponseca, M. E. Messing, L. R. Wallenberg, P. Chábera, M.Abdellah, V. Sundström and T. Pullerits, *J. Am. Chem. Soc.* **2012**, *134*, 12110−12117.

[13] K. Zheng, K. Žídek, M. Abdellah, M. Torbjörnsson, P. Chábera, S. Shao, F. Zhang and T. Pullerits, *J. Phys. Chem. A*, **2013**, *117*, 5919−5925.

[14] K. Žídek, K. Zheng, M. Abdellah, N. Lenngren, P. Chábera, and T. Pullerits, *Nano Lett.*, **2012**, *12*, 6393−6399.

[12] W. Tu, Y. Zhou, and Z. Zou, *Adv. Funct. Mater.*, **2013**, DOI: 10.1002/adfm.201203547

[13] S. Guo et al, *Adv. Funct. Mater*., **2013**, DOI: 10.1002/adfm.201203652

[14] a) I. V. Lightcap and P. V. Kamat, *J. Am. Chem. Soc.*, **2012**, *134*, 7109; b) Q. Li, B. Guo, J. Yu, J. Ran, B. Zhang, H. Yan and J. R. Gong, *J. Am. Chem. Soc.* **2011**, *133*, 10878; c) P. K. Santra and P. V. Kamat, *J. Am. Chem. Soc.,* **2012**, *134*, 2508; d) T. Dufaux, J. Boettcher, M. Burghard and K. Kern, *Small* **2010**, *6*, 1868; e) C. X. Guo, H. B. Yang, Z. M. Sheng, Z. S. Lu, Q. L. Song and C. M. Li, *Angew. Chem. Int. Ed.*, **2010**, *49*, 3014.

[15] a) H. Bi, F. Q. Huang, J. Liang, X. M. Xie, M. H. Jiang, *Adv. Mater.*, **2011**, *23*, 3202; b) C. L. Hsu, C. T. Lin, J. H. Huang, C. W. Chu, K. H. Wei, L. J. Li, *ACS Nano*, **2012**, *6*, 5031; c) X. Geng, L. Niu, Z. Xing, R. Song, G. Liu, M. Sun, G. Cheng, H. Zhong, Z. Liu, Z. Zhang, L. Sun, H. Xu, L. Lu and L. Liu, *Adv. Mater.*, **2010**, *22*, 638; d) G. Eda, M. Chhowalla, *Adv. Mater.*, **2010**, *22*, 2392 .

[16] a) A. Gray, M. Balooch, S. Allegret, S. De Gendt and W. E. Wang, *J. Appl. Phys.*, **2008**, *104*, 053109; b) I. Jung, M. Vaupel, M. Pelton, R. Piner, D. A. Dikin, S. Stankovich, J. An and R. S. Ruoff, *J. Phys. Chem. C*, **2008**, *112*, 8499; c) C. Lee, J. Y. Kim, S. Bae, K. S. Kim, B. H. Hong and E. J. Choi, *Appl. Phys. Lett*., **2011**, *98*, 07190 .

[17] a) B. Gao, G. Hartland, T. Fang, M. Kelly, D. Jena, H. Xing and L. Huang, *Nano Lett.*, **2011**, *11*, 3184; b) L. Huang, B. Gao, G. Hartland, M. Kelly and H. Xing, *Surf. Sci*., **2011**, *605*, 1657.

[18] H. Yamaguchi, G. Eda, C. Mattevi, H. Kim and M. Chhowalla, *ACS Nano*, **2010**, *4*, 524.

[19] G. Eda, G. Fanchini and M. Chhowalla, *Nat. Nanotechnol*., **2008**, *3*, 270.

[20] H. L. Li, S. P. Pang, S. Wu, X. L. Feng, K. Müllen and C. Bubeck, *J. Am. Chem. Soc.*, **2011**, *133*, 9423.

[21] X. Li, G. Zhang, X. Bai, X. Sun, X. Wang, E. Wang and H. Dai, *Nat. Nanotechnol.*, **2008**, *3*, 538.

[22] a) Y. Zhu, W. Cai, R. D. Piner, A. Velamakanni and R. S. Ruoff, *Appl. Phys. Lett.*, **2009**, *95*, 102; b) S. Biswas, L. T. Drzal, *Nano Lett*., **2009**, *9*, 167; c) F. M. Chen, S. B. Liu, J. M. Shen, L. Wei, A. D. Liu, M. B. Chan-Park and Y. Chen, *Langmuir*, **2011**, *27*, 9174.

[23] S. Gan, L. Zhong, T. Wu, D. Han, J. Zhang, J. Ulstrup, Q. Chi and L. Niu, *Adv. Mater.*, **2012**, *24*, 3958–3964.

[24] I. Mora-Seró, S. Giménez, T.Moehl, F.Fabregat-Santiago, T. Lana-Villareal, R.Gómez and J.Bisquert, *Nanotechnology*, **2008**, *19*, 424007.

[25] Z. Lu, M. Xu, S. Bao, K. Tan, H. Chai, C. Cai, C. Ji and Q. Zhang, *J. Mater. Sci.*, **2013**, *48*, 8101–8107.

[26] X. Chen, J. L. Hutchison, P. J. Dobson and G. Wakefield, *Journal of Materials*

Science, **2009**, *44*, 285–292.

[27] L. Que, *Physical Methods in Bioinorganic Chemistry. Sasuolito*, California: University Science Books, **2000**

[28] P. M. H. Kroneck, W. E. Antholine, D. H. W. Kastrau, G. Buse, G. C. M. Steffens and W. G. Zumft, *Eur. J. Biochem*., **1992**, *209*, 875-881.

[29] J. A. Farrar, P. Lappalainen, W. G. Zumft, M. Saraste and A. J.Thomson, *Eur. J. Biochem.*, **1996**, *232*, 294-303.

[30] J. J. Rehr and R.C. Albers, *Reviews of Modern Physics*, **2000**, *72*, 621-654.

[31] C.A. Ashley and S. Doniach, *Physical Review B.*, **1975**, *11*, 1279-1288.

[32] a) B. Gao, G. Hartland, T. Fang, M. Kelly, D. Jena, H. Xing and L. Huang, *Nano Lett*., **2011**, *11*, 3184; b) L. Huang, B. Gao, G. Hartland, M. Kelly and H. Xing, *Surf. Sci.*, **2011**, *605*, 1657.

Part IV: Conclusions and Appendices

12. Concluding Summary

Some specifically designed inorganic hybrid nanostructures (nanoparticles and graphene) as electrocatalysts in interfacial molecular and biomolecular electron transfer and electrocatalysis have been prepared and used in this project. Emphasis is on both fundamental properties of the nanostructures and on their use in chemical and biological sensing devices, ultra-small even at single nanoparticle or molecular scale. The project is focused on electroactive (or redox) Prussian blue nanoparticles (PBNPs) and its analogues (PBA), as well as graphene and quantum dots for the understanding of fundamental biological charge transport, electronic properties and application in the next generation ultra-sensitive biosensors and other interesting biophysical devices.

6 nm water soluble PBNPs with excellent redox electroactivity have been synthesized and proved to be highly efficient both in interfacial ET and as enzyme-like nanoscale electrocatalysts. Fast and reversible interfacial PBNP four-electron transfer on an Au (111) electrode surface modified with functional alkanethiols was detected by cyclic voltammetry. The ET kinetics can be controlled by adjusting the chain length of amino terminated alkanethiols and depends exponentially on the ET distance, with the decay factor (β) 0.85 per CH_2. This feature suggests a tunneling mechanism and resembles similar observations for redox metalloproteins (cytochrome *c* and azurin)[1] in a similar assembly. The immobilized PBNPs display, further high-efficient electrocatalysis towards the reduction of H_2O_2, and a quantitative relationship between the ET kinetics and electrocatalytic activity.

Secondly, the interfacial electrochemical electron transfer (ET) and electrocatalysis of this PBNPs immobilized on Au(111)-electrode surfaces modified by variable-length differently functionalized thiol-based self-assembled molecular monolayers (SAMs)

were explored. The SAMs were functionalized by positively ($–NH_3^+$) and negatively charged groups ($-COO^-$) as well as neutral hydrophobic groups ($-CH_3$), with decay factors (β) of 0.9, 1.1, and 1.3 per CH_2, respectively. Interfacial ET rate constants and characteristic tunneling decay factors were, further found to follow the order $–NH_3^+ < -COO^- < -CH_3$ for the decay constants and the inverse order for the rate constants. The positively charged terminal group offers clearly the most facile ET route, while the order of the negatively charged and hydrophobic terminal groups is less obvious.

Furthermore, three-dimensional networks of cross-linked [Poly(ethyleneimine) (PEI)] onto which PBNPs are attached by electrostatic forces have been fabricated and assembled on single-crystal Au(111) electrode surfaces to enhance the electrocatalysis process resulting from this 3D nanostructure skeleton. Together with the two-dimensional alkanethiol immobilized PBNPs, the three-dimensional Au(111)/DTSP/PEI/PBNP surface system has offered a new class of well characterized highly efficient substrates for electrocatalytic reduction of H_2O_2 alone and in combination with glucose oxidation, with excellent performance. *In situ* AFM of the different assembled layers in the electrolyte solution shows molecular scale structures on the surface, in keeping with the observed electrochemical behavior.

To increase the conductivity of PBNPs as an active electrode, reduced graphene oxide (RGO) and PBNPs were exploited as building ingredients to prepare with increased electrical conductivity and functional variability nanohybrid electrocatalysts, which were further transformed into free-standing graphene papers. PBNPs doped graphene papers show highly efficient electrocatalysis towards reduction of hydrogen peroxide and can be used alone as flexible chemical sensors for potential applications in detection of hydrogen peroxide or/and other organic peroxides. On the basis of notable advantages of high stability, low cost and efficient electrocatalysis, the as-prepared PBNPs–RGO papers have potential to be produced in a large scale and offers a broad range of possible applications as electron transfer mediators and nanoscale electrocatalysts, particularly in fabrication of flexible sensing devices as well as in electrocatalytic energy conversion.

In addition, the graphene/PBNPs paper obtained using Au filter substrate shows high electrical conductivity, outstanding mechanical strength, excellent thermal stability and structural uniformity. Samples based on graphene mixed with PBNPs in the aqueous solution, and free-standing flexible graphene-PBNPs paper with gold filter as an assist-substrate, have been prepared by vacuum assisted flow-filtration. This type of mixed materials paper has good electrochemical performance and shows high electrocatalytic properties. This variety of flexible active electrode could be freely used for monitoring H_2O_2, glucose or other enzyme detection in the electrocatalysis.

A new method of one-step O/W interface method for fast fabricating large-area graphene nanosheets doped with CdSe QDs on the surface has been developed. This kind of mixed nanomaterials RGO-CdSe QDs shows close interaction between RGO and CdSe QDs, and gives a new fine structure for significant enhancement of photoinduced electron or energy transfer. Fast one-step large-area graphene nanosheets doped with CdSe QDs can therefore be widely used in the field of photovoltaics for photocatalysts and electron or energy transfer.

In the future, the methods of designed inorganic hybrid nanostructures (nanoparticles, graphene and quantum dots) will play an important role in electrocatalysts of interfacial molecular and biomolecular for electron transfer and electrocatalysis. It is further an essential step for promotion of efficient energy storage/conversion and chemical/biological sensing. The development of efficient electrocatalysis of nanomaterial systems will lead to the innovation of electrocatalysts and their operation. Synthesis, characterization, and applications of electrocatalysts are currently approached towards the nanoscale level, and research and development (R&D) are carried out in the context of nanoscience and nanotechnology.

References

[1] Q. J. Chi; J. D. Zhang; J. E. T. Andersen; J. Ulstrup, *J Phys Chem B* **2001**, *105*, 4669-4679.

Appendix A: Publications and Conferences Activities

I. List of Publications

1. **Nan Zhu**, Shuang Han, Jens Ulstrup and Qijin Chi*, "Graphene Paper Doped with Chemically Compatible Prussian Blue Nanoparticles as Nanohybrid Electrocatalyst"
   Advanced Functional Materials. 2013, 23, 5297-5306. (**IF=9.765**)
2. Xian Hao, **Nan Zhu**, Jens Ulstrup and Qijin Chi*, "Direct measurement and modulation of single-molecule coordinative bonding forces in a transition metal complex",
   Nature Communications. 2013, 4, 3121 (pp 1-10). (**IF=10.015**)
3. **Nan Zhu**, Xian Hao, Jens Ulstrup and Qijin Chi*, "Electron Transfer and Electrocatalysis of Prussian Blue Nanoparticles Self-assembled on Modified Au (111) Surfaces", In submitted.
4. **Nan Zhu**, Jens Ulstrup and Qijin Chi*, "Three-dimensional nanostructure of Prussian Blue nanoparticles as biosensors for high electrocatalysis", In submitted.
5. Kaibo Zheng, Karel Žídek, Mohamed Abdellah, **Nan Zhu**, Pavel Chábera, Nils Lenngren, Qijin Chi and Tõnu Pullerits, "Directed Energy Transfer in Films of CdSe Quantum Dots: Beyond Point Dipole Approximation", In submitted.
6. **Nan Zhu**, Jens Ulstrup and Qijin Chi*, "Electron Transfer and electrocatalysis of Prussian Blue Nanoparticles Immobilized on Surfaces with Different Chemical Properties", To be submitted.
7. **Nan Zhu**, Jens Ulstrup and Qijin Chi*, "Gold-substrate graphene paper entrapped Prussian blue nanoparticles of electrocatalysis for biosensors", In preparation.
8. **Nan Zhu**, Kaibo Zheng, Mohamed Abdellah, Tõnu Pullerits, Jens Ulstrup and Qijin Chi*, "Graphene Nanofilms Doped with Quantum Dots for Efficient Promotion of Photoinduced Charge Separation and Electron Transfer", In preparation.

9. Shuang Han, **Nan Zhu**, Jens Ulstrup, Qijin Chi*, "One-step Green Preparation and Polymeric Derivation of RGO Nanosheets for Biocompatible Encapsulation of Enzymes", In preparation.

II. Conference Activities and Experience Study

1. "Exchange Study" in Lund University, Sweden, 01/05/2013-30/06/2013.
2. "8th Workshop in Protein·DTU", DTU, 11/2012.
3. "63rd Annual Meeting of the International Society of Electrochemistry (ISE)" Prague, Czech Republic, Poster Presentation, 08/2012.
4. NanoDay of "5th joint meeting for the nanocenters in the EuroTech Universities Alliance", DTU, Poster Presentation, 06/2012.
5. "XIV. Annual Linz Winter School and Worshop", Linz, Austria, 02/2012.
6. "Joint meeting for members and students from the Nano-Science Center and Nano·DTU" of NanoDay, DTU, Poster Presentation, 09/2011.
7. NanoDay of "Joint meeting for the nanocenters in the EuroTech Universities Alliance", Munich, Germany, Poster Presentation, 06/2011.

III. Awards

1. Awarded "Best Poster Prize" in "63rd Annual Meeting of the International Society of Electrochemistry (ISE)" , Prague, Czech Republic, 2012
2. Technical University of Denmark Funding for Publication (DTU), 2013

Appendix B: The First Pages of Two Representative Publications

1. **Nan Zhu**, Shuang Han, Jens Ulstrup and Qijin Chi*, "Graphene Paper Doped with Chemically Compatible Prussian Blue Nanoparticles as Nanohybrid Electrocatalyst"
   Advanced Functional Materials. 2013, 23, 5297-5306. (**IF=9.765**)

2. Xian Hao, **Nan Zhu**, Jens Ulstrup and Qijin Chi*, "Direct measurement and modulation of single-molecule coordinative bonding forces in a transition metal complex",
   Nature Communications. 2013, 4, 3121 (pp 1-10). (**IF=10.015**)

ADVANCED FUNCTIONAL MATERIALS
www.afm-journal.de

Graphene Paper Doped with Chemically Compatible Prussian Blue Nanoparticles as Nanohybrid Electrocatalyst

*Nan Zhu, Shuang Han, Shiyu Gan, Jens Ulstrup, and Qijin Chi**

Along with reduced graphene oxide (RGO), water soluble Prussian blue nanoparticles (PBNPs, around 6 nm) are synthesized and broadly characterized. These two types of highly stable, low-cost and chemically compatible nanomaterials are exploited as building ingredients to prepare electrically enhanced and functionally endorsed nanohybrid electrocatalysts, which are further transformed into free-standing graphene papers. PBNPs doped graphene papers show highly efficient electrocatalysis towards reduction of hydrogen peroxide and can be used alone as flexible chemical sensors for potential applications in detection of hydrogen peroxide or/and other organic peroxides. The as-prepared PBNPs–RGO papers are further capable of biocompatible accommodation of enzymes for development of free-standing enzyme based biosensors. In this regard, glucose oxidase is used as an example for electrocatalytic oxidation and detection of glucose. The present work demonstrates a facile and highly reproducible way to construct free-standing and flexible graphene paper doped with electroactive catalyst. Thanks to high stability, low-cost and efficient electrocatalytic characteristics, this kind of nanohybrid material has potential to be produced on a large scale, and offers a broad range of possible applications, particularly in the fabrication of flexible sensing devices and as a platform for electrocatalytic energy conversion.

1. Introduction

Graphene papers are a novel type of layered materials emerged very recently. Since the pioneering work reported by Ruoff and co-workers in 2007,[1] graphene paper has added an attractive form to the scientific catalogue of rapidly surging graphene-based nanomaterials. Through wet-chemical methods,[2,3] graphene papers can be made of either graphene oxide (GO) or reduced graphene oxide (RGO) by relatively simple and low-cost procedures that involve synthesis and vacuum filtration of individual and liquid suspended graphene nanosheets.[1] As a free-standing material, graphene paper has several remarkable characters, reflected by practically high electrical conductivity, mechanical robustness, excellent thermal stability, structural uniformity, and geometric flexibility.[1] These features have altogether enabled expanding the application scope of graphene materials to a much wider range of various demands. Several possible applications have been demonstrated mainly at the laboratory level, for example, the use for flexible sensors,[4–9] energy storage,[10–18] biocompatible materials,[19–21] and even antibacterial agents.[22,23] With still limited exploration to date, however, the development of graphene papers and their applications in various areas remain at the infant stage. In the other words, there is plenty of room at the bottom to explore unfulfilled potentials of graphene papers as an advanced materials source. Three major research lines towards this end are anticipated and currently being carried out in parallel: 1) refinement and optimization of preparation procedures to further enhance electrical and mechanical properties,[24–28] 2) high-resolution structural characterization towards the atomic scale understanding of structural features and their relations to physicochemical properties,[29,30] and 3) versatile modifications of graphene papers to endorse specific and new functions.[31]

Functionalization is an essential step for most possible applications of graphene papers, because this material itself lacks desired specific functions such as catalysis, redox activity and molecular recognition. Decoration of graphene paper with nanoparticles (NPs) represents one of the most attractive ways for catalytic functionalization of this material that can be consistently used, for example, for sensing devices and energy conversion. This has been achieved by several different methods such as electrodeposition,[5,6] two-phase interfacial transfer,[7] and polymer-assisted encapsulation,[20] with most studies focused on metallic and metal oxide nanoparticles. Also, in these studies decoration (or modifications) is limited largely to the surface of graphene papers rather than inter-layered integration of functional materials into graphene papers. Recent efforts have offered an alternative approach.[8,31–33] For example, nanoparticles were first mixed with graphene nanosheets to prepare hybrid nanosheets, and this was then followed by flow-directed assembly of these individual hybrid nanosheets into graphene papers. A shortcoming of this approach is the lack of specific and robust interaction between the nanoparticles and graphene

N. Zhu, Dr. S. Han, S. Gan, Prof. J. Ulstrup, Prof. Q. Chi
Department of Chemistry
Technical University of Denmark
DK-2800 Kongens Lyngby, Denmark
E-mail: cq@kemi.dtu.dk

DOI: 10.1002/adfm.201300605

nature COMMUNICATIONS

ARTICLE

Received 26 Jan 2013 | Accepted 6 Jun 2013 | Published 2 Jul 2013

DOI: 10.1038/ncomms3121

Direct measurement and modulation of single-molecule coordinative bonding forces in a transition metal complex

Xian Hao[1,2], Nan Zhu[1], Tina Gschneidtner[3], Elvar Ö. Jonsson[4], Jingdong Zhang[1], Kasper Moth-Poulsen[3], Hongda Wang[2], Kristian S. Thygesen[4], Karsten W. Jacobsen[4], Jens Ulstrup[1] & Qijin Chi[1]

Coordination chemistry has been a consistently active branch of chemistry since Werner's seminal theory of coordination compounds inaugurated in 1893, with the central focus on transition metal complexes. However, control and measurement of metal–ligand interactions at the single-molecule level remain a daunting challenge. Here we demonstrate an interdisciplinary and systematic approach that enables measurement and modulation of the coordinative bonding forces in a transition metal complex. Terpyridine is derived with a thiol linker, facilitating covalent attachment of this ligand on both gold substrate surfaces and gold-coated atomic force microscopy tips. The coordination and bond breaking between terpyridine and osmium are followed *in situ* by electrochemically controlled atomic force microscopy at the single-molecule level. The redox state of the central metal atom is found to have a significant impact on the metal–ligand interactions. The present approach represents a major advancement in unravelling the nature of metal–ligand interactions and could have broad implications in coordination chemistry.

[1] Department of Chemistry, Technical University of Denmark, Kemitorvet, Building 207, DK-2800 Kongens Lyngby, Denmark. [2] State Key Laboratory of Electroanalytical Chemistry, Changchun Institute of Applied Chemistry, Chinese Academy of Sciences, Changchun 130022, China. [3] Department of Chemical and Biological Engineering, Chalmers University of Technology, SE-412 96 Gothenburg, Sweden. [4] Department of Physics, Technical University of Denmark, DK-2800 Kongens Lyngby, Denmark. Correspondence and requests for materials should be addressed to Q.C. (email: cq@kemi.dtu.dk) or to H.W. (email: hdwang@ciac.jl.cn).